Polycrystalline Plasticity: Application to Deformation Processing of Lightweight Metals

by

Srihari Balasubramanian

B.Tech., Mechanical Engineering, Indian Institute of Technology, Madras, 1992
S.M., Mechanical Engineering, Massachusetts Institute of Technology, 1995

Submitted to the Department of Mechanical Engineering
in partial fulfillment of the requirements for the degree of

Doctor of Philosophy

at the

MASSACHUSETTS INSTITUTE OF TECHNOLOGY

February 1998

Author .....
Department of Mechanical Engineering
September 12, 1997

Certified by .....
Lallit Anand
Professor
Thesis Supervisor

Accepted by .....
Ain Sonin
Chairman, Departmental Committee on Graduate Students

Polycrystalline Plasticity: Application to Deformation Processing of Lightweight Metals

by

Srihari Balasubramanian

Submitted to the Department of Mechanical Engineering
on September 12, 1997, in partial fulfillment of the
requirements for the degree of
Doctor of Philosophy

Abstract

The major cause of anisotropic plastic response in polycrystalline metals is crystallographic texturing resulting from the reorientation of the crystal lattices of grains during deformation. There has been considerable recent progress in the continuum modeling of texture effects on the plastic deformation of polycrystalline materials. Most of the previous work is based on a simple power-law description for the shearing rates on the crystallographic slip systems. Although this is a useful description of the viscoplastic response of crystals in a narrow range of strain rates and temperatures, it is not able to capture the real strain-rate and temperature sensitivity of flow of crystalline materials under high strain rates and/or low temperatures.

A physically motivated constitutive function based on the thermally-activated theory for plastic flow in face-centered-cubic (f.c.c.) materials together with the slip system hardening equations has been incorporated in a polycrystalline plasticity model. The constitutive model has been implemented in a finite element program to facilitate simulations of quasi-static as well as dynamic non-homogeneous deformations of polycrystalline f.c.c. materials. The material parameters in the model have been determined by calibrating it against existing experimental data for aluminum. The physical description for the plastic flow enables the model to reproduce the macroscopic stress-strain response and crystallographic texture evolution upto large strains ($\approx 100\%$) for a wide range of strain-rates (10^{-3} - 10^{2} sec^{-1}) and temperatures (77 - 298 K). The important differences in the behavior of f.c.c. and b.c.c. materials with regards to strain hardening and strain-rate and temperature history effects are also shown to be captured by the constitutive model.

In order to evaluate the applicability of the crystal plasticity model to actual deformation processing operations, the phenomenon of formation of earing defects in cup-drawing has been studied. Cup-drawing experiments were carried out on aluminum 2008-T4 sheets. The predictions from the model for the load-displacement response, the number of ears, their locations, and heights are shown to be in very good *quantitative* agreement with the experiments.

The recent progress in the formulation of a mathematical theory of polycrystalline plasticity has occurred primarily for materials with cubic structure. Much less work of this type has been carried out for materials with hexagonal-close-packed (h.c.p.) crystal structure, e.g., titanium. A large deformation, crystal-plasticity based constitutive model for high-temperature deformation of titanium has been developed. The constitutive model and the computational procedures have been implemented in a finite-element

scheme. Nominally homogeneous experiments have been conducted on commercially-pure titanium at 750°C, and the resulting macroscopic stress-strain response and evolution in crystallographic texture have been measured. Full 3D finite element simulations of these deformation modes have also been carried out. The predictions are in very good agreement with the corresponding experimental measurements.

Thesis Supervisor: Lallit Anand
Title: Professor

Acknowledgments

The past five years at MIT have been very stimulating and enriching. I would like to express my sincere acknowledgements to everyone whose input has proved invaluable in my endeavor. I begin by thanking my thesis advisor and mentor, Prof. Lallit Anand, without whose guidance and encouragement this work would not have been possible. Discussions with him have always been educative. I am very grateful to him for helping me hone my analytical skills. He has instilled in me the motivation and confidence necessary to pursue a career in research and I am very thankful to him for the same. I express my sincere thanks to Prof. Ali Argon, Prof. David Parks and Prof. Jung-Hoon Chun for serving on my thesis committee. Their thoughtful and insightful suggestions have been very helpful in my research. I would also like to thank Prof. David Hardt for kindly allowing me to perform the deep-drawing experiments at the Laboratory for Manufacturing Productivity and Dr. Barlat at ALCOA Technical Center who kindly provided us the aluminum sheets.

Research support for this work was provided by U. S. National Science Foundation under Grant Numbers 9215246-DDM and CMS-9610130.

I am grateful to my colleagues in the Mechanics and Materials Lab, Manish Kothari, Clarence Chui, Brian Gally, Suryaprakash Ganti, Chunguang Gu, Chuang-Chia Lin, Hong Dai, Prakash Thamburaja, Michael Kim, Brian Gearing, Ronald Rezac, Alexander Staroselsky, Oscar Yeh for their fruitful discussions and help, technical and otherwise. They were instrumental in making the five years very enjoyable. I would like to thank my close friend and colleague, Manish Kothari, for his important contributions in my work. I owe him a debt of gratitude for being patient in teaching me valuable experimental skills. I thank Ray Hardin for his help and patience. I acknowledge Peter Morley at the Laboratory for Nuclear Science Machine Shop, for his kind help in designing experimental setups and machining test specimens.

My special thanks go to my parents, brother, sister-in-law and sister whose affection and constant encouragement has given me tremendous impetus in my academic pursuits.

Contents

Chapter 1

Introduction

The major factors that influence the degree of deformation that can be achieved in any deformation processing operation without failure are: (*i*) the external *process* variables such as stress, temperature, strain, strain rate, frictional and heat-transfer boundary conditions and their evolution and (*ii*) the internal *microstructural* features such as porosity, crystallographic texture, deformation localization and their evolution. In order to optimize a particular deformation processing scheme (Process Design) and/or to improve the performance of a structural component (Product Design), a complete understanding of the individual effects of these factors and their interactions is desired. This investigation is aimed at developing accurate anisotropic thermo-elastic-viscoplastic constitutive equations and computational procedures for the modeling and simulation of inelastic deformations in some industrially important face-centered-cubic (f.c.c.) and hexagonal-close-packed (h.c.p.) metals and alloys. The computational capability will be useful in simulating the development of anisotropy due to the evolution of crystallographic texture and the development of some material processing defects such as earing in cup-drawing associated with the evolution in texture during deformation processing.

The major cause of anisotropic plastic response in polycrystalline metals is crystallographic texturing resulting from the reorientation of the crystal lattices of grains during deformation. There has been considerable recent progress in the continuum modeling of texture effects on the plastic deformation of polycrystalline materials (e.g., Gil Sevillano *et al.* [1980]; Wenk [1985]; Asaro and co-workers [1983a, 1983b, 1988, 1989], Anand and co-workers [1992, 1994], Dawson and co-workers [1989, 1990, 1994]; and various proceedings

of ICOTOM [1991]). The theory is able to predict the macroscopic anisotropic stress-strain response, shape changes and the evolution of crystallographic texture in complex deformation modes.

Most of the previous work on crystal plasticity is based on a simple power-law description for the shearing rates $\dot{\gamma}^\alpha$ on the slip systems:

$$\dot{\gamma}^\alpha = \dot{\gamma}_0 \left| \frac{\tau^\alpha}{s^\alpha} \right|^{1/m} \text{sign}(\tau^\alpha) \tag{1.1}$$

In the equation above, τ^α is the resolved shear stress on the slip system, and $s^\alpha (> 0)$ is the slip system deformation resistance. The parameter $\dot{\gamma}_0$ is a reference rate of shearing, and the parameter m characterizes the material rate sensitivity. The rate-independent limit is $m \to 0$. The slip system shear rate is uniquely specified by this equation, and is nonvanishing as long as the resolved shear stress τ^α on that system is not identically zero. Although this simple power-law description is a useful simplification of the viscoplastic response of crystals in a narrow range of strain-rates and temperatures, it is not able to capture the real strain-rate and temperature sensitivity of flow of crystalline materials under dynamic loading conditions and/or low homologous temperatures. Deformation processing operations are typified by wide range of strain-rates ($10^{-3} - 10^3 \text{sec}^{-1}$) and temperatures ($0.2\,\theta_m - 0.6\,\theta_m$). Hence, there is a need for an improved kinetic equation for plastic flow, and this issue is addressed in this work.

The recent progress in the formulation of a mathematical theory of polycrystalline plasticity has occurred primarily for materials with cubic structure. Much less work of this type has been accomplished for materials with hexagonal-close-packed crystal structure. Titanium is a h.c.p. metal which serves as an excellent candidate for applications demanding high strength and light-weight. The development of constitutive models and computational procedures for simulating the deformation processing of titanium is of substantial technological importance.

The hexagonal materials, owing to their lower symmetry in comparison with the f.c.c. materials, exhibit more complex modes of deformation. Inelastic deformation by slip in hexagonal materials at the single-crystal level is highly anisotropic, *i.e.*, the deformation resistances of different classes of slip systems can be substantially different. Also, due to the difficulty in operating certain slip systems at low homologous temperatures the

accomodation of arbitrary strains through deformation twinning is quite common in these materials. As a result of mechanical twinning, the yield loci of textured h.c.p. materials are usually not centered around the origin in stress space. Plane stress yield loci for sheets of titanium are given by Lee and Backofen [1966].

This work is focused on the plastic deformation of h.c.p. titanium. Titanium exists in two allotropic forms: the α-phase which has a h.c.p. structure, and the β-phase which has a b.c.c. structure. In pure titanium, the h.c.p. α-phase is stable up to 883^oC, the β *transus temperature*, above which it transforms to the b.c.c. β-phase. The most common slip modes that have been reported in pure h.c.p. titanium are the prismatic slip systems $\{10\bar{1}0\} < 11\bar{2}0 >$, the pyramidal slip systems $\{10\bar{1}1\} < 11\bar{2}0 >$ and the basal slip systems $(0001) < 11\bar{2}0 >$ with a marked difference in their slip system deformation resistances (Rosi *et al.* [1953]; Churchman [1954]).

Two important factors that influence the nature of plastic deformation in titanium are the temperature and the impurity content. Conrad [1981] observed a dramatic decrease in the critical resolved shear stress with temperature for basal and prismatic slip in single crystals of h.c.p. titanium. Also, the ratio of the critical resolved shear stress for these two families of slip systems changes significantly with temperature. The studies of slip traces by Rosi, Dube and Alexander [1953] showed no evidence of basal slip at room temperature owing to the large critical resolved shear stress associated with the basal slip system at this temperature. At higher temperatures, the critical resolved shear stress for both types of slip become less disparate, which then allows for the possibility of slip on either of the planes. Rosi, Perkins and Seigle [1956] observed that the propensity for pyramidal slip along $< 11\bar{2}0 >$ directions also increased with increase in temperature.

The studies by Churchman [1954] and Conrad [1981] indicate that the nature of plastic deformation in titanium is significantly affected by the presence of impurities like nitrogen, oxygen, carbon and hydrogen. These authors noticed that an increase in impurity content affected not only the critical resolved shear stresses on the slip systems but also their relative values.

The $< \mathbf{a} >$-slip on the basal, prismatic and pyramidal slip systems does not provide for a mechanism for strain parallel to the **c**-axis of the crystals. Other slip or twin systems are required to supply this missing degree of kinematic freedom. These additional mechanisms, whether pyramidal slip on systems with $< \mathbf{c}+\mathbf{a} >$ slip-directions or twinning, have a

strong influence on the overall inelastic behavior of the polycrystal. At low temperatures, due to the inability in activating $< \mathbf{c} + \mathbf{a} >$-slip, most of the deformation is accomodated through twinning. The two common twinning modes for titanium that have been observed at room temperature are the six equivalent "tensile" systems $\{10\bar{1}2\} < \bar{1}011 >$, and the six equivalent "compressive" systems $\{11\bar{2}2\} < 11\bar{2}\bar{3} >$; the first set of twinning systems produces an extension parallel to the **c**-axis, and the second a shortening. Paton and Backofen [1970] have reported that other twin systems are operational at elevated temperatures ($> 400°$C), namely, the tensile systems $\{11\bar{2}1\} < \bar{1}\bar{1}26 >$ and $\{11\bar{2}3\} < \bar{1}\bar{1}22 >$ and the compressive systems $\{11\bar{2}4\} < 22\bar{4}3 >$ and $\{10\bar{1}1\} < 10\bar{1}2 >$. However, the tendency for titanium crystals to twin decreases with increase in temperature. At high temperatures, slip along $< 11\bar{2}3 >$ directions ($< \mathbf{c} + \mathbf{a} >$-slip) on pyramidal planes of the $\{10\bar{1}1\}$ and $\{11\bar{2}2\}$ families has been observed to provide straining along the **c**-axis (Paton and Backofen [1970]; Williams and Blackburn [1968]). Above 700°C, the mechanism of plastic deformation seems to be predominantly crystallographic slip. This can be attributed to the ease of operation of $< \mathbf{a} >$-slip on all the three slip-planes at these temperatures, plus $< \mathbf{c} + \mathbf{a} >$-slip on the pyramidal systems.

Crystal mechanics based treatments of plasticity of titanium are incomplete and scattered. There does not exist a coherent set of data — stress-strain curves[1], microstructure, and crystallographic texture evolution under controlled simple tension/compression, plane strain compression and torsion. Further, the constitutive modeling of the deformation of polycrystalline titanium taking into account the variety of deformation modes is still an active field of research. The deformation resistances of different classes of slip systems can be substantially different. In this context, a Taylor approximation in which each grain is assumed to undergo the same deformation as the polycrystalline aggregate would yield incorrect macroscopic stress-strain response. Hutchinson [1977] proposed a self-consistent scheme[2] that allows for variations in deformation from grain to grain depending on the orientations. Accordingly, grains whose **c**-axes are aligned along

[1]Doner and Conrad [1973] provide stress-strain curves of CP-Titanium in the high-temperature regime (0.31 to 0.59 θ_m) while dynamic stress-strain curves of CP-Titanium at low temperatures are provided by Eleiche [1980]. However, the measurements of texture in conjunction with the stress-strain response are lacking.

[2]Self-consistent theory (Hill [1965]) assumes that each grain is a spherical inclusion embedded in an infinite matrix whose properties are those desired of the polycrystal. The overall stress and strain-rate are determined by self-consistent averaging over all grain orientations.

the loading direction are "hard" inclusions that do not deform while the grains in "softer" orientations undergo deformation. Hutchinson has applied this model to provide estimates for the overall uniaxial yield stress of a polycrystalline aggregate for different ratios of critical resolved shear stress of the basal and prismatic slip systems. Hutchinson's analysis is limited to small strains and does not deal with the aspects of texture development with large straining of hexagonal crystals. Parks and Ahzi [1990] have proposed a Taylor-type rigid-viscoplastic "constrained-hybrid" model which not only accounts for the local kinematic constraints in hexagonal crystals lacking five independent slip systems but also provides a method to calculate the "kinematically indeterminate" part of the deviatoric stress tensor. The model has been used to accurately predict the deformation textures as well as macroscopic stress-strain response in polymers with orthorhombic structure e.g., High-density Polyethylene. Shoenfeld *et al.* [1995] have extended the same model to account for elasticity. Recently, Prantil, Jenkins and Dawson [1995] have formulated a model for simulating the large deformation behavior of polycrystalline titanium under slip-dominated conditions. However, the predictions of their analyses have not been compared with experimental results.

With this as background, the following tasks have been accomplished in this work:

1. A physically-motivated constitutive function based on the thermally-activated theory of plastic flow in f.c.c. and b.c.c. materials together with the slip system hardening equations are presented in Chapter 2. These constitutive equations have been incorporated in a large deformation Taylor-type crystal plasticity model. The constitutive model has been implemented in a "static,implicit" finite element program (ABAQUS/Standard) as well as in a "dynamic,explicit" finite element program (ABAQUS/Explicit).

2. In Chapter 2, the ability of the constitutive model to reproduce the macroscopic stress-strain response and the crystallographic texture evolution in f.c.c. aluminum for strains up to 100%, at strain rates from 10^{-3} to 10^{3}sec^{-1} and at temperatures from 77K to 298K are evaluated. The capability of the model to describe important differences in the behavior of f.c.c. and b.c.c. materials with regards to strain-hardening and strain-rate and temperature history effects has also been investigated.

3. In Chapter 3, the constitutive equations and computational procedures are used to simulate the formation of earing defects during cup-drawing of face-centered cubic materials. The results of the numerical simulations have been compared with existing experimental

results on earing in single crystalline sheets of aluminum. In order to be useful in improving designs of the cup-drawing process, a quantitative prediction of the location and the heights of the ears is desired. To achieve this end, quasi-static cup-drawing experiments have been conducted on sheets of Al2008-T4 with an initial anisotropic texture. Numerical simulations of the deep-drawing process have also been performed, and the predictions of the earing profile and loads are compared with the same from the experiments.

4. In Chapter 4, results from simple tension, simple compression, plane-strain compression and torsion experiments conducted on commerically-pure polycrystalline titanium in the vicinity of 750°C are described. A large-deformation constitutive model for high temperature deformation of single-crystal titanium is presented. The predictions of the stress-strain response and lattice reorientation in simple tension of a titanium single crystal are compared with existing experimental results. Full 3D finite-element calculations, where each element represents a grain and the constitutive response is given through a single-crystal constitutive model, have been performed. The slip systems operative during high-temperature deformation of polycrystalline CP-Titanium are identified. The ability of the constitutive model to predict the texture evolution and macroscopic stress-strain response up to large strains for the different deformation modes are evaulated.

The conclusions and suggestions for future work are presented in Chapter 5.

Chapter 2

Plasticity of Polycrystalline F.C.C. and B.C.C. materials

In this chapter, a finite-deformation, rate- and temperature-dependent constitutive model for plasticity of single crystals of face-centered-cubic (f.c.c.) and body-centered-cubic (b.c.c.) materials is first described. For the shearing rates on slip systems, a physically-motivated constitutive function based on the thermally-activated theory for plastic flow is employed. For polycrystalline materials, the classical Taylor assumption is invoked. The implementation of the constitutive model in a finite-element program is briefly discussed. A procedure for estimating the material parameters in the model is described, and the predictions of the stress-strain response and texture evolution are compared with corresponding experimental results. Face-centered-cubic aluminum and body-centered-cubic tantalum are taken as representative model materials. Important differences in the behavior of the two model materials with regards to strain-hardening and strain-rate and temperature history effects are highlighted and the capability of the constitutive model to describe the distinguishing behaviors is demonstrated.

2.1 Single Crystal Constitutive Model

The foundations for the constitutive model for single crystal elasto-plasticity considered here may be traced to the papers by Teodosiu [1970], Rice [1971], Hill and Rice [1972], Mandel [1974], Teodosiu and Sidoroff [1976], Asaro and Rice [1977] and Asaro [1983a, 1983b] from a continuum mechanics viewpoint, and Conrad [1964], Kocks *et al.* [1975], Frost and

Ashby [1982] and Argon [1995] from a materials science viewpoint.

The deformation of a crystal is taken as the sum of contributions from two independent atomic mechanisms: (*i*) an overall "elastic" distortion of the lattice, and (*ii*) a "plastic" deformation that does not disturb the lattice geometry. In a large range of low (< 0.3) homologous temperatures and at sufficiently high stress levels, the major mechanism of plastic deformation in ductile single crystals is dislocation glide on well-defined crystallographic slip systems in the crystal. Attention is confined to this type of plastic deformation.

The governing variables in the constitutive model are: (*i*) The Cauchy stress, $\mathbf{T}$. (*ii*) The deformation gradient, $\mathbf{F}$. (*iii*) The absolute temperature θ. (*iv*) Crystal slip systems, labeled by integers α. Each slip system is specified by a unit normal $\mathbf{n}_o^\alpha$ to the slip plane, and a unit vector $\mathbf{m}_o^\alpha$ denoting the slip direction. The slip systems $(\mathbf{m}_o^\alpha, \mathbf{n}_o^\alpha)$ are assumed to be known in the reference configuration. (*iv*) A plastic deformation gradient, $\mathbf{F}^p$, with $\det\mathbf{F}^p = 1$. (*v*) The slip system deformation resistance $s^\alpha > 0$, with units of stress.

An elastic deformation gradient is defined by

$$\mathbf{F}^e \equiv \mathbf{F}\,\mathbf{F}^{p-1}, \qquad \det\mathbf{F}^e > 0. \tag{2.1}$$

This equation may be rearranged as $\mathbf{F} = \mathbf{F}^e\,\mathbf{F}^p$. The plastic part $\mathbf{F}^p$ in this multiplicative decomposition of $\mathbf{F}$ represents the cumulative effect of dislocation motion on the active slip systems in the crystal, and the elastic part $\mathbf{F}^e$ describes the elastic distortion of the lattice.

Next, with $\bar{\mathbf{S}} = (\det\mathbf{F})\mathbf{T}\mathbf{F}^{-T}$ denoting the first Piola-Kirchoff stress, the stress power per unit reference volume is $\dot{\omega} = \bar{\mathbf{S}} \cdot \dot{\mathbf{F}}$, which, since $\det\mathbf{F}^p = 1$, is also equal to the stress power per unit volume of the isoclinic relaxed configuration determined by $\mathbf{F}^p$. This stress power may be additively decomposed as $\dot{\omega} = \dot{\omega}^e + \dot{\omega}^p$, where $\dot{\omega}^e = \mathbf{T}^* \cdot \dot{\mathbf{E}}^e$ is the elastic stress power per unit volume of the relaxed configuration, with

$$\mathbf{E}^e \equiv (1/2)\left\{\mathbf{F}^{eT}\mathbf{F}^e - 1\right\} \quad \text{and} \quad \mathbf{T}^* \equiv (\det\mathbf{F}^e)\,\mathbf{F}^{e-1}\mathbf{T}\mathbf{F}^{e-T} \tag{2.2}$$

the Green elastic strain measure and the symmetric second Piola-Kirchoff stress tensor relative to the relaxed configuration, respectively, and

$$\dot{\omega}^p = (\mathbf{C}^e\,\mathbf{T}^*) \cdot \left(\dot{\mathbf{F}}^p\,\mathbf{F}^{p-1}\right), \qquad \mathbf{C}^e \equiv \mathbf{F}^{eT}\mathbf{F}^e, \tag{2.3}$$

is the plastic stress power per unit volume of the relaxed configuration.

2.1.1 Constitutive Equation For Stress

Elastic stretches in metallic single crystals are generally small. Temperature changes need not be small, but for simplicity attention here is restricted to small temperature changes about a reference temperature θ_0. Accordingly, the constitutive equation for the stress in a metallic single crystal is taken as the linear relation

$$\mathbf{T}^* = \boldsymbol{\mathcal{C}}\,[\mathbf{E}^e - \mathbf{A}\;(\theta - \theta_0)]\,, \tag{2.4}$$

where $\boldsymbol{\mathcal{C}}$ is a fourth-order anisotropic elasticity tensor, and $\mathbf{A}$ is a second-order anisotropic thermal expansion tensor. Also, $\mathbf{E}^e$ and $\mathbf{T}^*$ are the strain and stress measures defined in equation (2.2).

2.1.2 Flow Rule

The evolution of the plastic deformation gradient is given by

$$\dot{\mathbf{F}}^p\mathbf{F}^{p-1} = \sum_\alpha \dot{\gamma}^\alpha\,\mathbf{S}_0^\alpha, \qquad \mathbf{S}_0^\alpha \equiv \mathbf{m}_0^\alpha \otimes \mathbf{n}_0^\alpha, \tag{2.5}$$

where $\mathbf{S}_0^\alpha$ is the Schmid tensor, and

$$\dot{\gamma}^\alpha = \rho_m^\alpha\, b\, \bar{v}^\alpha \tag{2.6}$$

is the plastic shearing rate on the α-th slip system. The expression $\dot{\gamma} = \rho_m\, b\, \bar{v}$ is due to Orowan [1940], and it represents the physical picture that the strain rate $\dot{\gamma}$ is produced by a density ρ_m of mobile dislocations with Burgers vector magnitude b (in the slip direction $\mathbf{m}_0$), moving with an average velocity $\bar{v}$ through a field of obstacles.

Using (2.5) and (2.3), the *resolved shear stress* τ^α for the slip system α is defined through the relation $\dot{\omega}^p = \sum_\alpha \tau^\alpha \dot{\gamma}^\alpha$, which yields

$$\tau^\alpha \equiv (\mathbf{C}^e\,\mathbf{T}^*)\cdot\mathbf{S}_0^\alpha. \tag{2.7}$$

With the resolved shear stress so defined, the average dislocation velocity on the slip system

α is taken to be governed by a constitutive function,

$$\bar{v}^\alpha = \hat{\bar{v}}^\alpha (\tau^\alpha, \theta, s^\alpha), \tag{2.8}$$

where

$$s^\alpha = \hat{s}^\alpha(\theta, \text{microstructural state}) > 0$$

is a temperature dependent *critical slip resistance* (units of stress) for the slip system α. The average dislocation velocity $\bar{v}^\alpha$ at applied shear stress τ^α and a temperature θ depends on the waiting time of mobile dislocations at obstacles, and s^α reflects the strength, density and arrangement of these obstacles.

The constitutive equation for the average dislocation velocity is formulated as follows. At a temperature of absolute zero let $\hat{s}^\alpha(0)$ denote the critical slip resistance; then the sign of $\bar{v}^\alpha$ is the same as that of the resolved shear stress τ^α, and its magnitude is idealized as

$$|\bar{v}^\alpha| = \left\{ \begin{array}{lll} 0 & & \text{if } |\tau^\alpha| < \hat{s}^\alpha(0), \\ > 0 \quad \text{(and large)} & & \text{if } |\tau^\alpha| = \hat{s}^\alpha(0), \end{array} \right\} \tag{2.9}$$

with stress levels $|\tau^\alpha| > \hat{s}^\alpha(0)$ unattainable. The slip resistance $\hat{s}^\alpha(0)$ at absolute zero is called the *mechanical threshold* (Kocks *et al.* [1975]; Argon [1995]). Because of the usual variability of the microstructural state of real materials the transition from no dislocation velocity to a high velocity will not be as sharp as idealized in equation (2.9), but it should still exhibit a "threshold" behavior. At a temperature $\theta > 0$ this response is modified in two important ways. First, since the underlying mechanism which governs the magnitude of s^α is an elastic interaction on the atomic scale of a mobile dislocation segment with the microstructural state, an increase in temperature results in a decrease in the magnitude of s^α, primarily due to the attendant decrease in the elastic moduli, that is $\hat{s}^\alpha(\theta) < \hat{s}^\alpha(0)$. Second, and more importantly, with increasing temperature the local energy barriers to dislocation motion due to *short-range* obstacles (less than $\approx$10 atomic diameters) can be overcome at a lower applied shear stress with the help of thermal fluctuations, and a finite dislocation velocity should be observable below the slip resistance s^α. Accordingly, it is useful to distinguish between barriers that can be overcome with the aid of thermal fluctuations, and those that cannot — *thermal* and *athermal*, respectively; and to assume

that the slip resistance s^α is decomposable as

$$s^\alpha = s_*^\alpha(\theta, \text{microstructural state}) + s_a^\alpha(\theta, \text{microstructural state}), \tag{2.10}$$

where s_*^α represents the part of the resistance due to thermally-activatable obstacles to slip, and s_a^α the part of the resistance due to the athermal obstacles to slip. Typical examples of athermal barriers are dislocation groups and large incoherent precipitates, whereas the Peierls resistance, solute atoms, and forest dislocations typify thermally-activatable barriers. In pure f.c.c. and h.c.p. materials the dislocations glide easily without any appreciable Peierls resistance, and s_*^α is governed by interactions with localized forest dislocations. In pure b.c.c. crystals, s_*^α is controlled by the interactions with the Peierls resistance, which increases rapidly with decreasing temperature.

Let

$$\tau_*^\alpha \equiv |\tau^\alpha| - s_a^\alpha \tag{2.11}$$

denote an *effective stress*, then equation (2.8) is modified as

$$\bar{v}^\alpha = \hat{\bar{v}}^\alpha(\tau_*^\alpha, \theta, s_*^\alpha) \tag{2.12}$$

At temperatures $\theta > 0$ the motion of the mobile dislocation segments is thermally activated. Using the framework of transition-state theory (e.g. Krausz and Eyring [1975]), with ΔG_*^α denoting the difference in the free enthalpy between the saddle point and the ground point for a shear increment, the quantity $\left[\exp\left\{-\frac{\Delta G_*^\alpha}{k_B\theta}\right\}\right]$ is the probability that a thermal fluctuation of the required energy (or larger) for a shear increment can be supplied at a temperature $\theta > 0$. ΔG_*^α is called the *activation free enthalpy* or the *Gibbs' free energy for activation*, and k_B is the Boltzmann's constant. The rate at which dislocations overcome the obstacles is given by $\nu\left[\exp\left\{-\frac{\Delta G_*^\alpha}{k_B\theta}\right\}\right]$, where ν is a characteristic frequency factor of the order of 10^{12}sec^{-1} (10^{-2} - 10^{-1} times the Debye frequency of atoms). Then, with $\bar{l}^\alpha$ denoting the mean distance of advance of a mobile dislocation segment, the magnitude of the average dislocation velocity may be written as

$$|\bar{v}^\alpha| = \left\{ \begin{array}{ll} 0 & \text{if } \tau_*^\alpha \leq 0, \\ \bar{l}^\alpha \nu \exp\left\{-\frac{\Delta G_*^\alpha(\tau_*^\alpha, s_*^\alpha)}{k_B\theta}\right\} & \text{if } 0 < \tau_*^\alpha < s_*^\alpha, \end{array} \right\} \tag{2.13}$$

using which, the shearing rates may be written as

$$\dot{\gamma}^\alpha = \left\{ \begin{array}{ll} 0 & \text{if } \tau_*^\alpha \leq 0, \\ \dot{\gamma}_0^\alpha \exp\left\{ -\frac{\Delta G_*^\alpha(\tau_*^\alpha, s_*^\alpha)}{k_B \theta} \right\} \text{sign}(\tau^\alpha) & \text{if } 0 < \tau_*^\alpha < s_*^\alpha, \end{array} \right\}, \tag{2.14}$$

with

$$\dot{\gamma}_0^\alpha = \rho_m^\alpha \, b \, \bar{l}^\alpha \, \nu.$$

Henceforth, for simplicity, the pre-exponential term $\dot{\gamma}_0^\alpha$ is taken to be the same for all slip systems, and is denoted by $\dot{\gamma}_0$. This pre-exponential term has a typical magnitude of $\dot{\gamma}_0 \approx 10^6$ to 10^7sec^{-1}. Also, the mobile dislocation density, which contributes to $\dot{\gamma}_0$, is expected to be a function of the applied stress and the temperature (Kocks *et al.* [1975]), but any such dependence is neglected here.

The considerations of Kocks *et al.* [1975] (also see Frost and Ashby [1982]) concerning the nature of the activation free enthalpy suggest that ΔG_*^α may be expressed as

$$\Delta G_*^\alpha = \Delta F_* \left[1 - \left(\frac{\tau_*^\alpha}{s_*^\alpha} \right)^p \right]^q, \tag{2.15}$$

where ΔF_*, the activation free energy required to overcome the obstacles to slip without the aid of an applied shear stress, is taken to be the same for all slip systems and is expected to remain constant provided the character of the obstacles does not change. ΔF_* typically lies in the range

$$0.05 \leq \frac{\Delta F_*}{\mu b^3} \leq 2, \tag{2.16}$$

with μ denoting an appropriate shear modulus for anisotropic materials; for example, $\mu \approx \sqrt{0.5(C_{11} - C_{12})C_{44}}$ for a f.c.c. material and $\mu \approx C_{44}$ for a b.c.c. material, where (C_{11}, C_{12}, C_{44}) are the elastic moduli for a cubic crystal. The quantities p and q are suggested to lie in the ranges

$$0 \leq p \leq 1, \quad \text{and} \quad 1 \leq q \leq 2, \tag{2.17}$$

and they control the shape of the ΔG_*^α versus $\left(\frac{\tau_*^\alpha}{s_*^\alpha} \right)$ curve.

Note that for the case of non-zero plastic shearing rates we may write

$$|\tau^\alpha| = s_a^\alpha + Z\left(\theta, |\dot{\gamma}^\alpha|\right) s_*^\alpha, \tag{2.18}$$

where

$$Z = \left[1 - \left(\frac{\theta}{\theta_c}\right)^{1/q}\right]^{1/p} \leq 1, \quad \text{with} \quad \theta_c = \left\{\frac{\Delta F_*}{k_B \ln\left(\frac{\dot{\gamma}_0}{|\dot{\gamma}^\alpha|}\right)}\right\}. \tag{2.19}$$

These equations show the temperature and strain rate sensitivity of resolved shear stress at a *fixed* value of the deformation resistance $s^\alpha = s^\alpha_* + s^\alpha_a$, Fig. 2-1. At $\theta = 0$ the parameter $Z = 1$, and at $\theta = \theta_c$, $Z = 0$. That is, at temperatures above θ_c there is enough thermal energy for the barriers to be overcome by thermal activation alone, without the aid of a stress. At a given strain rate $\dot{\gamma}^\alpha$, the temperature θ_c sets the limit of applicability of the thermal-activation model for the plastic flow of metals at low homologous temperatures.

2.1.3 Evolution Equations For Slip System Resistances

The slip system resistance parameters s^α are taken to evolve according to

$$\dot{s}^\alpha = \sum_\beta h^{\alpha\beta} \left|\dot{\gamma}^\beta\right|,$$

where $\dot{\gamma}^\beta$ is the shearing rate on slip system β, and the matrix $h^{\alpha\beta}$ describes the rate of increase of the deformation resistance on slip system α due to shearing on slip system β; it describes both self-hardening and latent hardening of the slip systems. The use of the absolute value of $\dot{\gamma}^\beta$ in the hardening equation reflects the assumption that the hardening behavior is not significantly affected by the direction of shearing on a slip system. Each element $h^{\alpha\beta}$ depends on the deformation history.

Since s^α has been decomposed as

$$s^\alpha = s^\alpha_*(\theta, \text{microstructural state}) + s^\alpha_a(\theta, \text{microstructural state}),$$

it is important to distinguish whether the source of macroscopic strain hardening is due to the change of s^α_* or s^α_a, or both.

For pure f.c.c. materials, since the magnitudes of both s^α_* and s^α_a are controlled by the interactions of glide dislocations with forest dislocations (Argon and East [1979]), both s^α_* and s^α_a evolve with strain and contribute to the macroscopic strain hardening. Cottrell and Stokes [1955] performed temperature-jump tension tests on aluminum single crystals oriented for single slip. Fig. 2-2 is a schematic representation of their measured stress-strain

curves. In Cottrell and Stokes' experiments, let σ_1 and σ_2, respectively, denote the flow stresses immediately before and after the temperature-jump from θ_1 to θ_2. Let ϵ be the tensile strain at which the temperature-jump is performed. They report that the ratio of the flow stresses $\frac{\sigma_2}{\sigma_1}$ obtained by changing the temperature from θ_1 to θ_2 ($< \theta_1$) was essentially *independent* of the level of strain at which the ratio was measured. That is, with $\frac{\sigma_2}{\sigma_1}$ and $\frac{\sigma_2'}{\sigma_1'}$ denoting the stress ratios measured in temperature jump experiments at strains ϵ and ϵ', respectively,

$$\frac{\sigma_2}{\sigma_1} \approx \frac{\sigma_2'}{\sigma_1'}. \tag{2.20}$$

Let the resolved shear stress on the primary slip system corresponding to the flow stress levels of σ_1, σ_2, σ_1' and σ_2' be τ_1, τ_2, τ_1' and τ_2' respectively. Since the Schmid factor pertaining to this slip system is the same immediately before and after the temperature-jump, equation (2.20) can be rewritten as

$$\frac{\tau_2}{\tau_1} \approx \frac{\tau_2'}{\tau_1'}. \tag{2.21}$$

Substituting for the expression for the resolved shear stress (2.18) in equation (2.21), we obtain,

$$\frac{1 + \left(\frac{s_*}{s_a}\right) Z(\dot{\gamma}, \theta_2)}{1 + \left(\frac{s_*}{s_a}\right) Z(\dot{\gamma}, \theta_1)} \approx \frac{1 + \left(\frac{s_*'}{s_a'}\right) Z(\dot{\gamma}, \theta_2)}{1 + \left(\frac{s_*'}{s_a'}\right) Z(\dot{\gamma}, \theta_1)} \tag{2.22}$$

where s_* and s_a are the thermal and athermal parts of the slip resistance at the tensile strain ϵ respectively and s_*' and s_a' are the corresponding quantities at the tensile strain ϵ'. Equation (2.22) implies that

$$\frac{s_*}{s_a} \approx \frac{s_*'}{s_a'}. \tag{2.23}$$

Since ϵ and ϵ' were arbitrary, *the ratio $\frac{s_*}{s_a}$ is essentially independent of the strain.* This ratio is denoted by the parameter χ, and for simplicity, χ is assumed to be the same for all the slip systems:

$$\chi = \frac{s_*^\alpha}{s_a^\alpha}. \tag{2.24}$$

Cottrell and Stokes' experimental observations suggest that χ lies in the range

$$0.5 \leq \chi \leq 1$$

for aluminum single crystals.

Using the relation (2.24) the evolution equation for s^α for f.c.c. crystals may be written as

$$\dot{s}^\alpha = \dot{s}_a^\alpha + \dot{s}_*^\alpha \doteq \dot{s}_a^\alpha \{1 + \chi\} = \sum_\beta h^{\alpha\beta} \left|\dot{\gamma}^\beta\right|. \tag{2.25}$$

In contrast with the behavior of f.c.c. materials, for pure b.c.c. materials, since s_* is controlled by the interactions with the Peierls lattice resistance, it is reasonable to assume that it is a constant:

$$s_* \approx \text{constant}. \tag{2.26}$$

Hence,

$$\dot{s}^\alpha \doteq \dot{s}_a^\alpha = \sum_\beta h^{\alpha\beta} \left|\dot{\gamma}^\beta\right|. \tag{2.27}$$

Several simple phenomenological forms for the hardening matrix have been proposed in the past; these have been reviewed by Peirce *et al.* [1982], and more recently by Havner [1992], and Bassani [1993]. In their numerical calculations Peirce *et al.* [1982] (also see Asaro and Needleman [1985]) used the following simple form for the hardening moduli:

$$h^{\alpha\beta} = \left[q_l + (1 - q_l)\delta^{\alpha\beta}\right] h^\beta, \tag{2.28}$$

with h^β denoting the self-hardening rate and the parameter q_l representing a latent-hardening parameter. The latent hardening parameter q_l is not necessarily a constant, and may of course be history-dependent just as the self-hardening parameter h^β is. This simple form for $h^{\alpha\beta}$ yields an acceptable description of the physical phenomena of latent hardening, and this form is adopted here without modification.

The eventual goal in this study is to formulate constitutive equations for polycrystalline ductile metals undergoing complex deformations encountered in metal-forming operations. Thus the typical fine-scale description of hardening (Stage I, Stage II, etc.) during single slip of single crystals is not considered here; instead, following Kalidindi *et al.* [1992], the following specific form is adopted for the f.c.c. single-crystals:

$$h^\beta = h_0^\beta \left|1 - \frac{s^\beta}{s_s^\beta}\right|^r \text{sign}\left(1 - \frac{s^\beta}{s_s^\beta}\right), \tag{2.29}$$

where

$$h_0^\beta = \hat{h}_0^\beta \left(\left|\dot{\gamma}^\beta\right|, \theta\right) \tag{2.30}$$

is the initial hardening rate, and

$$s_s^\beta = \hat{s}_s^\beta \left(\left| \dot{\gamma}^\beta \right|, \theta \right) \tag{2.31}$$

is a saturation value of s^β. Both h_0^β and s_s^β are in general expected to be strain rate- and temperature-dependent.

For the b.c.c. single-crystals, a hardening form similar to (2.29) is adopted for the change in s_a^α:

$$h^\beta = h_0^\beta \left| 1 - \frac{s_a^\beta}{s_{a,s}^\beta} \right|^r \operatorname{sign} \left(1 - \frac{s_a^\beta}{s_{a,s}^\beta} \right), \tag{2.32}$$

where

$$h_0^\beta = \hat{h}_0^\beta \left(\left| \dot{\gamma}^\beta \right|, \theta \right) \tag{2.33}$$

is the initial hardening rate, and

$$s_{a,s}^\beta = \hat{s}_{a,s}^\beta \left(\left| \dot{\gamma}^\beta \right|, \theta \right) \tag{2.34}$$

is a saturation value of s_a^β.

2.2 Polycrystal Constitutive Model

For polycrystalline materials the Taylor assumption (Taylor [1938a, 1938b]) is adopted, according to which the local deformation gradient in each grain is homogeneous and identical to the macroscopic deformation gradient at the continuum material point level. For such a model, with $\mathbf{T}^{(k)}$ denoting the constant Cauchy stress in each grain, the volume-averaged Cauchy stress is given by (Asaro and Needleman [1985])

$$\bar{\mathbf{T}} = \sum_{k=1}^{N} v^{(k)} \mathbf{T}^{(k)}, \tag{2.35}$$

where $v^{(k)}$ is the volume fraction of each grain in a representative volume element. When all grains are assumed to be of equal volume, the stress $\bar{\mathbf{T}}$ is just the number average over all the grains:

$$\bar{\mathbf{T}} = \frac{1}{N} \sum_{k=1}^{N} \mathbf{T}^{(k)}. \tag{2.36}$$

The accuracy of such an approximate Taylor-type polycrystal constitutive model (with a simple power-law type of flow rule) has been previously evaluated by Bronkhorst *et al.* [1992]. Their experiments and calculations showed that the Taylor-type model is in reasonable agreement with experiments with regards to the texture evolution and the macroscopic stress-strain response for single-phase f.c.c. materials. Recently, Kothari and Anand [1997] have shown that the Taylor-type polycrystal model is also reasonably accurate for b.c.c. tantalum which possesses numerous slip systems.

2.3 Computational Procedures

The constitutive model has been implemented in a finite element program ABAQUS [1994], which contains capabilities for both "static, implicit," and "dynamic, explicit" solution procedures. In a finite-element implementation, (*i*) the time-independent slip systems $(\mathbf{m}_0^\alpha, \mathbf{n}_0^\alpha)$ are known; (*ii*) the list of variables $\{\mathbf{F}(t), \mathbf{F}^p(t), s^\alpha(t), \mathbf{T}(t)\}$ and an estimate of $\mathbf{F}(t+\Delta t)$ are given. The computational task is the stable, accurate and efficient computation of $\{\mathbf{F}^p(t+\Delta t), s^\alpha(t+\Delta t), \mathbf{T}(t+\Delta t)\}$.

A brief summary of the constitutive time-integration procedures for use in ABAQUS/Standard and ABAQUS/Explicit is given in Appendix A. For the implementation in ABAQUS/Standard a stable implicit time-integration procedure is used for the constitutive equations. However, for the implementation in ABAQUS/Explicit, a simple Euler-foward scheme is used to solve for the list of constitutive variables at time $t+\Delta t$. Note that a central-difference integration rule is used in the "dynamic, explicit" procedure to solve for velocities and accelerations from the momentum balance equations. This integration procedure is only conditionally stable, and the stable time increment is given by

$$\Delta t_{\text{cr}} = \min\left(\frac{L^e}{c_d}\right),$$

where L^e is the characteristic element length, and c_d is the dilatational elastic wave speed[1] in the material. For the Euler-forward scheme used in the constitutive time-integration procedure to be stable, the strain increment is bounded from above as given by the following

[1]For a cubic material $c_d = \sqrt{\frac{C_{12}+2C_{44}}{\rho}}$ where C_{12}, C_{44} are the elastic moduli and ρ is the density.

inequality (Lush [1990]),

$$\dot{\epsilon}\,\Delta t \leq \beta m \epsilon_y, \tag{2.37}$$

where m is the rate-sensitivity[2] parameter, ϵ_y is the yield strain and β is a small fraction ≈ 0.5.

With $\Delta\epsilon = \dot{\epsilon}\Delta t$ and $\Delta t = \frac{L^e}{c_d}$, Equation (2.37) yields

$$\dot{\epsilon} \leq \beta m \epsilon_y \frac{c_d}{L^e} \tag{2.38}$$

For instance, with $\beta = 0.5$, $m = 0.02$, $\epsilon_y = 0.001$, $c_d = 5000\,\mathrm{m\ sec^{-1}}$ and $L^e = 10^{-4}\mathrm{m}$, we have $\dot{\epsilon} \leq 500\ \mathrm{sec}^{-1}$. For situations where $\dot{\epsilon} \geq 500\ \mathrm{sec}^{-1}$, an unconditionally stable Euler-backward scheme (*e.g.*, Kalidindi *et al.* [1992]), which allows for large time steps, is used.

For ABAQUS/Standard, the implicit finite-element procedure requires the computation of a Jacobian matrix to be used in a Newton-Raphson type iterative method for revising the estimated displacement field. A detailed computation of the analytical Jacobian matrix[3] for the constitutive model and the attendant fully-implicit Euler-backward method is presented in Appendix B.

The sheet-metal forming application that is considered in the next chapter is essentially quasi-static. Although a static, implicit finite element procedure is preferable for modeling such processes, it has been found that the dynamic explicit procedure in which the solution of individual time increments is inexpensive, is computationally more efficient for large three-dimensional problems which are dominated by contact (Nagtegaal and Taylor [1968]).

The computational procedures are at present limited to the isothermal case for ABAQUS/Implicit, and to the isothermal or completely adiabatic case for ABAQUS/Explicit. For the adiabatic case, the temperature rise is calculated using

$$\rho c \dot{\theta} = \xi \sum_{k=1}^{N} \left(\sum_{\alpha} \tau^{\alpha} \dot{\gamma}^{\alpha} \right)^{(k)} . \tag{2.39}$$

[2]The rate-sensitivity parameter for the kinetic equation of the plastic flow used in the crystal plasticity model is given by $m \approx \frac{k_B \theta}{\Delta F^*}$.

[3]In contrast with the numerical Jacobian employed by Kalidindi *et al.* [1992], the Jacobian used in this work is analytical. A comparative study has shown that the analytical Jacobian provides a faster rate of convergence to the solution, resulting in substantial reduction in computational times. A preliminary version of the analytical Jacobian was first suggested by Dr. Simona Socrate, MIT.

Here, the first sum is over all slip systems in a grain, and the second sum is over all grains in a polycrystalline aggregate comprising a material point. Also, $\rho = \hat{\rho}(\theta)$ denotes the mass density, $c = \hat{c}(\theta)$ the specific heat, and $0.85 \leq \xi \leq 1$ denotes the fraction of plastic work converted to heat.

2.4 Evaluation of the Constitutive Model

In this section a procedure for estimating the material parameters in the model is given. The experimental results of Carreker and Hibbard [1957] on 99.987% pure polycrystalline aluminum, and those of Senseny, Duffy and Hawley [1978] on aluminum alloy 1100-O are used for this purpose. The predictions of the model of the macroscopic stress-strain response and the crystallographic texture evolution are compared with our own experiments on commercially-pure 1100 at two different temperatures.

Recently, Kothari and Anand [1997] have demonstrated the applicability of the model for large-strain deformations of b.c.c. tantalum for a wide range of strain rates and temperatures. The material parameters estimated for tantalum and the results for the predictions of the crystallographic texture evolution and macroscopic stress-strain response reported by these authors are also briefly summarized here to contrast the response of a b.c.c. material with that of a f.c.c. material. The material parameters estimated for f.c.c. aluminum and those reported by Kothari and Anand [1997] for b.c.c. tantalum are used to simulate strain-rate jump and temperature jump tests at different levels of strain. The predictions of the model are compared against existing experimental results to demonstrate the model's ability to capture strain-rate history and temperature-history effects in both f.c.c. aluminum and b.c.c. tantalum.

2.4.1 Estimation of Material Parameters for Aluminum

Elastic Moduli

For f.c.c. crystals the anisotropic elasticity tensor $\boldsymbol{\mathcal{C}}$ may be specified in terms of three stiffness parameters, C_{11}, C_{12} and C_{44}. The values of the elastic parameters for aluminum vary significantly in the range of temperatures of interest, Fig. 2-3 (from Simmons and

Wang [1971]). This variation is approximated by a polynomial fit:

$$
\begin{aligned}
C_{11} &= \left(123.323 + 6.7008 \times 10^{-8}\theta^3 - 1.1342 \times 10^{-4}\theta^2 - 7.8788 \times 10^{-3}\theta\right) \text{ GPa}, \\
C_{12} &= \left(70.6512 + 4.4105 \times 10^{-8}\theta^3 - 7.5498 \times 10^{-5}\theta^2 + 3.9992 \times 10^{-3}\theta\right) \text{ GPa}, \\
C_{44} &= \left(31.2071 + 7.0477 \times 10^{-9}\theta^3 - 1.2136 \times 10^{-5}\theta^2 - 8.3274 \times 10^{-3}\theta\right) \text{ GPa}.
\end{aligned}
$$

Slip Systems

For f.c.c. crystals crystallographic slip is assumed to occur on the twelve $\{111\} < 110 >$ slip systems. The components of the slip plane normals and slip directions with respect to an orthonormal basis associated with the crystal lattice, for these slip systems are presented in Table 2-1. The Schmid and Boas [1935]) convention of labeling the slip systems is also shown in this table.

Table 2-1. Slip Systems

α	$[\mathbf{n}_o^\alpha]_c$	$[\mathbf{m}_o^\alpha]_c$	Label
1	111	$1\bar{1}0$	A2
2	111	$\bar{1}01$	A3
3	111	$01\bar{1}$	A6
4	$\bar{1}11$	101	D4
5	$\bar{1}11$	$\bar{1}\bar{1}0$	D1
6	$\bar{1}11$	$01\bar{1}$	D6
7	$1\bar{1}1$	$\bar{1}01$	C3
8	$1\bar{1}1$	$0\bar{1}\bar{1}$	C5
9	$1\bar{1}1$	110	C1
10	$\bar{1}\bar{1}1$	$\bar{1}10$	B2
11	$\bar{1}\bar{1}1$	101	B4
12	$\bar{1}\bar{1}1$	$0\bar{1}\bar{1}$	B5

Flow Parameters

The flow parameters are determined by calibrating the model against experimental data of Carreker and Hibbard [1957] on 99.987% pure aluminum and Duffy [1974] on 1100-O for the temperature sensitivity of the yield strength. Since the initial material in both these cases have been reported to be well-annealed, in the calculations the initial texture is assumed to be isotropic. This was represented by a set of 400 unweighted grain orientations. In order to

speed-up the curve-fitting procedure, the data is first fit to an isotropic version of the model, and the values of the material parameters so determined are then used as initial estimates for the numerical calculations based on the crystal-plasticity model. In particular, the flow parameters $\{\Delta F^*, p, q\}$ are taken to be equal to those obtained for the isotropic model, and the parameter $\dot{\gamma}_0$ is obtained from the corresponding quantity $\dot{\epsilon}_0$ in the isotropic model by setting $\dot{\gamma}_0 = \sqrt{3}\,\dot{\epsilon}_0$. Initial estimates for the resistance parameters $s_{*,0}$ and $s_{a,0}$ are taken as the values obtained for the isotropic model, divided by a "Taylor Factor" of $M \approx 3.06$ that corresponds to a random texture. In order to account for the significant change in the elastic modulus with temperature, the data for the initial yield have been normalized by the factor $\frac{E}{E_0}$ where E_0 is the Young's modulus at absolute zero. Also, for simplicity, $s_{*,0}$ and $s_{a,0}$ are assumed to be identical for all the slip systems.

The fit of the model against Carreker and Hibbard's data and Duffy's data are shown in Figs. 2-4(a) and 2-4(b) respectively. The flow parameters obtained from these fits are:

Table 2-2. Flow Parameters

	$\dot{\gamma}_0$	ΔF^*	p	q	$s_{*,0}$	$s_{a,0}$	χ
Carreker & Hibbard [1957]	$1.732 \times 10^6\,\mathrm{s}^{-1}$	3×10^{-19}J	0.141	1.1	8.76MPa	8.76MPa	1
Duffy [1974]	$1.732 \times 10^6\,\mathrm{s}^{-1}$	3×10^{-19}J	0.141	1.1	8.82MPa	12.09MPa	0.73

The fit parameters for both cases are identical except for a difference in the initial value of the athermal resistance which could be attributed to the difference in the alloy content in the materials. Also, the parameter χ is in the range suggested by Cottrell and Stokes [1955] for both the sets of data.

Hardening Parameters

The hardening parameters are determined by fitting the predictions of the crystal plasticity model against the stress-strain data of Carreker and Hibbard [1957] and Senseny, Duffy and Hawley [1978]. The experimental data was obtained by digitizing the curves presented in the papers by these authors. Carreker and Hibbard's tests (tensile) were all performed at a constant true strain rate of $6.667 \times 10^{-4}\mathrm{s}^{-1}$ and temperatures ranging from 20 K to 300 K. Senseny, Duffy and Hawley provide data for the stress-strain response at two different

strain rates, one at a quasi-static rate of $1.155 \times 10^{-4}\text{s}^{-1}$ and the other at a high rate of 173.2s^{-1}; and at two different temperatures of 77 K and 298 K.

In order to determine the hardening parameters, a two step procedure is followed. In the first step, s_s is taken to be a free parameter. Finite-element calculations are performed in ABAQUS/Explicit for simple tension on a single ABAQUS-C3D8R element subjected to the appropriate strain rate and initial temperature, and the predicitons are fit to the experimental results. The integration point in the element is assigned the 400 random unweighted grain orientations and the macroscopic stress is calculated using Taylor-averaging. For the stress-strain data of Senseny *et al.* [1978] corresponding to the strain rate of 173.2sec^{-1}, we expect appreciable temperature rise in the sample owing to adiabatic heating. Hence, the stress-strain curve for this case is simulated by computing the temperature rise according to equation (2.39), by assuming that all the plastic work is converted into heat ($\xi = 1.0$), and using values of $\rho = 2.77\,\text{Mg/m}^3$, and $c = 920\,\text{J/kg K}$ for aluminum. Figs. 2-5(a) and 2-5(b) show the fits of the finite-element calculations to the experimental data. As indicated earlier, the hardening quantities $\{\hat{h}_0^\alpha(|\dot{\gamma}^\alpha|, \theta), \hat{s}_s^\alpha(|\dot{\gamma}^\alpha|, \theta)\}$ are in general expected to be strain rate and temperature-dependent. However, for aluminum in the range of strain rates and temperatures examined, the initial hardening rate h_0 was found to be essentially independent of both temperature and strain rate. However, the saturation value of slip system resistance s_s, was found to be dependent both on temperature and strain rate

In the second step, the strain-rate and temperature sensitivity of s_s is fit to the the following phenomenological form suggested by Kocks [1976]:

$$s_s^\beta = \tilde{s}\left\{\frac{\dot{\gamma}^\beta}{\dot{\gamma}_{0,s}}\right\}^{\frac{k_B\theta}{\Delta F_*^1}}. \tag{2.40}$$

Here $\tilde{s}$, $\dot{\gamma}_{0,s}$ and ΔF_*^1 are additional material parameters. This form is meant to capture the observed increase in the saturation stress with increase in the strain rate, and with decrease in temperature. The results from this fit are shown in Figs. 2-6(a) and 2-6(b). As shown in Fig. 2-7, the goodness of the fit is preserved up to a temperature of 600 K . The extrapolated plot captures the variation in the saturation value of the slip resistance with temperature indicated by the data of Kocks [1976] for 99.99% pure aluminum.

The values of the hardening parameters estimated[4] by this procedure for the two sets of data are:

Table 2-3. Hardening Parameters

	h_0	r	$\tilde{s}$	ΔF_*^1	$\dot{\gamma}_{0,s}$	q_l
Carreker & Hibbard [1957]	250 MPa	2	210 MPa	0.85×10^{-19}J	$1 \times 10^{12}\,s^{-1}$	1.4
Senseny, Duffy & Hawley [1978]	250 MPa	2	200 MPa	1.4×10^{-19}J	$1 \times 10^{12}\,s^{-1}$	1.4

Again, the hardening parameters for both sets of data agree closely with each other.

In order to evaluate the accuracy of the constitutive model, numerical simulations are performed using the final set of material parameters listed in Table 2-2 and Table 2-3 for each of the experimental data that was used to obtain the parameters. Figs. 2-8(a) and 2-8(b) show the final curve-fits of the model for the stress-strain response for both sets of data compared against their corresponding experimental results. The fits are in good agreement with the experiments.

2.4.2 Material Parameters for Tantalum

Elastic Moduli

The values of the elastic parameters for tantalum as a function of temperature are taken as (Simmons and Wang [1978]):

$$\begin{aligned} C_{11} &= (268.2 - 0.024\,\theta)\ \text{GPa}, \\ C_{12} &= (159.6 - 0.011\,\theta)\ \text{GPa}, \\ C_{44} &= (87.1 - 0.015\,\theta)\ \text{GPa}. \end{aligned}$$

[4] As for the flow parameters, the hardening parameters are also first estimated for the isotropic model, and the values so determined are used as initial estimates for the corresponding quantities in the anisotropic model. Specifically, initial estimates for s_s are taken to be equal to those obtained in the isotropic model divided by a Taylor factor of $M \approx 3.06$, and the initial estimate for h_0 is taken to be equal to the value obtained in the isotropic model divided by $M^2 \approx 9.36$.

Slip systems

Plastic deformation of b.c.c. tantalum is modeled to occur solely due to crystallographic slip on the twelve $\{110\} < 111 >$, plus the twelve $\{112\} < 111 >$ slip-systems. The slip-systems are listed in Table 2-4.

Table 2-4. Slip Systems

α	$\mathbf{n}_o^\alpha$	$\mathbf{m}_o^\alpha$	α	$\mathbf{n}_o^\alpha$	$\mathbf{m}_o^\alpha$
1	110	$1\bar{1}1$	13	$21\bar{1}$	$\bar{1}\bar{1}1$
2	011	$1\bar{1}1$	14	112	$11\bar{1}$
3	110	$\bar{1}11$	15	$\bar{1}12$	$1\bar{1}1$
4	011	$11\bar{1}$	16	$1\bar{1}2$	$\bar{1}11$
5	011	$1\bar{1}1$	17	$1\bar{2}1$	111
6	101	$11\bar{1}$	18	121	$1\bar{1}1$
7	101	$\bar{1}11$	19	$\bar{1}21$	$11\bar{1}$
8	$\bar{1}10$	111	20	$1\bar{2}1$	111
9	$\bar{1}10$	$11\bar{1}$	21	$12\bar{1}$	$\bar{1}11$
10	$\bar{1}01$	111	22	211	$\bar{1}11$
11	$\bar{1}01$	$1\bar{1}1$	23	$\bar{2}11$	111
12	$0\bar{1}1$	111	24	$2\bar{1}1$	$11\bar{1}$

Flow Parameters

The other necessary material parameters are the quantities $\{\dot{\gamma}_0, \Delta F^*, p, q, s_*\}$ in the flow equations, the quantities $\{\hat{h}_0^\alpha(|\dot{\gamma}^\alpha|, \theta), a, \hat{s}_{a,s}^\alpha(|\dot{\gamma}^\alpha|, \theta), q_l\}$ in the hardening equations, and the initial value of the athermal slip-system resistance $s_{a,0}$, which are taken to be identical for all the slip-systems. Kothari and Anand [1997] have determined these material parameters and functions by calibrating the model against existing experimental results of Hoge and Mukherjee [1977] on commercially pure tantalum.

The flow parameters are determined by fitting the experimental data of Hoge and Mukherjee (1977) for the strain-rate and temperature sensitivity of the yield strength of a tantalum rod. The initial texture of the tantalum rod was not reported by Hoge and Mukherjee [1977]. To approximate this initial texture, Kothari and Anand [1997] measured the texture of their own commercially-procured and annealed tantalum rod, and represented this texture by a set of 400 weighted grain orientations by using the texture conversion program popLA (Kallend, *et al.* [1994]). The experimentally-measured and numerically-

represented pole figures are presented in Fig. 2-9. The flow parameters obtained by the fitting procedure are:

$$\dot{\gamma}_0 = 1.73 \times 10^7 \,\mathrm{sec}^{-1},\ \Delta F^* = 2.77 \times 10^{-19}\mathrm{J},\ p = 0.28,\ q = 1.34,\ s_* = 400\mathrm{MPa}, \quad (2.41)$$

with

$$s_{a,0} = 22\mathrm{MPa}.$$

The quantities s_* and $s_{a,0}$ are taken to be the same for all slip-systems. The fit of the model against the experimental data of Hoge and Mukherjee [1977] for the strain-rate and temperature sensitivity of the yield strength of tantalum is presented in Figs. 2-10 and 2-11, respectively.

Hardening Parameters

Kothari and Anand [1997] determine the hardening parameters for pure tantalum by fitting the predictions from the crystal plasticity model against data from the compression split Hopkinson bar experiments of Vecchio [1994] and Nemat-Nasser, Li and Isaacs [1994]. These experiments were performed on specimens cored from tantalum discs which were produced by cross-rolling the initial ingots. Since these authors do not report the initial texture of these discs, Kothari and Anand [1997] approximated the initial texture by using their own texture measurements of a similarly-produced tantalum plate, and representing this texture by a set of 400 weighted grain orientations by using popLA, Fig. 2-12. For the curve-fitting procedure, both the isothermal[5] and adiabatic stress-strain curves of tantalum at different temperatures and strain rates were calculated by performing Taylor-model simple compression ABAQUS/Explicit simulations on a single ABAQUS-C3D8R element subjected to the appropriate strain rate and initial temperature in the experiment. For tantalum, the hardening quantities $\{\hat{h}_0^\alpha(|\dot{\gamma}^\alpha|, \theta), \hat{s}_{a,s}^\alpha(|\dot{\gamma}^\alpha|, \theta), q_l\}$, are adequately described by taking the initial hardening rate h_0 and the saturation value of the athermal slip-system resistance $s_{a,s}$ to be independent of both temperature and strain rate, and the latent-hardening parameter

[5]The technique used by Nemat-Nasser and co-workers to deduce the isothermal stress-strain curves at high rates is to strain the specimen incrementally and unload, allow the specimen to cool to the test temperature, and then re-load at the same initial strain rate. The curve connecting the peaks of these incremental tests provides an estimate of the isothermal stress-strain curve at a high strain rate. For additional details, see Nemat-Nasser, Li and Isaacs [1994].

q_l as a constant[6] equal to 1.4. The adiabatic stress-strain curves are simulated by computing the temperature rise according to equation (2.39), by assuming that all the plastic work is converted into heat ($\xi = 1.0$), and using values of $\rho = 16.6\,\mathrm{Mg/m^3}$, and $c = 138\,\mathrm{J/kg\,K}$. In the simulations, the flow parameters are the same as those determined above from the data of Hoge and Mukherjee [1977], equation (2.41). The values of the hardening parameters estimated by the fitting procedure for the three sets of data are: Kothari and Anand [1997]

Table 2-5. Hardening Parameters

	$s_{a,0}$	h_0	$s_{a,s}$	r	q_l
Nemat-Nasser and Isaacs [1994]	20 MPa	80 MPa	110 MPa	1.1	1.4
Vecchio [1994]	49 MPa	160 MPa	100 MPa	1.1	1.4

attribute the different values of the hardening parameters to the different initial states of the specimens used in the two sets of experiments by the two sets of authors. The quality of the fit to the data is shown in Figs. 2-13 and 2-14.

2.4.3 Predictions of the Constitutive Model

Strain Hardening to Large Strains and Evolution of the Crystallographic Texture

The stress-strain data of Carreker and Hibbard and Duffy and co-workers are limited to strains of $\bar{\epsilon}^p \approx 0.125$. Since the strains in typical deformation processes are considerably larger, and since there is a scarcity of stress-strain data for large strains, quasi-static *compression* tests were performed at a constant true strain rate of $3 \times 10^{-3}\mathrm{s}^{-1}$ on 1100-O at 84 K and 298 K up to true strains of $|\epsilon| = 1$. The cryogenic temperature of 84 K was obtained by immersing the sample in a liquid nitrogen bath while testing. The temperature was measured using a K-type {nickel-10% chromium (+) and nickel-5% aluminum and silicon(-)} thermocouple. Teflon sheets were used to minimize the friction in the platen-sample interface. The samples showed very little barreling.

Cylindrical samples of aluminum 1100 0.5" diameter and 0.75" tall were machined with the axis of the sample coinciding with the initial rod axis. Prior to the tests the samples

[6]Kothari and Anand [1997]) report that their predictions were not very sensitive to the value of the latent-hardening parameter.

were annealed. The annealing schedule consisted of heating the specimens in an inert atmosphere (Argon) in a Lindberg furnace to 260° C, holding for 1 hour, increasing the temperature to 538° C holding for another 15 minutes, and then furnace cooling to room temperature (Brown, Kim and Anand [1989]). The initial crystallographic texture of the as-annealed specimen was measured by x-ray irradiation. The details of the procedure adopted for the preparation of the specimen and the methodology adopted for texture measurement are described in Appendix C. Fig. 2-15(a) shows the measured pole-figures (equal-area projections). Under the specified annealing schedule, the specimens retain a large amount of the initial rod texture. The initial measured texture was represented by a set of discrete weighted Euler angles using the popLA package[7]. The ratio of the weight of a grain orientation divided by the sum of the weights of all grain orientations comprising the representation approximates the volume fraction of the grains that are oriented in a small neighborhood of a particular grain orientation, assuming that all grains are of equal volume. Since, in the computational procedure to follow unweighted grain orientations are used to represent the initial texture, each weighted grain orientation computed by the popLA package is replaced by a number of grain orientations equal to the integer nearest to the weight and these grains are distributed in a small neighborhood (of $\approx 5°$ in each of the three dimensions in Euler angle space) around the given orientation[8] . To increase (decrease) the total number of represented discrete orientations used to represent the initial texture, the weights are simply multiplied (divided) by an appropriate numerical constant. Using this procedure, the initial texture, Fig. 2-15(a), is represented by 400 unweighted discrete orientations. The numerical representation is shown in Fig. 2-15(b).

The same set of flow parameters as obtained from fitting the data of Duffy and co-workers' are used for the following simulations. These parameters are repeated below for convenience:

$s_{*,0} = 8.82$ MPa, $s_{a,0} = 12.09$ MPa, $\dot{\gamma}_0 = 1.732 \times 10^6 \text{sec}^{-1}$, $\Delta F_* = 1.38 \times 10^{-23}$ J,

$p = 0.141$, $q = 1.1$.

The values of the initial thermal and athermal part of the slip resistances of all the slip

[7]A detailed outline of the scheme for generating the weights is reported in Kocks, Kallend and Biondo [1991].

[8]The discrete numerical representation of measured crystallographic texture is still an area of research that requires considerable additional work. A more rigorous methodology would facilitate a direct quantitative comparison between measured and computed textures.

systems in the representative polycrystalline aggregate are assumed to be equal. The slip system hardening parameters and saturation value of the slip system resistance are estimated from the stress-strain curve for simple compression at room-temperature. The numerical simulation was performed using ABAQUS/Standard on a single ABAQUS-C3D8 continuum element where the faces of the element initially perpendicular to the compression axis were constrained to remain plane and perpendicular to the loading axis through out the deformation. The bottom face of the element was fixed in the loading direction while the top face was subjected to displacement boundary condition which resulted in an axial true strain rate of -0.003 $\sec^{-1}$. Each integration point in the finite-element was assigned the set of 400 orientations employed for the representation of the initial texture. Fig. 2-16 shows the numerical fit to the measured stress-strain response. This fit yields the following material parameters:

$h_0 = 200$ MPa, $\tilde{s} = 220$ MPa, $r = 2$, $\dot{\gamma}_{0,s} = 1 \times 10^{12}\sec^{-1}$, $\Delta F_*^1 = 1.4 \times 10^{-19}$ J.

Here, the values for the parameters $\dot{\gamma}_{0,s}$ and ΔF_*^1 are taken as shown in Table 2-3. Fig. 2-17 shows the measured[9] and the numerically calculated crystallographic texture at a true strain level of -1.0. We observe that the final texture is the ideal compression texture with {110} planes oriented perpendicular to the compression axis in contrast with the initial texture which had a strong concentration of {111} and {100} poles along the rod axis, Fig. 2-15. Both {111} and {100} textures are unstable under simple compression. The texture departs from these components rapidly with progressive deformation leading to the stable {110} texture at large strains. The constitutive model captures this evolution of texture quite accurately.

Next, we simulate the stress-strain response and the evolution of texture for the simple compression test at 84 K using the material parameters estimated above. Fig. 2-18 shows the predicted stress-strain curve compared with the measured response, the prediction closely matches the experimental stress-strain curves. Fig. 2-19 shows a comparison of the measured and predicted texture at ϵ = -0.75. The numerical predictions are in good agreement with the experimental results.

In order to evaluate the accuracy of the constitutive model for a different mode of deformation, plane-strain compression experiments were performed on the same 1100-O. The plane-strain compression specimens were machined such that the constrained direction

[9]The tested specimens were sectioned approximately along their mid-plane prior to texture measurement.

was along the rod axis. The dimensions of the specimens were 7.62 mm in the compression direction ($\mathbf{e}_2$), 9.53 mm in the free direction ($\mathbf{e}_1$) and 14.73 mm in the constrained direction ($\mathbf{e}_3$). The specimen and the sliding contact surfaces of the channel-die fixture were lubricated with two sheets of teflon film containing a layer of MoS_2 between them. The initial texture was represented by the same set of 400 grain orientations, Fig. 2-15. The simulations were performed on an ABAQUS-CPE4 plane-strain element. The measured and calculated stress-strain response are shown in Fig. 2-20. The prediction is in reasonable agreement with the experimental result. Fig. 2-21 shows the experimental and simulated textures, at a true axial strain of -0.9. We observe that the measured texture is quite different from the usually reported plane-strain compression texture for f.c.c. materials deforming by crystallographic slip (e.g., Bronkhorst, Kalidindi and Anand [1992]). This is directly attributable to the initial texture in the specimens. Unlike the situation studied by Bronkhorst, Kalidindi and Anand [1992], the specimen in our experiments were strongly textured along the constrained direction[10]. We observe a reasonably good agreement between the measurements and predictions indicating that the constitutive model provides good predictions for stress-strain response and texture evolution to large strains even for initially anisotropic materials.

Kothari and Anand [1997] have evaluated the ability of the constitutive model to predict the texture evolution and the stress-strain response of b.c.c. tantalum in some quasi-static experiments. In the following, their results for simple compression and plane-strain compression are summarized.

The simple compression and plane-strain compression tests were performed on specimens machined from a tantalum rod. The initial crystallographic texture of the annealed rod and its representation by 400 weighted grain orientations are shown in Fig. 2-9. Kothari and Anand [1997] take the flow parameters to be the same as estimated from Hoge and Mukerjee [1977] data. They estimate the initial value of the athermal part of the slip system resistance and its hardening parameters by fitting the data from a constant true strain-rate simple compression test performed along the rod axis, Fig. 2-22. The values estimated from the curve-fitting procedure are:

[10] In their experiments with initially anisotropic polycrystalline f.c.c. materials, Kalidindi and Anand [1994] have also previously observed that initial texture had a significant effect on the texture evolution even at large strains.

$$s_{a,0} = 15\text{MPa}, h_0 = 70\text{MPa}, s_{a,s} = 160MPa, r = 1.1, q_l = 1.4$$

The experimentally-measured and numerically-predicted {222}, {110} and {200} pole figures at a strain of -1.1 are presented in Fig. 2-23. The initial {110} texture of the rod is unstable under simple compression and the texture evolves to the stable, ideal compression texture of {222} and {200} components for b.c.c. materials.

Similar to the plane-strain compression tests on 1100-O, the specimen in the plane-strain compression of tantalum was oriented with the rod axis along the constraint direction. The predicted stress-strain response is compared with the experimental measurement in Fig. 2-24, and the predicted crystallographic texture is compared with the experimentally measured one in Fig. 2-25. The predicted stress-strain curve and texture approach the corresponding experimental measurements, but the agreement could be better. We observe in passing that the plane strain compression texture for b.c.c. tantalum, Fig. 2-25 bears a close resemblance to that measured for f.c.c. aluminum, Fig. 2-21. The {110} pole-figure in Fig. 2-21 is quite similar to {222} pole figure in Fig. 2-25 while the {111} pole-figure in Fig. 2-21 is strikingly similar to the {110} pole figure in Fig. 2-25.

Strain Rate and Temperature History Effects

It is well known that the plastic behavior of metals is influenced by previous plastic flow and, generally, by the strain rate and temperature at which that flow occured (Lindholm [1964]; Klepaczko [1967, 1968, 1975]; Campbell and Dowling [1970]). The magnitude of these strain-rate and temperature history effects[11] depends among other factors on the particular material and its structure. These effects become evident in experiments in which a rapid change in strain-rate or temperature is imposed during the deformation. There are interesting differences in the stress-strain behavior of f.c.c. and b.c.c. materials when they are subjected to strain-rate or temperature jumps. In this subsection, the ability of the constitutive model to capture these important differences is demonstrated.

Fig. 2-26(a) illustrates schematically the typical stress-strain response of f.c.c. metals for constant strain-rate and strain-rate jump tests. The flow-stresses immediately before

[11] A comprehensive review of the investigations of history effects in f.c.c., b.c.c and h.c.p. metals is provided by Duffy [1982].

and after the jump reflect the *constant state*, strain-rate dependence of the flow stress. The difference in the flow-stress levels in the constant strain-rate and strain-rate jump tests at a strain ϵ_j, $\sigma_2' - \sigma_2$, is an outcome of the strain-rate history. The flow-stresses σ_2 and σ_2' correspond to the same strain level but *different states*. The difference in the states is due to the *strain-rate dependence* of the slip system hardening. As the strain level at which the jump is performed increases, this difference in the states increases and as a consequence $\sigma_2' - \sigma_2$ also increases. However, since the steady-state structure is the same for both types of tests, at large strains beyond the jump, the stress-strain curve for the jump test asymptotically approaches the curve for the constant strain-rate test. This pronounced strain-rate history effect is a characteristic of f.c.c. metals.

Fig. 2-27(a) shows the stress-strain curves reported by Senseny *et al.* [1978] demonstrating the effects of strain-rate history. At each temperature, the results from two types of tests are shown: (*i*) Constant true strain-rate tests performed at two strain rates, $1.155 \times 10^{-4}\text{s}^{-1}$ and 173.2s^{-1}. (*ii*) Strain rate jump tests conducted between these strain rates at three different levels of strain. The experimentally observed strain-rate history effects are captured quite well by the predictions from the model which are shown in Fig. 2-27(b).

Analogous to tests probing strain-rate history effects, temperature jump tests can be performed to study the temperature-history effects. Fig. 2-26(b) shows a schematic typifying the stress-strain response from an isothermal and a temperature-decrement test. Here, the flow-stresses immediately before and after the temperature jump signify *constant state*, temperature dependence of the flow stress. As in the strain-rate jump tests, the constant temperature and temperature jump tests essentially highlight the difference in the flow stress levels due to difference in the states, the latter arising from the temperature dependence of the slip system hardening. Dorn, Goldberg and Tietz [1949] have reported temperature-decrement experiments on commercially-pure aluminum (2S-O annealed at 811 K for 20 minutes) that illustrate the effects of temperature history, Fig. 2-28(a). These tensile tests were performed between two temperatures [12], 78 K and 292 K. The strain rate was maintained at a constant value of 0.0011s^{-1}. The material parameters from Duffy and co-workers's data is used to show the predictions from the constitutive model for

[12]Unlike the strain-rate jump tests, temperature changes here were not instantaneous. Instead, the tests were interrupted between changes in the temperature of the baths.

these conditions, Fig. 2-28(b). Again, the predictions are in very good agreement with the experiments. As shown in Fig. 2-29, the predictions of the model are also in good agreement with the experimental results for high-purity aluminum.

Dorn *et al.* [1949] also report temperature-increment tests where the initial part of the tensile test was conducted at 78K which was followed by a change of bath-temperature to 292K where the test was completed, Fig. 2-30(a). The predictions from the model for this situation are shown in Fig. 2-30(b). The decrease in the flow stress is predicted reasonably well at lower levels of strain, but at larger strains the model underpredicts the change in the flow stress. It is known that during temperature-increment tests, the work-hardened state reached due to straining at the lower temperature is unstable at the higher temperature. This results in some initial work-softening leading to a larger decrease in flow stress than would be possible with a temperature-increment at a *constant state* (Cottrell and Stokes [1955]). The discrepancy in the predicted levels of flow stress can be attributed to the inability in maintaining the state a constant between the changes in the temperature of the bath. Nevertheless, the qualitative aspects of a temperature-increment test are adequately captured by the constitutive model.

Fig. 2-31 typifies the stress-strain behavior in b.c.c. materials under changes in strain-rate history. We observe that though the flow stresses of both niobium and molybdenum are sensitive to strain-rate they show *little sensitivity to strain-rate history.* Lopatin *et al.* [1992] have reported the stress-strain response of pure tantalum under constant strain-rate and strain-rate increment conditions, Fig. 2-32(a). The figure illustrates that pure tantalum is quite insensitive to strain-rate history even at large strains. The slight overshoot in the flow stress after the strain-rate increment above the flow stress level attained while straining constantly at the higher strain rate can be attributed to yield-point phenomenon commonly observed in b.c.c. materials. For the constant strain-rate and strain-rate jump simulations on pure tantalum, the flow parameters estimated by Kothari and Anand [1997] for pure tantalum are used:

$$\dot{\gamma}_0 = 1.73 \times 10^7 \,\mathrm{sec}^{-1},\ \Delta F^* = 2.77 \times 10^{-19}\mathrm{J},\ p = 0.28,\ q = 1.34,\ s_* = 430\mathrm{MPa}.$$

The initial value of the athermal part of the slip system resistance and its hardening parameters are estimated by fitting the model to the measured "isothermal" stress-strain

curve, Fig. 2-32(a). The fit yields:

$$s_{a,0} = 48\text{MPa}, s_{a,s} = 245\text{MPa}, h_{a,0} = 100\text{MPa}, r = 1.1.$$

A latent hardening factor of $q_l = 1.4$ is assumed. Lopatin *et al.* [1992] do not report the initial texture of their compression samples. In the simulations to follow, an initial isotropic texture[13] is assumed. Fig. 2-32(b) shows the predictions of the stress-strain behavior for constant strain-rate and strain-rate jump situations. The predictions reproduce the qualitative aspects of the stress-strain behavior. In contrast with the situation in the modeling of f.c.c. materials, in b.c.c. materials the thermally activatable part of the slip system resistance s_* is approximately *constant with strain.* Also, the hardening of the athermal part of the slip system resistance s_a is *independent* of the strain-rate. As a consequence, the state, as quantified by the slip system deformation resistance, after the strain-rate jump at any given level of strain is *identical* to the state at the same strain attained through constant straining at the higher strain-rate. Thus, the flow stress level at the end of the strain-rate jump is the same as the flow stress reached at the same strain through a constant strain-rate test at the higher strain-rate. Fig. 2-33(a) and 2-33(b) show the experimental and numerical prediction for the stress-strain response under strain-rate decrements. The predictions again capture the lack of history effects reasonably well.

In conclusion, the rate and temperature-dependent polycrystal plasticity model developed in this chapter has been demonstrated to capture the macroscopic stress-strain response and predict the crystallographic texture evolution up to large strains under a wide range of strain rates and temperatures for both f.c.c. and b.c.c. materials. Also, the model accurately predicts the differences in the strain-rate and temperature history effects between the f.c.c. and b.c.c. materials studied here.

[13]The nature of the initial texture should not affect the qualitative aspects of the results.

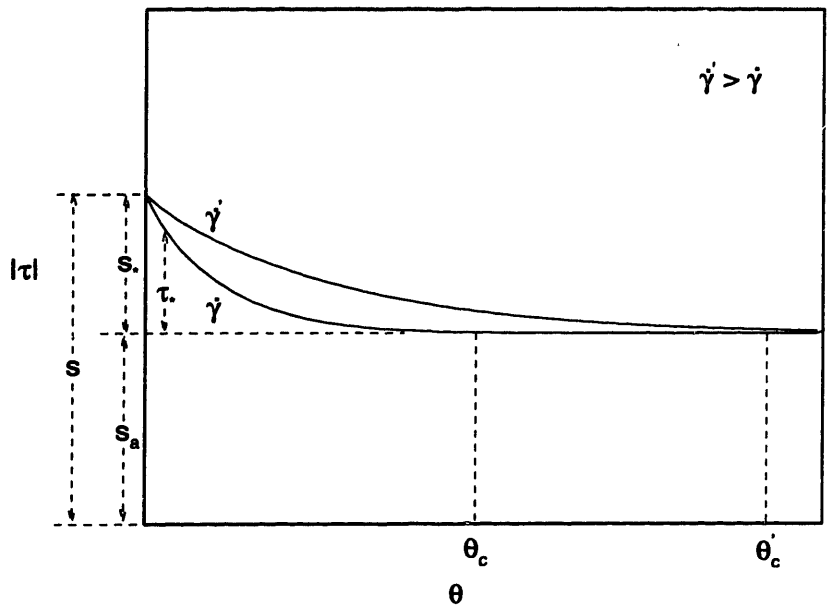

Figure 2-1: Schematic diagram illustrating the temperature and strain rate sensitivity of resolved shear stress at a fixed value of the deformation resistance $s = s_* + s_a$. θ_c is the temperature above which there is enough thermal energy for the barriers to be overcome by thermal activation alone. As shown in the figure, θ_c is a function of the strain rate.

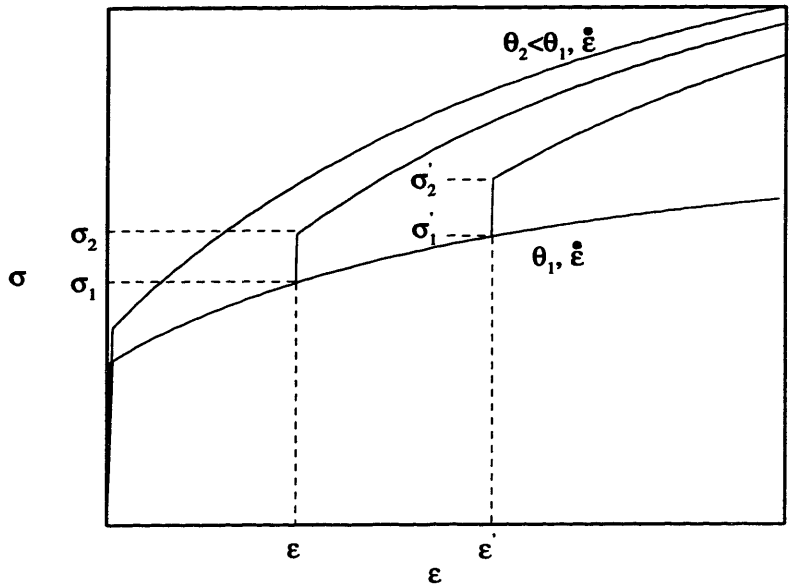

Figure 2-2: Schematic diagram illustrating the stress-strain curves observed in Cottrell and Stokes' [1955] experiments. The notation used in the text for the relevant variables is also shown.

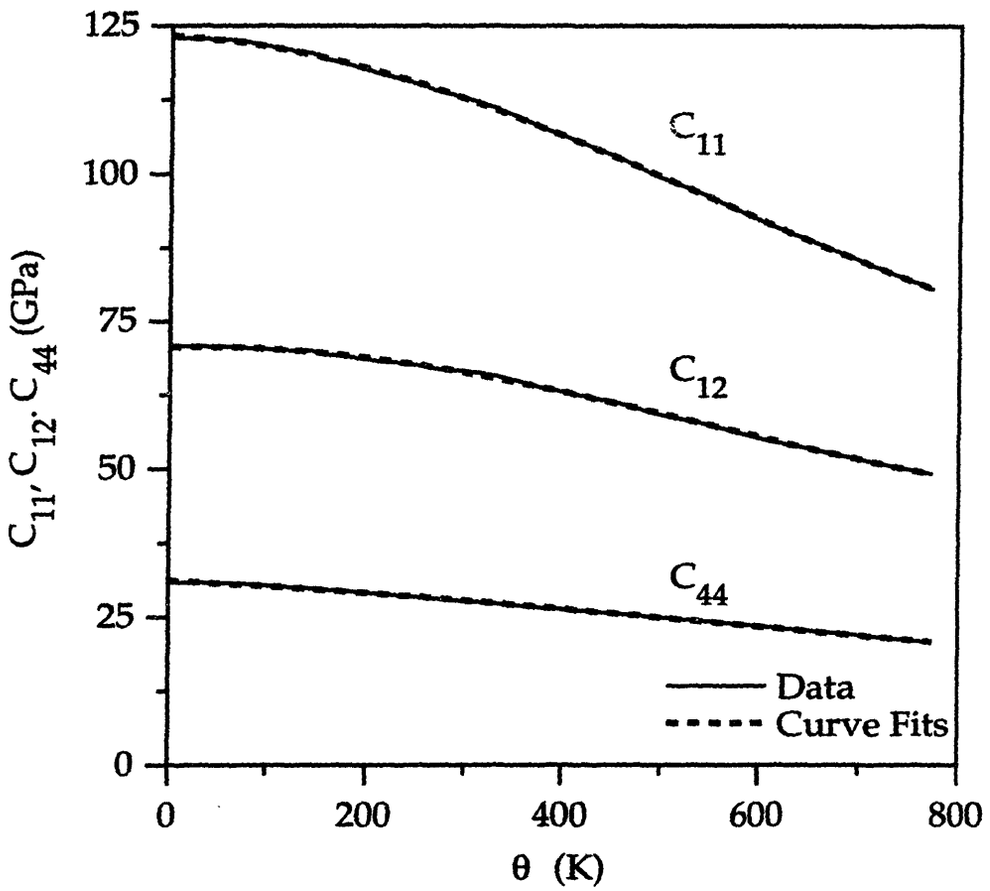

Figure 2-3: Variation of elastic constants for pure aluminum with temperature (Simmons and Wang [1971]). The experimental data is fit through a third-degree polynomial function.

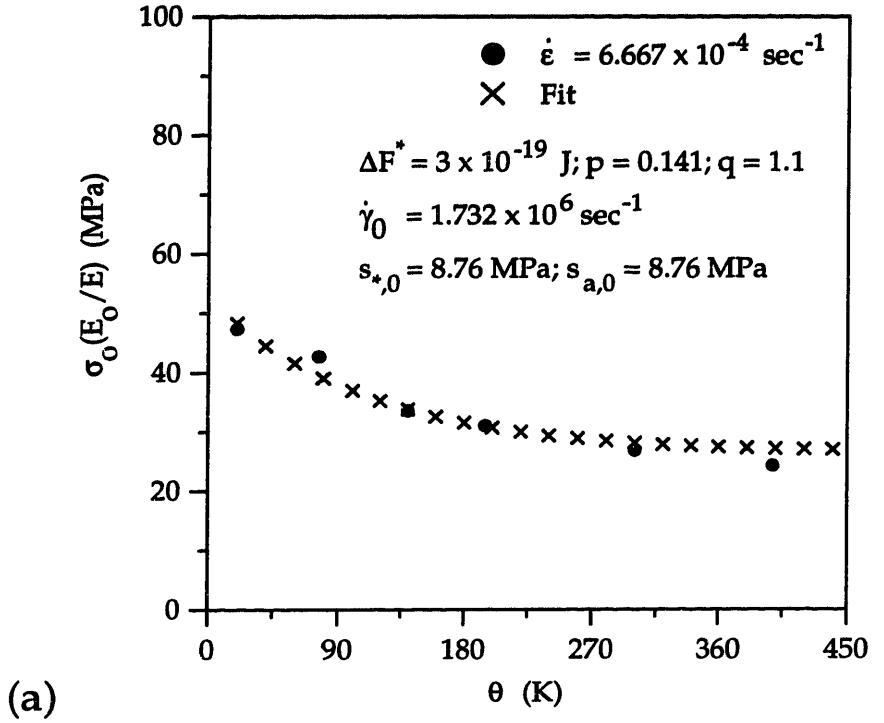

(a)

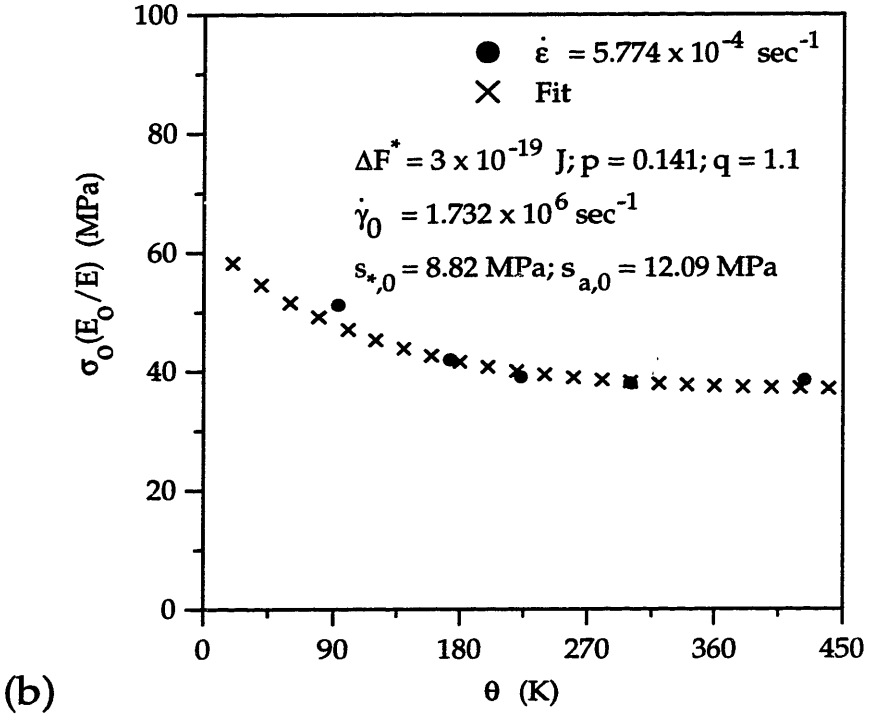

(b)

Figure 2-4: Experimental data for the yield strength as a function of temperature and the model's fit for the data of (a) Carreker and Hibbard [1957] for polycrystalline aluminum (b) Duffy [1974] for aluminum alloy 1100-O.

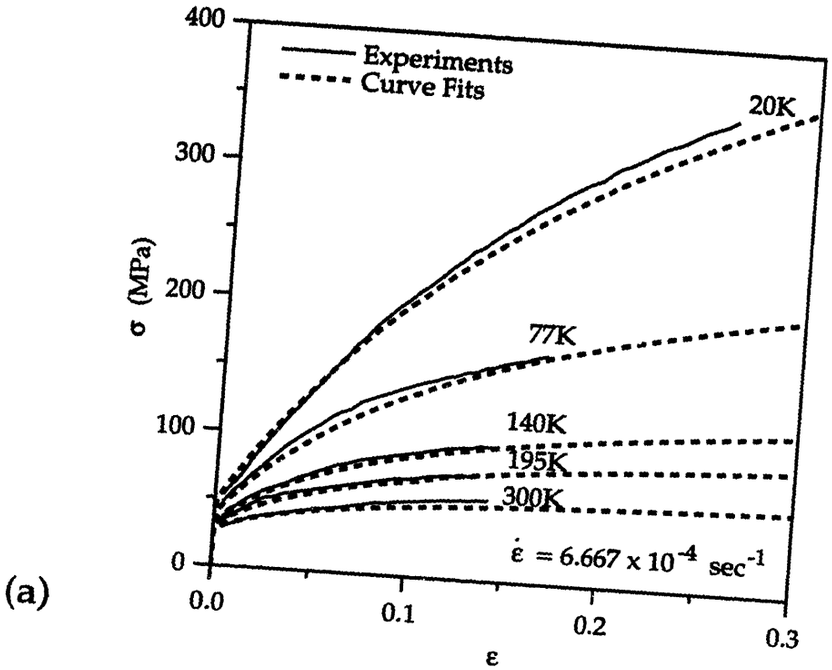

(a)

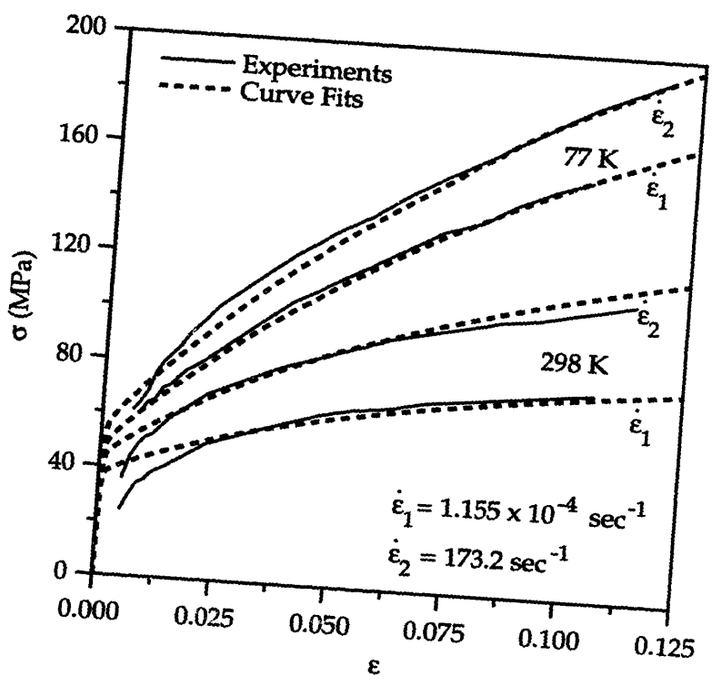

(b)

Figure 2-5: Experimental data for the stress-strain response at different temperatures and strain rates and the model's fit for the data of (a) Carreker and Hibbard [1957] (b) Senseny, Duffy and Hawley [1978].

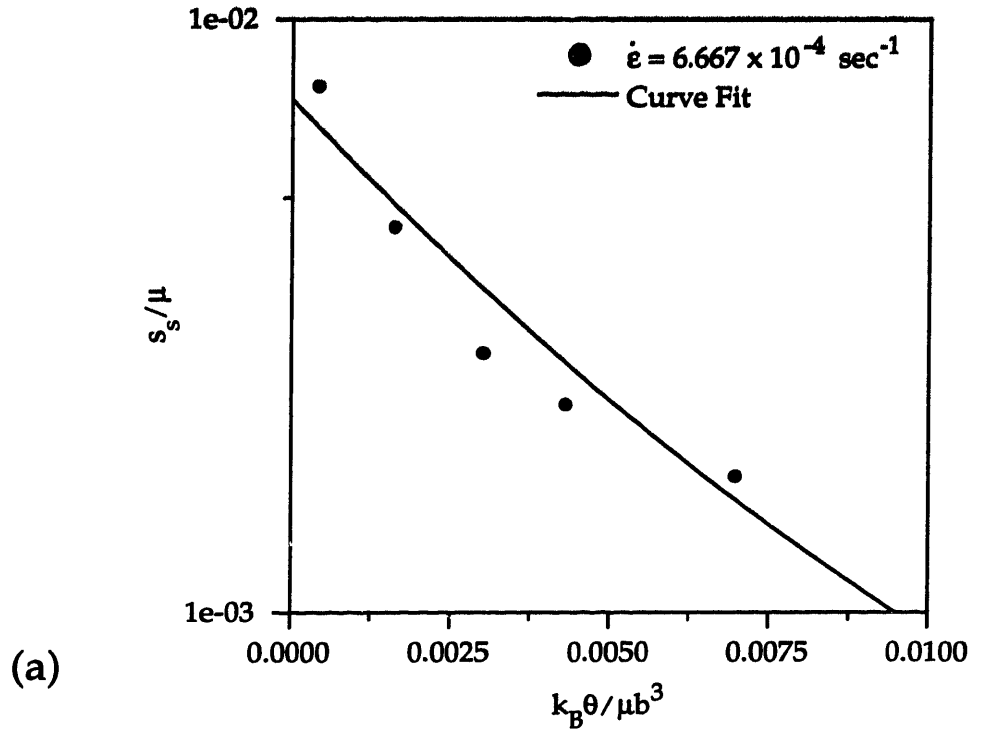

(a)

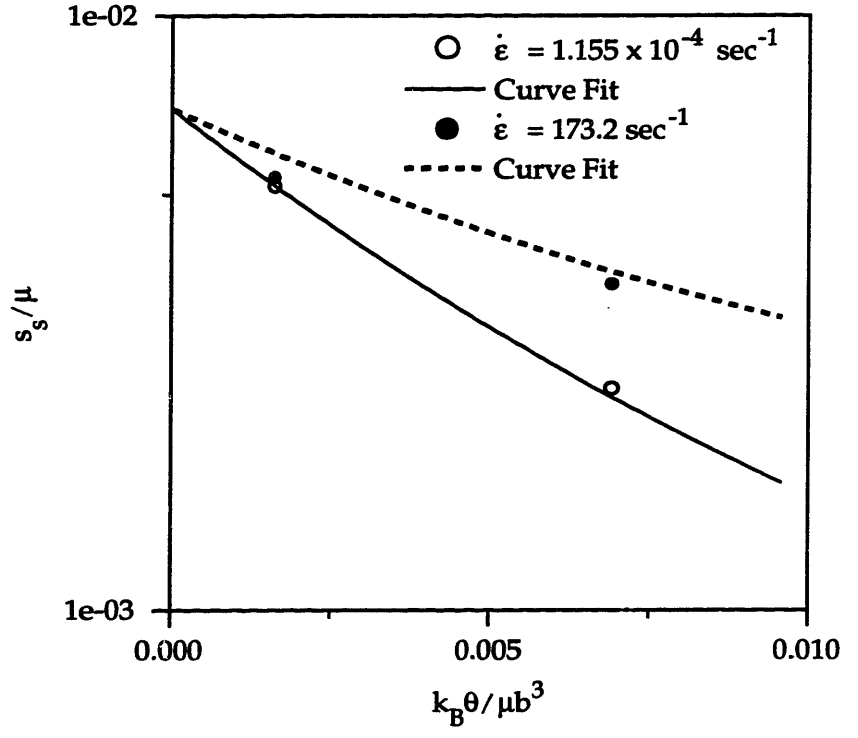

(b)

Figure 2-6: Saturation slip resistance plotted as a function of temperature and the model's fit to the data of: (a) Carreker and Hibbard [1957] (b) Senseny, Duffy and Hawley [1978]. Both axes are normalized by the temperature dependent shear modulus μ. k_B is the Boltzmann constant and b is the Burgers vector.

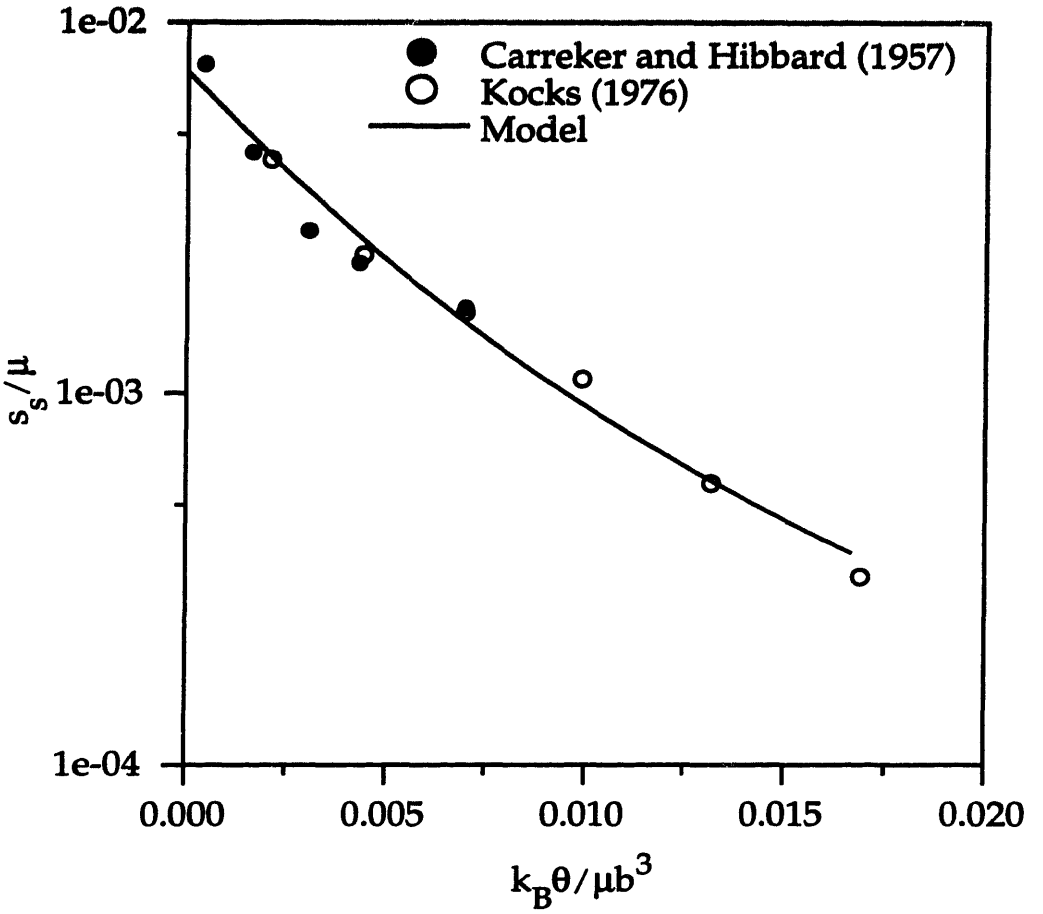

Figure 2-7: Saturation slip resistance plotted as a function of temperature and the constitutive model's fit obtained using Carreker and Hibbard's data. The plot also shows the extrapolation of the fit to elevated temperatures along with the data of Kocks [1976].

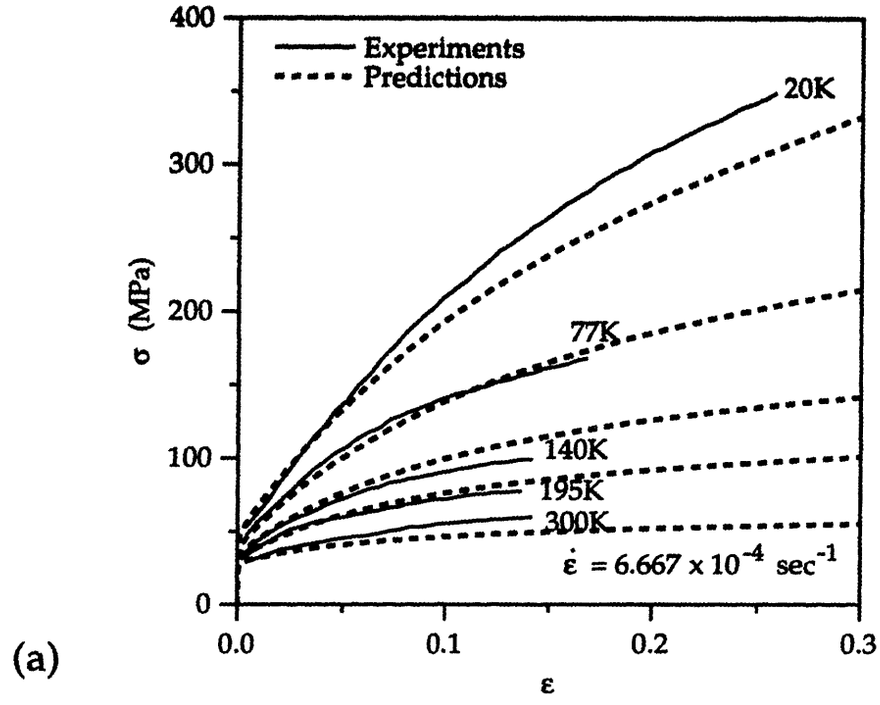

(a)

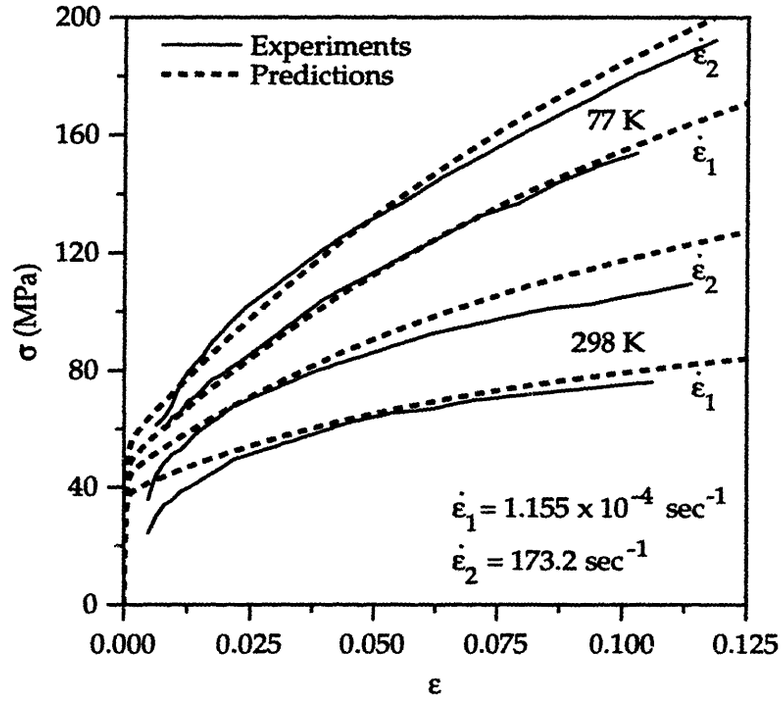

(b)

Figure 2-8: Comparison of the experimental data for the stress-strain response with the model's predictions based on the parameters obtained from the fits: (a) Carreker and Hibbard [1957] (b) Senseny, Duffy and Hawley [1978].

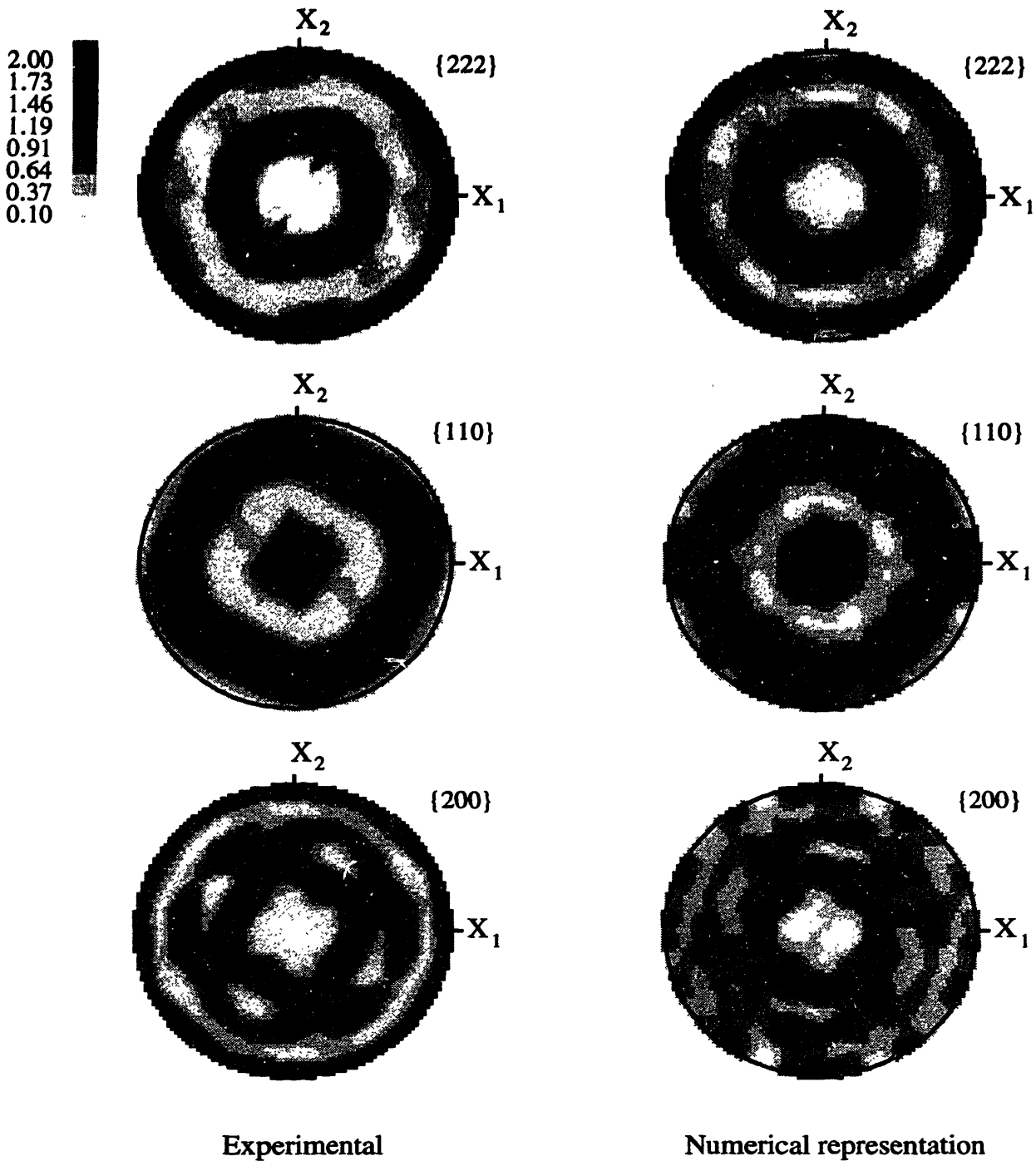

Figure 2-9: Representation of the texture of annealed b.c.c. tantalum with 400 weighted grains (Kothari and Anand [1997]).

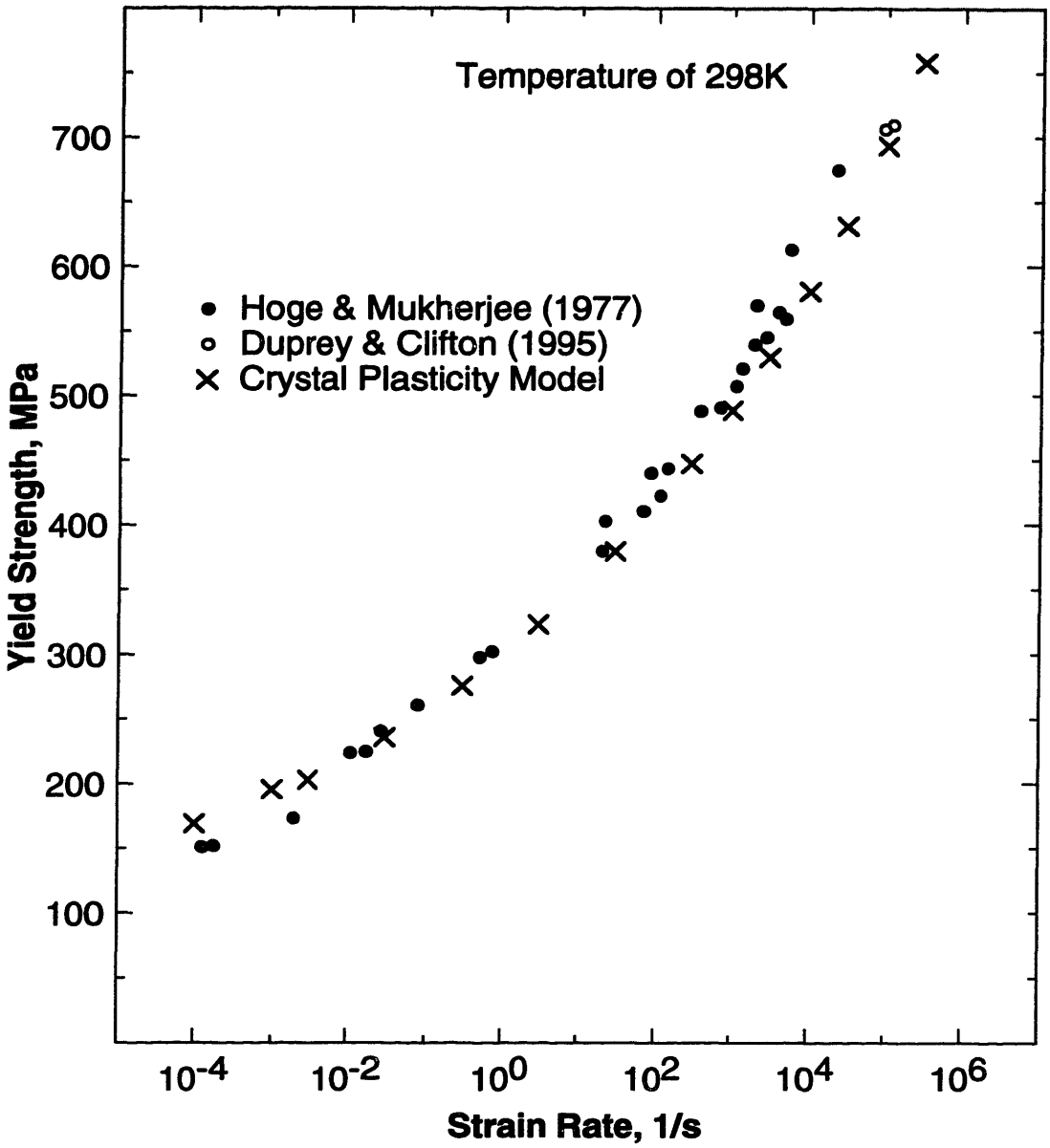

Figure 2-10: Fit of the Taylor-type crystal plasticity model to the data of Hoge and Mukherjee [1977] and Duprey and Clifton [1995] on the strain rate dependence of the yield strength of b.c.c. tantalum (Kothari and Anand [1997]).

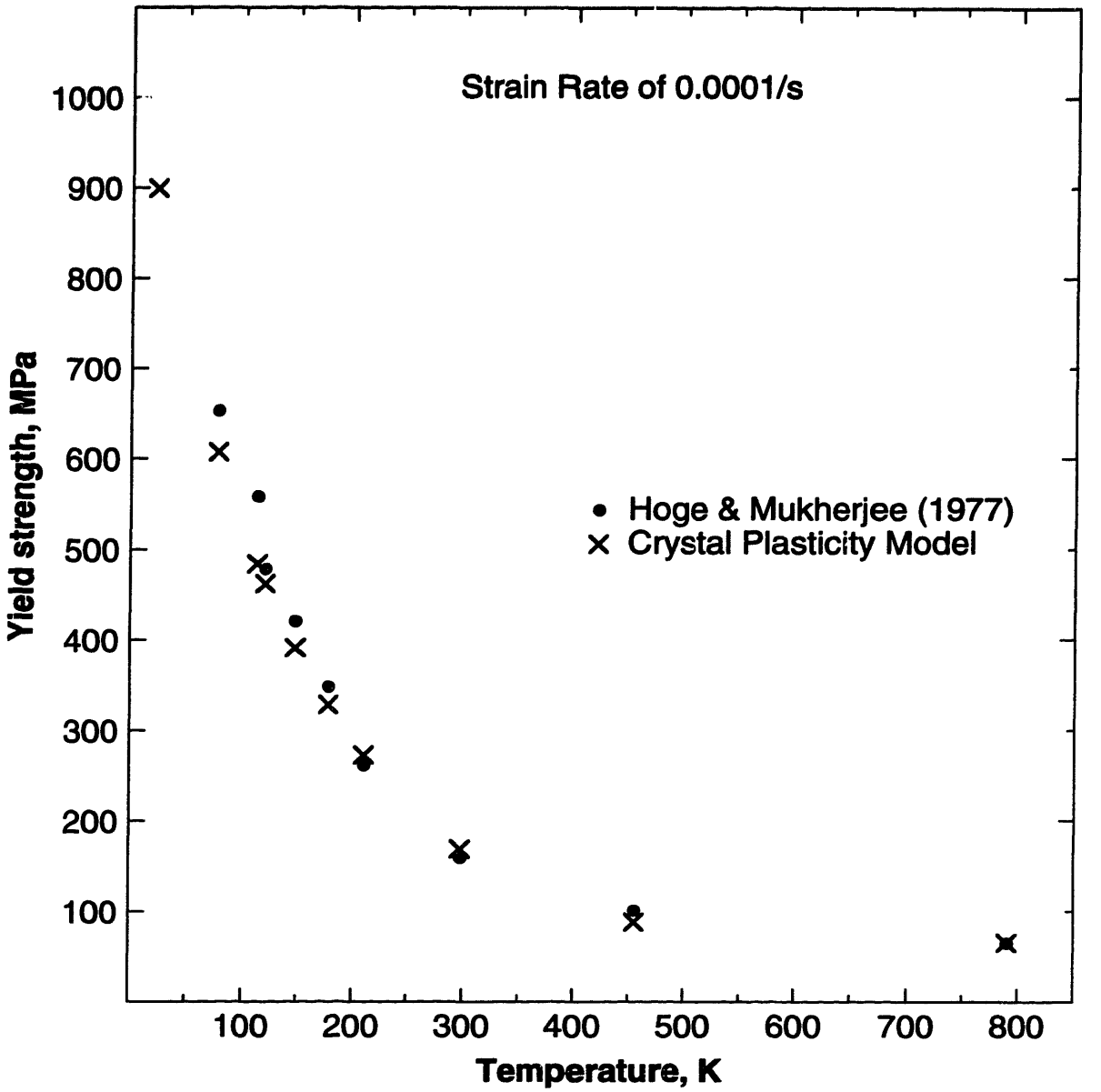

Figure 2-11: Fit of the Taylor-type crystal plasticity model to the data of Hoge and Mukherjee [1977] on the temperature dependence of the yield strength of b.c.c. tantalum (Kothari and Anand [1997]).

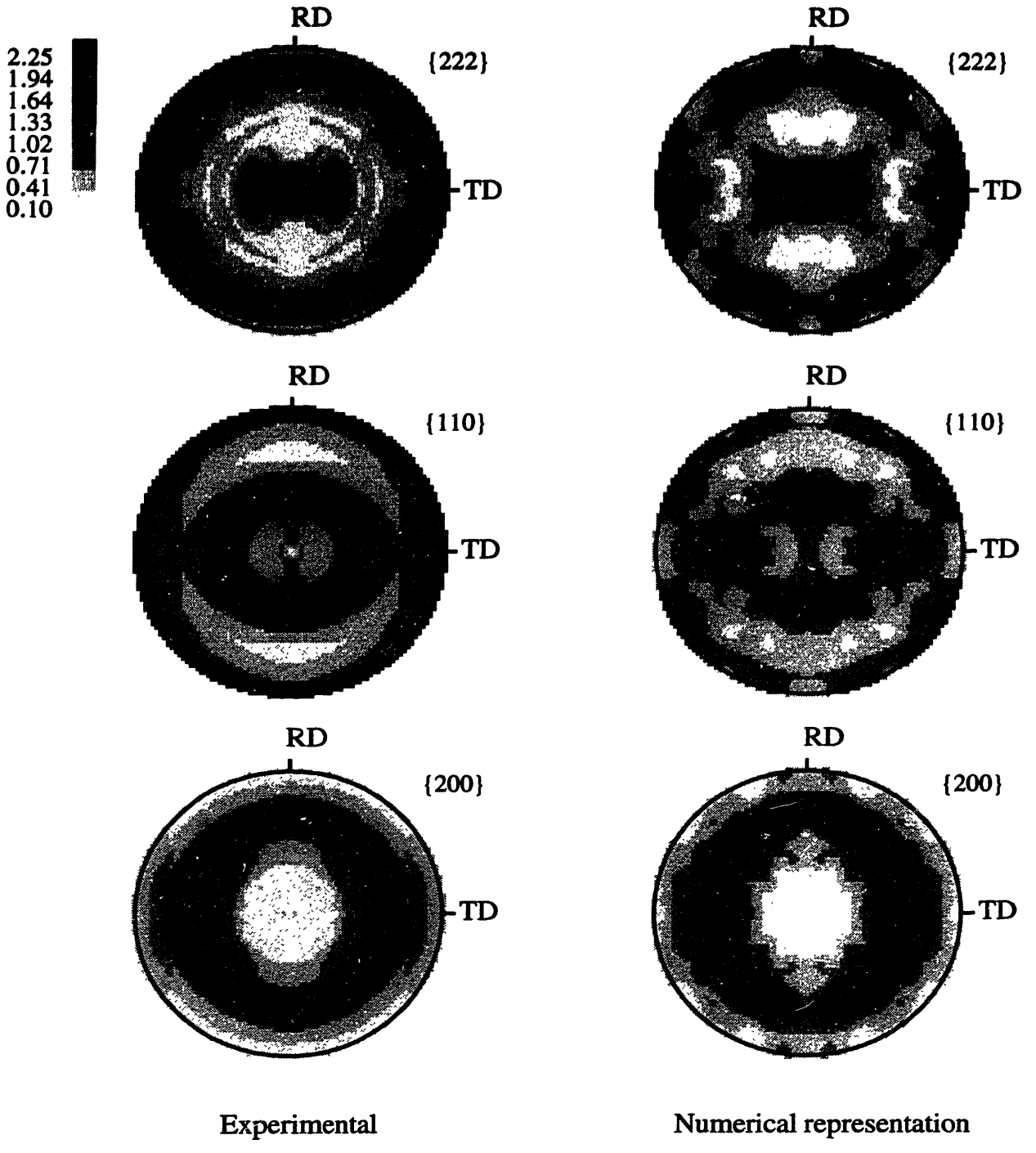

Figure 2-12: Representation of the texture of tantalum plate with 400 weighted grains (Kothari and Anand [1997]).

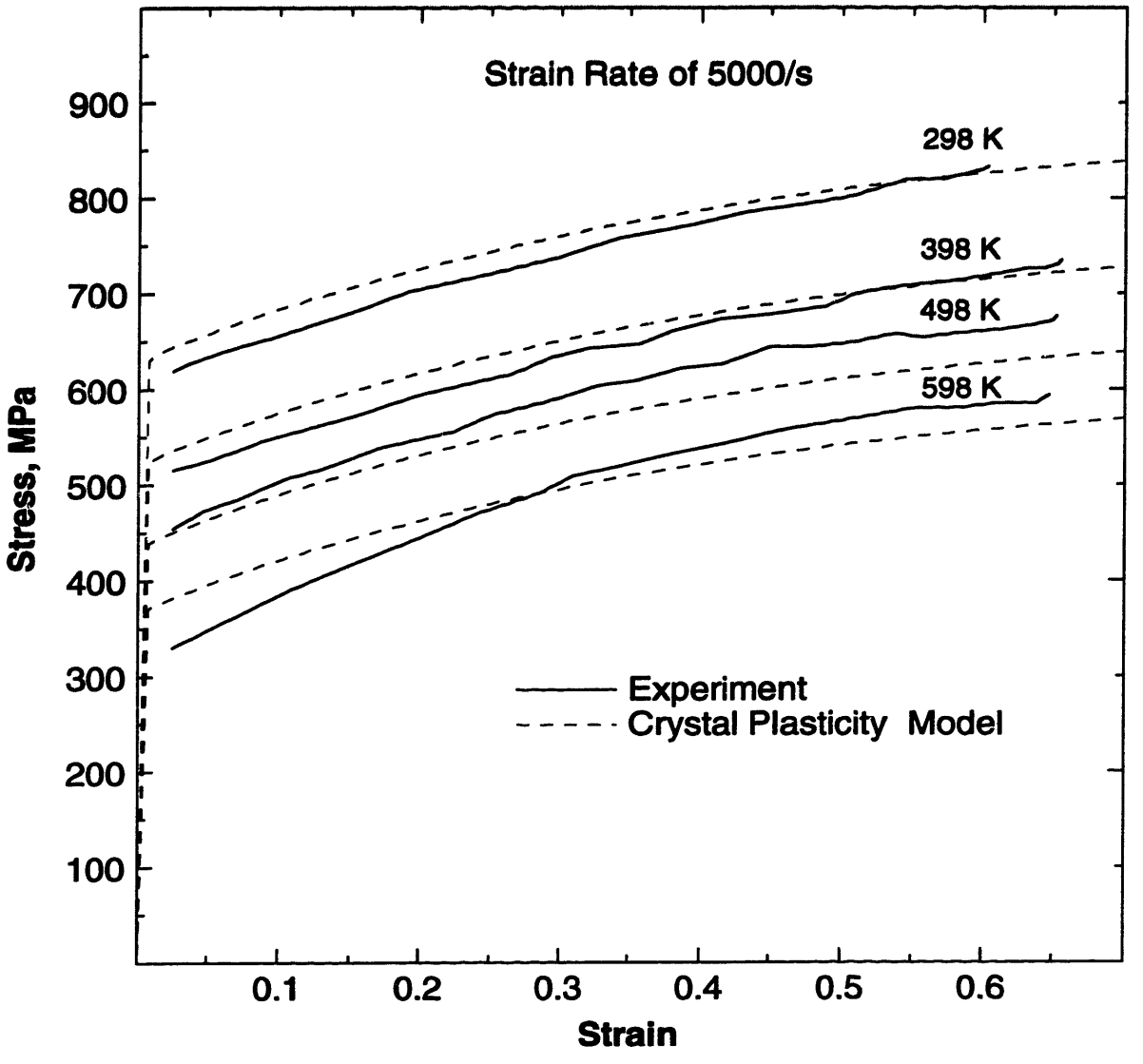

Figure 2-13: Comparison of the predictions from the Taylor-type crystal plasticity model against the *isothermal* experiments of Nemat-Nasser and Issacs [1996] (Kothari and Anand [1997]).

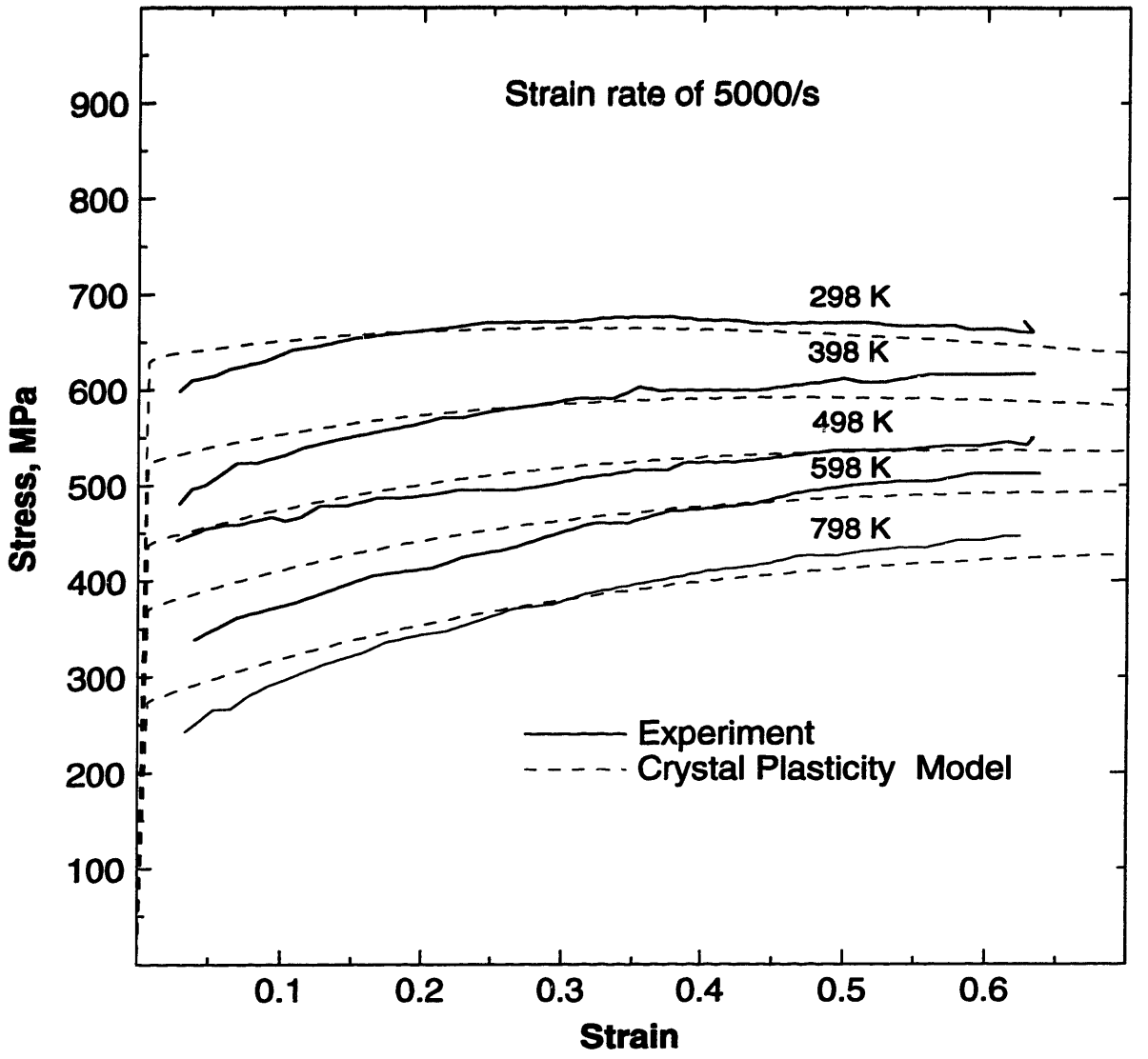

Figure 2-14: Comparison of the predictions from the Taylor-type crystal plasticity model against the *adiabatic* experiments of Nemat-Nasser and Issacs [1996] (Kothari and Anand [1997]).

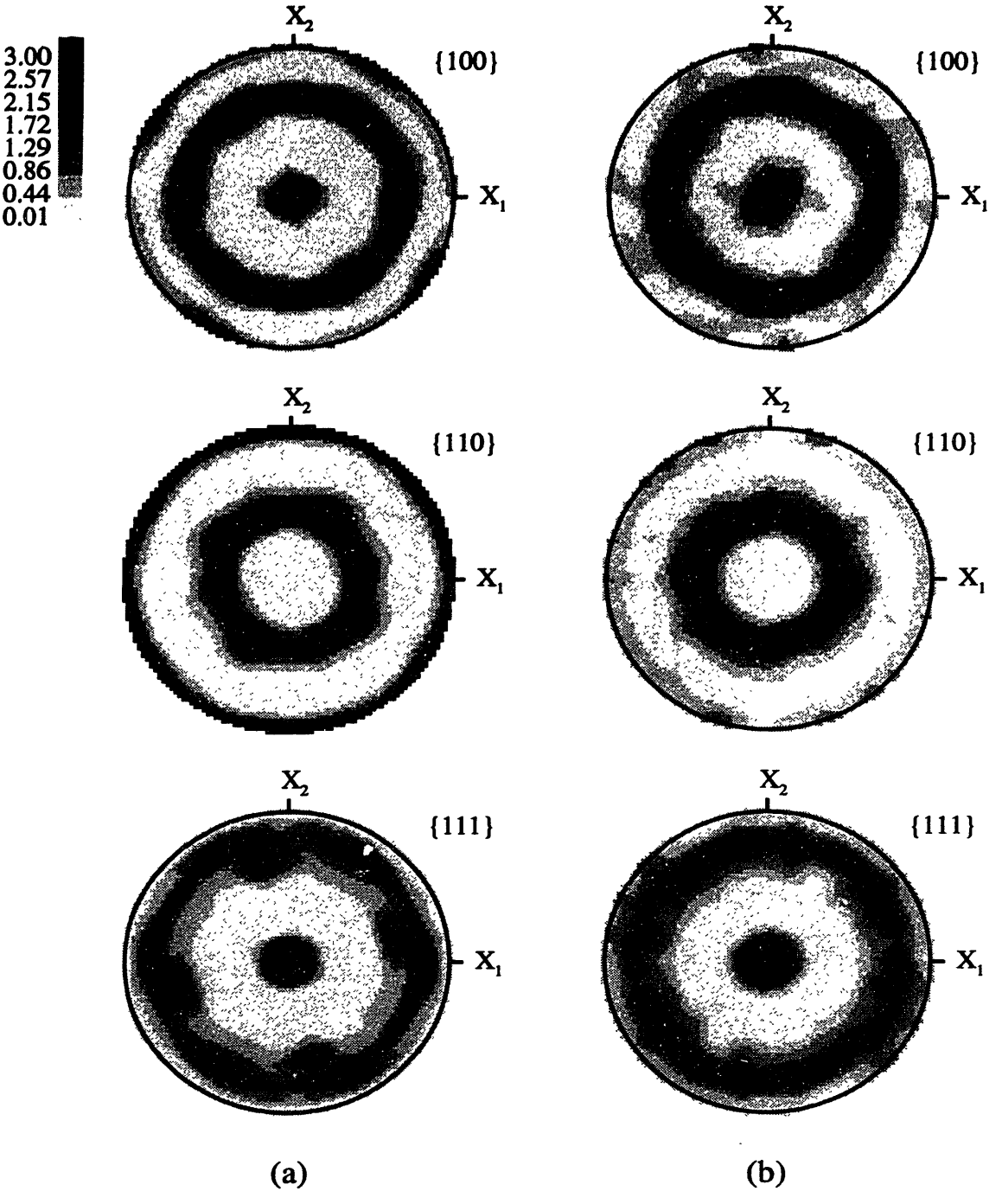

Figure 2-15: (a) Experimentally measured texture in the as-annealed aluminum 1100-O rod and (b) its numerical representation using 400 unweighted discrete grain orientations.

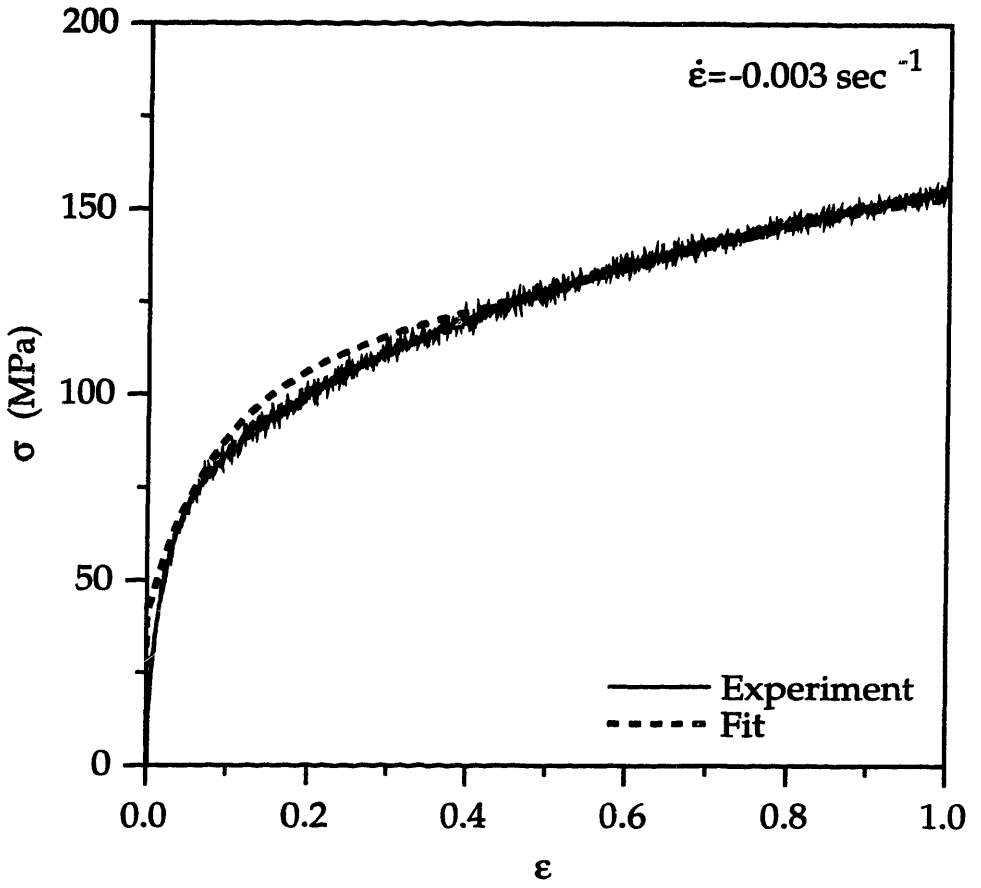

Figure 2-16: The measured compressive stress-strain response for 1100-O at room temperature and the numerical fit from the model.

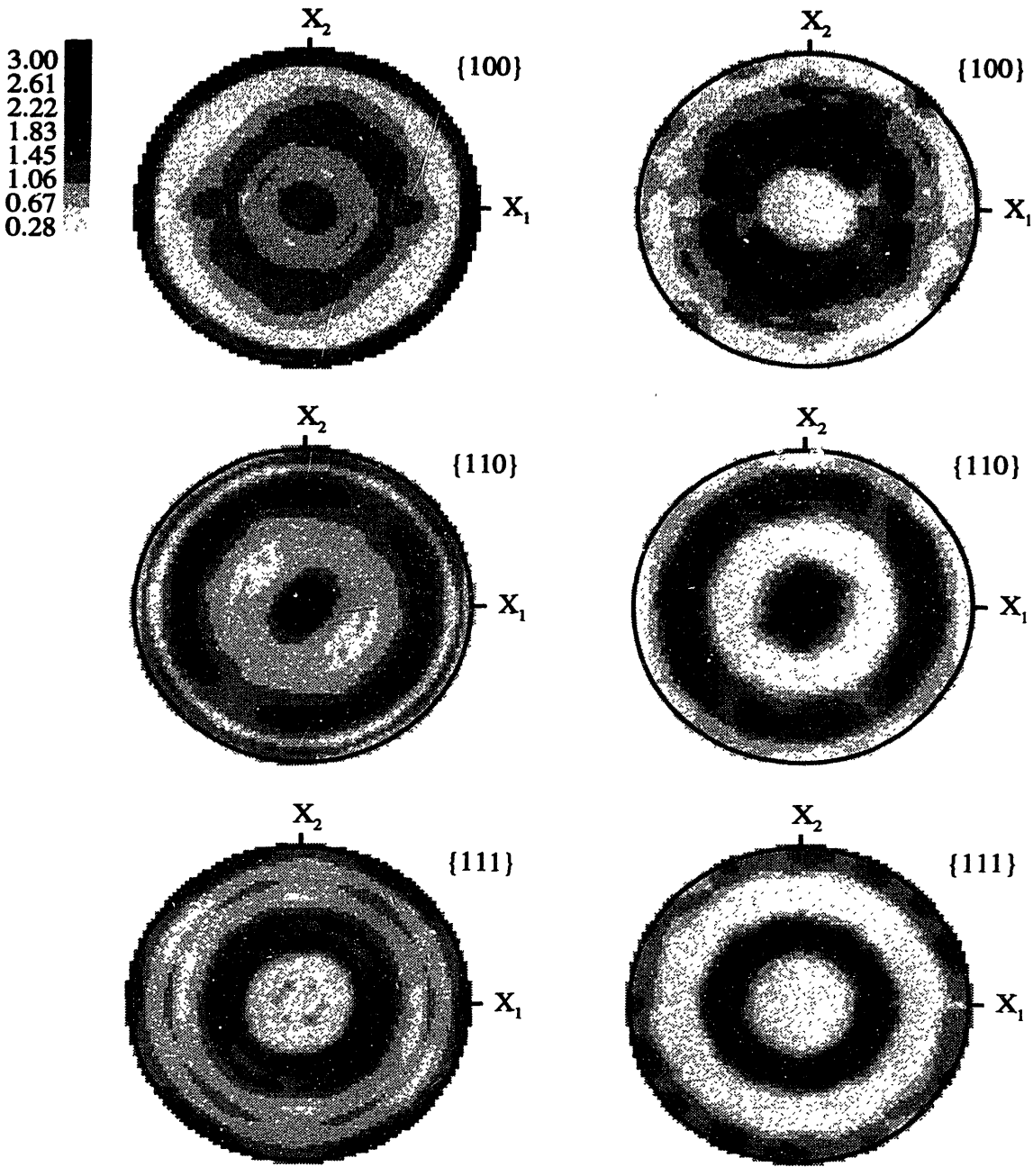

Figure 2-17: Comparison of the experimentally measured texture in the simple compression experiment on 1100-O at room temperature with the texture predicted by the Taylor-type crystal plasticity model.

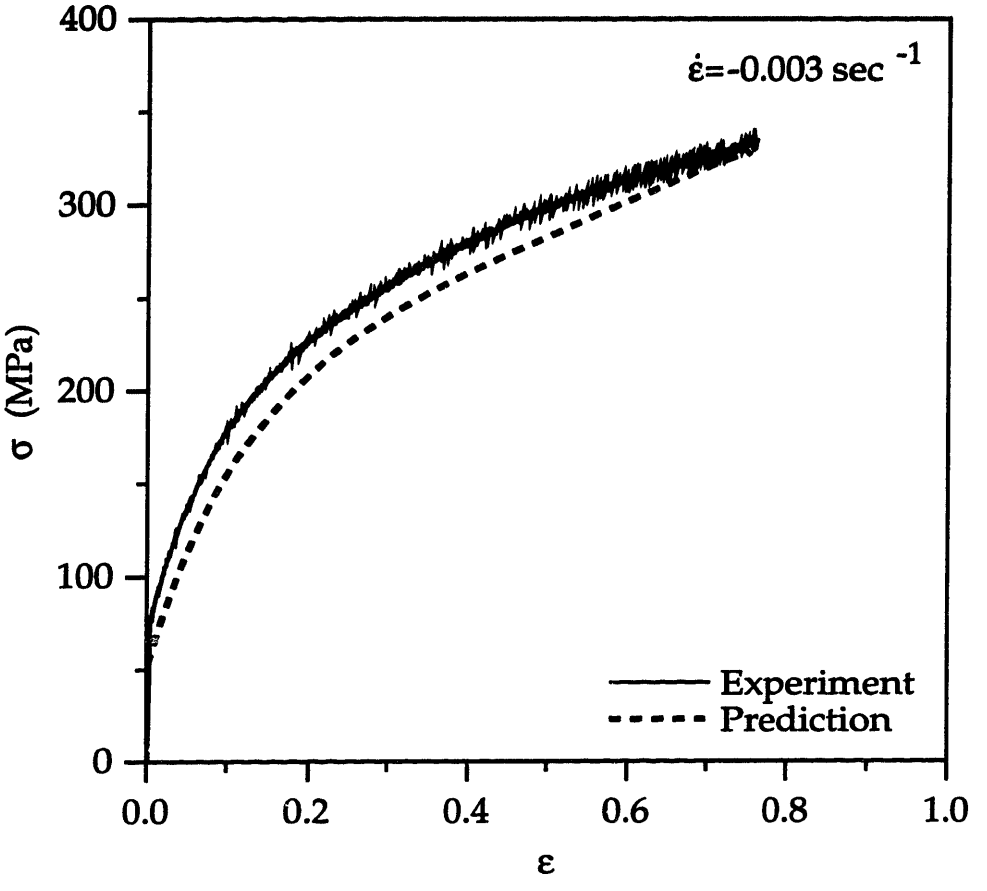

Figure 2-18: Comparison of the measured compressive stress-strain response for 1100-O at 84 K with the numerical prediction.

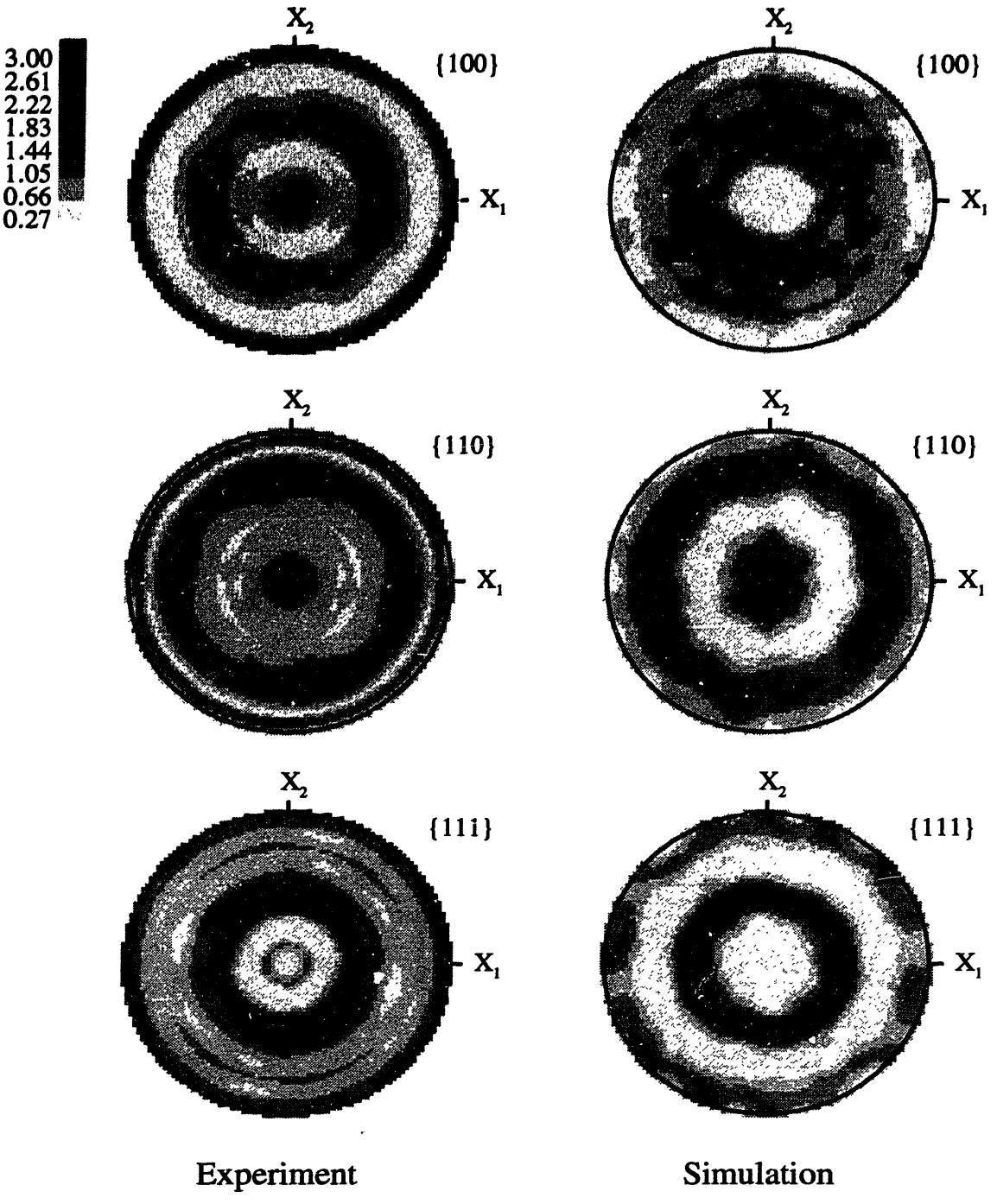

Figure 2-19: Comparison of the experimentally measured texture in the simple compression experiment on 1100-O at 84 K with the texture predicted by the Taylor-type crystal plasticity model.

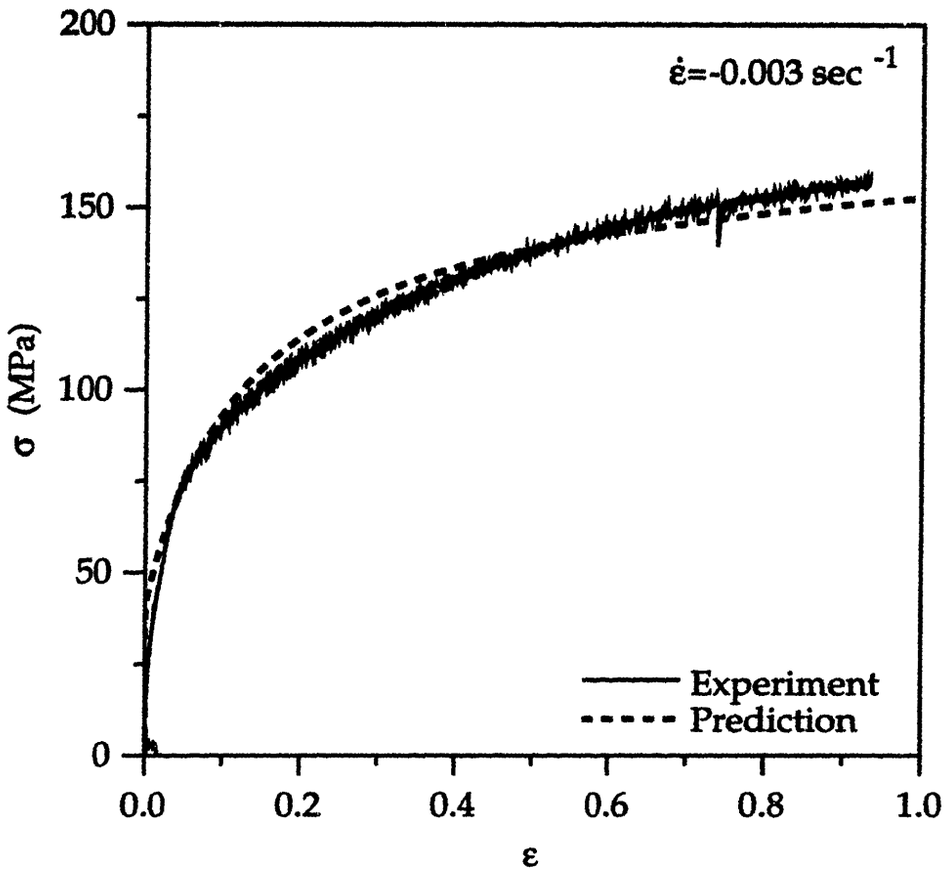

Figure 2-20: Comparison of the measured stress-strain response for plane-strain compression of 1100-O at 298 K with the numerical prediction.

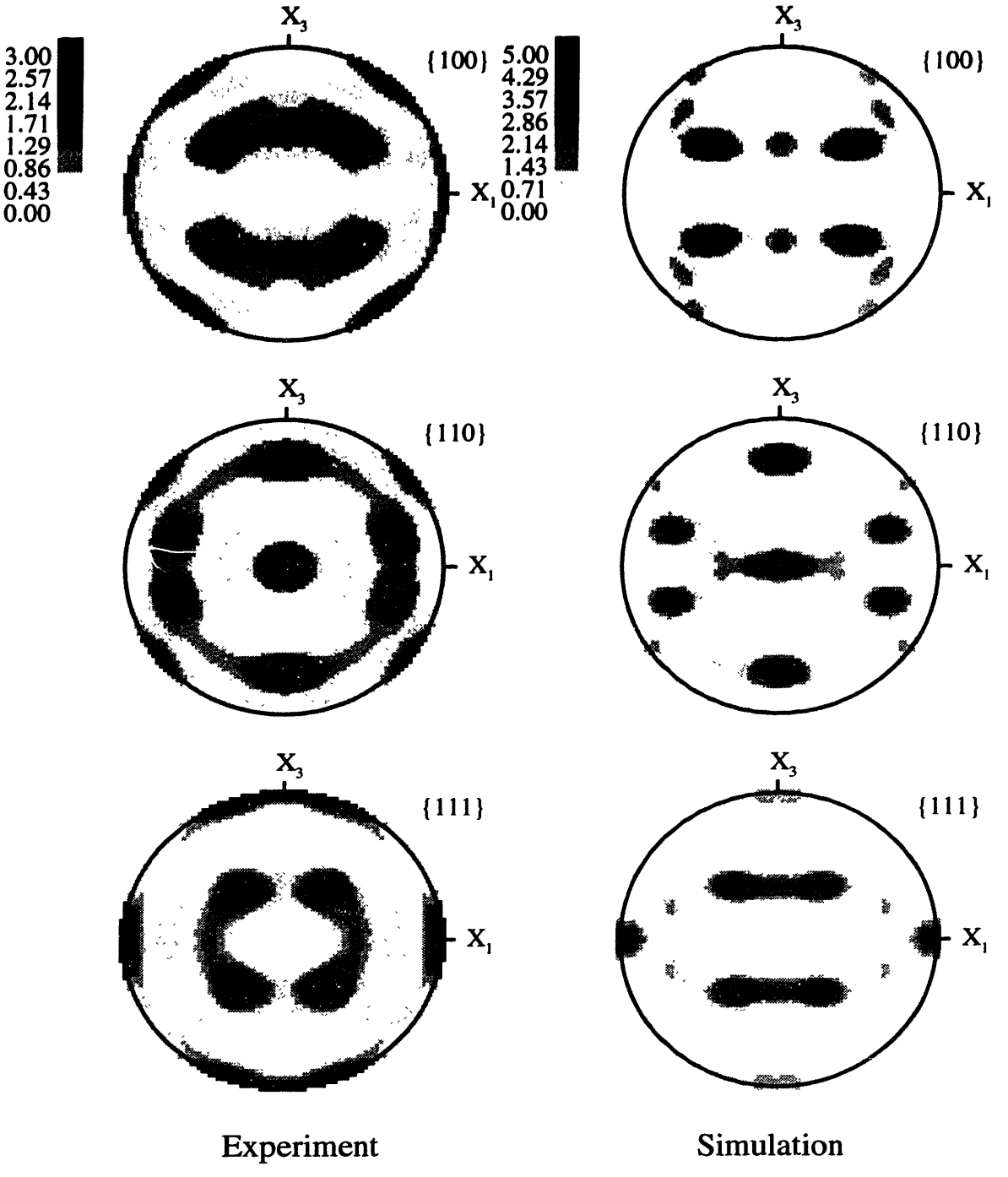

Figure 2-21: Comparison of the experimentally measured texture in the plane-strain compression experiment on 1100-O at 298 K with the texture predicted by the Taylor-type crystal plasticity model.

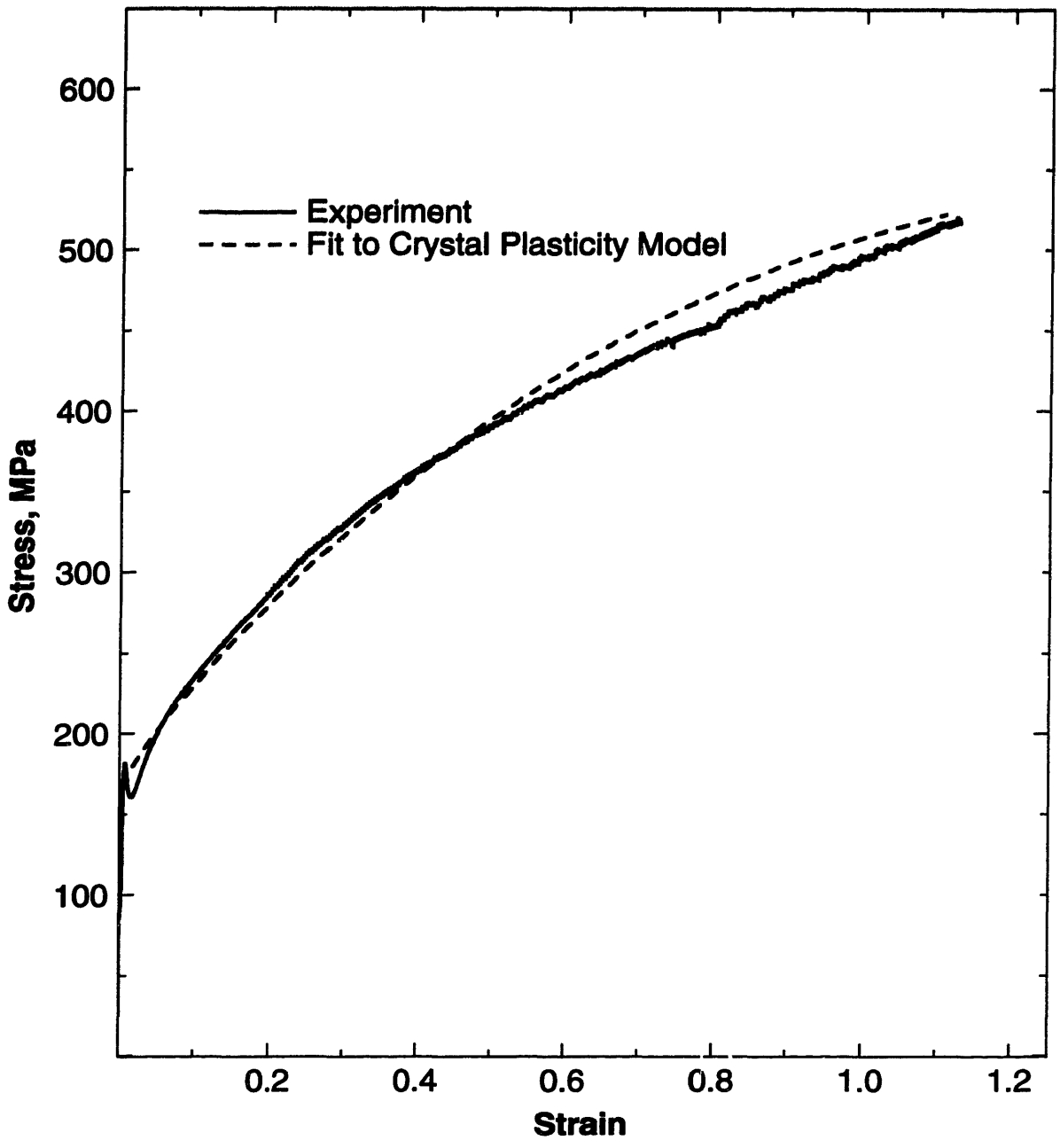

Figure 2-22: Fit of the prediction from the Taylor-type crystal plasticity model against the measured stress-strain response in simple compression experiment on annealed b.c.c. tantalum (Kothari and Anand [1997]).

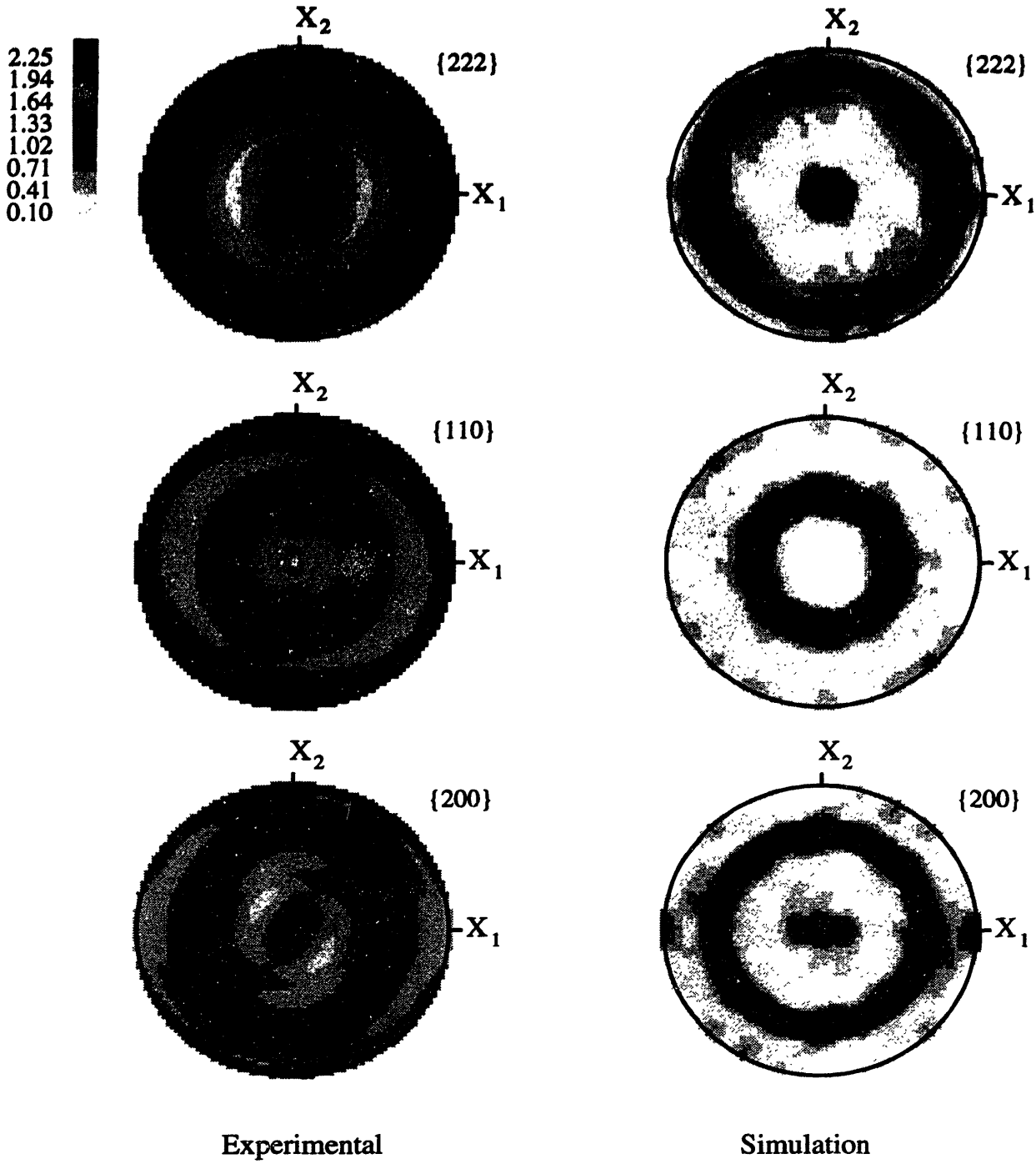

Figure 2-23: Comparison of the measured texture in the simple compression experiment on annealed b.c.c. tantalum against the texture predicted by the Taylor-type crystal plasticity model (Kothari and Anand [1997]).

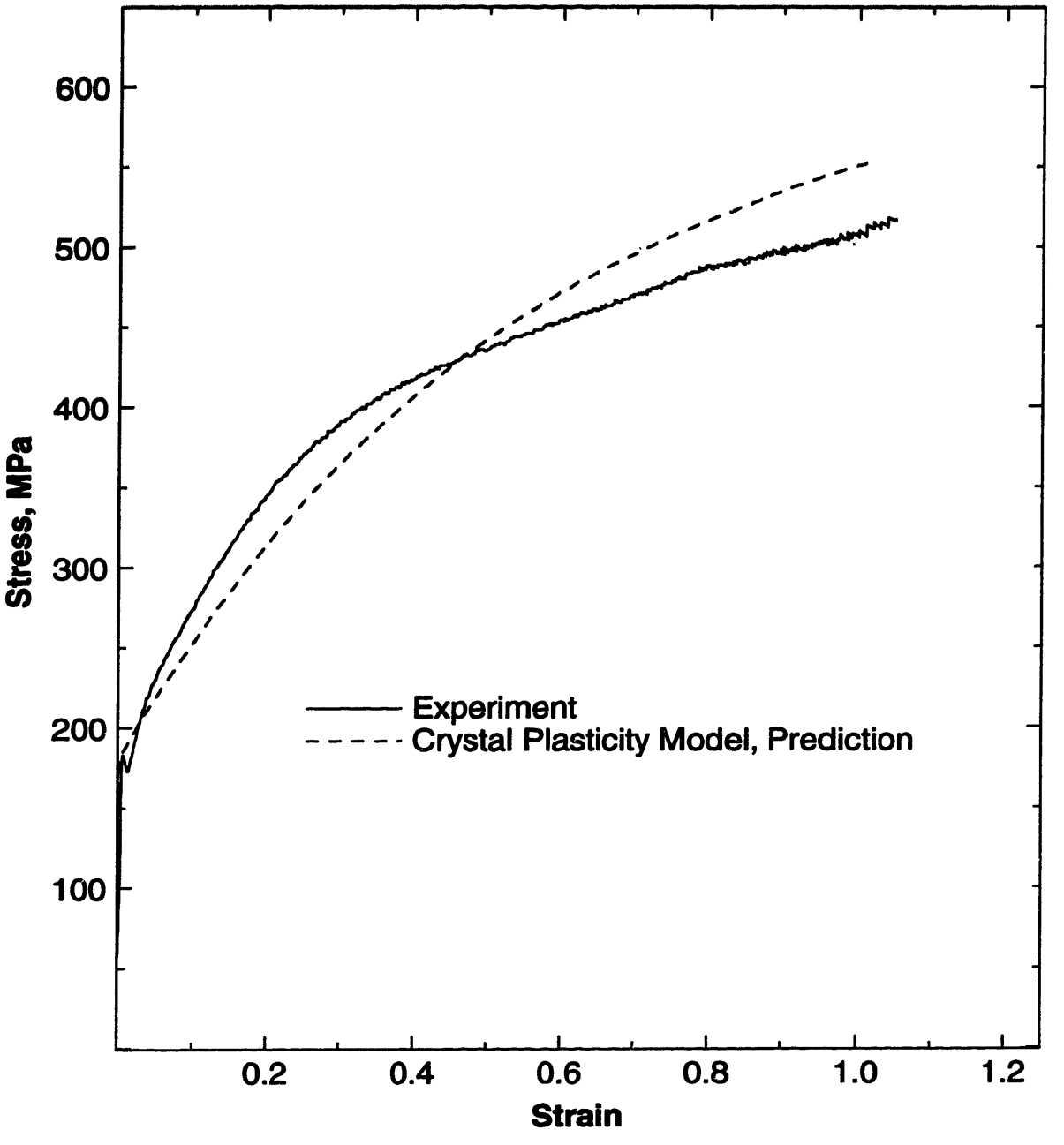

Figure 2-24: Measured and simulated stress-strain response from the Taylor-type crystal plasticity model for the plane strain compression experiment on annealed b.c.c. tantalum (Kothari and Anand [1997]).

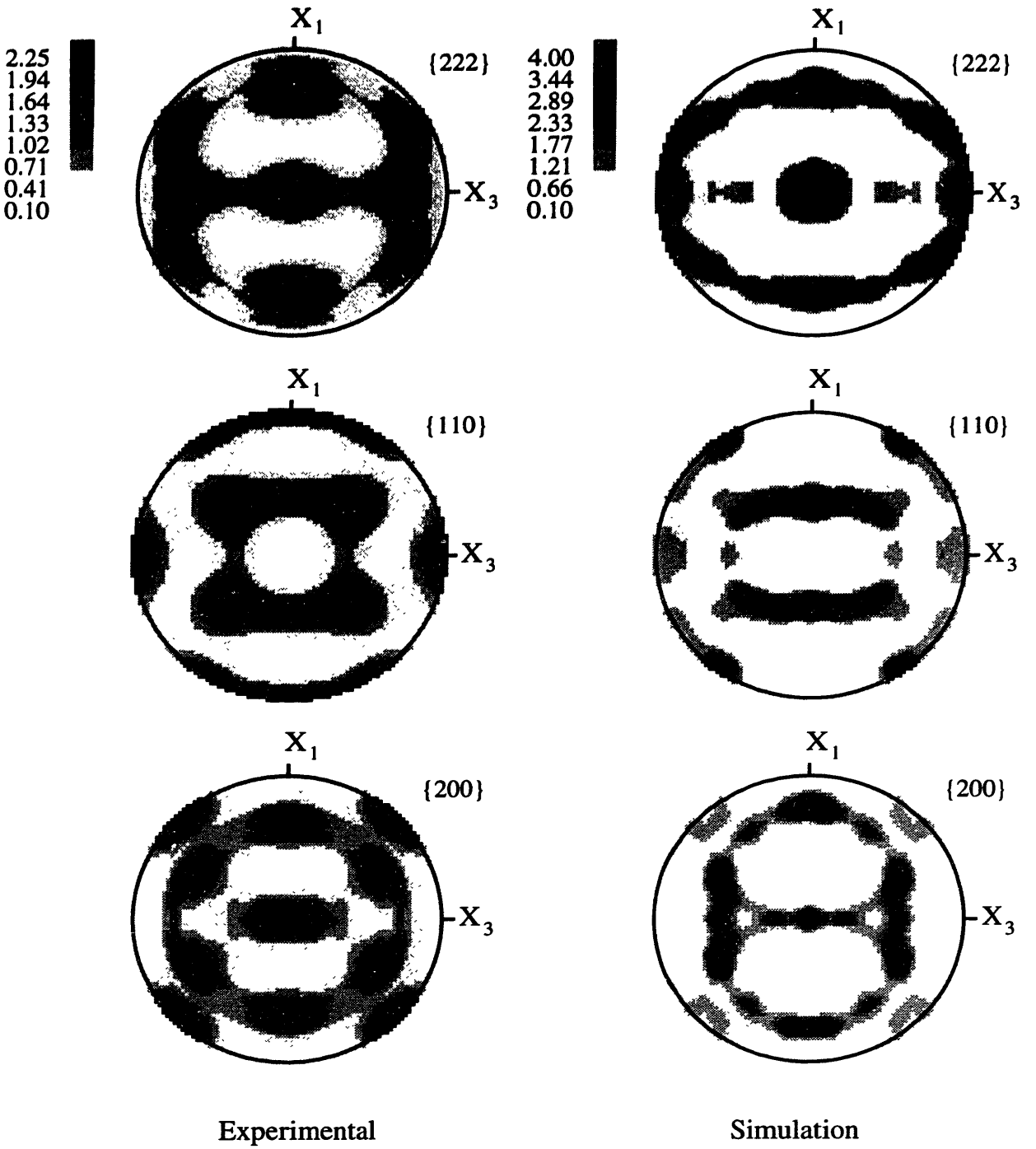

Figure 2-25: Comparison of the measured texture in the plane strain compression experiment on annealed b.c.c. tantalum against the texture predicted by the Taylor-type crystal plasticity model (Kothari and Anand [1997]).

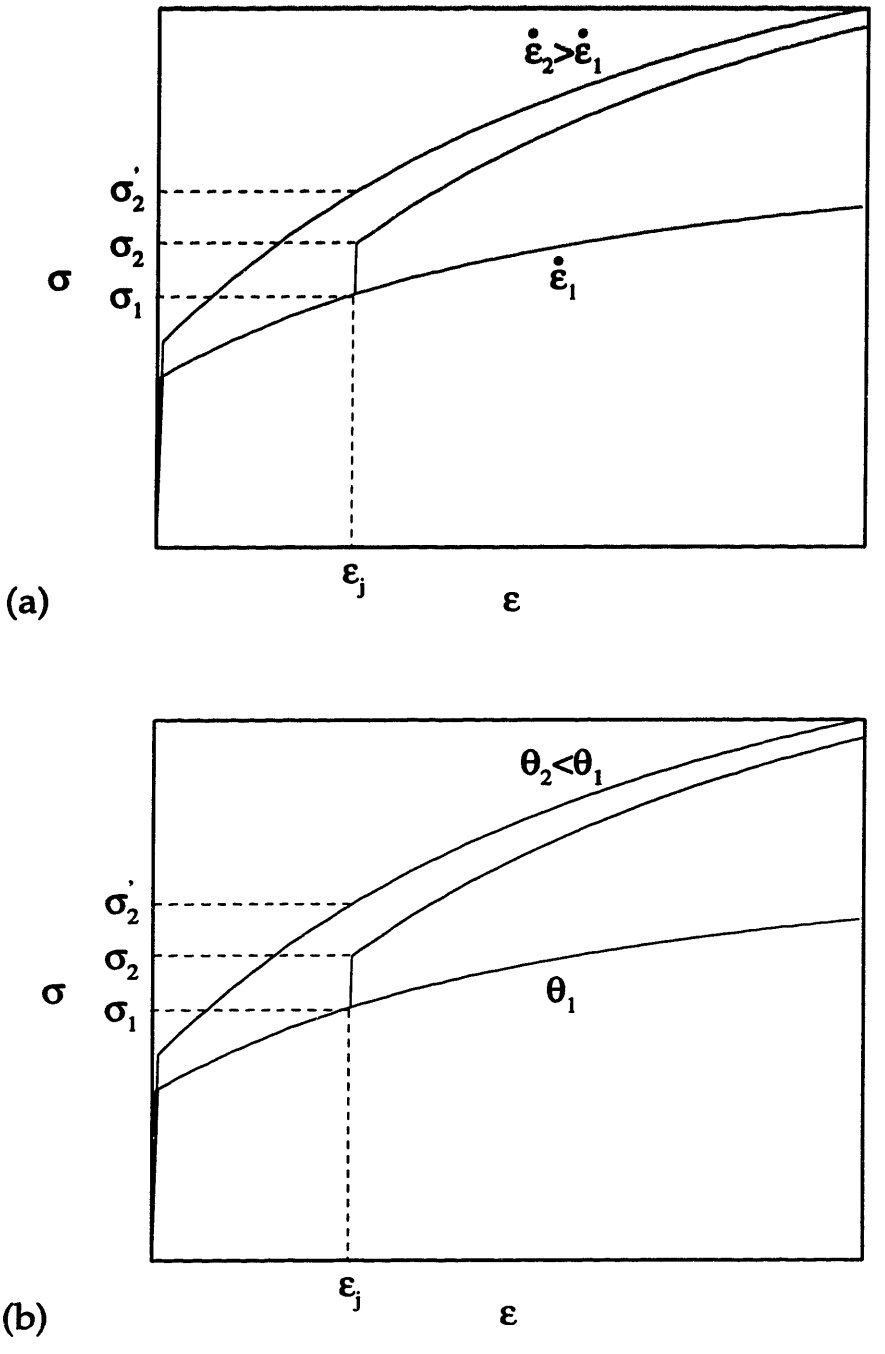

Figure 2-26: Schematic diagram illustrating the difference in the stress-strain response for (a) constant strain rate and strain-rate jump test (b) constant temperature and temperature jump tests in f.c.c. materials.

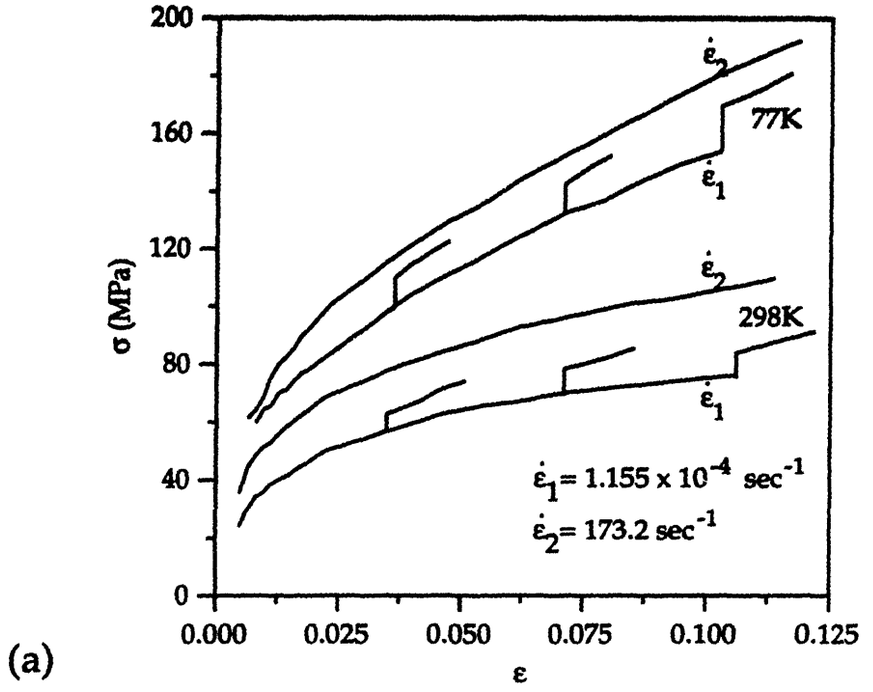

(a)

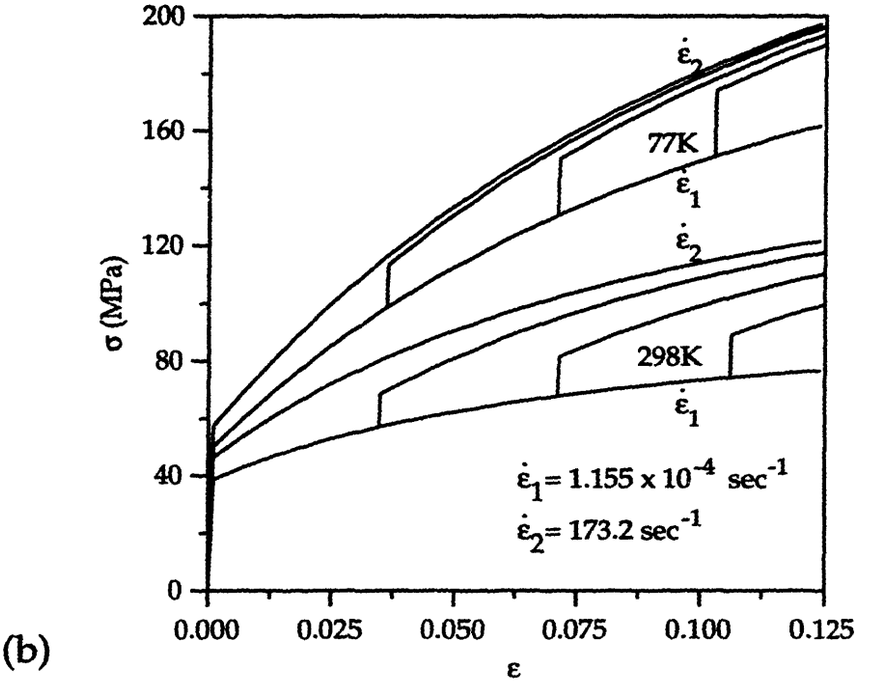

(b)

Figure 2-27: Stress-strain curves for constant true strain rate and strain-rate jump tests on 1100-O: (a) Experimental results of Senseny, Duffy and Hawley [1978] (b) Predictions of the constitutive model.

(a)

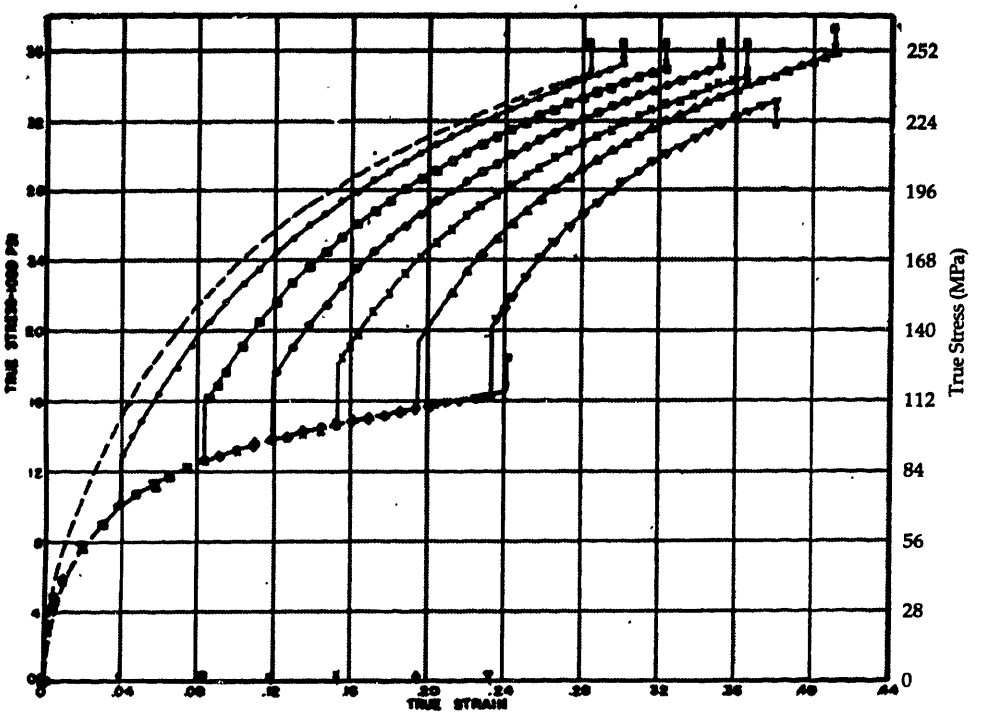

(b)

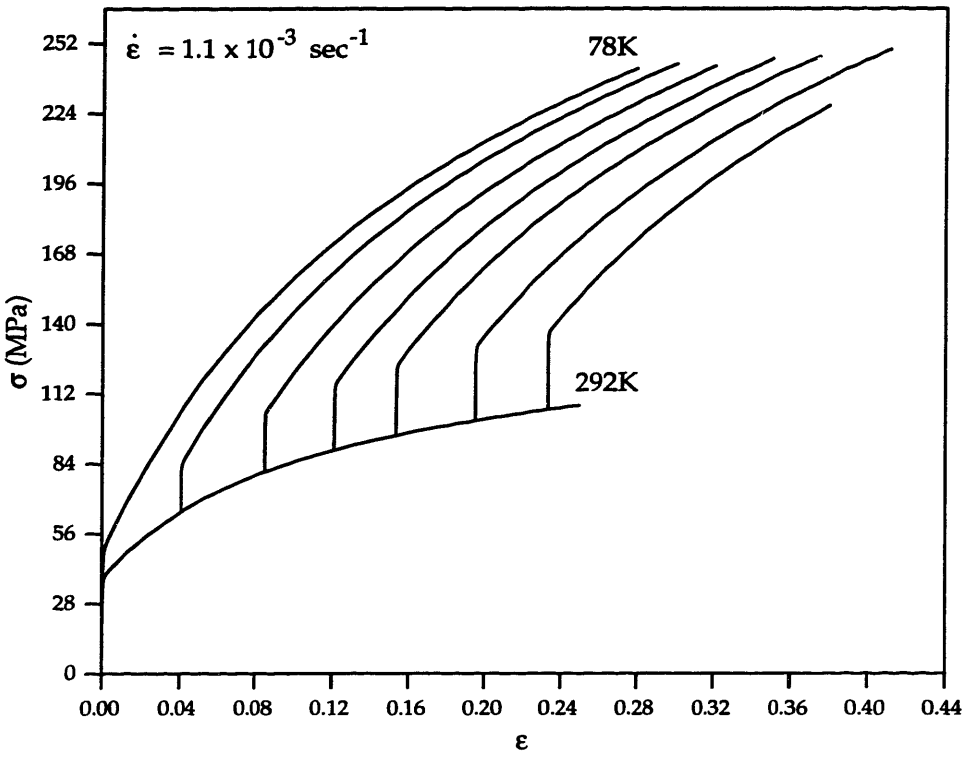

Figure 2-28: Stress-strain curves for isothermal and temperature-decrement tests on 2S-O aluminum: (a) Experimental results of Dorn, Goldberg and Tietz [1949] (b) Predictions of the constitutive model with material parameters based on the data of Senseny, Duffy and Hawley [1978].

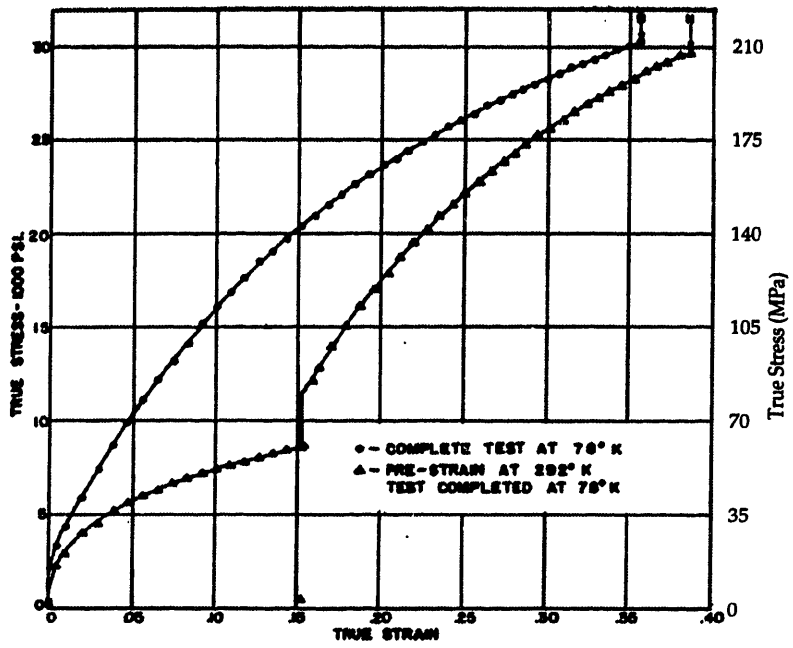

(a)

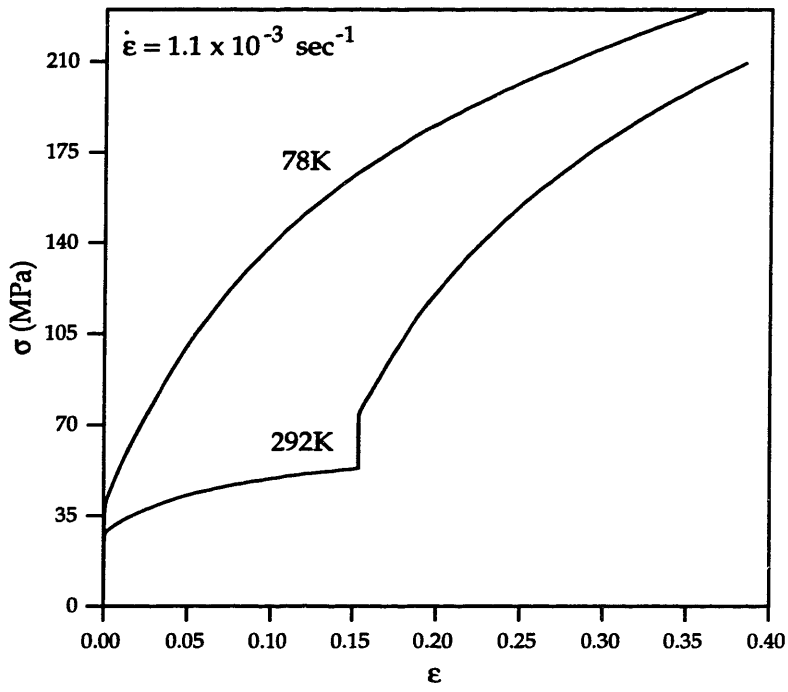

(b)

Figure 2-29: Stress-strain curves for isothermal and temperature-decrement tests on 99.98% pure aluminum: (a) Experimental results of Dorn, Goldberg and Tietz [1949] (b) Predictions of the constitutive model with material parameters based on the data of Carreker and Hibbard [1957].

(a)

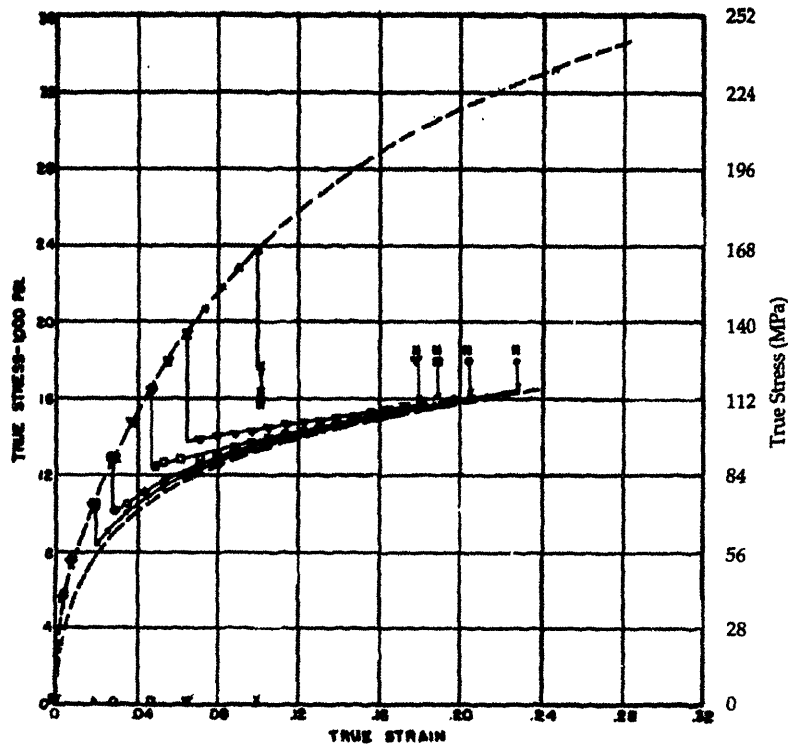

(b)

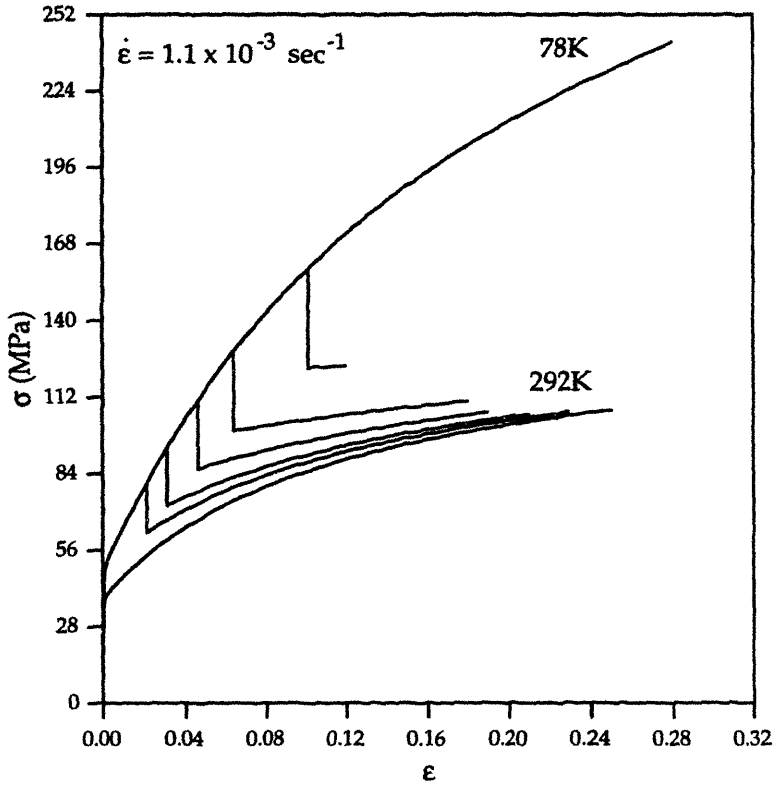

Figure 2-30: Stress-strain curves for isothermal and temperature-increment tests on 2S-O aluminum: (a) Experimental results of Dorn, Goldberg and Tietz [1949] (b) Predictions of the constitutive model.

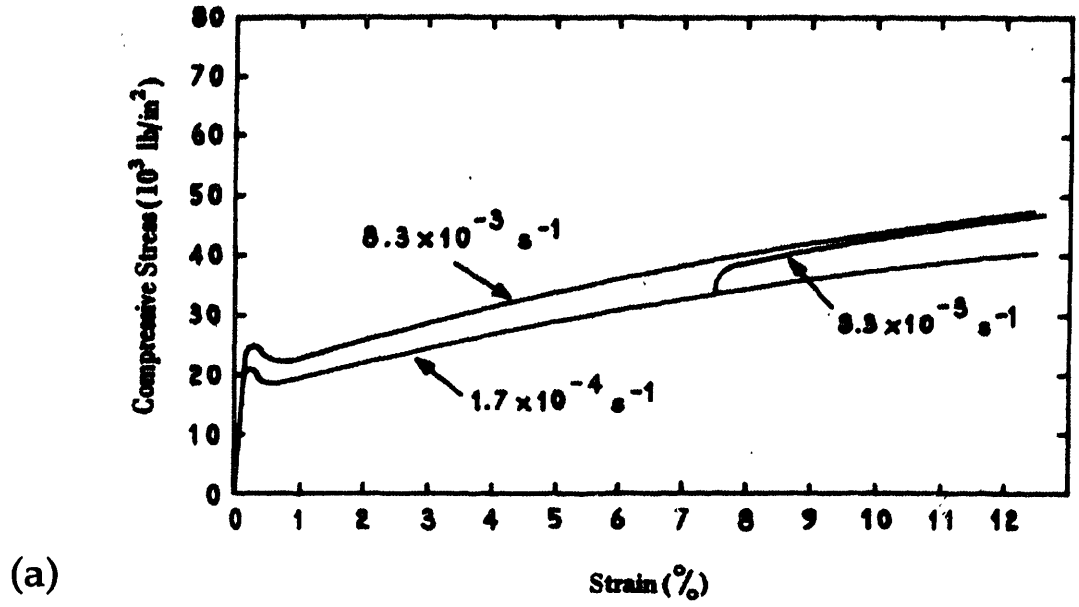

(a)

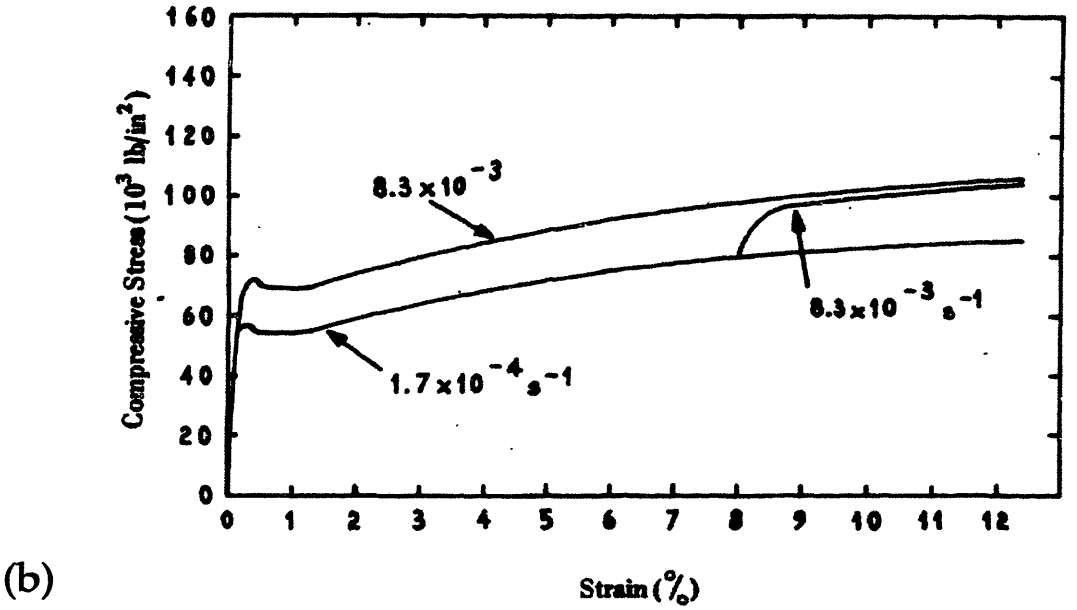

(b)

Figure 2-31: Stress-strain curves for constant true strain rate and strain-rate jump tests on (a) b.c.c. niobium and (b) b.c.c. molybdenum (Campbell [1970])

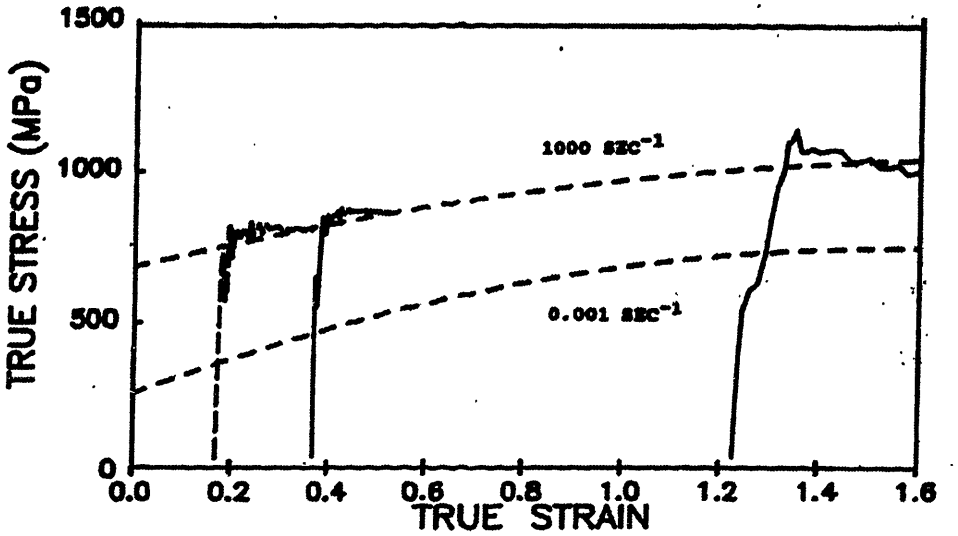

(a)

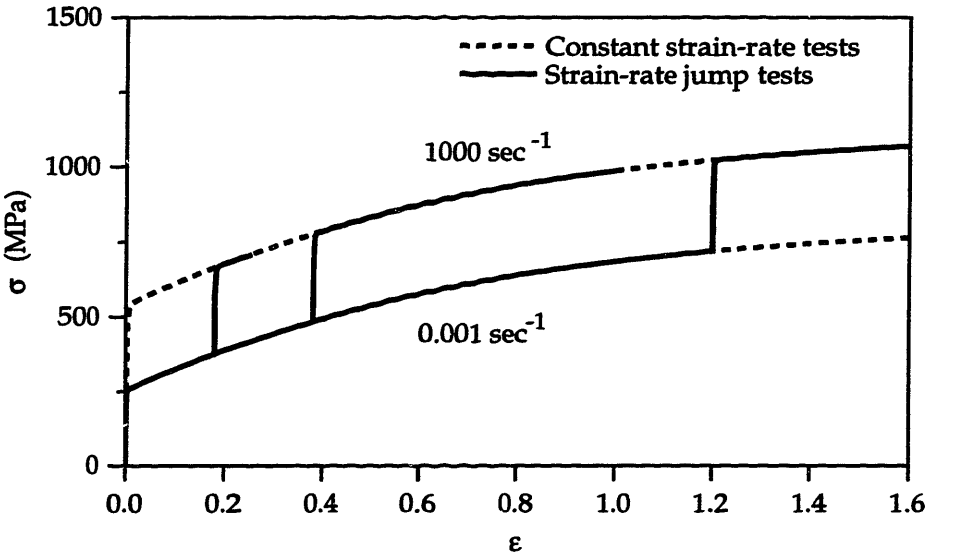

(b)

Figure 2-32: Stress-strain curves for constant true strain rate and strain-rate increment tests on b.c.c. tantalum: (a) Experimental results of Lopatin *et al.* [1992] (b) Predictions of the constitutive model.

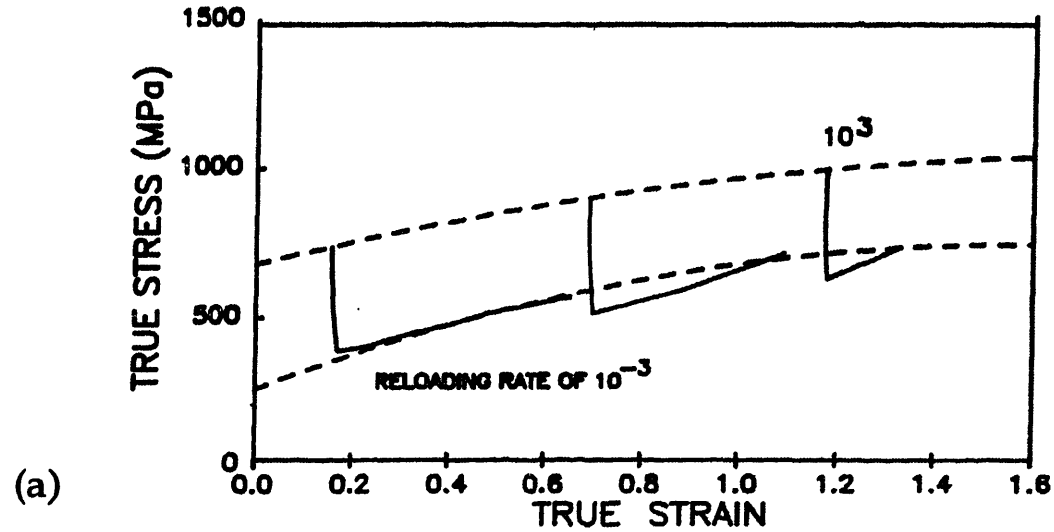

(a)

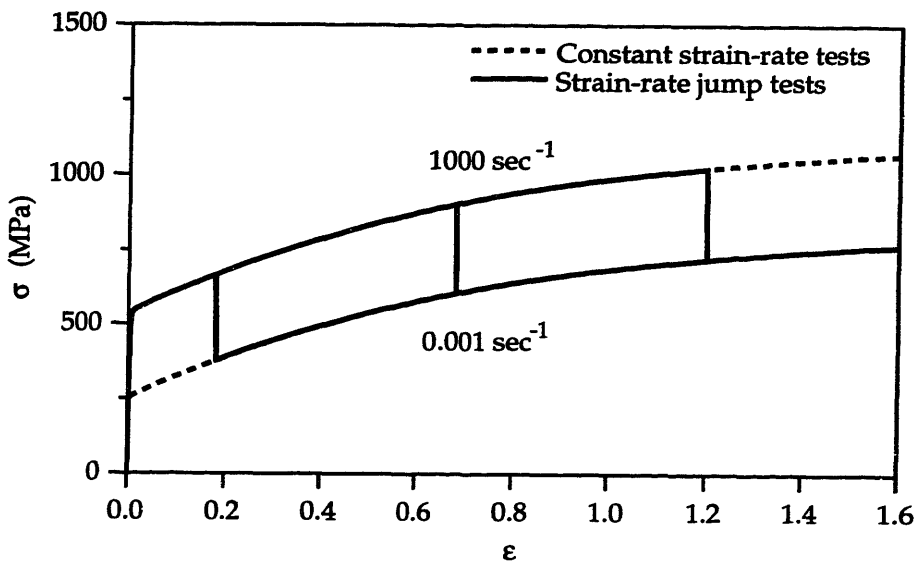

(b)

Figure 2-33: Stress-strain curves for constant true strain rate and strain-rate decrement tests on b.c.c. tantalum: (a) Experimental results of Lopatin *et al.* [1992] (b) Predictions of the constitutive model.

Chapter 3

Application to Deformation Processing of F.C.C. materials

Ears which develop during the drawing of anisotropic sheets are important defects that form during the production of deep-drawn containers. These ears must be trimmed to produce the desired height and shape of the container. A better understanding of the process of development of ears during forming should lead to improved process designs which reduce earing, and possibly eliminate the need for trimming. The quantitative prediction of earing patterns is a classical outstanding problem in anisotropic plasticity (e.g., Tucker [1961]; Wilson and Butler [1961]). Becker *et al.* [1993] have attempted to predict earing patterns in polycrystalline aluminum sheets. While their calculations are noteworthy, they were unable to obtain fully-drawn cups in their simulations. In this chapter, the constitutive equations and computational procedures presented in Chapter 2 are employed to simulate the formation of earing defects in (*i*) single crystal sheets of pure aluminum and (*ii*) polycrystalline sheet of Al2008-T4. The finite element simulations on the single crystal sheets are compared with the experimental results of Tucker [1961] while the numerical simulation for the polycrystalline sheet is compared with experiments performed on Al2008-T4.

3.1 Earing in Single Crystal Cups of Aluminum

Tucker [1961], in some pioneering work, reported on the different earing patterns in cups drawn from circular blanks of aluminum with different initial orientations. Depending

on the initial orientation of a blank, there is a wide variety in the number of ears, their positions and heights, Fig. 3-1(a). In this study, the earing behavior in cups drawn from circular blanks which were initially in the [001] and [111] orientations, Figs. 3-1(b) and 3-1(c) respectively, where these orientations refer to the crystallographic directions that are normal to the blank are considered.

The geometry of the cup-drawing in the simulations approximates the apparatus used by Tucker in his experiments, Fig. 3-2(a) (Becker *et al.* [1993]). Circular blanks 79 mm diameter and 0.81 mm thick are drawn in an apparatus consisting of a punch and a die of diameters 41.2 mm and 44 mm, respectively. Fig. 3-2(b) shows the finite element mesh used for the simulation. Both the [001] and [111] orientations possess rotational symmetries about the punch axis; accordingly, only a sector of the circular blank need be considered in each analysis. Also, since the inplane-deformation of the sheet is of primary interest, the sheet is modelled with two elements through the thickness ABAQUS continuum C3D8R and C3D6 elements are used. The interfaces between the punch and the blank, the blank and the blankholder, and the blank and the die are modeled as frictionless. Also, the die, blankholder and the punch are treated as rigid surfaces. A constant force of 10 KN is applied on the blankholder, and the punch speed is taken to be 1 mm/sec.

3.1.1 Material Parameters for Single-Crystal sheets of Aluminum

Tucker [1961] does not report the material properties for the single-crystal sheets used in his experiments. The parameters used in our simulations are based on single-crystal data available in the literature. The data of Cottrell and Stokes [1955] for the variation of the yield-stress with temperature in single-crystals of 99.992% pure aluminum is used to determine the flow parameters for the sheets in the simulations. The parameters obtained from this fit, Fig. 3-3(a), are:

$\dot{\gamma}_0 = 1.732 \times 10^6 \text{sec}^{-1}$, $\Delta F^* = 2.5 \times 10^{-19}$ J, $p = 0.131$, $q = 1.1$, $\chi = 0.695$.

The flow parameters for the single crystal aluminum are in close agreement with the corresponding values for relatively-pure polycrystalline aluminum enlisted in Chapter 2.

The slip-system hardening parameters for the simulations are obtained by fitting the model's predictions for the stress-strain response with that obtained in the channel-die compression experiments of Becker *et al.* [1991] on single-crystals of commercial purity

aluminum as shown in Fig. 3-3(b). This yields the following parameters[1]:

$s_{*,0} = 10$ MPa,$s_{a,0} = 14$ MPa,$h_0 = 65$ MPa,$r = 2$,$s_s = 186$ MPa.

Also, the latent hardening parameter for all the deep-drawing simulations is taken to be $q_l = 1.4$.

3.1.2 Cup-drawing simulation for the [001] and [111] oriented blanks

Fig. 3-4(a) is a schematic diagram of the earing pattern observed by Tucker in aluminum single crystals in the [001] orientation (Fig. 3-1(b)). A total of four ears form along the [100], [010], [$\bar{1}$00] and [0$\bar{1}$0] initial directions in the blank. The symmetry of this orientation permits a model which uses only a 45° sector of the blank. The 0° and 45° planes are symmetry planes and are free of shear tractions.

Fig. 3-5(a), taken from Tucker's [1961] paper, shows the final shape of the aluminum single-crystal cup in this orientation. Fig. 3-6(a) shows the predicted shape of the fully-drawn cup. For clarity, the entire cup has been shown by suitably reflecting the 45° sector that was simulated. This figure also shows the contours of the equivalent tensile plastic strain $\bar{\epsilon}^p$ in the cup at the end of the drawing process[2]. The accumulated plastic strain is maximum in the ears. The prediction of the number of ears and their position is accurate. No attempt was made to compare the heights of the ears as the material in our simulation is different from that used by Tucker in his experiments.

Fig. 3-1(c) shows that in the [111] orientation six ears form. Fig. 3-4(b) is a schematic view of the earing pattern. The symmetry of this orientation permits a model which uses only a 60° sector of the blank. The 0° and 60° planes are symmetry planes and are free of shear tractions.

Fig. 3-5(b) (from Tucker [1961]) shows the final shape of the aluminum single-crystal cup in this orientation. Fig. 3-6(b) shows the predicted shape of the fully-drawn cup. The entire cup has been shown by suitably reflecting the 60° sector that was simulated. This figure also shows the contours of the equivalent tensile plastic strain $\bar{\epsilon}^p$ in the cup at the

[1]Due to the lack of single-crystal stress-strain data up to large strains for different strain rates and temperatures, the dependence of the saturation value of the slip system resistance s_s on the strain-rate and temperature is ignored. Since the deep-drawing experiments of Tucker [1961] were performed in isothermal and quasi-static conditions, the qualitative aspects of the results are not expected to be affected by this assumption.

[2]For single crystals the equivalent tensile plastic strain is defined as $\bar{\epsilon}^p = \int \dot{\bar{\epsilon}}^p \, dt$, where $\dot{\bar{\epsilon}}^p = \left\{\sum_\alpha \tau^\alpha \dot{\gamma}^\alpha\right\}/\bar{\sigma}$, with $\bar{\sigma} = \sqrt{(3/2)\bar{\mathbf{T}}' \cdot \bar{\mathbf{T}}'}$.

end of the drawing process. Again, the accumulated plastic strain is larger in the ears, and the prediction of the number of ears and their position is accurate.

3.2 Earing in Polycrystal Cups of Al2008-T4

3.2.1 Characterization of Al2008-T4 Sheet

Polycrystalline Al2008-T4 sheet[3], 0.7874 mm in thickness, was kindly provided by ALCOA Technical Center. Metallographic specimens from the sheet were polished and then etched with Keller's reagent (2mL 48% HF, 3mL conc. HCl, 5mL conc. HNO_3 and 190mL H_2O) to reveal the grains. The average grain diameter in the rolling plane was $\sim 60\mu$m. The initial crystallographic texture of the as-received sheet was measured by x-ray irradiation using a Rigaku RU200 diffractometer. The proçedure for the texture measurement is provided in detail in Appendix C. Fig. 3-7(a) shows the measured pole-figures (equal-area projections). Fig. 3-7(b) shows a numerical representation of this texture using a weighted average over 192 components. Fig. 3-7(c) shows a numerical representation of the texture using a weighted average over only 33 components. Although the texture representation using 192 components is more accurate, in the numerical calculations for cup drawing the computationally less expensive numerical representation, which employs only 33 components, is used. Figs. 3-8(a) and 3-8(b) are inverse pole-figure plots for the rolling and transverse directions, respectively.

Due to the lack of data for the yield-stress variation with temperature for Al2008-T4, for the deep-drawing simulation, the plastic flow parameters[4] obtained from the data of Duffy [1974] for 1100-O are employed,

$$\dot{\gamma}_0 = 1.732 \times 10^6 \text{sec}^{-1}, \Delta F^* = 3 \times 10^{-19} \text{J}, \chi = 0.73, p = 0.141, q = 1.1.$$

In order to obtain the material parameters for the slip system deformation resistance and its evolution, a tension test was conducted on a sheet-tension specimen (ASTM E8) cut parallel to the rolling direction. The strains in the gauge section were measured using an extensometer. Fig. 3-9(a) shows a schematic of the sheet-tension specimen. A finite-

[3] Al2008-T4 is an automotive alloy widely used in car-body panels.

[4] We expect that due to the presence of alloying elements, ΔF^* for 2008-T4 would be higher than that for 1100-O. However, due to lack of the relevant data this difference is neglected in the calculation.

element representation of the specimen using 180 ABAQUS C3D8R continuum elements is shown in Fig. 3-9(b). The measured load-displacement and stress-strain curves prior to the onset of diffuse-necking are shown in Figs. 3-10(a) and 3-10(b), respectively. The values for the hardening parameters were adjusted so that the numerical results matched the corresponding experimental data. The numerical fit to the data is also shown in Figs. 3-10(a) and 3-10(b). The material parameters obtained from the fit are:

$$s_{*,0} = 40\,\text{MPa}, s_{a,0} = 55\,\text{MPa}, h_0 = 542\,\text{MPa}, s_s = 337\,\text{MPa}, r = 2.$$

Fig. 3-10(b) also shows the stress-strain curve from a numerical simulation of tension on a single element with the sheet texture represented by 192 components. The stress-strain response obtained by using the dominant 33 components is almost identical to the stress-strain curve for the 192 components.

3.2.2 Cup-Drawing Experiment

A schematic diagram of the geometry of the cup-drawing apparatus is shown in Fig. 3-11(a). Circular blanks of diameter 101.6 mm and thickness 0.7874 mm, were drawn in an apparatus comprising a round-nosed punch and die of diameters 50.8 mm and 53.035 mm, respectively. All surfaces in contact with the deforming blank were polished to a surface finish of 4. The punch, blankholder and die were machined from AISI/SAE D2-steel with a Rockwell hardness of 62. The cup-drawing experiments were performed on a double-action hydraulic press, powered by two dual-acting hydraulic cylinders. The hydraulic cylinders could apply a maximum binder force of 35 tons and a maximum punch force of 20 tons. The hydraulic cylinder applying the binder force was servo-controlled to produce a constant binder force, and the hydraulic cylinder applying the punch force was servo-controlled to produce a desired punch position. The press was instrumented to measure the forces and displacements. Strain gauges detected the binder and punch forces, while LVDT's sensed the punch position. The press was controlled through a microcomputer (IBM-486 PC) equipped with a real-time data-acquisition board (DT2801-A). Strain-gauge signal conditioners (2B31K) were used to output the force signals from the binder and punch force strain gauge Wheatstone bridge circuits. A constant binder force of 10 KN was applied and the cup was drawn with a punch speed of 1mm/sec. Teflon sheets were used

as lubricants, to minimize the friction in the interfaces between the punch and the blank, the blank and the blankholder, and the blank and the die.

The cups showed four ears: two along the rolling direction and two along the transverse direction of the sheet, as shown in Fig. 3-12(a). Note that a cup drawn from a sheet with a classical rolling texture (*e.g.*, Hirsch *et al.* [1978]) forms four ears at $\sim 45°$ to the rolling direction. The difference in the earing pattern between that situation and the situation in our experiments, arises directly from the differences in the two initial textures. The inverse pole-figure plots in Figs. 3-8(a) and 3-8(b) for the rolling and transverse directions provide a clearer understanding of this situation. The texture contains predominantly two ideal[5] components, namely, the $\{100\} < 010 >$ Cube component and the $\{110\} < 001 >$ Goss component. Both of these orientations are known to form ears at 0° and 90° to the rolling direction (Rollett *et al.* [1987]).

The thickness strains at the bottom and along the cup wall were measured at 0°, 56° (location of the trough) and 90° from the rolling direction, as shown in Fig.3-13. The sheet thins at the bottom and at the nose of the cup while it thickens along most portion of the wall. For all the three direcitons, the thickness strain is the minimum at the nose of the cup. We observe that the thickness strains at the wall along the trough (56° from the rolling direction) is higher than that along the rolling and transverse directions.

3.2.3 Simulation of Cup-Drawing

Fig. 3-11(b) shows the finite-element mesh used for the numerical simulation. A total of 672 ABAQUS continuum C3D8R and C3D6 elements were used, with 2 elements through the thickness[6]. Since the initial texture of the sheet, Fig. 3-7(a), possesses orthotropic symmetry, only a 90° sector of the circular blank was considered for the analysis. The die, blankholder and punch were treated as rigid surfaces. A friction coefficient[7] of $\mu = 0.1$ was used for the interface between the punch and the sheet top, and the interfaces between all

[5]The indices $\{hkl\}$ in the metallurgical notation $\{hkl\} < uvw >$ denote the crystallographic planes that are parallel to the rolling plane and the indices $< uvw >$ refer to the crystallographic directions aligned with the rolling direction.

[6]The simulation with two elements in the thickness direction was found to provide a better quantitative prediction of the cup-height when compared with that obtained from the calculation with one element through the thickness. However, even with two elements in the thickness direction the bending strains are captured only crudely. A further refined mesh was not employed owing to computational limitations.

[7]Although teflon sheets were used for lubrication, there was some contact between the punch and sheet as a result of the tearing of the teflon sheet at large bending strains. The friction coefficient was *assumed* to be 0.1. The results were not very sensitive to changes in this value.

other contacting surfaces were considered frictionless. In order to speed-up the simulation, the density of the blank was artificially increased to increase the stable time increment[8].

Fig. 3-12(b) shows the predicted shape of the fully-drawn cup. This figure also shows the equivalent tensile plastic-strain $\bar{\epsilon}^p$ contours in the cup at the end of the drawing process. The prediction of the number of ears and their positions is accurate. The equivalent plastic strains in the ears are quite large suggesting significant texture evolution in these areas. Fig. 3-14(a) shows a comparison of the predicted cup-height with the experimentally-measured height. The discrepancy in the predicted cup-height is due to the difference between the predicted and measured cup-thickness. Fig. 3-15(a), 3-15(b) and 3-15(c) show the comparison between the measured and predicted cup thickness strains at 0°, 56° and 90° from the rolling direction, respectively. We observe that the increase in thickness of the cup-wall is underpredicted by the model. A better agreement of the prediction with the experiment is anticipated with an increase in the number of elements through the thickness. Fig. 3-14(b) shows a comparison of the predicted punch load-displacement curve with the values measured in the experiments. The prediction is in reasonable agreement with the measured response.

Overall, the *quantitative* prediction of (*i*) the punch force versus punch displacement, and (*ii*) the number of ears, their positions, and their heights, is very good.

Earing could be minimized by either of the following two methods: (*i*) tailor the processing scheme prior to the cup-drawing operation to produce a "near-isotropic" initial texture in the sheet; (*ii*) choose an initial shape[9] for the blank that would minimize the earing. The capability to quantitatively predict the earing pattern, developed in this work, could serve as a useful design and analysis tool in either of the two methods.

[8] In such "density-scaled" simulations one must ensure that the inertial effects are small. To do this one must monitor the ratio of the total kinetic energy to the total internal (stored elastic + dissipated plastic) energy during the simulation, and ensure that this ratio does not exceed $\approx$ 0.01-0.05 at any time during the simulation.

[9] A shape which has more material along directions where troughs form would reduce the apparent earing in the fully-drawn cup.

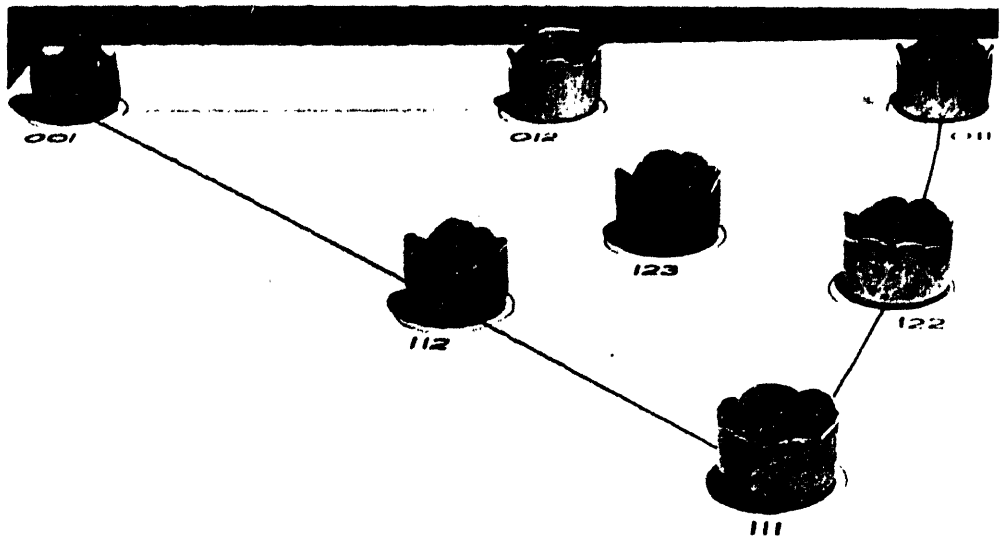

(a)

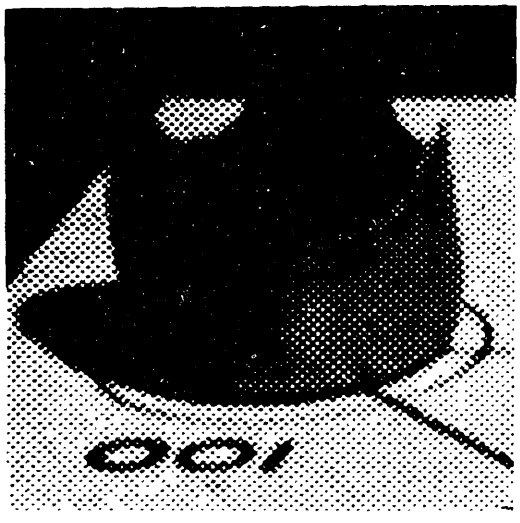

(b)

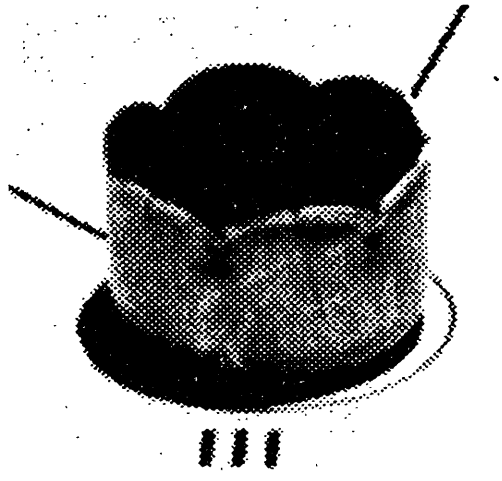

(c)

Figure 3-1: (a) Deep-drawn cups from single crystal sheets of pure aluminum arranged on stereographic projection of the standard unit triangle (Tucker [1961]). (b) Cup drawn from blank with the [001] direction initially along the punch axis. (c) Cup drawn from blank with the [111] direction initially along the punch axis.

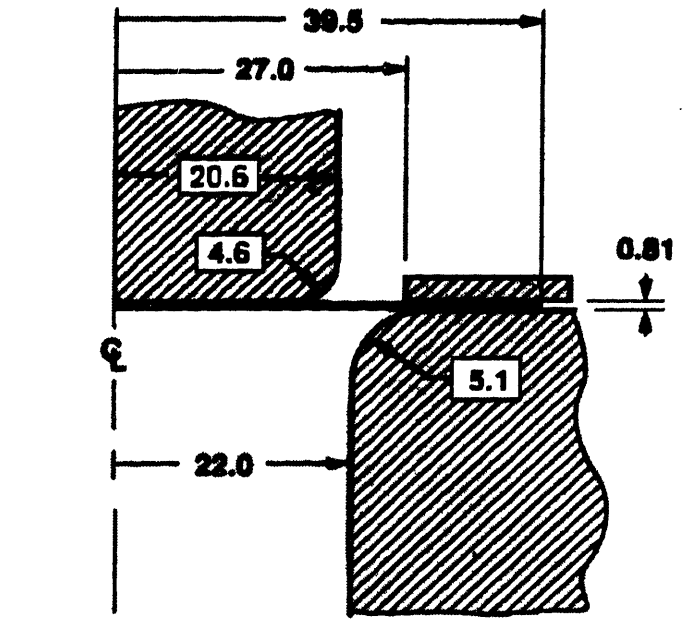

(a)

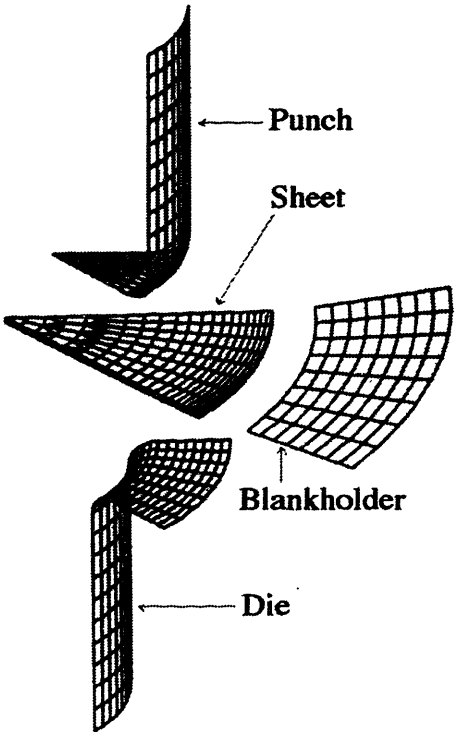

(b)

Figure 3-2: (a) Geometry of the cup-drawing aparatus for the deep-drawing of single crystal sheets. (b) Exploded view of the finite element mesh used in the simulations

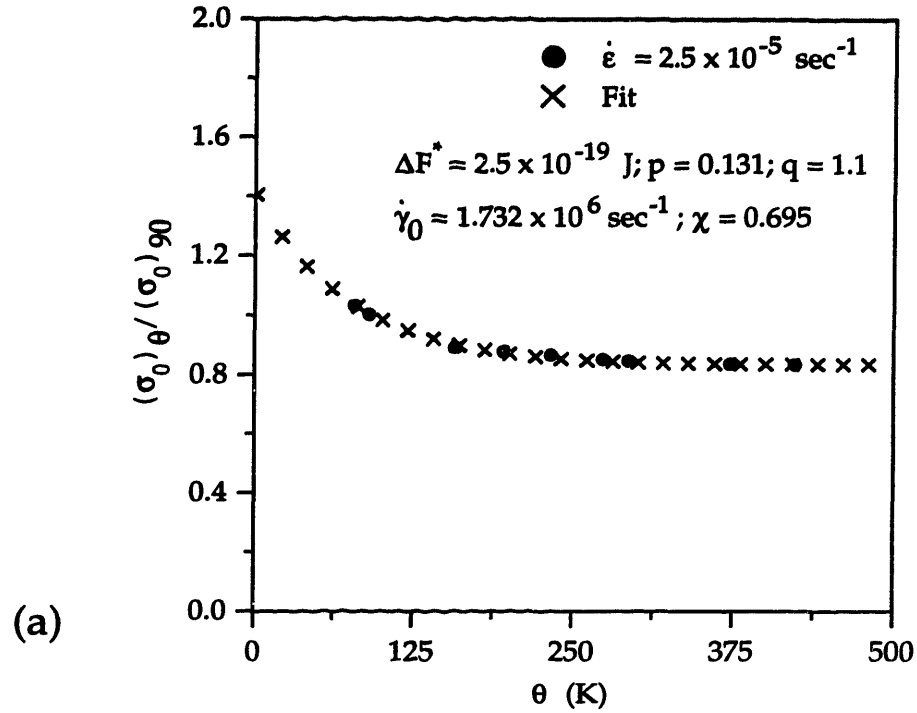

(a)

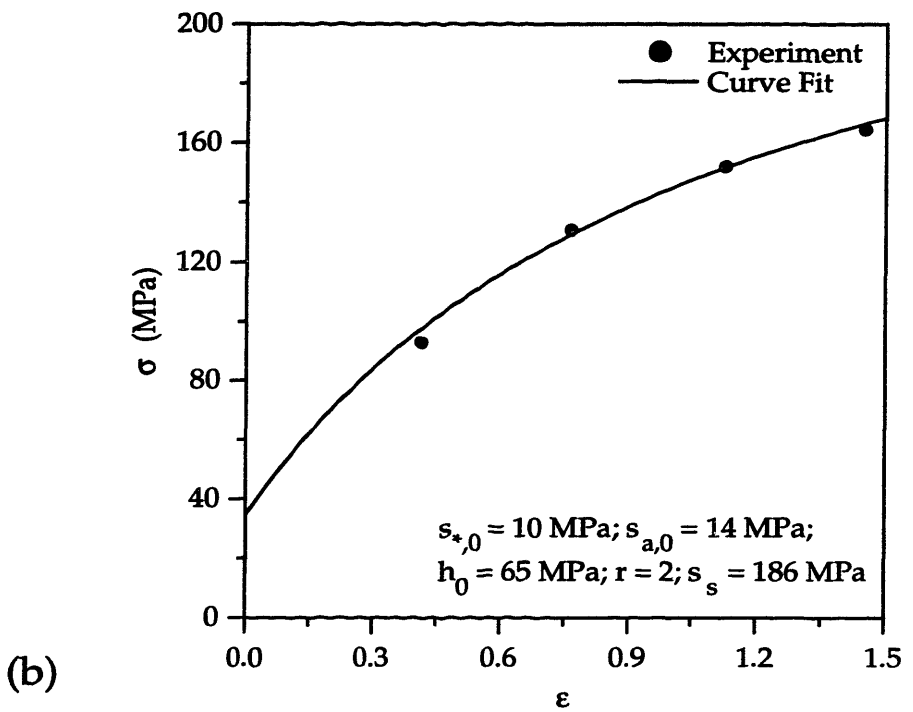

(b)

Figure 3-3: (a) Experimental data for the variation of flow stress with temperature in 99.992% pure aluminum single crystals (Cottrell and Stokes [1955]) and the constitutive model's fit. The stress at each temperature is normalized by the value at 90K. Also, the flow stress has been corrected for changes in the elastic moduli with temperature. (b) Experimental stress-strain response from channel-die compression of aluminum single crystal with the initial orientation (001)[110] (Becker *et al.* [1991]) and the model's fit.

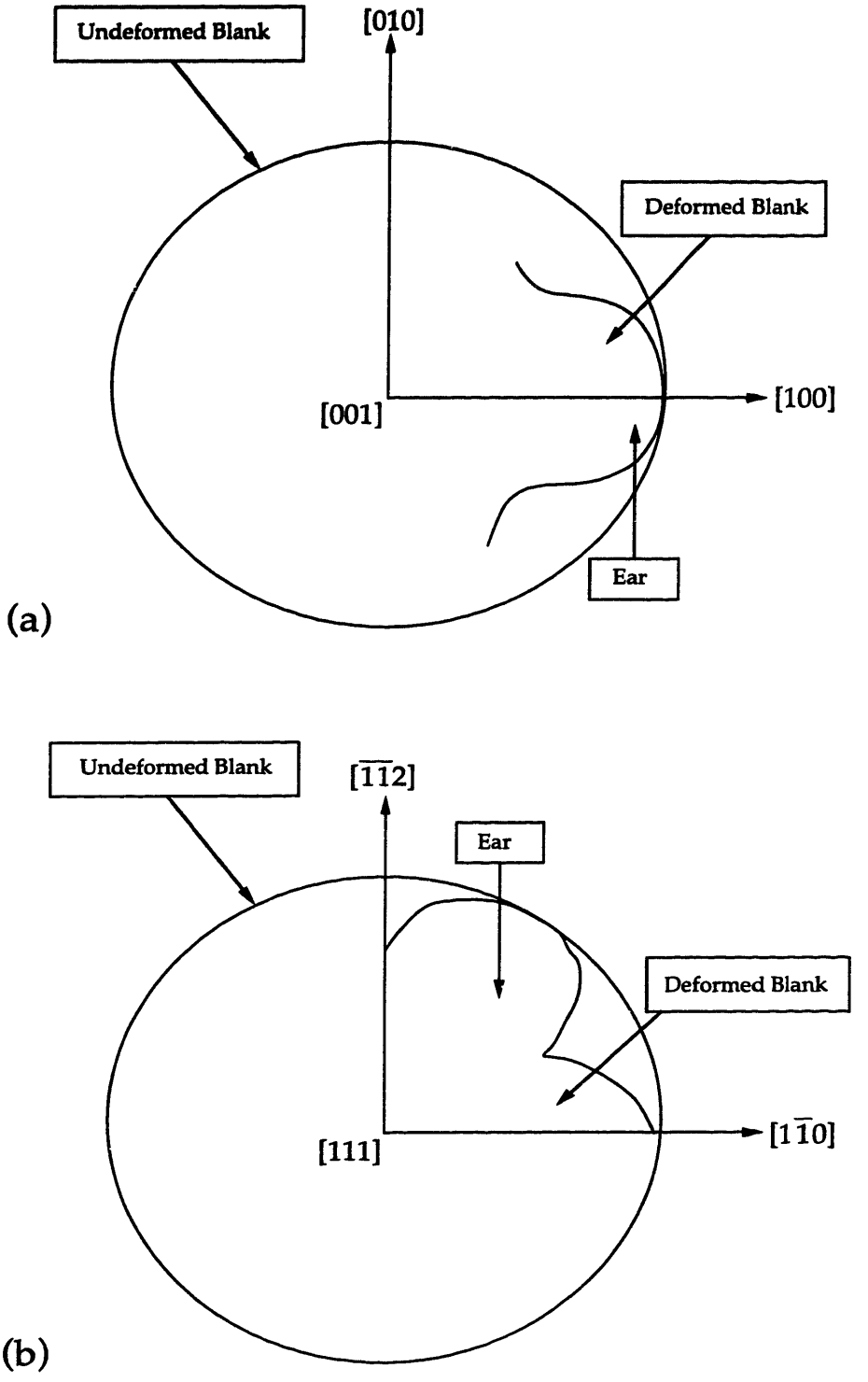

Figure 3-4: Schematic view of the earing pattern observed in the drawing of f.c.c. single crystals for (a) [001] oriented blank (b) [111] oriented blank.

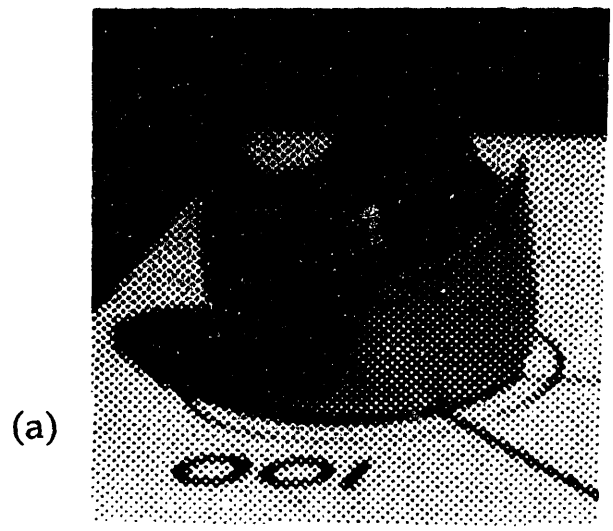

(a)

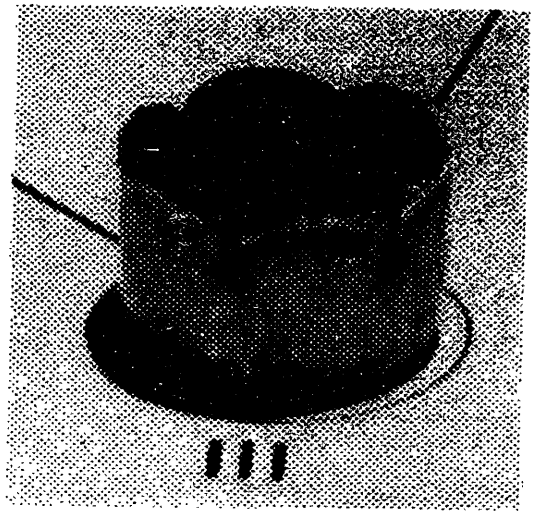

(b)

Figure 3-5: The earing pattern observed by Tucker [1961] for: (a) a [001] oriented blank. (b) a [111] oriented blank.

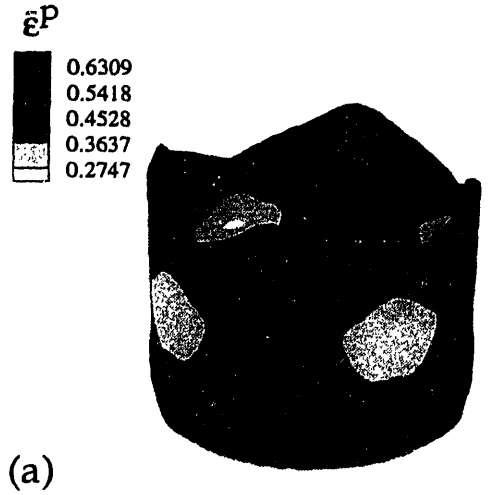

(a)

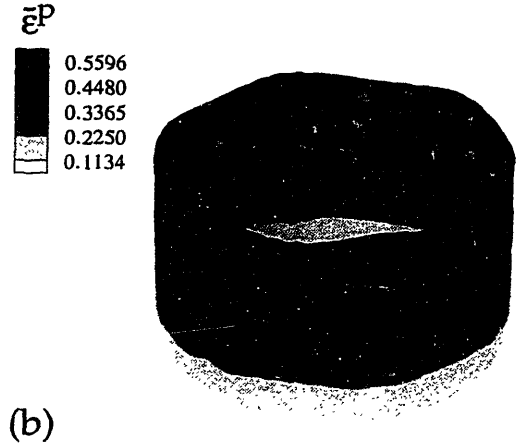

(b)

Figure 3-6: The predicted earing pattern for: (a) a [001] oriented blank. (b) a [111] oriented blank. The equivalent plastic strain contours are also shown.

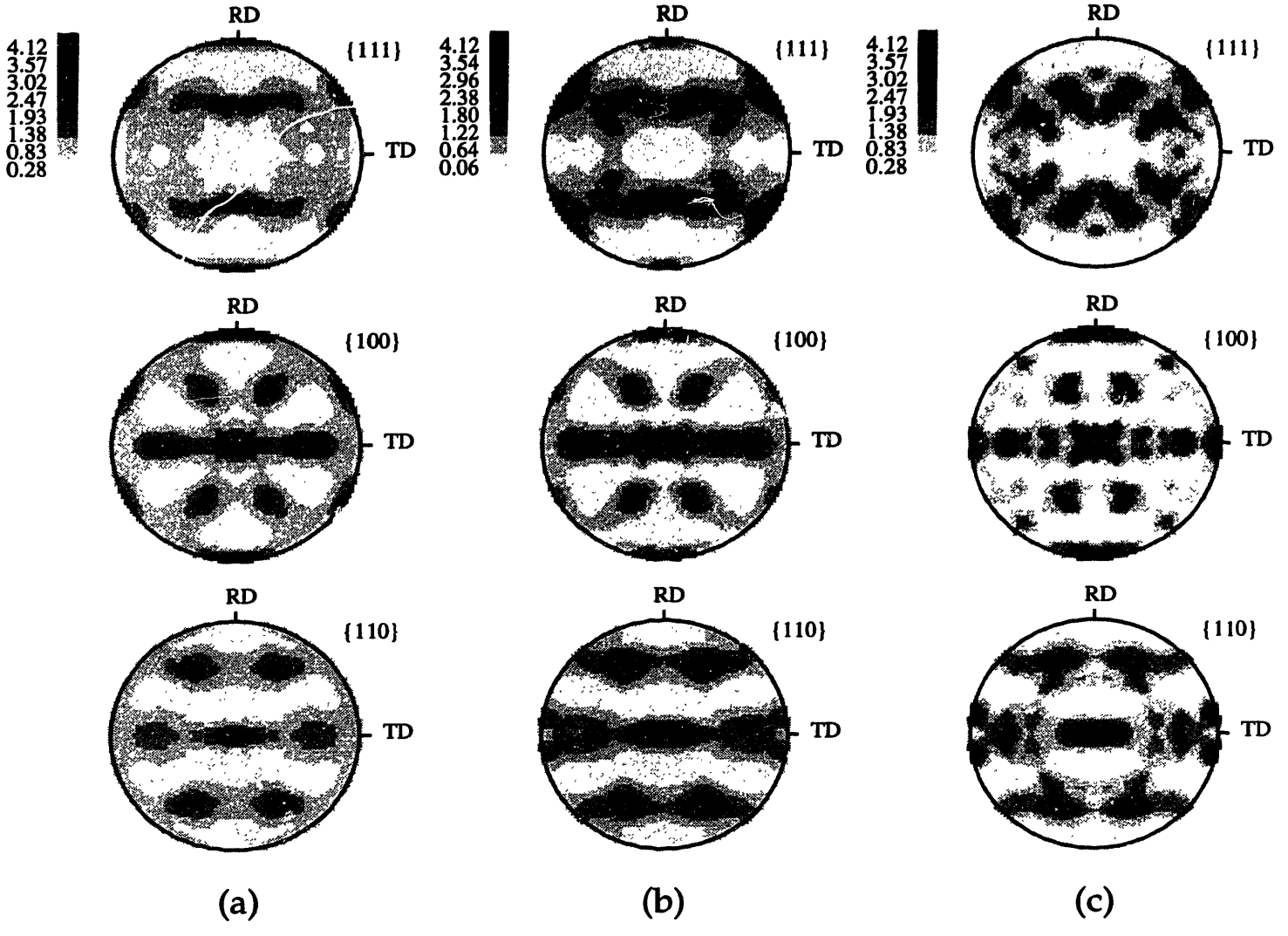

Figure 3-7: (a) Experimentally measured initial texture of the sheet. (b) Numerical representation of the measured texture using 192 weighted grains. (c) Numerical representation of the measured texture using 33 weighted grains.

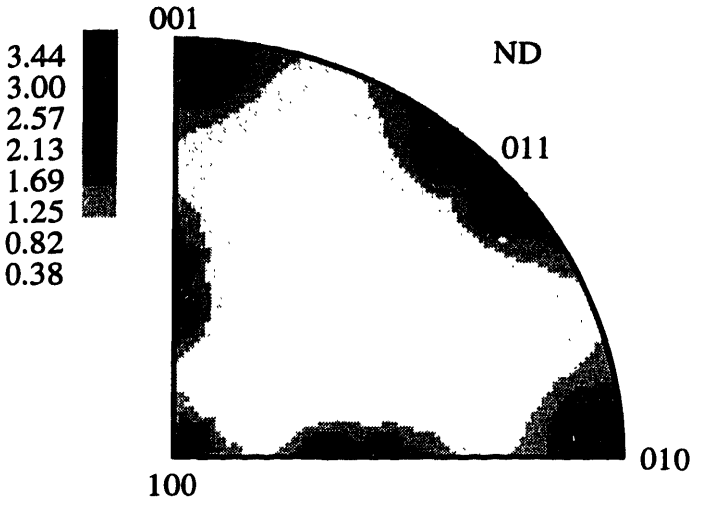

(a)

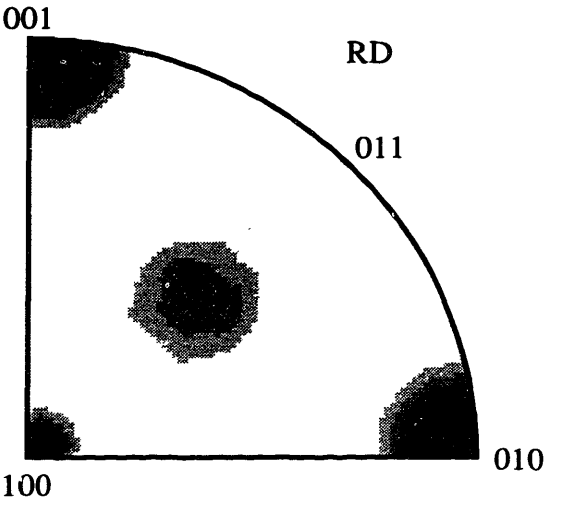

(b)

Figure 3-8: Inverse pole-figures computed from the measured texture for (a) the normal direction and (b) the rolling direction of the Al2008-T4 sheet. The texture shows the presence of the Cube – $\{100\} < 010 >$ and Goss – $\{110\} < 001 >$ orientations.

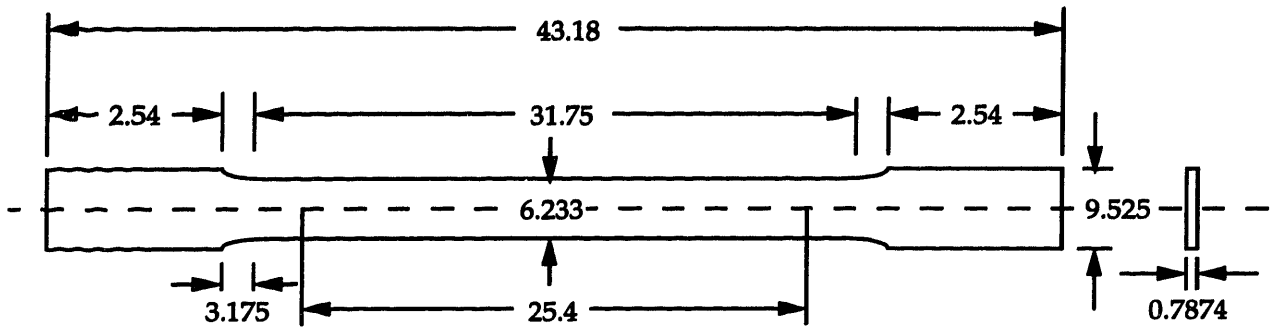

(a)

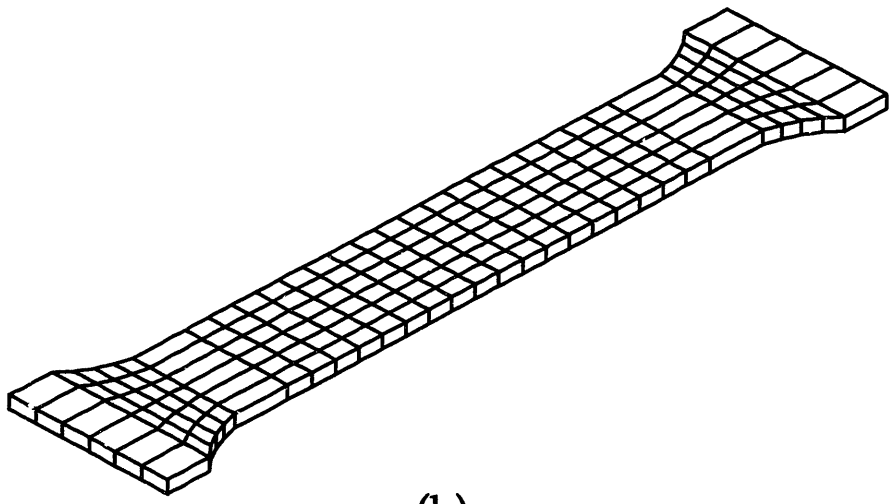

(b)

Figure 3-9: (a) Geometry of the sheet-tension specimen (ASTM E8) (All dimensions are in millimeters). (b) Finite element mesh used for the sheet-tension simulation.

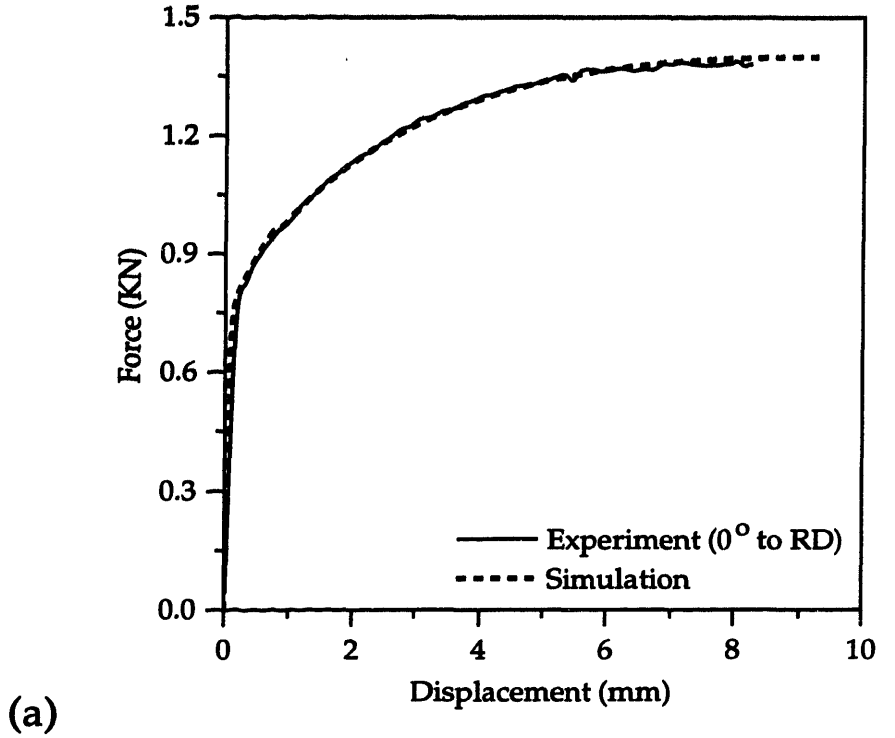

(a)

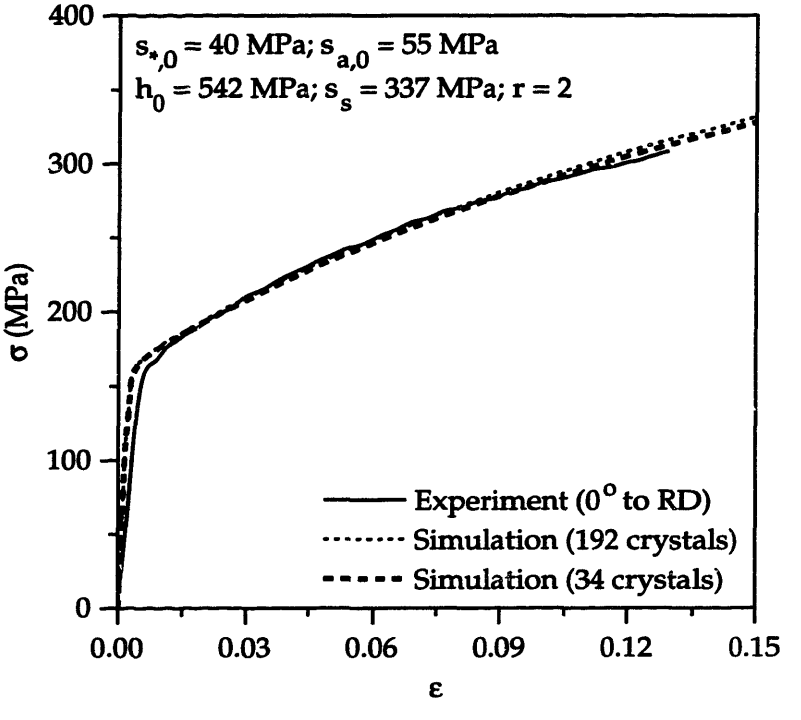

(b)

Figure 3-10: (a) Load-displacement response for sheet-tension. (b) Stress-strain response for sheet-tension.

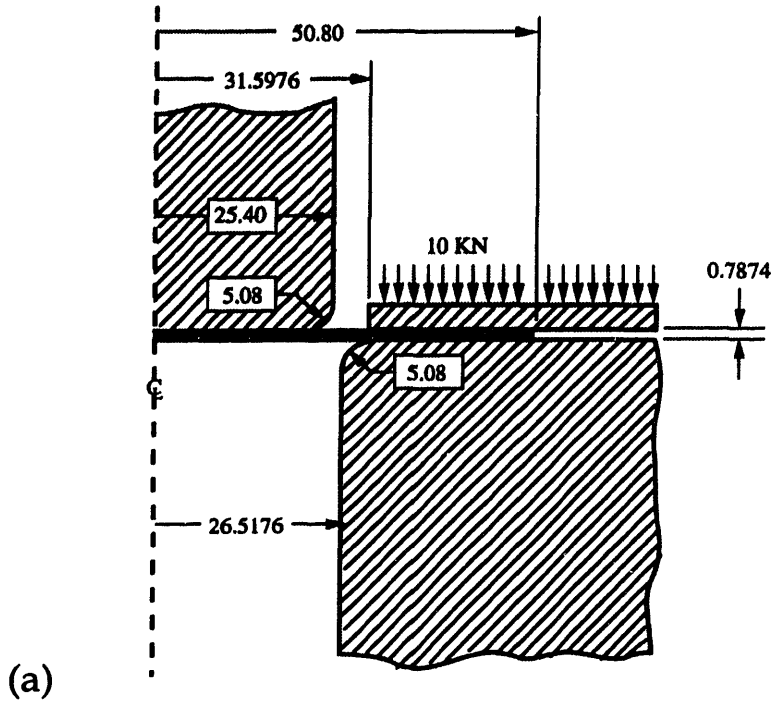

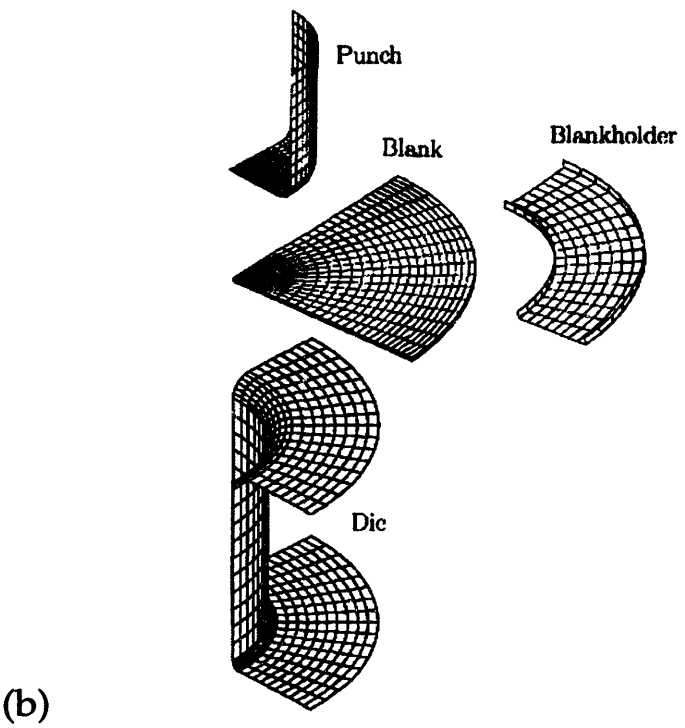

Figure 3-11: (a) Geometry of the cup-drawing apparatus (All dimensions are in millimeters). (b) Exploded view of the finite element mesh used in the simulation.

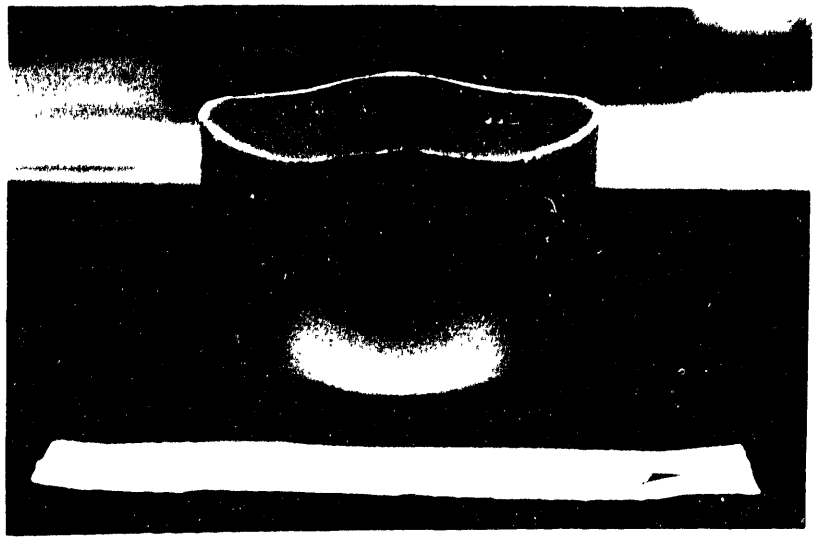

(a)

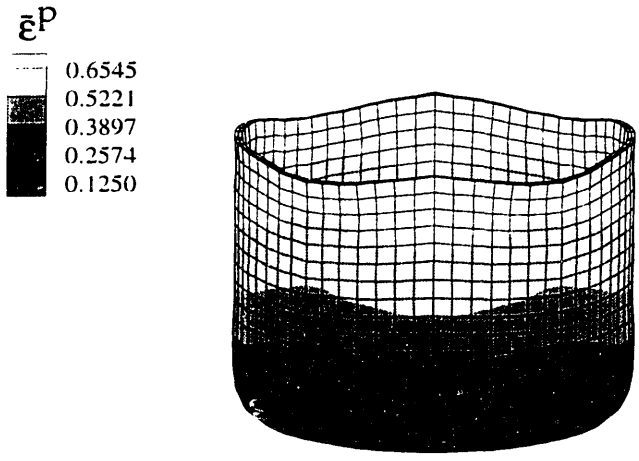

(b)

Figure 3-12: Comparison of the predicted earing pattern with that observed in the experiment. (a) Observed earing pattern (The rolling direction is indicated by the arrow). (b) Numerical prediction. The numerical simulation also shows the equivalent plastic strain contours.

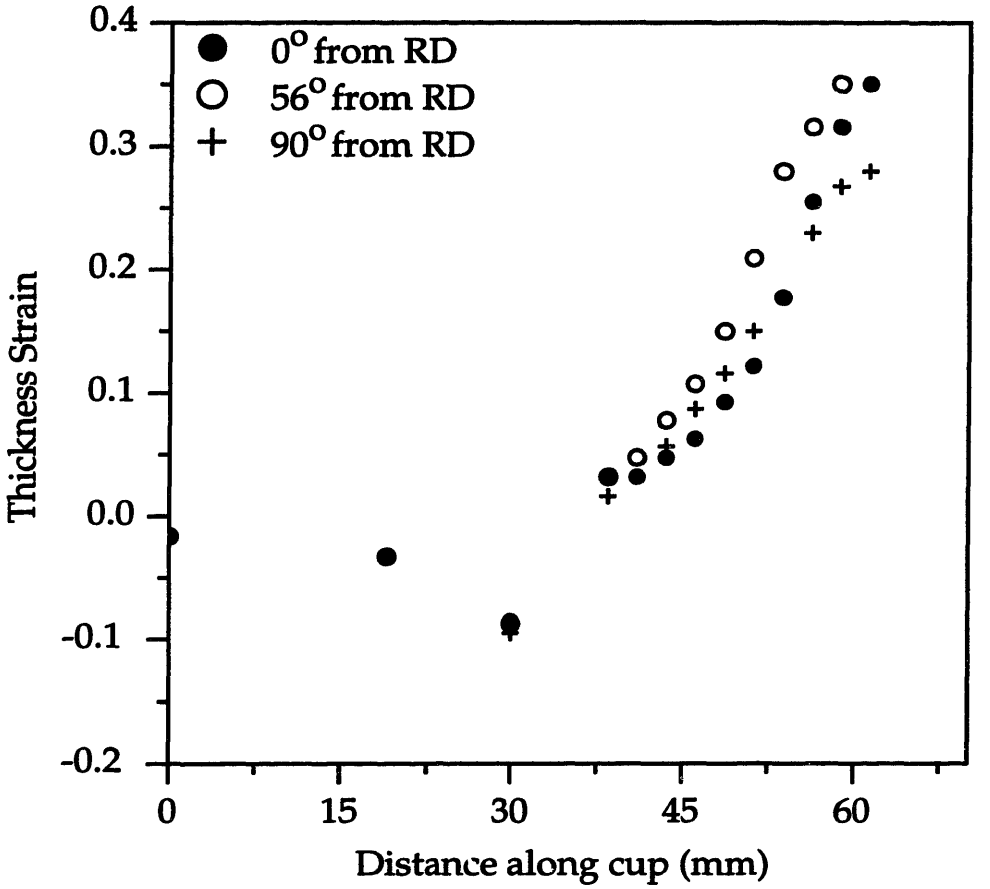

Figure 3-13: Experimentally measured thickness strain profile for the cup.

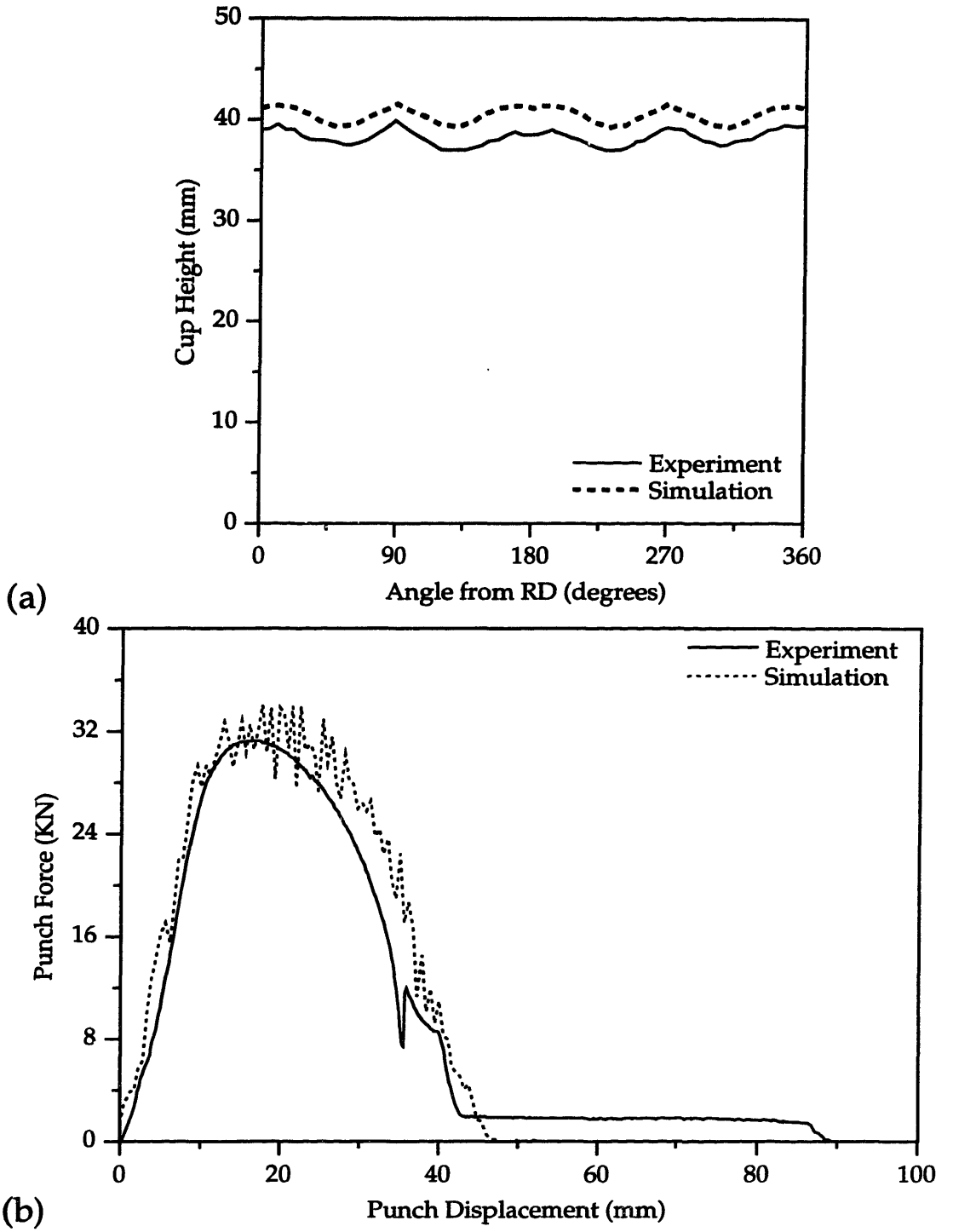

Figure 3-14: (a) Comparison of the predicted cup-height profile with the experimentally measured height. (b) Comparison of the measured load-displacement response during the cup-drawing process with the numerical prediction.

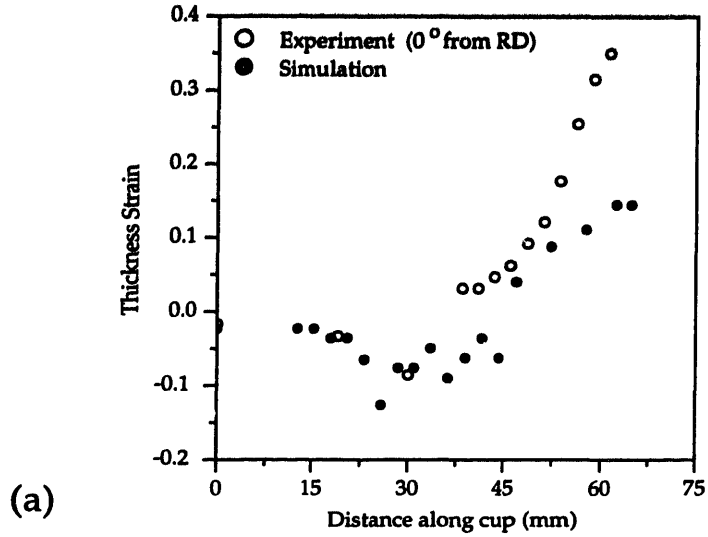

(a)

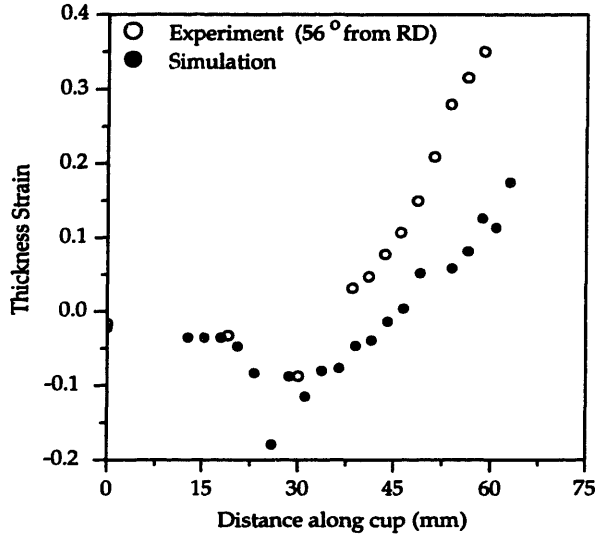

(b)

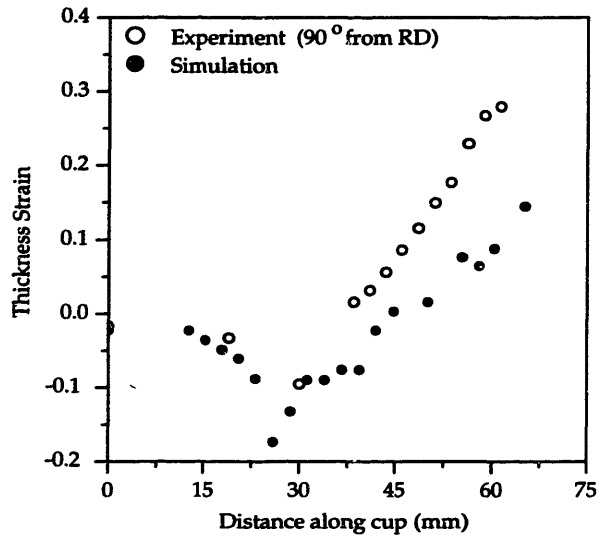

(c)

Figure 3-15: Comparison of the experimentally measured and predicted thickness strain profile for the cup along (a) 0° from the rolling direction (b) 56° from the rolling direction (c) 90° from the rolling direction.

Chapter 4

Plasticity of Polycrystalline H.C.P materials

In this chapter, a finite-deformation constitutive model for plasticity of hexagonal materials deforming by crystallographic slip is proposed. A full 3D finite-element model in which each element represents a grain and the constitutive response is given through a single-crystal constitutive model is used to simulate the response of a polycrystalline aggregate. Particular attention is given to the modeling of isothermal high-temperature deformation of h.c.p. titanium. However, the constitutive model is expected to be applicable to the modeling of deformation of other hexagonal materials in temperature and strain-rate regimes where the predominant mode of plastic deformation is crystallographic slip.

The hexagonal crystal structure (h.c.p.) is created when close-packed layers of atoms are stacked in the order *ABABAB*... such that every third layer is in exactly the same relative position as the first, Fig. 4-1(a). The interatomic spacing on the A plane is denoted by a while the spacing between adjacent A planes is denoted by c. The ratio c/a is termed the *axial ratio*. This ratio is different in different hexagonal metals; it has an ideal[1] value of 1.633. Titanium has an axial ratio of $c/a = 1.587$.

Unlike the cubic crystals, the *native basis* in a h.c.p. lattice is non-orthogonal, Fig. 4-1(b). The native basis is denoted by the set of non-orthogonal base vectors, $\{\mathbf{a}_1, \mathbf{a}_2, \mathbf{a}_3, \mathbf{c}\}$ with $\mathbf{a}_1 + \mathbf{a}_2 + \mathbf{a}_3 = \mathbf{0}$. For computational purpose, an orthonormal basis is defined from

[1]The ideal value of the axial ratio is derived from a hexagonal-close-packed arrangement of equal-sized hard spheres.

a combination of these crystallographic vectors. Fig. 4-1(b) shows the relation between a simple hexagonal cell with base vectors, $\{\mathbf{a}_1, \mathbf{a}_2, \mathbf{a}_3, \mathbf{c}\}$ and its corresponding orthohexagonal cell with base vetors, $\{\mathbf{a}, \mathbf{b}, \mathbf{c}\}$ which is used to calculate an orthonormal basis associated with a h.c.p. lattice structure. The orthohexagonal and the hexagonal cells share the base vector $\mathbf{c}$. The other base vectors are related to the native base vectors by the relations, $\mathbf{a} = \mathbf{a}_2$ and $\mathbf{b} = \mathbf{a}_3 - \mathbf{a}_1$. The orthonormal basis, $\{\mathbf{e}_1^c, \mathbf{e}_2^c, \mathbf{e}_3^c\}$, is obtained by normalizing these components, *i.e.*, $\mathbf{e}_1^c = \frac{\mathbf{a}}{|\mathbf{a}|}$, $\mathbf{e}_2^c = \frac{\mathbf{b}}{|\mathbf{b}|}$ and $\mathbf{e}_3^c = \frac{\mathbf{c}}{|\mathbf{c}|}$.

The hexagonal materials owing to their lower symmetry exhibit complex modes of deformation. Unlike the cubic crystals, hexagonal crystals possess more than one family of slip systems. Also, the deformation resistances of the different families of slip systems can be substantially different resulting in a highly anisotropic response at the single-crystal level. For titanium, studies on single crystal[2] (Rosi, Dube and Alexander [1953], Churchman [1954], Akhtar [1975a, 1975b]) and coarse-grained polycrystals (McHargue and Hammond [1953], Rosi, Perkins and Seigle [1956] and Paton, Williams and Rauscher [1973]), aimed at determining the operative deformation modes in titanium, indicate that the commonly observed slip systems in pure h.c.p. titanium are: the three equivalent basal $\{0001\} < 11\bar{2}0 >$, the three equivalent prismatic $\{10\bar{1}0\} < 11\bar{2}0 >$ and the six equivalent pyramidal $\{10\bar{1}1\} < 11\bar{2}0 >$ slip systems, as illustrated in Fig. 4-2. All of the three classes of slip systems share a common slip direction, $< 11\bar{2}0 >$ or $< \mathbf{a} >$-direction. For convenience, we shall refer to slip on these three classes of slip systems as $< \mathbf{a} >$-slip.

Temperature is an important factor that affects the nature of plastic deformation in titanium crystals. Conrad [1981] has reported the change in the critical resolved shear stress with temperature for the basal-$< \mathbf{a} >$ and prismatic-$< \mathbf{a} >$ slip in single crystals, Fig. 4-3. Both these slip resistances decrease dramatically with increase in temperature. At temperatures below 300°C, the critical resolved shear stress for the basal-$< \mathbf{a} >$ slip is nearly 5-6 times higher than that for the prismatic-$< \mathbf{a} >$ slip. At higher temperatures, the critical resolved shear stress for both types of slip become less disparate, which then allows for the possibility of slip on either of the planes. Rosi, Perkins and Seigle [1956] observed that the propensity for pyramidal-$< \mathbf{a} >$ slip also increased with increase in temperature. But these authors do not report the critical resolved shear stress on this slip system.

The $< \mathbf{a} >$-slip on the prismatic $\{10\bar{1}0\}$, basal (0001) and pyramidal $\{10\bar{1}1\}$ planes

[2]Studies on single crystals of titanium are limited due to the difficulty in growing them.

constitute twelve *physically different* slip systems but comprise only four *independent* ones (Groves and Kelly [1963]). Slip on these systems does not provide for a mechanism for strain parallel to the **c**-axis of the crystals. Other slip or twinning deformation modes are required to accommodate a strain parallel to the **c**-axis of the hexagonal system. These additional mechanisms whether slip on pyramidal planes with $< 11\bar{2}3 >$ ($< \mathbf{c}+\mathbf{a} >$) slip directions or twinning, have a strong influence on the overall inelastic behavior of a polycrystal. At low homologous temperatures, the high deformation resistance on the pyramidal $< \mathbf{c}+\mathbf{a} >$-slip systems precludes their operation. Under these conditions, the ability to undergo generalized plastic flow is achieved through deformation twinning. The two common twinning modes in titanium that have been observed at room temperature are the six equivalent $\{10\bar{1}2\} < \bar{1}011 >$, and the six equivalent $\{11\bar{2}2\} < 11\bar{2}\bar{3} >$ twin systems (shown in Fig. 4-4). The direction of shear on the twin system $(10\bar{1}2)[\bar{1}011]$ depends on the axial ratio. For $c/a < \sqrt{3}$, which is the case for titanium, the direction of shear is $[\bar{1}011]$ and twinning will occur under tension parallel to the **c**-axis. For this reason, the $\{10\bar{1}2\} < \bar{1}011 >$ twin systems are referred to as the "tensile" twin systems. The magnitude of twin shear strain on the $\{10\bar{1}2\} < \bar{1}011 >$ twin system in titanium is 0.1751. The $\{11\bar{2}2\} < 11\bar{2}\bar{3} >$ twin systems are "compressive" systems (for $c/a > \sqrt{2}$) that operate under compression parallel to the **c**-axis. The magnitude of twin shear strain on the $\{11\bar{2}2\} < 11\bar{2}\bar{3} >$ twin systems is 0.218. The propensity of titanium crystals to twin decreases with increase in temperature, Fig. 4-5(a). Lii *et al.* [1970] performed tension tests in a wide range of temperatures on specimens cut from a rolled plate with a strong alignment of the basal planes parallel to the rolling plane. They observed that the volume fraction of twins at a particular strain level decreased with increase in temperature, Fig. 4-5(b). At temperatures in the vicinity of 700°C, the volume fraction of twins was quite small (< 3%) *even at large strains*, $|\epsilon| \approx 0.8$. In this temperature regime, $< \mathbf{c}+\mathbf{a} >$-slip on pyramidal planes of the $\{10\bar{1}1\}$ and $\{11\bar{2}2\}$ families (see Fig. 4-2) has been observed to provide straining along the **c**-axis (Paton and Backofen [1970]; Williams and Blackburn [1968]). Since the focus of this study is the deformation of titanium single- and polycrystals in the vicinity of 750°C, attention is confined to plastic deformation solely by crystallographic slip.

In summary, at elevated temperatures, generalized plastic flow is maintained through $< \mathbf{a} >$-slip on the prismatic, pyramidal and basal planes in conjunction with $< \mathbf{c}+\mathbf{a} >$-slip on the pyramidal planes. It is important to note that even at high temperatures, $< \mathbf{c}+\mathbf{a} >$-

slip is a significantly harder mode of deformation. As a consequence, the crystals in a polycrystalline aggregate are to some degree still kinematically restricted.

4.1 Single Crystal Constitutive Model

The mathematical framework for the constitutive model of hexagonal materials is the same as that for the face-centered-cubic and body-centered-cubic materials described in Chapter 2. For the sake of clarity, the same is summarized below.

The constitutive equation for stress is given in terms of the linear elastic relation:

$$\mathbf{T}^* = \mathcal{C}\,[\mathbf{E}^e]\,, \tag{4.1}$$

where

$$\mathbf{E}^e \equiv (1/2)\left\{\mathbf{F}^{eT}\mathbf{F}^e - 1\right\} \quad \text{and} \quad \mathbf{T}^* \equiv (\det \mathbf{F}^e)\ \mathbf{F}^{e-1}\mathbf{T}\mathbf{F}^{e-T} \tag{4.2}$$

are the work-conjugate elastic strain and stress measures, respectively, and $\mathcal{C}$ is a fourth-order anisotropic elasticity tensor. $\mathbf{F}^e$ is an elastic deformation gradient defined by

$$\mathbf{F}^e \equiv \mathbf{F}\,\mathbf{F}^{p-1}, \qquad \det \mathbf{F}^e > 0, \tag{4.3}$$

where $\mathbf{F}$ is the deformation gradient and $\mathbf{F}^p$ is the plastic deformation gradient with $\det \mathbf{F}^p = 1$.

Hexagonal materials exhibit transverse isotropy in their elastic behavior. As a result, five independent elastic constants are required to describe the anisotropic elasticity tensor $\mathcal{C}$. These five constants are defined as follows,

$$C_{11} = (\mathbf{e}_1{}^c \otimes \mathbf{e}_1{}^c) \cdot \mathcal{C}[\mathbf{e}_1{}^c \otimes \mathbf{e}_1{}^c], \tag{4.4}$$

$$C_{12} = (\mathbf{e}_1{}^c \otimes \mathbf{e}_1{}^c) \cdot \mathcal{C}[\mathbf{e}_2{}^c \otimes \mathbf{e}_2{}^c], \tag{4.5}$$

$$C_{13} = (\mathbf{e}_1{}^c \otimes \mathbf{e}_1{}^c) \cdot \mathcal{C}[\mathbf{e}_3{}^c \otimes \mathbf{e}_3{}^c], \tag{4.6}$$

$$C_{33} = (\mathbf{e}_3{}^c \otimes \mathbf{e}_3{}^c) \cdot \mathcal{C}[\mathbf{e}_3{}^c \otimes \mathbf{e}_3{}^c], \tag{4.7}$$

$$C_{55} = (\mathbf{e}_1{}^c \otimes \mathbf{e}_3{}^c) \cdot \mathcal{C}[2\,\mathrm{sym}\,\{\mathbf{e}_1{}^c \otimes \mathbf{e}_3{}^c\}], \tag{4.8}$$

with $C_{22} = C_{11}$, $C_{23} = C_{13}$, $C_{44} = C_{33}$ and $C_{66} = \frac{1}{2}(C_{11} - C_{12})$. In eqns. 4.4-4.8, $\mathbf{e}_i{}^c$,

$i = 1, 2, 3$ is an orthonormal basis aligned with the $[\bar{1}2\bar{1}0]$, $[\bar{1}010]$, [0001] directions of the hcp crystal lattice, respectively, Fig. 4-1(b). The values of these constants for a variety of materials are tabulated as a function of temperature in Simmons and Wang [1971].

The evolution equation for the plastic deformation gradient is given by the flow rule:

$$\dot{\mathbf{F}}^p \mathbf{F}^{p-1} = \sum_\alpha \dot{\gamma}^\alpha \, \mathbf{S}_0^\alpha, \qquad \mathbf{S}_0^\alpha \equiv \mathbf{m}_0^\alpha \otimes \mathbf{n}_0^\alpha, \tag{4.9}$$

with $\mathbf{m}_0^\alpha$ and $\mathbf{n}_0^\alpha$ denoting the slip direction and the slip plane normal of the slip system α, respectively, defined in the fixed reference configuration.

The components of the slip plane normals and slip directions with respect to an orthonormal basis, as defined in Fig. 4-1(b), for the three basal-$< \mathbf{a} >$ $(0001) < 11\bar{2}0 >$, the three prismatic-$< \mathbf{a} >$ $\{10\bar{1}0\} < 11\bar{2}0 >$, the six pyramidal-$< \mathbf{a} >$ $\{10\bar{1}1\} < 11\bar{2}0 >$, the twelve pyramidal-$< \mathbf{c}+\mathbf{a} >$ $\{10\bar{1}1\} < 11\bar{2}3 >$ and the six pyramidal-$< \mathbf{c}+\mathbf{a} >$ $\{11\bar{2}2\} < 11\bar{2}3 >$ slip systems are presented in Tables 4-4, 4-5, 4-6, 4-7 and 4-8 respectively.

For the high-temperature isothermal deformation of titanium, a simple power-law for the plastic shearing rate $\dot{\gamma}^\alpha$ on a slip system is adopted:

$$\dot{\gamma}^\alpha = \dot{\bar{\gamma}} \left| \frac{\tau^\alpha}{s^\alpha} \right|^{1/m} \text{sign}(\tau^\alpha); \; \dot{\bar{\gamma}} \approx A \exp\left(-\frac{Q}{k\theta}\right) \tag{4.10}$$

where $\dot{\bar{\gamma}}$ is a reference plastic shearing rate, τ^α and s^α are the resolved shear stress and the slip system deformation resistance respectively on the slip system α and the material parameter m characterizes the material rate-sensitivity.

Finally, the slip system resistance is taken to evolve as:

$$\dot{s}^\alpha = \sum_\beta h^{\alpha\beta} \left| \dot{\gamma}^\beta \right|, \tag{4.11}$$

where $h^{\alpha\beta}$ describes the rate of strain hardening on slip system α due to shearing on the slip system β; it describes both self-hardening and latent-hardening of the slip systems. Each element $h^{\alpha\beta}$ in this matrix depends on the deformation history. It is fair to state that the characterization of these instantaneous hardening moduli $h^{\alpha\beta}$ for hexagonal crystals is a formidable task if not an impossible one. For example, in a titanium crystal deforming by three equivalent basal-$< \mathbf{a} >$ $(0001) < 11\bar{2}0 >$, three equivalent prismatic-$< \mathbf{a} >$ $\{10\bar{1}0\} < 11\bar{2}0 >$, six equivalent pyramidal-$< \mathbf{a} >$ $\{10\bar{1}1\} < 11\bar{2}0 >$, the twelve equivalent

pyramidal-$< \mathbf{c}+\mathbf{a} >$ $\{10\bar{1}1\}$ $< 11\bar{2}3 >$ and the six equivalent pyramidal-$< \mathbf{c}+\mathbf{a} >$ $\{11\bar{2}2\}$ $< 11\bar{2}3 >$ slip systems, there are $900(= 30 \times 30)$ elements in this matrix that need to be specified!

In order to obtain a tractable description of the crystal hardening, the following simple form for the slip system hardening matrix $h^{\alpha\beta}$ is adopted:

$$h^{\alpha\beta} = q^{\alpha\beta}\, h^{\beta} \tag{4.12}$$

Here, h^{β} denotes the self-hardening rate and $q^{\alpha\beta}$ is a matrix describing the latent hardening behavior of a hexagonal crystal.

Very little information is available in the literature regarding the latent hardening behavior of titanium crystals. Hence, a simple description for the matrix $q^{\alpha\beta}$ is adopted:

$$q^{\alpha\beta} = \begin{cases} 1 & \text{if } \alpha \text{ and } \beta \text{ are coplanar slip systems,} \\ q_l & \text{otherwise.} \end{cases} \tag{4.13}$$

The following is the set of coplanar slip systems:
(i) the three basal slip systems:
$\{(0001)[11\bar{2}0], (0001)[\bar{2}110], (0001)[1\bar{2}10]\}$
(ii) the six sets of first-order pyramidal slip systems:
$\{(10\bar{1}1)[\bar{1}2\bar{1}0], (10\bar{1}1)[\bar{2}113], (10\bar{1}1)[\bar{1}\bar{1}23]\}$,
$\{(01\bar{1}1)[\bar{2}110], (01\bar{1}1)[\bar{1}\bar{1}23], (01\bar{1}1)[1\bar{2}13]\}$,
$\{(\bar{1}101)[\bar{1}\bar{1}20], (\bar{1}101)[1\bar{2}13], (\bar{1}101)[2\bar{1}\bar{1}3]\}$,
$\{(\bar{1}011)[1\bar{2}10], (\bar{1}011)[2\bar{1}\bar{1}3], (\bar{1}011)[11\bar{2}3]\}$,
$\{(0\bar{1}11)[2\bar{1}\bar{1}0], (0\bar{1}11)[11\bar{2}3], (0\bar{1}11)[\bar{1}2\bar{1}3]\}$,
$\{(1\bar{1}01)[11\bar{2}0], (1\bar{1}01)[\bar{1}2\bar{1}3], (1\bar{1}01)[\bar{2}113]\}$.

The parameter q_l could in general be different for different types of slip system pairs, e.g., q_l for the interaction between basal-$< \mathbf{a} >$ and prismatic-$< \mathbf{a} >$ slip could be different from q_l for the interaction between basal-$< \mathbf{a} >$ and pyramidal-$< \mathbf{a} >$ slip. Due to lack of the relevant data, the same value of q_l is assumed for the interaction between *any* two non-coplanar slip systems. Also, any history-dependence of q_l is neglected; q_l is taken to be a constant for all deformation histories.

As in the case for the cubic crystals, the self-hardening rate h^{β} is taken to be given by

the following saturation form:

$$h^\beta = h_0^\beta \left| 1 - \frac{s^\beta}{s_s^\beta} \right|^r \text{sign}\left(1 - \frac{s^\beta}{s_s^\beta}\right). \tag{4.14}$$

For hexagonal materials, the initial hardening rate h_0 and the saturation slip deformation resistance s_s^β may in general be different for different families of slip systems. Also, for situations involving large changes in strain rates and/or high temperatures, the saturation value s_s^β cannot be taken as a constant. Therefore, the following phenomenological form (Anand [1982]) is employed for the saturation value s_s^β:

$$s_s^\beta = \tilde{s}(\frac{\dot{\gamma}^\beta}{\dot{\tilde{\gamma}}})^n \tag{4.15}$$

where $\tilde{s}$ and n are slip system parameters which may be different for different families of slip systems. The parameter m measures the *instantaneous* rate-sensitivity while $m + n$ measures the *total* macroscopic rate sensitivity in a strain-rate jump test.

The single crystal constitutive model has been implemented in a user-material subroutine for ABAQUS/Standard.

4.2 Study of Single Crystal Response

In this section, the single crystal constitutive model is evaluated in terms of its predictions for stress-strain response, slip system activity and evolution of the crystal lattice orientation for monotonic tension of a high-purity titanium single crystal at 750°C. The predictions are compared with the experimental results of Akhtar [1975a].

The values of elastic parameters for single crystal h.c.p. titanium at 750°C are taken as (Simmons and Wang [1971]):

$$C_{11} = 125.3\,\text{GPa},\ C_{12} = 99.4\,\text{GPa},\ C_{13} = 68.8\,\text{GPa},\ C_{33} = 154.5\,\text{GPa},\ C_{55} = 31.6\,\text{GPa}.$$

Fig. 4-6(a) shows the standard (0001) stereographic projection for titanium with the important poles. The location of the loading axis for the initial orientation chosen by Akhtar is shown as A inside the primary stereographic triangle in Fig. 4-6(b). This orientation is given by the following three Euler angles in the notation of Kalidindi *et al.* [1992]:

θ	ϕ	ω
43°	28°	0°

The crystal was oriented such that basal-< **a** > slip initiated the plastic flow. Akhtar measured the change in resolved shear stress on the active basal system and the evolution of the crystal lattice orientation with strain, which are shown in Figs. 4-7(a) and 4-7(b) respectively. He observed that the specimen deformed up to a resolved shear strain of 0.48 with virtually no work hardening at which point the resolved shear stress decreased gradually by roughly 30%, Fig. 4-7(a). Also, he noticed that the tensile axis initally rotated towards the $[11\bar{2}0]$ direction (A to B in Fig. 4-7(b)). At a shear strain (resolved on the basal slip system B1) of ≈ 0.48, the lattice reoriented sufficiently to activate prismatic-< **a** > slip. As a result, the tension axis changed its direction of rotation towards $[2\bar{1}\bar{1}0]$, the slip direction for the prismatic slip system (B to C in Fig. 4-7(b)). Akhtar reports that there was no evidence of pyramidal-< **a** > for this orientation. Accordingly for the simulation, only basal-< **a** > and prismatic-< **a** > slip systems are considered. Also, based on Akhtar's observation that there was very little work-hardening, the slip systems are assumed to be non-hardening.

The the slip system deformation resistance on the basal-< **a** > and prismatic-< **a** > slip systems are taken to be 8 MPa and 6.5 MPa, respectively. These values provide a reasonably good fit for the resolved shear stress -shear strain response. The reference shearing rate is taken to be $\dot{\tilde{\gamma}} = 0.001\text{sec}^{-1}$. The macroscopic strain-rate sensitivity of polycrystalline h.c.p. titanium at 750°C has been measured by a true strain-rate jump test in simple compression (see Fig. 4-8). The rate-sensitivity parameter obtained from this test is $m = 0.16$. The same value of m is assumed for our single crystal simulations.

The finite element calculation was carried out in ABAQUS/Standard. The finite element mesh contained 20 ABAQUS-C3D8 elements, as shown Fig. 4-9(a). In accordance with Akhtar's experiment, the simulation is performed at a constant true tensile strain rate of $1.66 \times 10^{-4}\text{sec}^{-1}$ in the $\mathbf{e}_3$ direction. The top and the bottom X_3 faces of the mesh are constrained to remain parallel to each other and perpendicular to the straining axis. Fig. 4-9(b) shows the deformed mesh. The deformation is reasonably homogeneous in the central portions of the mesh. The following analysis is based on the response of an element in this region of the mesh. Figs. 4-10(a) and 4-10(b) show the slip system activity and

the evolution of the crystal orientation with straining, respectively. Initially, the basal slip system B1 is activated, Fig. 4-10(a). This results in the rotation of the tension axis towards $[11\bar{2}0]$, Fig. 4-10(b). At $\epsilon \approx 0.2$, the prismatic slip system P2 becomes active, Fig. 4-10(a), with an attendant rotation in the tension axis towards $[2\bar{1}\bar{1}0]$, the slip direction for the slip system P2 as shown in Fig. 4-10(b). With continued straining, the activity on the basal slip system B1 is significantly reduced, Fig. 4-10(a). On approaching the $0001 - 10\bar{1}0$ boundary, another prismatic slip system P3 is activated. This results in the rotation of the tension axis towards the $(10\bar{1}0)$ pole. Fig. 4-10(c) shows the comparison of the predictions of the resolved shear stress - shear strain response with the experimentally measured response. The predictions are in very good agreement with the experiment. The model captures the drop in the resolved shear stress at $\epsilon \approx 0.5$ accurately.

4.3 Polycrystalline Plasticity of h.c.p. Titanium

In this section, we study the deformation of polycrystalline commercially-pure titanium at an elevated temperature. Simple compression, simple tension, plane-strain compression and tubular torsion experiments have been conducted on commerically-pure polycrystalline titanium at 750°C. The measured stress-strain response and evolution in crystallographic texture are presented. The operative slip-systems are inferred from the observed textural evolution. Finite element simulations of these simple deformations are performed on an aggregate of grains and the predictions of the evolution in crystallographic texture and the macroscopic stress-strain behavior are compared with experimental observations.

4.3.1 Simple Tension and Simple Compression of CP-Titanium at 750°C

Experimental Results

Nominally homogeneous tension and compression experiments have been performed on commercially-pure polycrystalline titanium (98.88% pure) at 750°C. The titanium stock used for all the experiments discussed below was obtained in the form of a 0.5" diameter rod.

The as-received rod was sectioned and polished to a mirror-finish. The polishing procedure adopted is outlined in Appendix C. The polished surface was then etched with Kroll's reagent (1-3 mL HF, 2-6 mL HNO_3 and 100 mL H_2O) to reveal the grains. Fig. 4-11

shows the micrographs for the longitudinal and transverse sections of the rod. The average grain diameter was determined to be approximately 110μm.

Samples were also prepared from the as-received titanium stock for the measurement of the initial crystallographic texture. The procedure employed for the measurement of the texture is presented in detail in Appendix C. Fig. 4-12 shows the (0001), $\{10\bar{1}1\}$ and $\{11\bar{2}0\}$ pole-figures for the as-received titanium rod. We observe that the rod possesses a strong texture with the basal planes aligned nearly perpendicular to the rod axis and the $< 11\bar{2}0 >$ directions along the rod axis.

After machining the specimens from the rod and prior to the experiments, the specimens were annealed in an atmosphere of argon. The annealing schedule comprised of heating the specimens to 750°C, holding them at that temperature for 45 minutes, and then furnace cooling the samples to room temperature (ASM Handbook Vol. 4 [1990]). The state of the annealed specimen was characterized by measuring its grain size and the crystallographic texture. Micrographs of the annealed sample are presented in Fig. 4-13. The grains were reasonably equiaxed and the average grain diameter was approximately 175μm. Fig. 4-14(a) shows the (0001), $\{10\bar{1}1\}$ and $\{11\bar{2}0\}$ pole-figures for the annealed titanium sample. On comparing the texture of the annealed specimen against that of the as-received specimen, Fig. 4-12, we observe that a significant portion of the initial texture of the as-received rod is retained after annealing. For the finite element simulations to be presented in later sections, the texture of the annealed rod is represented by a set of $729(= 9^3)$ unweighted discrete grain orientations as shown in Fig. 4-14(b). It is important to note that due to the lower symmetry of the hexagonal crystal, a smaller collection of grains for the polycrystalline aggregate would result in an artificially stiff response.

Two servo-hydraulic test systems manufactured by Instron Corporation were used to perform all the experiments presented. The first is a Model 1322 tension/torsion machine equipped with a high-temperature, vacuum furnace[3]. Maximum vacuum attainable is approximately 10^{-6} torr. Heating is provided by a cylindrical heating zone consisting of tungsten mesh heating elements surrounded by a multiple layer set of molybdenum heat shields. A Type R thermocouple {Platinum-13% Rhodium (+) versus
platinum (-)} spot welded to a titanium piece and placed close to the specimen served as the feedback transducer to the temperature controller. The maximum load capacities of

[3]The furnace was built by Centorr Associates, Suncook, New Hampshire.

the axial thrust cell and the torque thrust cell are 10,000 lbs and 10,000 lbs-in respectively.

The second test system features a custom manufactured high stiffness biaxial test frame. The load capacity of the frame is 50,000 lbs/20,000 lbs-in. Heating for experiments on this machine was provided through an Ameritherm Induction Heating System. The induction heating coil was approximately 1" in diameter with 5 turns, made of 0.25" diameter copper refrigeration tubing. Power was supplied by a 5KW self-tuning generator. The temperature was controlled with the aid of feedback from a K-type thermocouple spot-welded to the specimen in the gage-section by a Electromax V General-Purpose Single-Loop Controller from Leeds and Northrup Instruments. The hydraulic grips of the testing machine were water cooled making the ends of the specimens significantly cooler than the gage section. However, the specimen was heated uniformly in its gage section.

Simple Compression

The simple compression experiments were performed at 750°C, 5×10^{-6} torr in the Model 1322 Instron machine. Low thermal-conductivity 94% alumina ceramic rods were used for loading in compression. Compression platens used for the experiments were made from either TZM (Mo-Ti-Zr alloy) or MA956 (Fe-Cr-Al-Ti high-temperature superalloy). The platens were polished before each experiment to provide a smooth compression surface.

Compression specimens were initially 0.4" in diameter and 0.6" tall with the compression axis along the rod axis. Shallow concentric grooves were machined on the end-faces of the compression specimens to hold special high-temperature lubricant as shown in Fig. 4-15. The lubricant used was boron nitride[4] and powdered glass [5] (glass classification code: 0010) mixed in the ratio of 1:4 by weight (Brown, Kim and Anand [1989]). The lubricant mixture was suspended in a medium of methyl alcohol and applied to the specimen ends. On drying a thin layer of the lubricant mixture was deposited uniformly over the specimen end-faces. The specimens deformed (with only a slight roll-over) to a true strain of -1.0, at a constant true strain rate of -0.001 sec^{-1}. After the completion of the test, the specimens were allowed to cool[6] in the furnace under vacuum.

The measured stress-strain[7] response for the compression test is shown in Fig. 4-17.

[4]Boron Nitride powder, grade HCP, was purchased from Union Carbide Corporation.

[5]Glass was purchased as a powder from Corning corporation, Corning, New York.

[6]The typical duration for the deformed specimen to cool down to room temperature was approximately 30 minutes.

[7]The measured compressive strains were corrected for the compliance of the load-train in the test setup.

The initially circular cross-section of the specimen did not remain circular with progressive deformation due to the strong anisotropy of the initial texture. Fig. 4-18 shows the change in the shape of the cross-section with deformation.

In order to ascertain that crystallographic slip is the predominant contributor to plastic deformation in polycrystalline h.c.p titanium at high temperatures, the microstructure in the specimens deformed to a true strain of -1.0 were studied. There were very few twins in the deformed sample.

The deformed specimens were cut approximately along the mid-plane perpendicular to the compression axis, polished and the crystallographic texture was measured. Fig. 4-19 shows the measured (0001), $\{10\bar{1}1\}$ and $\{11\bar{2}0\}$ pole-figures at a true strain of -1.0. The directions $\mathbf{e}_1$, $\mathbf{e}_2$ and $\mathbf{e}_3$ in the global basis are aligned with the directions of the material axes, $\mathbf{e}'_1$, $\mathbf{e}'_2$ and $\mathbf{e}'_3$, respectively, which are illustrated in Fig. 4-16.

An *inverse pole-figure* of the compression axis provides more insight into the deformation mechanism leading to the evolution in texture. An inverse pole-figure plot is a representation of a particular sample direction with respect to crystal coordinates. Since the crystal bases of each crystal in a polycrystalline aggregate are oriented differently, the same specimen direction projects differently in different crystals. Hence, the inverse pole-figure plot is the *distribution* of a given sample direction when referred to the crystal bases.

The inverse pole-figure of the rod-axis for the deformed specimen at strain levels of 0, -0.5 and -1.0 are presented in Fig. 4-20. We observe that on straining, the compression axes at A migrate towards the $0001 - \bar{1}2\bar{1}0$ boundary, shown as the dashed lines from A to B in Fig. 4-20. On approaching the boundary, the compression axes rotate along the boundary towards the (0001) pole (B to C in Fig. 4-20). At a true strain of -1.0, the (0001) planes of the crystals are approximately 45° from the compression axis.

Simple Tension

The simple tension experiments were performed at 750°C. The specimen was induction heated in air. The tension specimen geometry is shown in Fig. 4-21. The gage section was 1" long and 0.25" in diameter. The tension test was performed at a nominal strain rate of 0.001 sec^{-1}. The true-strain in the gage-section at any point in the deformation was calculated based on the the cross-head displacement.

The measured stress-strain response is shown in Fig. 4-22. The gage-section deformed without necking up to a true strain of 0.3. The initially circular cross-section ovalized with

deformation suggesting a strong anisotropy. Lii *et al.* [1970] have also reported pronounced ovalization of their tension specimens with similar initial texture. The initial and deformed cross-sections of the specimen are shown in Fig. 4-23.

Fig. 4-24 shows the (0001), $\{10\bar{1}1\}$ and $\{11\bar{2}0\}$ pole-figures at a true strain of 0.3. The inverse pole-figure of the rod-axis for the deformed specimen at strain levels of 0, 0.2 and 0.3 are presented in Fig. 4-25. The tension axes migrate from a predominant $[\bar{1}2\bar{1}0]$ direction towards $0001 - \bar{1}100$ boundary (A to B in Fig. 4-25). At large strains, the tension axis is aligned in the neighborhood of the $(\bar{1}100)$ pole in most crystals.

Finite Element Simulations

In this section, full three-dimensional finite element simulations for simple compression and simple tension are performed. A continuum material point in a polycrystalline aggregate is represented by a 3D finite element mesh in which each element represents a grain. We numerically represent the initial texture by 729 discrete grain orientations, shown in Fig. 4-14. The set of grain orientations is *randomly* assigned to the elements (see Fig. 4-27(b)). In these simulations, both compatibility and equilibrium are satisfied in the "weak" finite element sense over the entire polycrystalline aggregate.

In order to identify the operative slip systems, simulations are carried out with different assumptions for the operative slip systems. The predictions for the evolution in texture are compared with the experimental measurements for each case. In these simulations, the individual slip systems are assumed to be non-hardening[8]. After identifying the operative slip systems, hardening is introduced on the different slip systems and the predictions of the stress-strain response and texture evolution are compared with the experimental results.

Identification of the Operative Slip Systems

In Appendix D, some simulations for a specially oriented single crystal which is representative of the initial texture observed in the annealed rod are shown. The calculations show that during simple compression basal-$< \mathbf{a} >$ slip rotates the compression axes towards the (0001) pole while prismatic-$< \mathbf{a} >$ slip or pyramidal-$< \mathbf{a} >$ slip rotates the compression axes towards the $0001 - \bar{1}2\bar{1}0$ boundary. During simple tension, basal-$< \mathbf{a} >$ slip rotates the tension axes towards the $\bar{1}100 - \bar{1}2\bar{1}0$ boundary while prismatic-$< \mathbf{a} >$ slip or pyramidal-

[8]We do not expect the qualitative aspects of the texture to change significantly due to slip system hardening.

$< \mathbf{a} >$ slip rotates the tension axes towards the $0001 - \bar{1}100$ boundary. The inverse pole figure plot for simple compression, Fig. 4-20, shows initial rotation of the compression axes towards the $0001 - \bar{1}2\bar{1}0$ boundary (A to B) indicating the presence of prismatic-$< \mathbf{a} >$ and/or pyramidal-$< \mathbf{a} >$ slip. On approaching the $0001 - \bar{1}2\bar{1}0$ boundary, the compression axes migrate along the boundary towards the (0001) pole indicating the operation of basal-$< \mathbf{a} >$ slip systems. The inverse pole figure plot for simple tension, Fig. 4-25, shows the rotation of the tension axes from the $[\bar{1}2\bar{1}0]$ direction towards the $0001 - \bar{1}100$ boundary (A to B) consistent with the rotations brought about by the operation of prismatic-$< \mathbf{a} >$ or pyramidal-$< \mathbf{a} >$ slip systems. In summary, the evolution of texture during simple tension and simple compression indicate the presence of basal-$< \mathbf{a} >$ slip in conjunction with prismatic-$< \mathbf{a} >$ and/or pyramidal-$< \mathbf{a} >$ slip. Since Akhtar did not observe any pyramidal-$< \mathbf{a} >$ slip in his experiments on single crystals in a wide range of orientations, the possibility of absence of pyramidal-$< \mathbf{a} >$ slip is also considered in the simulations.

In order to identify the operative slip systems, simple compression and simple tension simulations are performed for each of the following cases:
(A) All 5 families of slip systems: Basal $(0001) < 11\bar{2}0 >$, Prismatic $\{10\bar{1}0\} < 11\bar{2}0 >$, Pyramidal $\{10\bar{1}1\} < 11\bar{2}0 >$, Pyramidal $\{10\bar{1}1\} < 11\bar{2}3 >$ and
Pyramidal $\{11\bar{2}2\} < 11\bar{2}3 >$ slip systems.
(B) All families of slip systems with the exclusion of pyramidal-$< \mathbf{a} >$ slip: Basal $(0001) < 11\bar{2}0 >$, Prismatic $\{10\bar{1}0\} < 11\bar{2}0 >$, Pyramidal $\{10\bar{1}1\} < 11\bar{2}3 >$ and Pyramidal $\{11\bar{2}2\} < 11\bar{2}3 >$ slip systems.

All the slip systems are assumed to be non-hardening. With regards to the slip system deformation resistances, for the basal-$< \mathbf{a} >$ and prismatic-$< \mathbf{a} >$ slip systems, Akhtar's observations suggest that the ratio of the two deformation resistances ≈ 1 at elevated temperatures, as shown in Fig. 4-26. Accordingly, the *same* deformation resistance is assumed for both these families of slip systems. There is very little information available in the literature regarding the critical resolved shear stress for pyramidal-$< \mathbf{a} >$ slip at high temperatures. Rosi, Perkins and Seigle [1956] have reported some activity on these slip systems at 800°C but the authors do not report the critical resolved shear stress. In the simulations, the deformation resistance for the pyramidal-$< \mathbf{a} >$ slip systems is taken to be the same as that for the prismatic-$< \mathbf{a} >$ and basal-$< \mathbf{a} >$ slip systems. Regarding pyramidal-$< \mathbf{c} + \mathbf{a} >$ slip, Paton and Backofen's [1970] measurements of yield strengths at

750°C in titanium single crystals oriented parallel to **c**-axis, where pyramidal-$< \mathbf{c}+\mathbf{a} >$ slip is the only mode of deformation, and perpendicular to the **c**-axis, where prismatic-$< \mathbf{a} >$ slip is operational, indicate that the deformation resistance on the pyramidal-$< \mathbf{c}+\mathbf{a} >$ systems is $\approx$ 10-15 times that of the prismatic-$< \mathbf{a} >$ slip systems. For the simulations, the value of the deformation resistance for the pyramidal-$< \mathbf{c}+\mathbf{a} >$ slip systems is assumed to be 10 times that for the prismatic-$< \mathbf{a} >$ slip systems. Table 4-1 summarizes the assumptions made above.

Table 4-1. Deformation resistances for different slip systems

s_0 $(0001) < 11\bar{2}0 >$	s_0 $\{10\bar{1}0\} < 11\bar{2}0 >$	s_0 $\{10\bar{1}1\} < 11\bar{2}0 >$	s_0 $\{10\bar{1}1\} < 11\bar{2}3 > +$ $\{11\bar{2}2\} < 11\bar{2}3 >$
s_0	s_0	s_0	$10\ s_0$

The value for s_0 is determined by fitting the experimentally measured yield strength in compression. For the strain-rate sensitivity parameter m, the value measured from the strain-rate jump test, m=0.16, is used. The material parameters used in the simulations are tabulated in Table 4-2.

Table 4-2. Material Parameters for h.c.p. Titanium (Non-hardening)

s_0 $(0001) < 11\bar{2}0 >$	s_0 $\{10\bar{1}0\} < 11\bar{2}0 >$	s_0 $\{10\bar{1}1\} < 11\bar{2}0 >$	s_0 $\{10\bar{1}1\} < 11\bar{2}3 > +$ $\{11\bar{2}2\} < 11\bar{2}3 >$	h_0	m
8.2 MPa	8.2 MPa	8.2 MPa	82 MPa	0	0.16

The polycrystalline aggregate is represented by a 3D-Finite Element Mesh comprising of 729 (=9^3) ABAQUS-C3D8 elements, as shown in Fig. 4-27(a). This mesh represents one-eighth of a rectangular parallelopiped specimen. Each element represents a grain and is assigned an orientation which is chosen randomly from the set of 729 orientations. All the nodes on the planes $X_1 = 0, X_2 = 0$ and $X_3 = 0$ have zero displacements in the 1, 2 and 3 directions, respectively. All the nodes on the top X_3 face are moved in the $\mathbf{e}_3$ direction at a constant true strain rate of -0.001sec^{-1} for the simple compression simulation, and at a nominal strain rate of 0.001sec^{-1} for the simple tension simulation. Deformed finite element

meshes at late stages of the simulation are shown in Fig. 4-27(b) for compression and in Fig. 4-27(c) for tension. The deformation of the aggregate is highly non-homogeneous as is evident from the shape of the deformed finite elements.

The predicted macroscopic stress-strain curves for simple compression for the cases (A) and (B) are shown in Fig. 4-28. The predicted crystallographic texture for each of the case along with the experimentally measured texture is shown in Fig. 4-29. The stress-strain response in both the cases show initial geometric softening. The nature of the stress-strain curve is similar in both the cases; however, due to the additional slip systems available in case (A), there is an attendant decrease in the flow-stress levels. We observe that there is very little difference in the texture prediction for both cases, Fig. 4-29. Both predictions agree reasonably well with the experiment. These observations suggest that either of the assumed cases for the operating slip systems are plausible.

The predicted macroscopic stress-strain curves for simple tension for the cases (A) and (B) are shown in Fig. 4-30. The stress-strain response for both cases are similar but for a slight decrease in flow-stress levels for case (A). The measured and predicted texture for each case along with the experimentally measured texture is presented in Fig. 4-31. The texture prediction for case (B) matches the measured texture more closely. In particular, the presence of pyramidal $< \mathbf{a} >$ slip systems in case (A) accentuates the concentration of $\{11\bar{2}0\}$ poles along the tension axis. However, the measured texture shows a high concentration of $\{11\bar{2}0\}$ poles $\approx 10-15^{\circ}$ from the tension axis. *This feature is well-captured with the assumption of basal-*$< \mathbf{a} >$*, prismatic-*$< \mathbf{a} >$*, 1st-order pyramidal-*$< \mathbf{c}+\mathbf{a} >$ *and 2nd-order pyramidal-*$< \mathbf{c}+\mathbf{a} >$ *slip systems. Hence, for the simulations that follow we consider only these four sets of slip systems.*

Simulation of Simple Compression and Simple Tension with Hardening

Based on the study in the previous subsection, the operative slip systems are taken to be the basal-$< \mathbf{a} >$, prismatic-$< \mathbf{a} >$, 1st order pyramidal-$< \mathbf{c}+\mathbf{a} >$ and 2nd order pyramidal-$< \mathbf{c}+\mathbf{a} >$ slip systems.

For the slip system hardening, the forms presented in equations (4.12), (4.14) and (4.15) are adopted. Due to lack of relevant data, the initial hardening rate h_0 is assumed to be the same on all the slip systems. Also, the saturation parameter $\tilde{s}$ is taken to be the same for the basal-$< \mathbf{a} >$ and prismatic-$< \mathbf{a} >$ slip systems and 10 times this value for the pyramidal-$< \mathbf{c}+\mathbf{a} >$ systems. Since there is very little information available in the literature regarding

the nature of latent hardening in titanium crystals, simple tension and simple compression simulations have been performed with different values for the latent hardening parameter q_l in the range[9] , $0 \leq q_l \leq 1.5$. The simulations and results are presented in Appendix E. The study indicates that *there is very little effect of changes in the latent hardening parameter q_l on the crystallographic texture evolution.* The value, $q_l = 1$, is chosen for the simulations in the following sections.

The material parameters s_0, h_0, $\tilde{s}$ and r are determined by fitting the model to the measured stress-strain response in simple compression. The parameters m and n are determined by fitting the model to the strain-rate jump test. The curve-fits are shown in Fig. 4-32. The fits yield the following set of parameters:

Table 4-3. Material Parameters for h.c.p. Titanium

s_0 $(0001)<11\bar{2}0>$	s_0 $\{10\bar{1}0\}<11\bar{2}0>$	s_0 $\{10\bar{1}1\}<11\bar{2}3>+$ $\{11\bar{2}2\}<11\bar{2}3>$	h_0	r	m	n	q_l
8.2 MPa	8.2 MPa	82 MPa	12 MPa	1	0.16	0.1	1

$\tilde{s}$ $(0001)<11\bar{2}0>$	$\tilde{s}$ $\{10\bar{1}0\}<11\bar{2}0>$	$\tilde{s}$ $\{10\bar{1}1\}<11\bar{2}3>+$ $\{11\bar{2}2\}<11\bar{2}3>$
18 MPa	18 MPa	180 MPa

Figs. 4-33 and 4-34 show the comparison of the predicted texture with the measured texture at ϵ=-0.5 and ϵ=-1, respectively. The predictions agree closely with the experimental results.

Fig. 4-32 also shows the prediction of the stress-strain response for the case when pyramidal-$< \mathbf{c}+\mathbf{a} >$ *slip is absent.* We observe a severe locking in the stress-strain response. This highlights the significant role played by the pyramidal-$< \mathbf{c}+\mathbf{a} >$ slip systems. Although the deformation resistance of these slip systems are substantially higher

[9]In choosing the range of values for q_l, we were guided by observations in cubic crystals where this value has been experimentally determined to lie in the range, $0 \leq q_l \leq 1.5$.

than that of the basal-$< \mathbf{a} >$ and prismatic-$< \mathbf{a} >$ slip systems, *pyramidal-*$< \mathbf{c}+\mathbf{a} >$ *slip has a profound effect on the stress-strain response of the polycrystalline aggregate.* However, the slip activity on the pyramidal-$< \mathbf{c}+\mathbf{a} >$ systems is substantially lower than that on the basal-$< \mathbf{a} >$ and prismatic$< \mathbf{a} >$ systems. Hence, *pyramidal-*$< \mathbf{c}+\mathbf{a} >$ *slip has only a slight influence on the texture evolution.*

The parameters estimated from the fit to the simple compression experiment are used to predict the stress-strain response and texture evolution for simple tension. Fig. 4-35 shows the comparison between the predicted and the measured stress-strain response. The prediction is in very good agreement with the experimental result. The predicted textures at ϵ=0.2 and ϵ=0.3 are compared against the measured textures in Fig. 4-36 and Fig. 4-37, respectively. We observe important changes in texture in deforming from ϵ=0.2 to ϵ=0.3. The $\{11\bar{2}0\}$ poles are aligned very close to the tension axis at ϵ=0.2. When deformed to ϵ=0.3, the $\{11\bar{2}0\}$ poles rotate by $10-15^{\circ}$ from the tension axis. These changes in texture are accurately captured by the model.

The predictions of the stress-strain curves along with the corresponding measurements for the simple compression and simple tension experiments are presented in Fig. 4-38. We observe from Fig. 4-38(a) that at a large strain-level of $|\epsilon| \approx 0.3$, the flow-stress level for tension is higher than that for compression. This is due to the difference in the evolution of texture in the two situations. The calculations correctly predict this difference, Fig. 4-38(b).

4.3.2 Plane-Strain Compression of CP-Titanium at 750°C

Experimental Results

In order to probe the capability of the model to predict the stress-strain response and textural changes in other deformation modes, plane-strain compression experiments have been conducted on specimens machined from the rod. The plane-strain compression experiments were performed at 750°C in the Model 1322 Instron Machine under high vacuum. Fig. 4-39 shows a schematic of the plane-strain compression apparatus. The die and the plunger were machined from MA956. The die was seated on an alumina ceramic rod. The load was applied on the plunger through another ceramic rod. All the specimens were cubes with a side-length of 0.3". The tests were performed at a constant true strain rate of -0.001 sec^{-1}. An attempt was made to minimize the friction between all contacting

surfaces by the application of boron nitride-powdered glass mixture. However, frictional effects became significant at large strains, resulting in roll-over of the specimen sides.

The plane-strain compression samples were cored out from the rod as shown in Fig. 4-40. The $\mathbf{e}_1$, $\mathbf{e}_2$ and $\mathbf{e}_3$ directions of the global basis are aligned with the directions $\mathbf{e}'_1$, $\mathbf{e}'_2$ and $\mathbf{e}'_3$, respectively, of the material basis. Two types of plane-strain compression experiments were performed on the samples: (A) The compression direction was aligned with the rod axis, $\mathbf{e}'_1$ was the constraint direction and $\mathbf{e}'_2$ was the free direction; (B) The compression direction was aligned with the rod axis, $\mathbf{e}'_2$ was the constraint direction and $\mathbf{e}'_1$ was the free direction.

The measured stress-strain curves for the two types of tests are shown in Fig. 4-42. The plane-strain compression test with $\mathbf{e}'_1$ as the constraint direction shows a higher level of flow-stress. The texture measured at ϵ=-0.9 for the two tests are shown in Fig. 4-43.

Finite Element Simulations

Full 3D-finite element simulations are performed on the same finite element mesh, Fig. 4-41(a), as was used for the simple compression and simple tension simulations. $\mathbf{e}_3$ is the loading direction for both types of plane-strain compression simulations. All the nodes on the bottom X_3 face are fixed in the $\mathbf{e}_3$ direction and the nodes on the top X_3 face are moved in the $\mathbf{e}_3$ direction. In addition, for the first simulation, all the nodes on the outer faces normal to the $\mathbf{e}_1$ direction have zero displacements in the $\mathbf{e}_1$ direction, while in the second simulation, all the nodes on the outer faces normal to the $\mathbf{e}_2$ direction have zero displacements in the $\mathbf{e}_2$ direction.

Figs. 4-41(b) and 4-41(c) show the deformed meshes for the plane-strain compression simulations with $\mathbf{e}'_1$ and $\mathbf{e}'_2$ as the constraint direction, respectively. The predicted stress-strain response for the two cases are compared against the corresponding experimental results in Fig. 4-44. In both cases, the predicted initial flow-stress levels agree reasonably with the corresponding experimental result for $\epsilon < 0.5$. But, at larger strains, the model underpredicts the flow stress by a significant amount. The comparison of the predicted and measured textures at ϵ=-0.9 is presented in Figs. 4-45 and 4-46. The predictions are in reasonable first-order agreement for both cases.

The observed roll-over in the specimen at large strains and the attendant increase in the measured flow-stress suggest the presence of significant friction between the contacting

surfaces. Hence, both the calculations have been repeated with a friction coefficient[10] of $\mu = 0.05$ between all contacting surfaces. The predictions[11] of the stress-strain response are now in better agreement with the measurements, as shown in Fig. 4-47. The predictions of the texture at ϵ=-0.9 are shown in Figs. 4-48 and 4-49.

4.3.3 Tubular Torsion of CP-Titanium at 750°C

Experimental Results

Fixed-end, tubular torsion experiment has been conducted at 750°C. The initial geometry of the torsion specimen is shown in Fig. 4-50. The tubular specimen has an inner diameter of 6.35 mm and an outer diameter of 8.89 mm in the gage section. Two important geometric ratios in the tubular torsion experiment are l/d and d/t, where l, d and t denote the gage length, the mean diameter and the wall thickness, respectively. A large d/t ratio ensures a reasonably uniform shear strain distribution through the wall. For our specimen geometry[12], $d/t = 6$. The shear strain distribution in the wall is only approximately uniform. A large l/d ratio can cause the specimen to buckle. The specimen had a l/d ratio, 0.67. The specimen was twisted to a nominal shear strain of 1.0. The specimen walls did not buckle during the deformation. The rate of twisting was such that the nominal shear strain rate was 0.001sec^{-1}. The shear stress was evaluated using the torque measurements through the following relation:

$$\tau = \frac{2}{\pi t d^2}\text{Torque} \tag{4.16}$$

where t is the gage section thickness and $d = (d_i + d_o)/2$ is the mean diameter of the gage section. The normal stress was evaluated as:

$$\sigma = \frac{\text{Axial Load}}{\pi d t} \tag{4.17}$$

The crystallographic texture was measured by grinding flat and polishing a location on the radius of the gage section such that the measurement surface was perpendicular to the $\mathbf{e}_1'$

[10]In the presence of friction, the overall stress-strain respsonse is sensitive to the aspect ratio of the finite element mesh. Hence, the aspect ratio of the mesh is taken to be the ratio in the samples in our experiments.

[11]The results indicate that the use of an evolving coefficient of friction could further improve the predictions. But, such a task is not undertaken here.

[12]The outer diameter of the gage section was limited by the diameter of the rod and the wall thickness was made large enough to accomodate 10-15 grains through the thickness. Starting with a 0.5" diameter rod, this was the optimum geometry that could be obtained.

direction of the material axes.

Finite Element Simulations

The finite element simulation is performed on a 3D finite element mesh[13] containing 720 elements, shown in Fig. 4-51(a). Note that the initial texture, Fig. 4-14(a), is not axisymmetric about the specimen axis, $\mathbf{e}_3$. Figs. 4-52(a) and (b) show the pole-figures (viewed along a direction perpendicular to the plane of shear) for the situation when $2-3$ is taken to be the plane of shear and the situation when $1-3$ is taken to be the plane of shear, respectively. The two sets of pole-figures are quite different. This poses a problem in choosing the plane and direction of shear while approximating the torsion by a simple shear simulation. We overcome this problem by carrying out a *full 3D simulation* of torsion. The l/d and d/t ratios used for the simulation correspond to those of the experimental specimen. In the simulation, the nodes on the bottom X_3 face are fixed in the $\mathbf{e}_1$, $\mathbf{e}_2$ and $\mathbf{e}_3$ directions. The nodes on the top X_3 face are fixed in the $\mathbf{e}_3$ direction and prescribed a twisting motion about the axis of the torsion specimen with the twist rate used in the experiments. Fig. 4-51(b) shows the deformed mesh at a nominal shear strain of $\gamma = 1$.

Fig. 4-53 shows the calculated shear stress and normal stress response compared against the corresponding experimental measurements. The predictions match closely with the experiments up to a shear strain of $\gamma = 0.5$. In particular, the model captures the sign of the normal stress response. The sign of the normal stress is an outcome of the initial texture of the torsion specimen. Bronkhort *et al.* [1992] observed a *compressive* normal stress in their fixed-end thin-walled tubular torsion experiments on f.c.c. copper with an *isotropic* initial texture. It is interesting to note that the normal stress for the torsion test on titanium is *tensile*. This can be attributed to the strong "rod-type" initial texture in this case. For $\gamma > 0.5$, the model slightly overpredicts the shear stress. Also, the calculations show a decrease in the the normal stress level at a smaller shear strain than that observed in the experiments. The agreement could be improved by an increase in the number of grains used to represent the sample. A comparison of the experimentally measured and calculated[14] textures is presented in Fig. 4-54. The predictions are in close agreement with

[13] In order to capture any strain gradients that may occur through the thickness of the gage section, 5 elements were used along this direction.

[14] The texture was calculated from a set of 180 grains that were approximately perpendicular to the global $\mathbf{e}_1$ direction in the deformed configuration.

the measurements.

In conclusion, the constitutive model captures fairly accurately the anisotropic stress-strain response and the evolution of crystallographic texture in h.c.p. titanium under nominally homogeneous deformations to large strains at high temperatures. To the best of our knowledge, this is the first-time a combined experimental and computational effort of this nature has been carried out to study the deformation of hexagonal materials.

Table 4-4. Basal Slip Systems $(0001) < 11\bar{2}0 >$

α	Miller-Bravais Notation	$[\mathbf{n}_o^\alpha]_c$	$[\mathbf{m}_o^\alpha]_c$	Label
1	$(0001)[11\bar{2}0]$	0 0 1	$\frac{1}{2}$ $-\frac{\sqrt{3}}{2}$ 0	B1
2	$(0001)[\bar{2}110]$	0 0 1	$\frac{1}{2}$ $\frac{\sqrt{3}}{2}$ 0	B2
3	$(0001)[1\bar{2}10]$	0 0 1	-1 0 0	B3

Table 4-5. Prismatic Slip Systems $\{10\bar{1}0\} < 11\bar{2}0 >$

α	Miller-Bravais Notation	$[\mathbf{n}_o^\alpha]_c$	$[\mathbf{m}_o^\alpha]_c$	Label
1	$(10\bar{1}0)[\bar{1}2\bar{1}0]$	0 1 0	1 0 0	P1
2	$(01\bar{1}0)[\bar{2}110]$	$-\frac{\sqrt{3}}{2}$ $\frac{1}{2}$ 0	$\frac{1}{2}$ $\frac{\sqrt{3}}{2}$ 0	P2
3	$(\bar{1}100)[\bar{1}\bar{1}20]$	$-\frac{\sqrt{3}}{2}$ $-\frac{1}{2}$ 0	$-\frac{1}{2}$ $\frac{\sqrt{3}}{2}$ 0	P3

Table 4-6. Pyramidal $< \mathbf{a} >$ Slip Systems $\{10\bar{1}1\} < 11\bar{2}0 >$

α	Miller-Bravais Notation	$[\mathbf{n}_o^\alpha]_c$	$[\mathbf{m}_o^\alpha]_c$	Label
1	$(10\bar{1}1)[\bar{1}2\bar{1}0]$	$0\ -\frac{2c}{\sqrt{4c^2+3a^2}}\ \frac{\sqrt{3}a}{\sqrt{4c^2+3a^2}}$	1 0 0	R1
2	$(01\bar{1}1)[\bar{2}110]$	$\frac{\sqrt{3}c}{\sqrt{4c^2+3a^2}}\ -\frac{c}{\sqrt{4c^2+3a^2}}\ \frac{\sqrt{3}a}{\sqrt{4c^2+3a^2}}$	$\frac{1}{2}$ $\frac{\sqrt{3}}{2}$ 0	R2
3	$(\bar{1}101)[\bar{1}\bar{1}20]$	$\frac{\sqrt{3}c}{\sqrt{4c^2+3a^2}}\ \frac{c}{\sqrt{4c^2+3a^2}}\ \frac{\sqrt{3}a}{\sqrt{4c^2+3a^2}}$	$-\frac{1}{2}$ $\frac{\sqrt{3}}{2}$ 0	R3
4	$(\bar{1}011)[1\bar{2}10]$	$0\ \frac{2c}{\sqrt{4c^2+3a^2}}\ \frac{\sqrt{3}a}{\sqrt{4c^2+3a^2}}$	-1 0 0	R4
5	$(0\bar{1}11)[2\bar{1}\bar{1}0]$	$-\frac{\sqrt{3}c}{\sqrt{4c^2+3a^2}}\ \frac{c}{\sqrt{4c^2+3a^2}}\ \frac{\sqrt{3}a}{\sqrt{4c^2+3a^2}}$	$-\frac{1}{2}$ $-\frac{\sqrt{3}}{2}$ 0	R5
6	$(1\bar{1}01)[11\bar{2}0]$	$-\frac{\sqrt{3}c}{\sqrt{4c^2+3a^2}}\ -\frac{c}{\sqrt{4c^2+3a^2}}\ \frac{\sqrt{3}a}{\sqrt{4c^2+3a^2}}$	$\frac{1}{2}$ $-\frac{\sqrt{3}}{2}$ 0	R6

Table 4-7. Pyramidal $< \mathbf{c} + \mathbf{a} >$ Slip Systems $\{10\bar{1}1\} < 11\bar{2}3 >$

α	Miller-Bravais Notation	$[\mathbf{n}_o^\alpha]_c$	$[\mathbf{m}_o^\alpha]_c$	Label
1	$(10\bar{1}1)[\bar{2}113]$	$0 \; -\frac{2c}{\sqrt{4c^2+3a^2}} \; \frac{\sqrt{3}a}{\sqrt{4c^2+3a^2}}$	$\frac{a}{2(\sqrt{c^2+a^2})} \; \frac{\sqrt{3}a}{2(\sqrt{c^2+a^2})} \; \frac{c}{(\sqrt{c^2+a^2})}$	R7
2	$(01\bar{1}1)[\bar{1}\bar{1}23]$	$\frac{\sqrt{3}c}{\sqrt{4c^2+3a^2}} \; -\frac{c}{\sqrt{4c^2+3a^2}} \; \frac{\sqrt{3}a}{\sqrt{4c^2+3a^2}}$	$-\frac{a}{2(\sqrt{c^2+a^2})} \; \frac{\sqrt{3}a}{2(\sqrt{c^2+a^2})} \; \frac{c}{(\sqrt{c^2+a^2})}$	R8
3	$(\bar{1}101)[1\bar{2}13]$	$\frac{\sqrt{3}c}{\sqrt{4c^2+3a^2}} \; \frac{c}{\sqrt{4c^2+3a^2}} \; \frac{\sqrt{3}a}{\sqrt{4c^2+3a^2}}$	$-\frac{a}{\sqrt{c^2+a^2}} \; 0 \; \frac{c}{\sqrt{c^2+a^2}}$	R9
4	$(\bar{1}011)[2\bar{1}\bar{1}3]$	$0 \; \frac{2c}{\sqrt{4c^2+3a^2}} \; \frac{\sqrt{3}a}{\sqrt{4c^2+3a^2}}$	$-\frac{a}{2(\sqrt{c^2+a^2})} \; -\frac{\sqrt{3}a}{2(\sqrt{c^2+a^2})} \; \frac{c}{(\sqrt{c^2+a^2})}$	R10
5	$(0\bar{1}11)[11\bar{2}3]$	$-\frac{\sqrt{3}c}{\sqrt{4c^2+3a^2}} \; \frac{c}{\sqrt{4c^2+3a^2}} \; \frac{\sqrt{3}a}{\sqrt{4c^2+3a^2}}$	$\frac{a}{2(\sqrt{c^2+a^2})} \; -\frac{\sqrt{3}a}{2(\sqrt{c^2+a^2})} \; \frac{c}{(\sqrt{c^2+a^2})}$	R11
6	$(1\bar{1}01)[\bar{1}2\bar{1}3]$	$-\frac{\sqrt{3}c}{\sqrt{4c^2+3a^2}} \; -\frac{c}{\sqrt{4c^2+3a^2}} \; \frac{\sqrt{3}a}{\sqrt{4c^2+3a^2}}$	$\frac{a}{\sqrt{c^2+a^2}} \; 0 \; \frac{c}{\sqrt{c^2+a^2}}$	R12
7	$(10\bar{1}1)[\bar{1}\bar{1}23]$	$0 \; -\frac{2c}{\sqrt{4c^2+3a^2}} \; \frac{\sqrt{3}a}{\sqrt{4c^2+3a^2}}$	$-\frac{a}{2(\sqrt{c^2+a^2})} \; \frac{\sqrt{3}a}{2(\sqrt{c^2+a^2})} \; \frac{c}{(\sqrt{c^2+a^2})}$	R13
8	$(01\bar{1}1)[1\bar{2}13]$	$\frac{\sqrt{3}c}{\sqrt{4c^2+3a^2}} \; -\frac{c}{\sqrt{4c^2+3a^2}} \; \frac{\sqrt{3}a}{\sqrt{4c^2+3a^2}}$	$-\frac{a}{\sqrt{c^2+a^2}} \; 0 \; \frac{c}{\sqrt{c^2+a^2}}$	R14
9	$(\bar{1}101)[2\bar{1}\bar{1}3]$	$\frac{\sqrt{3}c}{\sqrt{4c^2+3a^2}} \; \frac{c}{\sqrt{4c^2+3a^2}} \; \frac{\sqrt{3}a}{\sqrt{4c^2+3a^2}}$	$-\frac{a}{2(\sqrt{c^2+a^2})} \; -\frac{\sqrt{3}a}{2(\sqrt{c^2+a^2})} \; \frac{c}{(\sqrt{c^2+a^2})}$	R15
10	$(\bar{1}011)[11\bar{2}3]$	$0 \; \frac{2c}{\sqrt{4c^2+3a^2}} \; \frac{\sqrt{3}a}{\sqrt{4c^2+3a^2}}$	$\frac{a}{2(\sqrt{c^2+a^2})} \; -\frac{\sqrt{3}a}{2(\sqrt{c^2+a^2})} \; \frac{c}{(\sqrt{c^2+a^2})}$	R16
11	$(0\bar{1}11)[\bar{1}2\bar{1}3]$	$-\frac{\sqrt{3}c}{\sqrt{4c^2+3a^2}} \; \frac{c}{\sqrt{4c^2+3a^2}} \; \frac{\sqrt{3}a}{\sqrt{4c^2+3a^2}}$	$\frac{a}{\sqrt{c^2+a^2}} \; 0 \; \frac{c}{\sqrt{c^2+a^2}}$	R17
12	$(1\bar{1}01)[\bar{2}113]$	$-\frac{\sqrt{3}c}{\sqrt{4c^2+3a^2}} \; -\frac{c}{\sqrt{4c^2+3a^2}} \; \frac{\sqrt{3}a}{\sqrt{4c^2+3a^2}}$	$\frac{a}{2(\sqrt{c^2+a^2})} \; \frac{\sqrt{3}a}{2(\sqrt{c^2+a^2})} \; \frac{c}{(\sqrt{c^2+a^2})}$	R18

Table 4-8. Pyramidal $< \mathbf{c} + \mathbf{a} >$ Slip Systems $\{11\bar{2}2\} < 11\bar{2}3 >$

α	Miller-Bravais Notation	$[\mathbf{n}_o^\alpha]_c$	$[\mathbf{m}_o^\alpha]_c$	Label
1	$(11\bar{2}2)[\bar{1}\bar{1}23]$	$\frac{c}{2(\sqrt{c^2+a^2})}\ -\frac{\sqrt{3}c}{2(\sqrt{c^2+a^2})}\ \frac{a}{(\sqrt{c^2+a^2})}$	$-\frac{a}{2(\sqrt{c^2+a^2})}\ \frac{\sqrt{3}a}{2(\sqrt{c^2+a^2})}\ \frac{c}{(\sqrt{c^2+a^2})}$	R19
2	$(\bar{1}2\bar{1}2)[1\bar{2}13]$	$\frac{c}{(\sqrt{c^2+a^2})}\ 0\ \frac{a}{(\sqrt{c^2+a^2})}$	$-\frac{a}{(\sqrt{c^2+a^2})}\ 0\ \frac{c}{(\sqrt{c^2+a^2})}$	R20
3	$(\bar{2}112)[2\bar{1}\bar{1}3]$	$\frac{c}{2(\sqrt{c^2+a^2})}\ \frac{\sqrt{3}c}{2(\sqrt{c^2+a^2})}\ \frac{a}{(\sqrt{c^2+a^2})}$	$-\frac{a}{2(\sqrt{c^2+a^2})}\ -\frac{\sqrt{3}a}{2(\sqrt{c^2+a^2})}\ \frac{c}{(\sqrt{c^2+a^2})}$	R21
4	$(\bar{1}\bar{1}22)[11\bar{2}3]$	$-\frac{c}{2(\sqrt{c^2+a^2})}\ \frac{\sqrt{3}c}{2(\sqrt{c^2+a^2})}\ \frac{a}{(\sqrt{c^2+a^2})}$	$\frac{a}{2(\sqrt{c^2+a^2})}\ -\frac{\sqrt{3}a}{2(\sqrt{c^2+a^2})}\ \frac{c}{(\sqrt{c^2+a^2})}$	R22
5	$(1\bar{2}12)[\bar{1}2\bar{1}3]$	$-\frac{c}{(\sqrt{c^2+a^2})}\ 0\ \frac{a}{(\sqrt{c^2+a^2})}$	$\frac{a}{(\sqrt{c^2+a^2})}\ 0\ \frac{c}{(\sqrt{c^2+a^2})}$	R23
6	$(2\bar{1}\bar{1}2)[\bar{2}113]$	$-\frac{c}{2(\sqrt{c^2+a^2})}\ -\frac{\sqrt{3}c}{2(\sqrt{c^2+a^2})}\ \frac{a}{(\sqrt{c^2+a^2})}$	$\frac{a}{2(\sqrt{c^2+a^2})}\ \frac{\sqrt{3}a}{2(\sqrt{c^2+a^2})}\ \frac{c}{(\sqrt{c^2+a^2})}$	R24

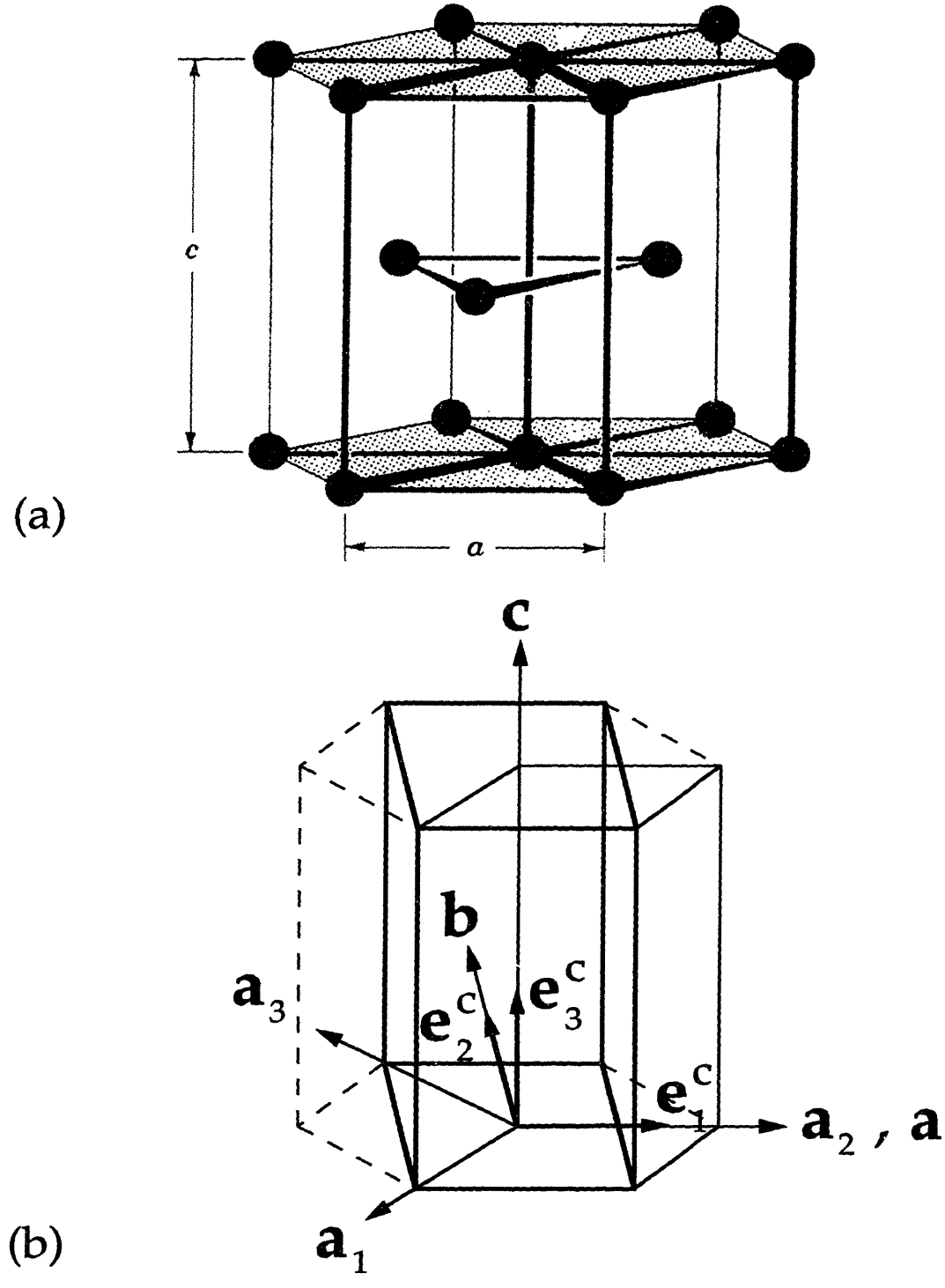

Figure 4-1: (a) Structure of the hexagonal lattice. (b) Schematic diagram illustrating the relation of the simple hexagonal cell (light lines) to the orthohexagonal cell (dark lines) and the hexagonal prism (dashed lines).

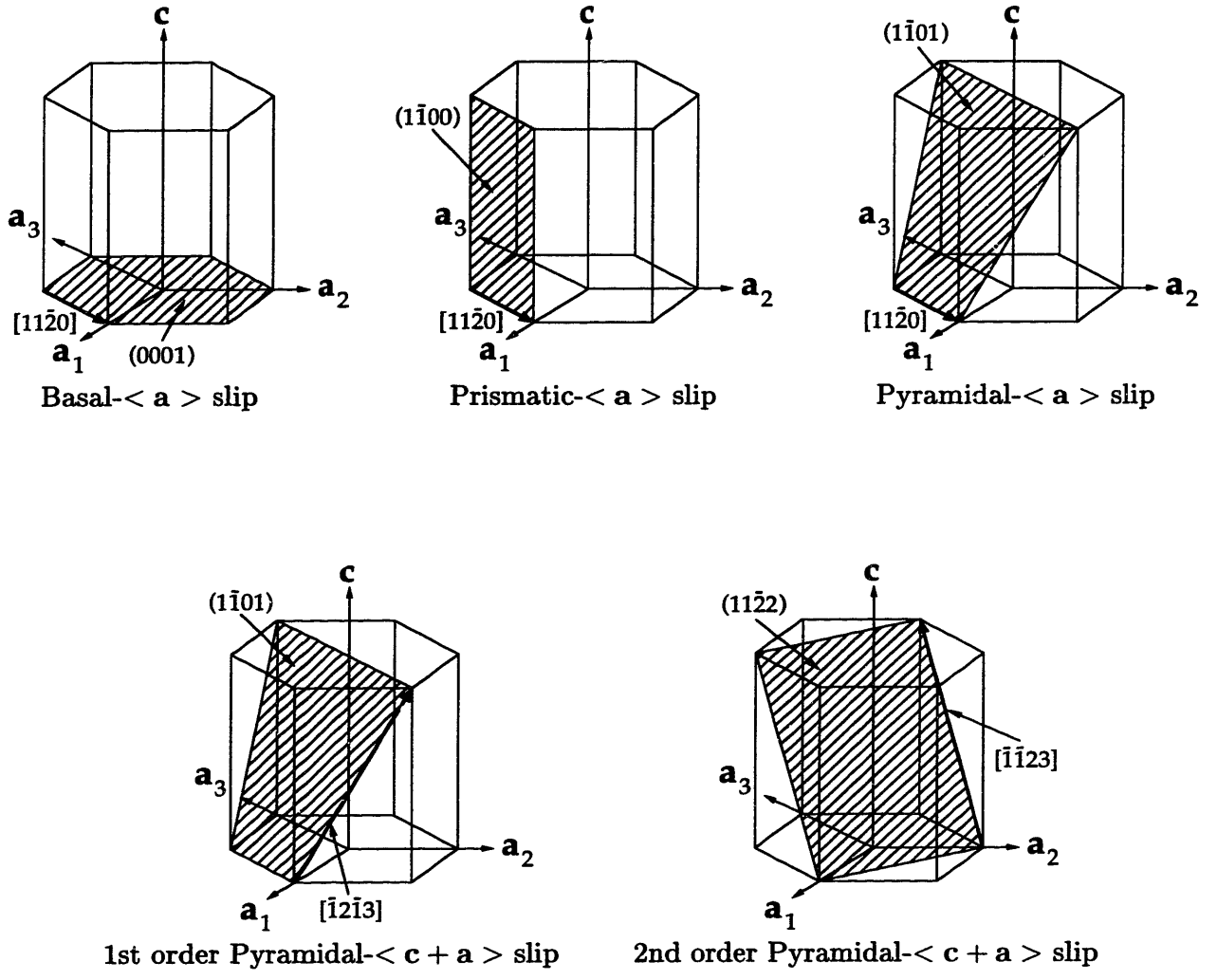

Figure 4-2: Slip systems in high-temperature deformation of h.c.p. titanium.

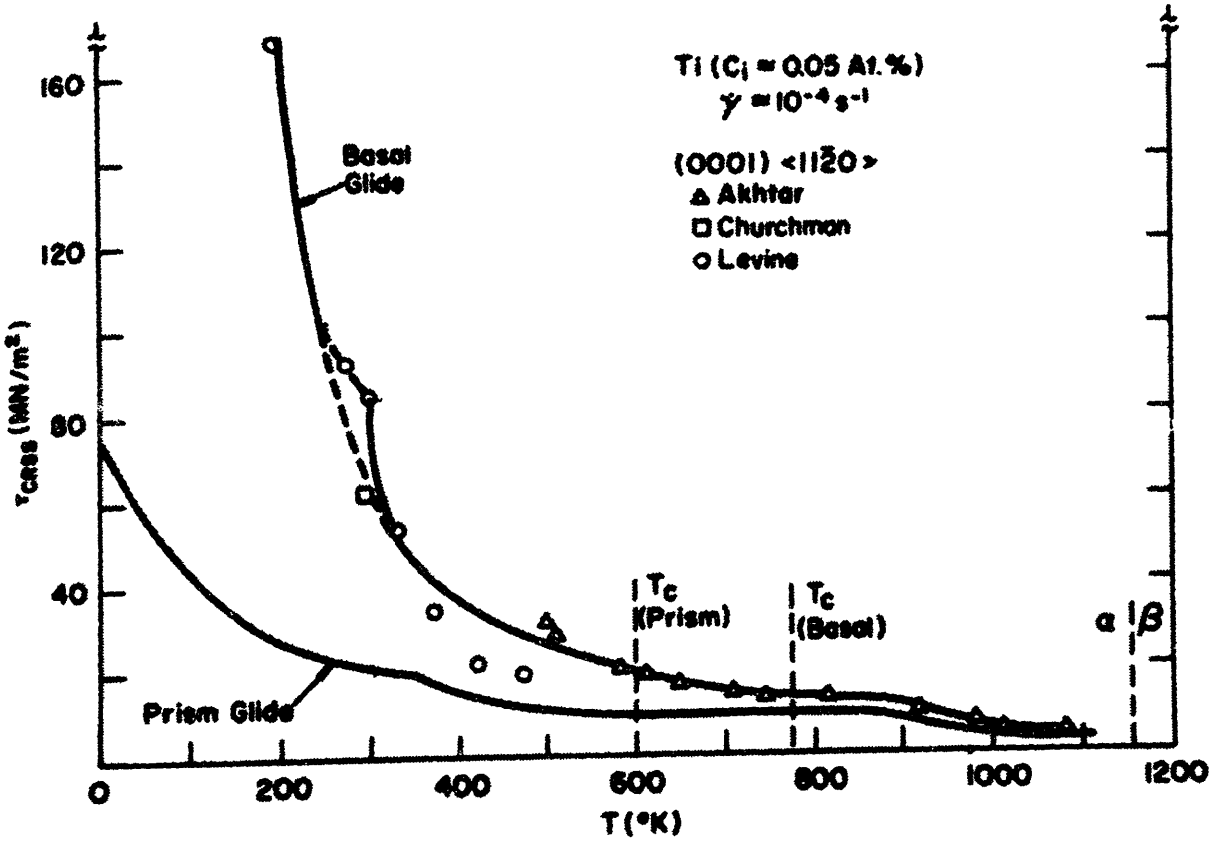

Figure 4-3: Effect of temperature on the critical resolved shear stress for basal and prismatic slip in high-purity titanium (Conrad [1981]).

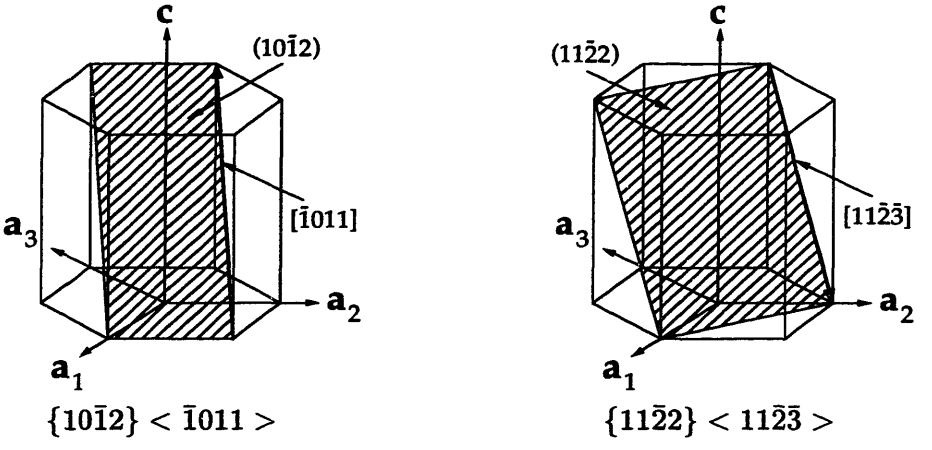

Figure 4-4: Twin systems in room-temperature deformation of h.c.p. titanium.

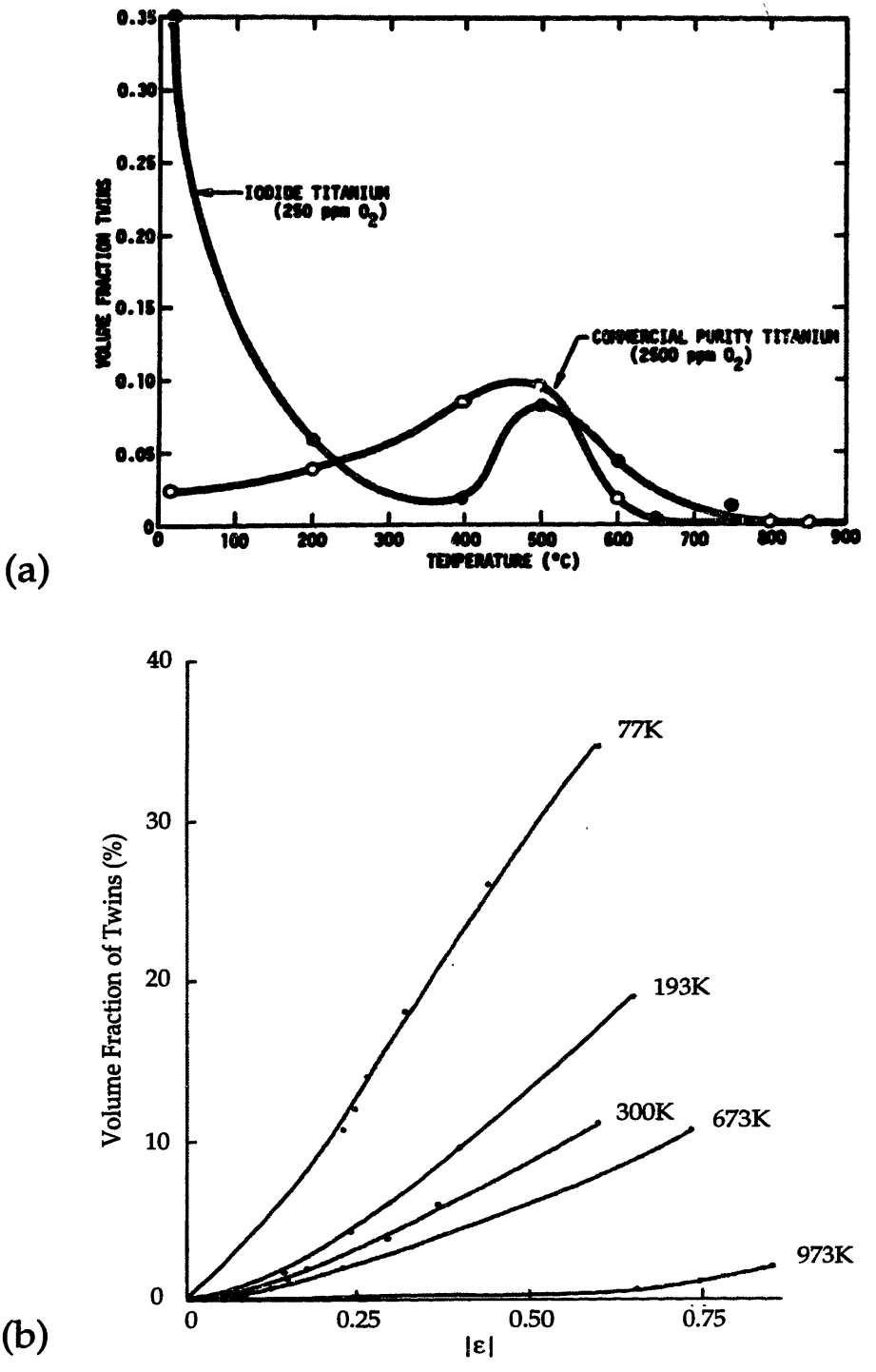

Figure 4-5: (a) Influence of temperature and purity on the volume fraction of twins at 5% compression in α-titanium (Paton, Williams and Rauscher [1973]). (b) Volume fraction of twins as a function of true strain in h.c.p. titanium deformed in tension at various temperatures (Lii, Ramachandran and Reed-Hill [1970]).

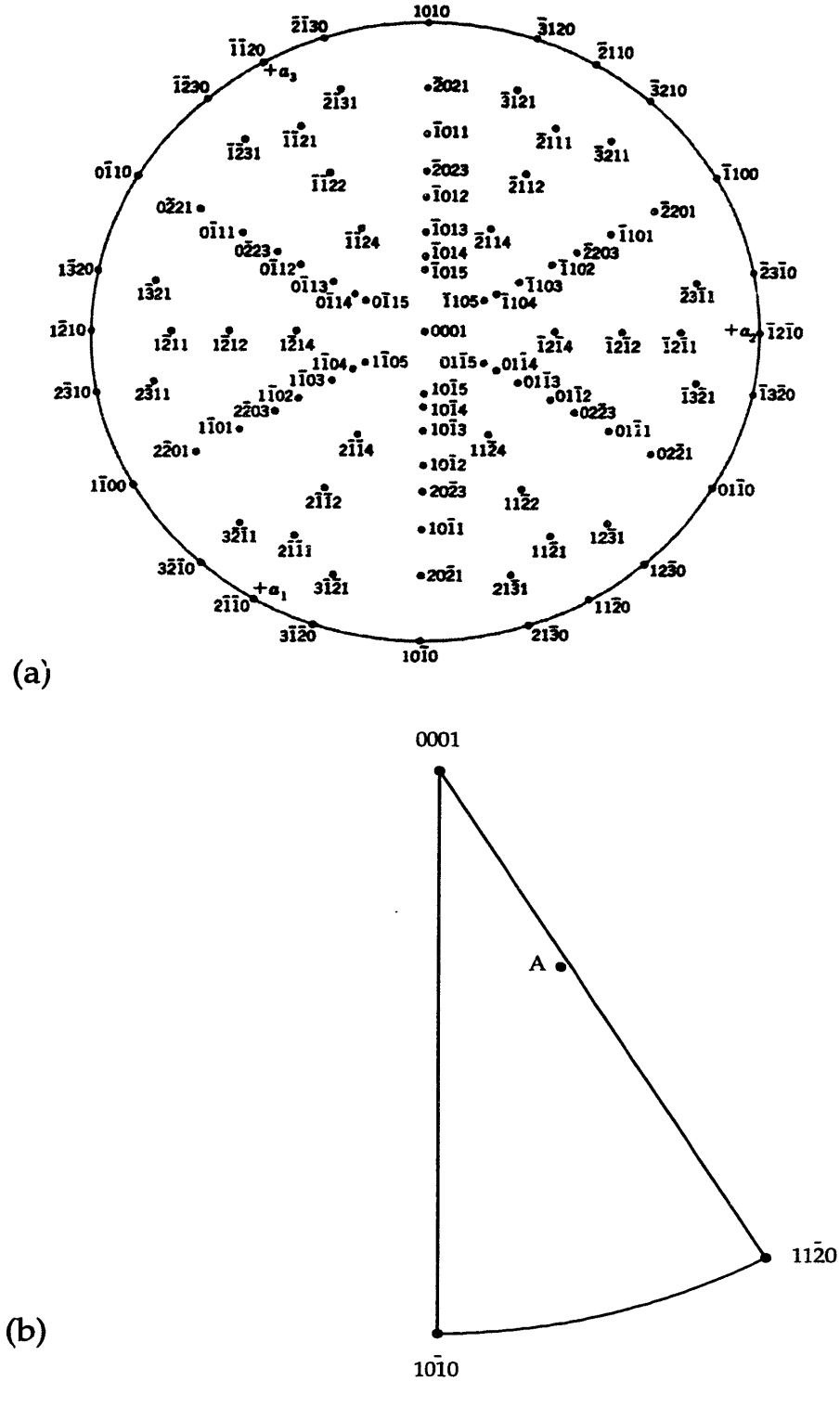

Figure 4-6: (a) Standard stereographic (0001) projection for titanium. (b) Primary orientation triangle showing the initial orientation of the tension axis.

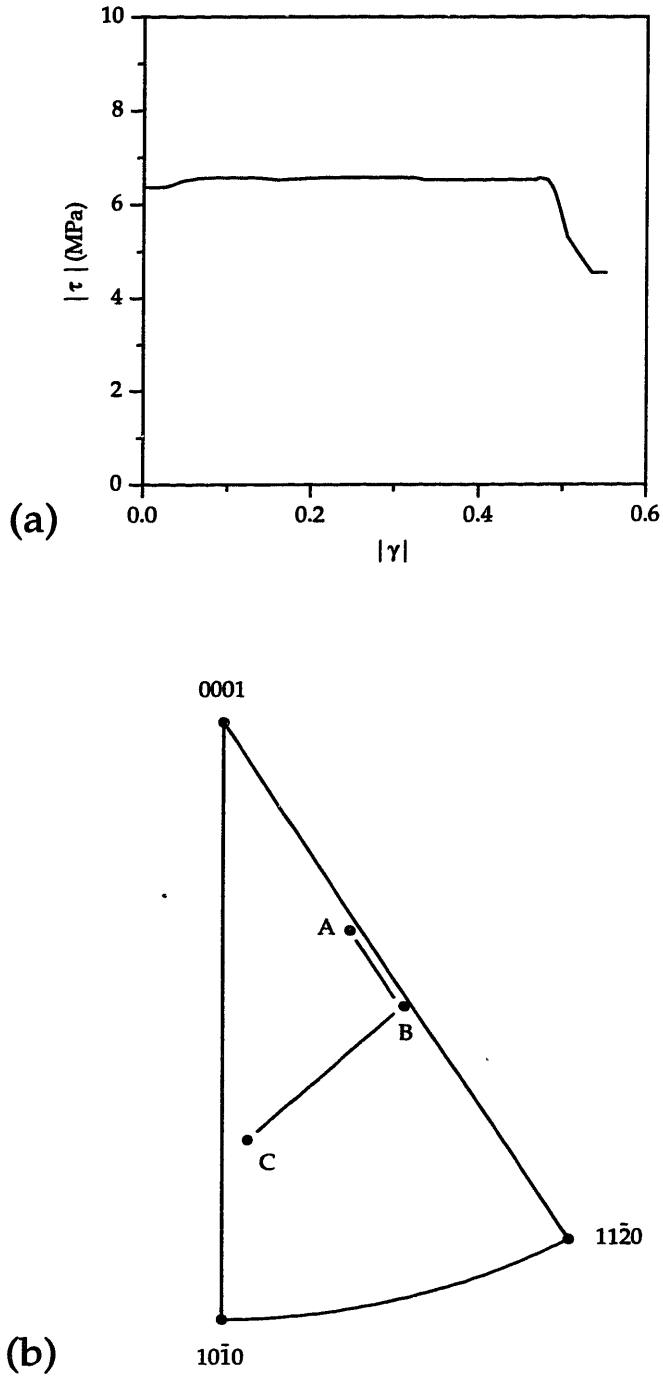

Figure 4-7: Simple tension experiment performed on a titanium single crystal at 750°C (Akhtar [1975a]): (a) Resolved shear stress vs. shear strain curves for basal slip. (b) Inverse pole figure showing the change in orientation of the tension axis with strain (A-B-C).

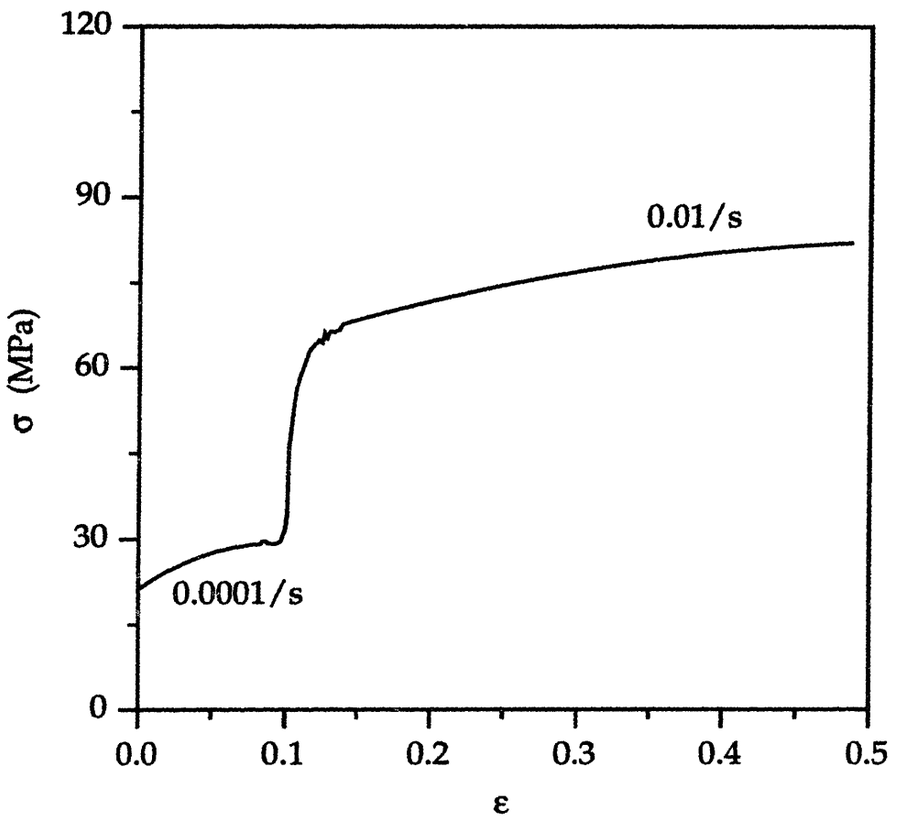

Figure 4-8: Experimentally measured stress-strain response during strain-rate jump from $\dot{\epsilon} = -0.0001\text{sec}^{-1}$ to $\dot{\epsilon} = -0.01\text{sec}^{-1}$.

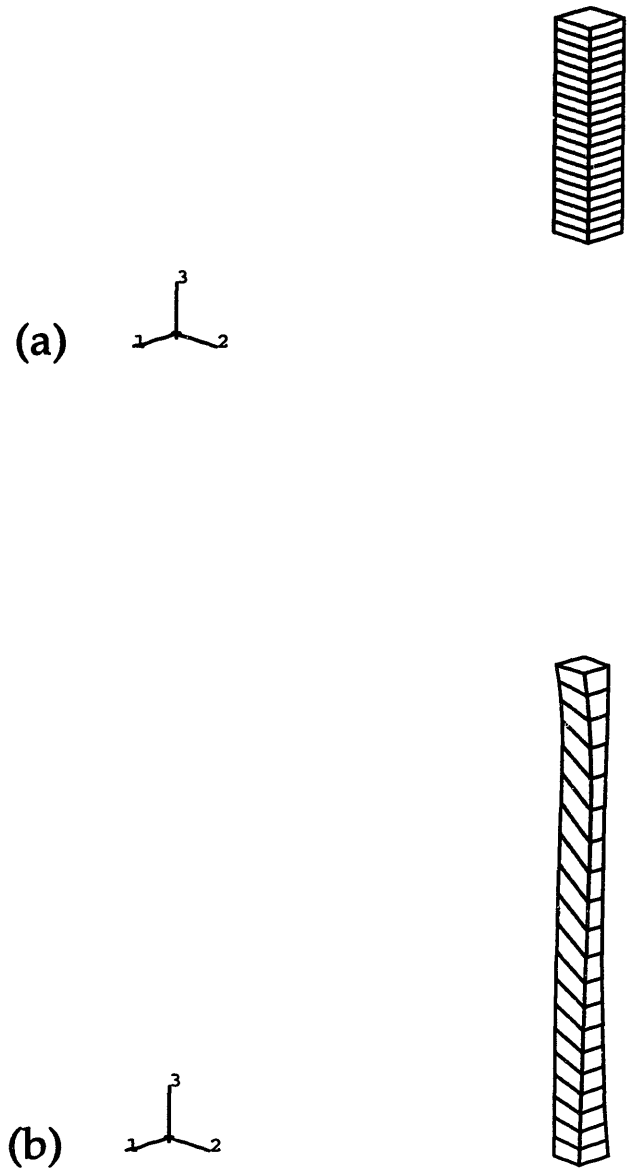

Figure 4-9: (a) The initial finite element mesh used in the simulation of tension of a titanium single crystal. (b) Deformed mesh at $\epsilon = 0.7$.

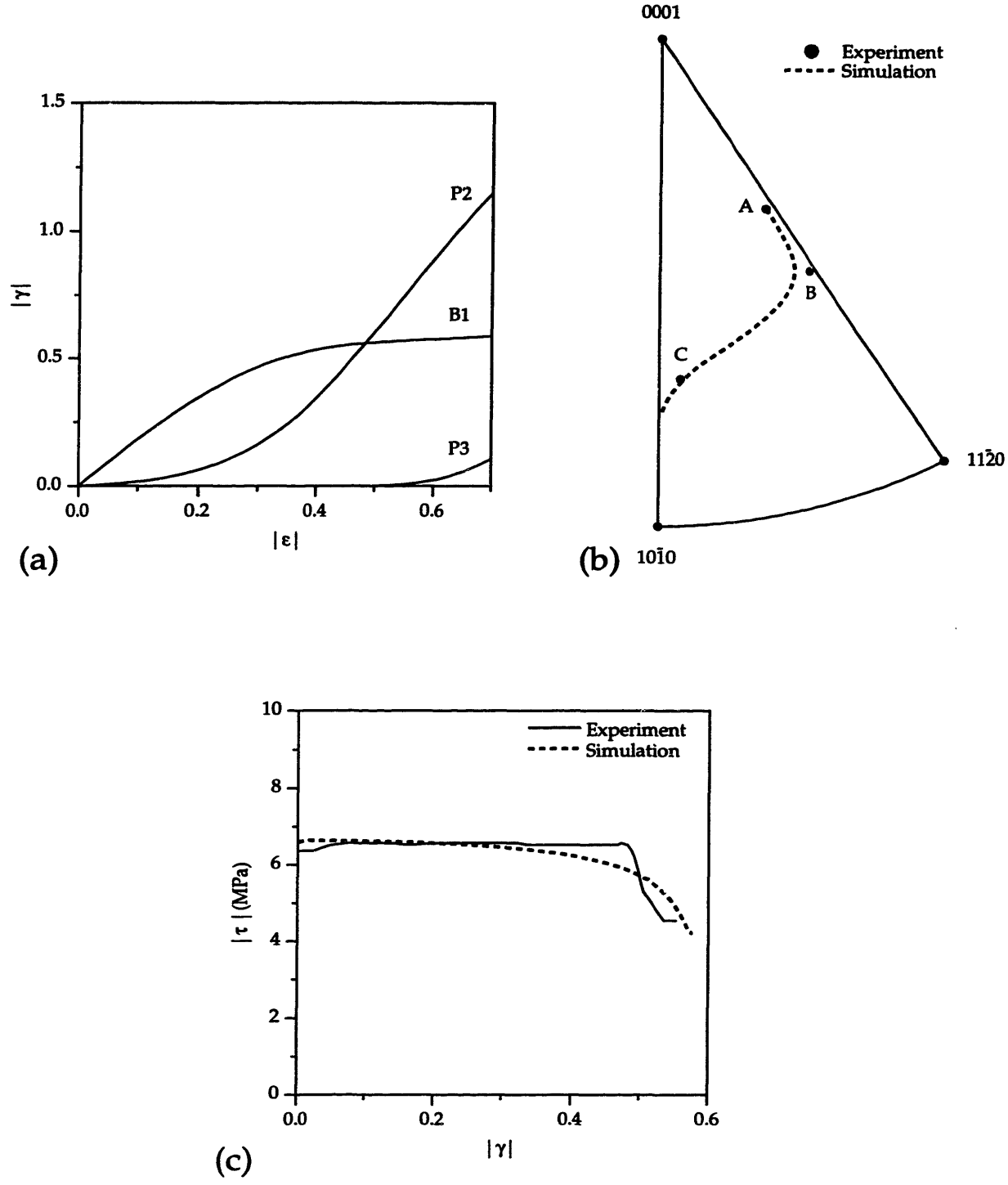

Figure 4-10: Comparison of the simple tension experiment performed on a titanium single crystal at 750°C (Akhtar [1975a]) with our numerical simulation: (a) Accumulated slip vs. macroscopic strain for active slip systems. (b) Inverse pole figure of the change in orientation of the tension axis. (c) Resolved shear stress vs. shear strain response on the basal slip system B1.

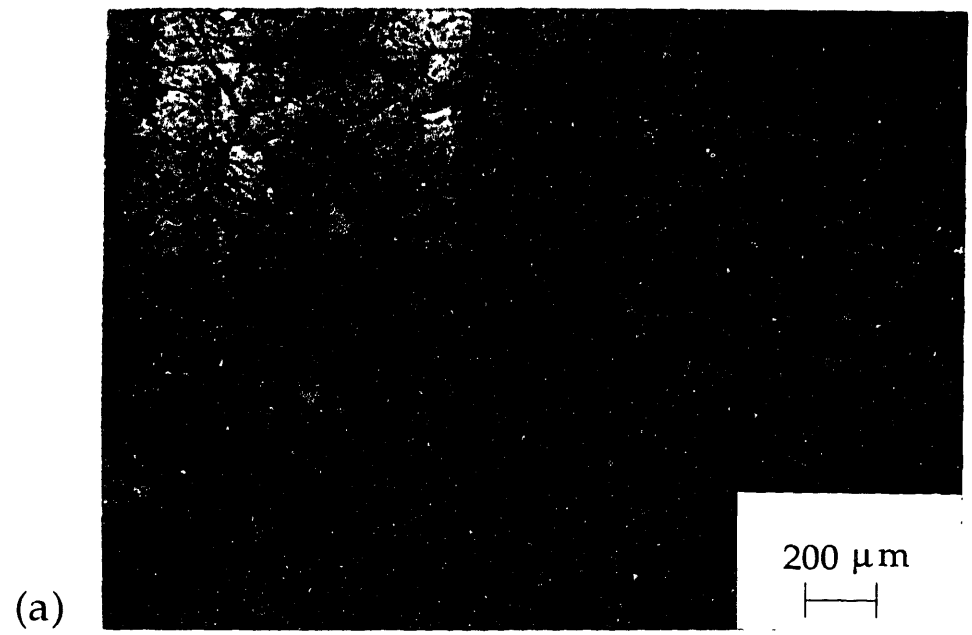

(a)

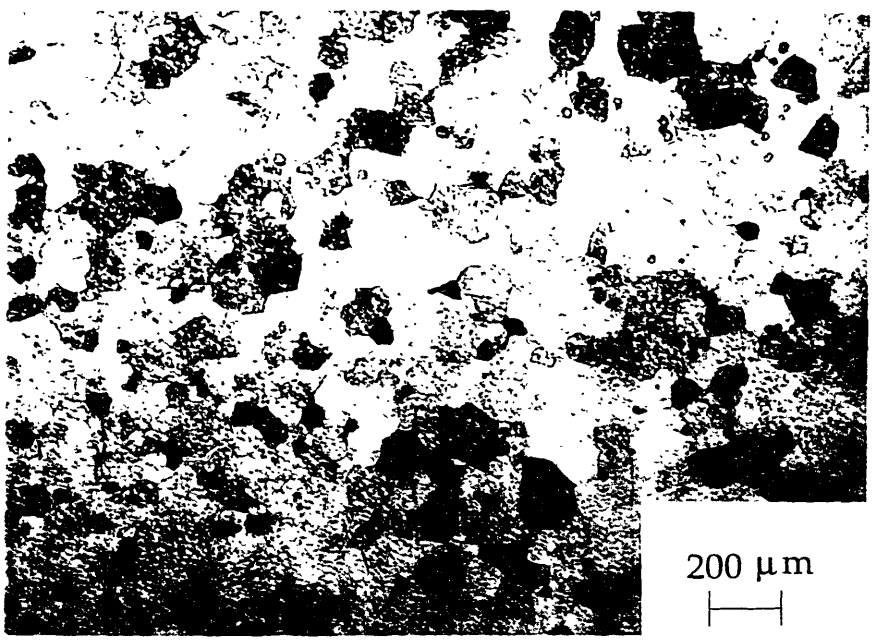

(b)

Figure 4-11: Micrograph of the as-received titanium rod, 50X: (a) Transverse Section (b) Longitudinal Section

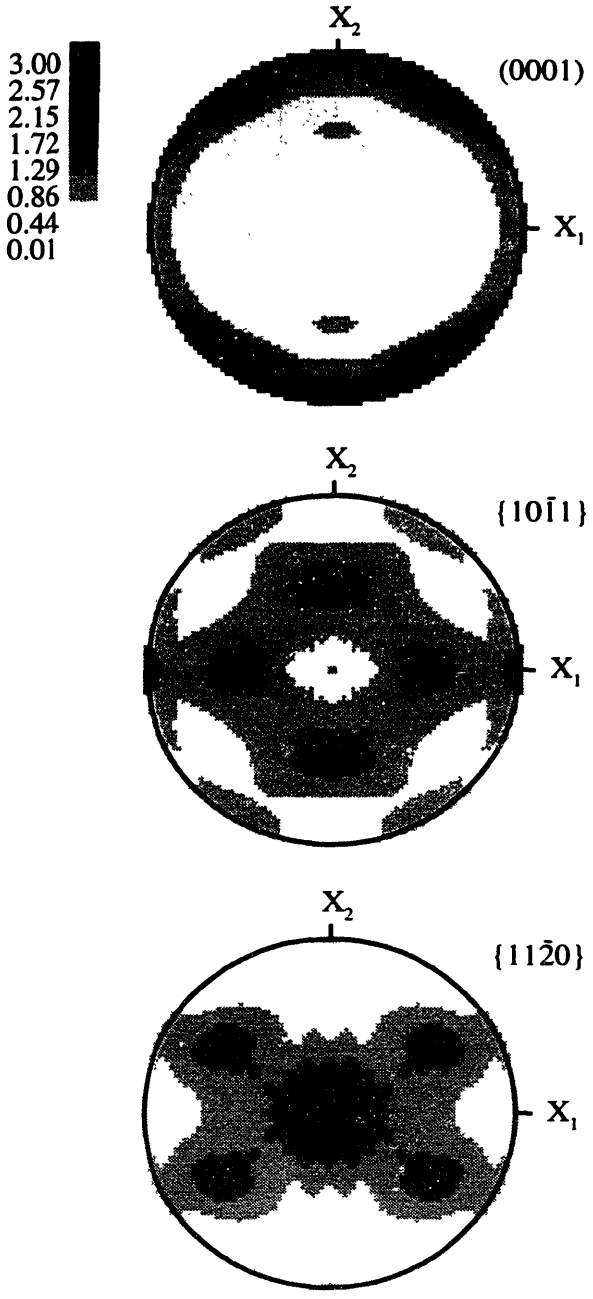

Figure 4-12: Experimentally measured crystallographic texture of the as-received titanium rod. The rod axis is aligned with the $\mathbf{e}_3$ direction.

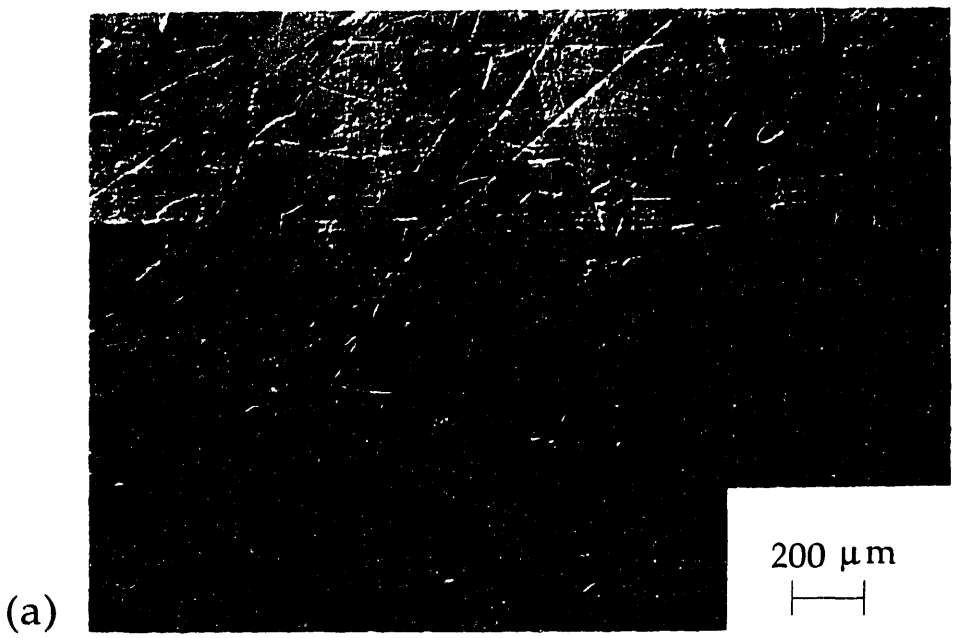

(a)

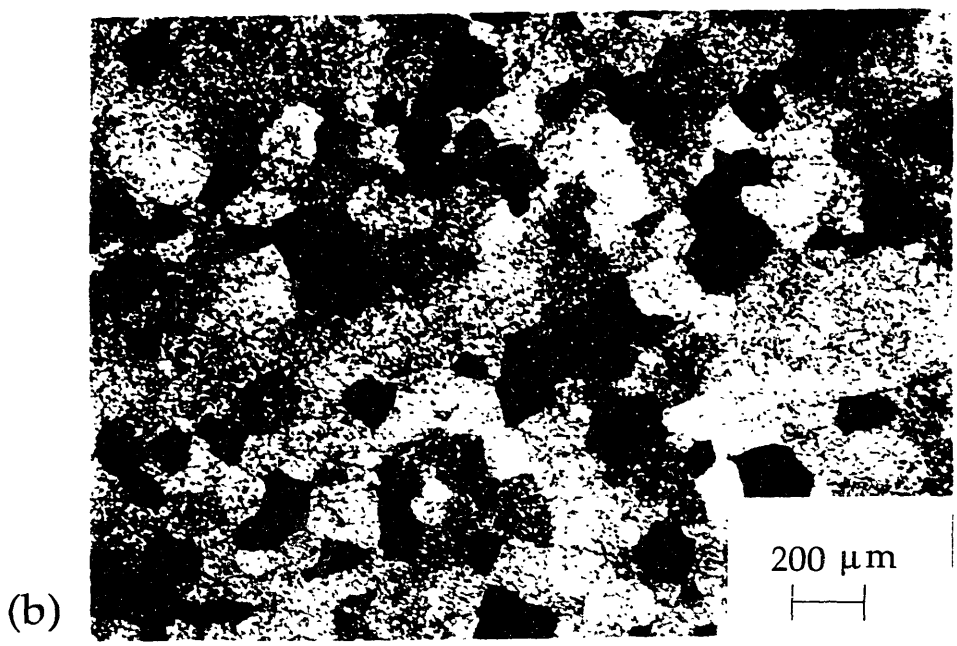

(b)

Figure 4-13: Micrograph of the annealed titanium rod, 50X: (a) Transverse Section (b) Longitudinal Section

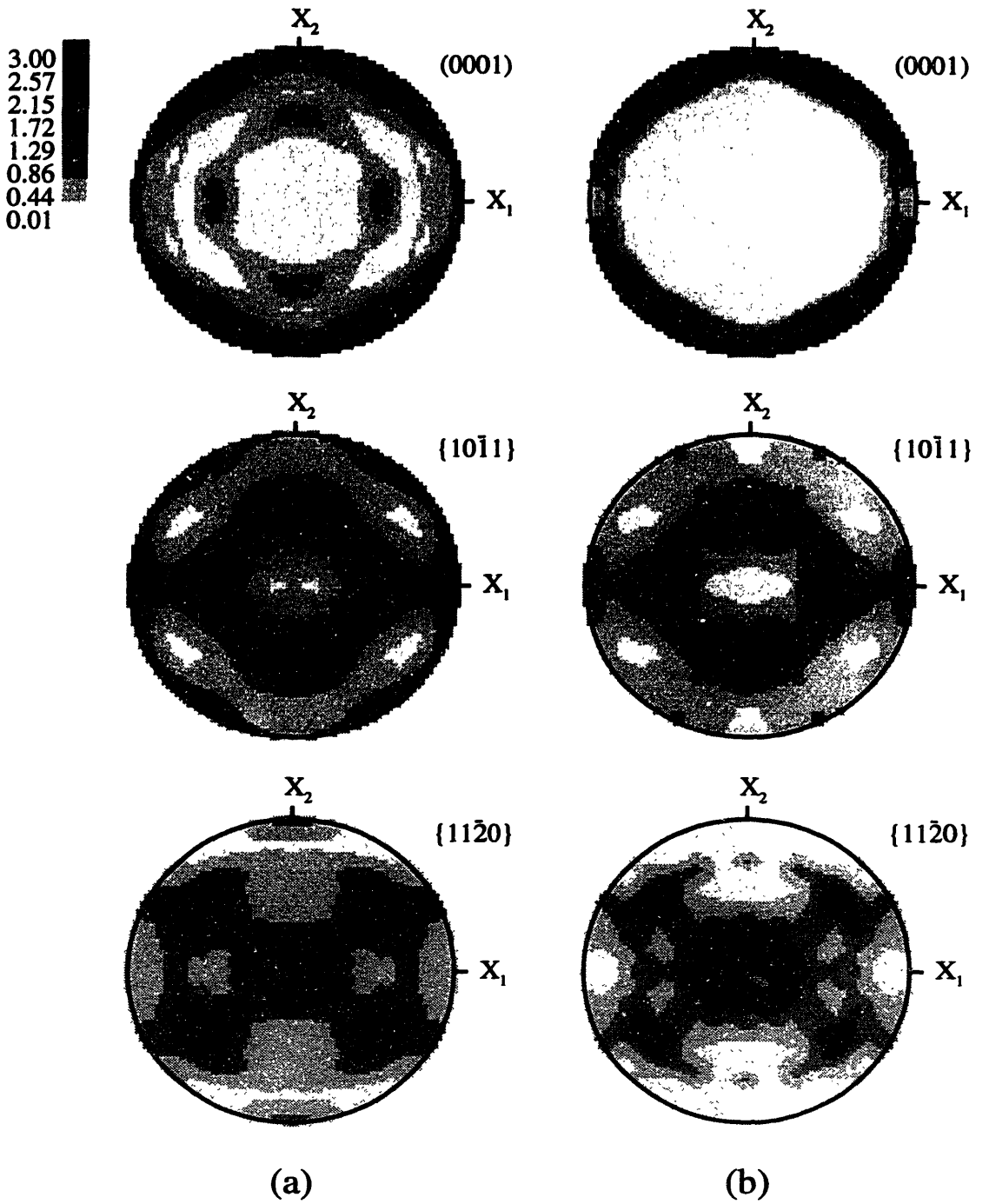

Figure 4-14: (a) Experimentally measured texture in the annealed CP-Titanium rod and (b) its numerical representation using 729 unweighted discrete grain orientations.

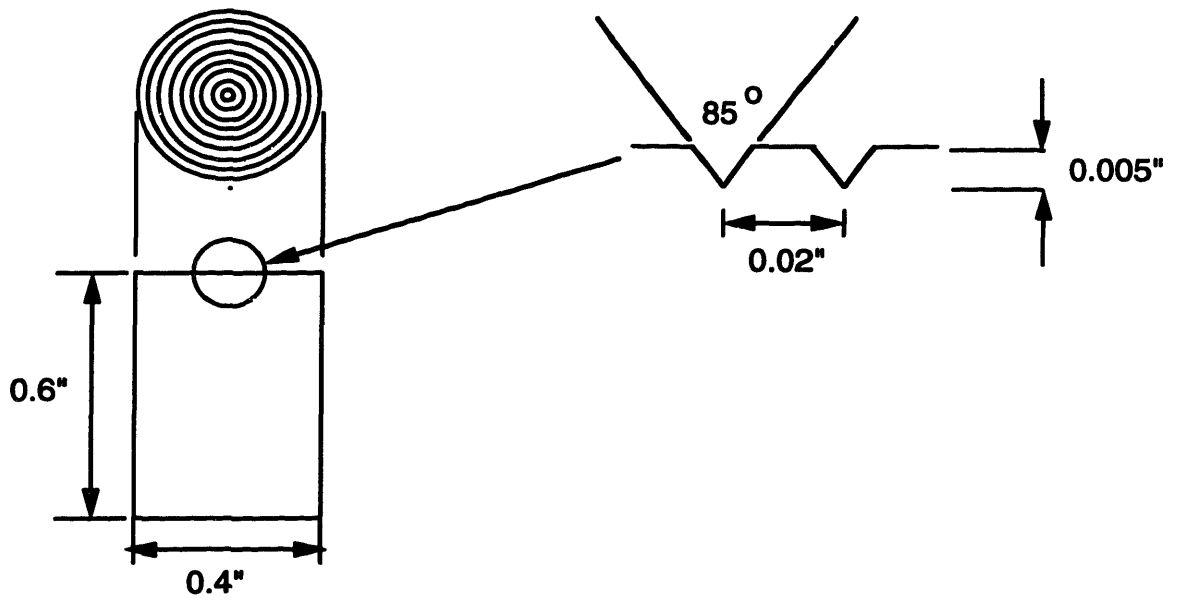

Figure 4-15: Geometry of compression specimens (All dimensions are in inches).

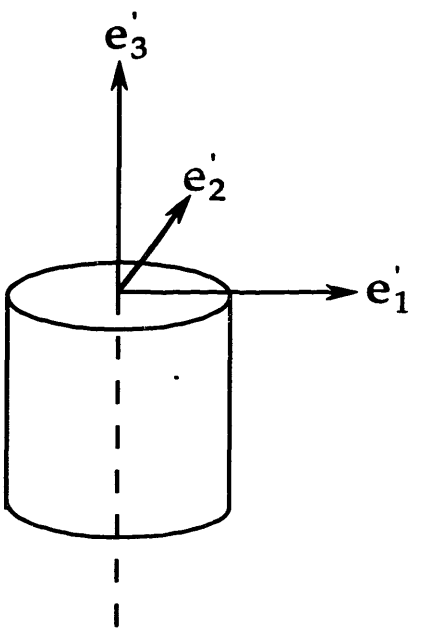

Figure 4-16: Schematic illustrating the orientation of the material axes in the compression specimen.

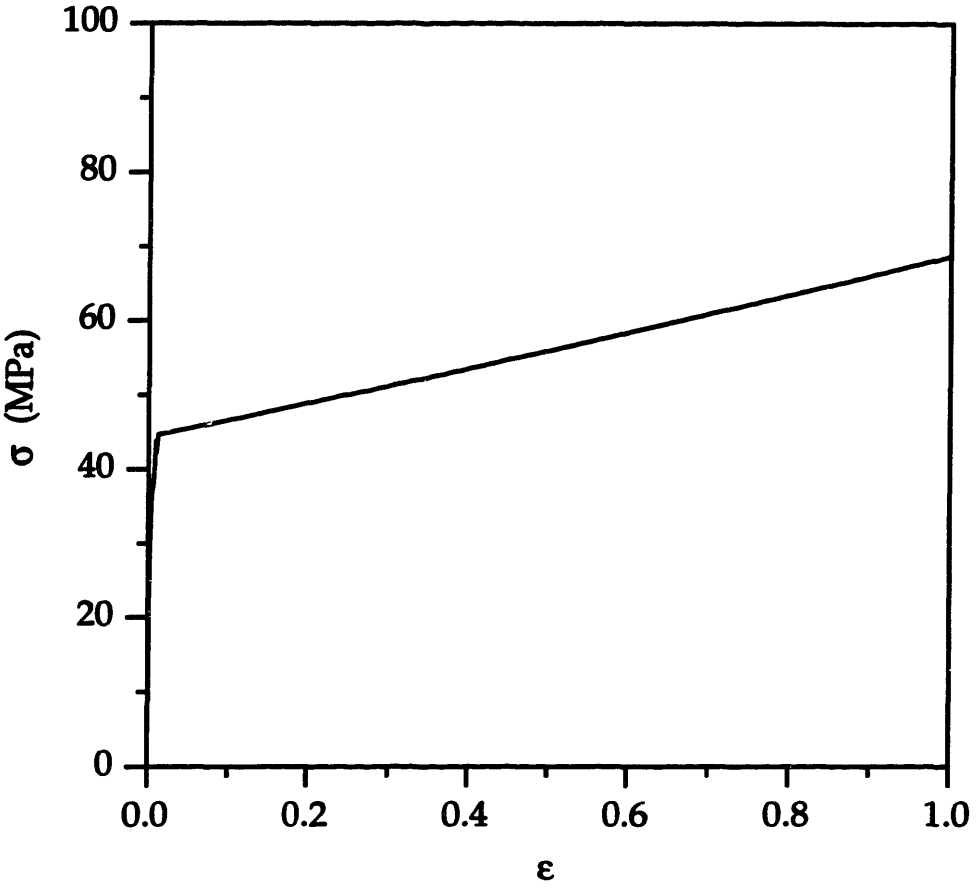

Figure 4-17: Experimentally measured stress-strain response during simple compression of CP-Titanium at 750°C.

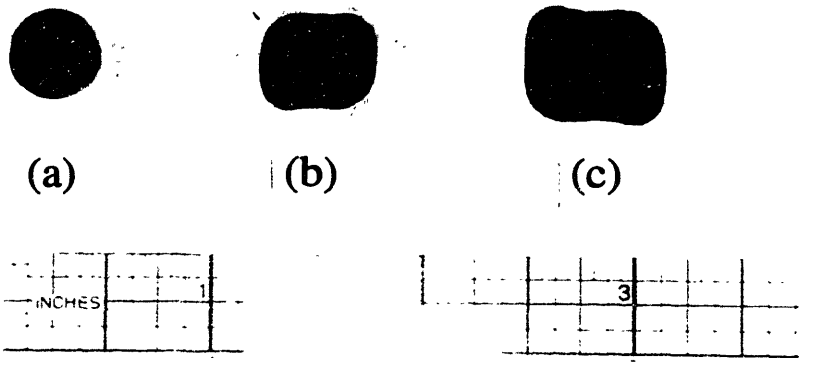

Figure 4-18: Photographs of the section of the compression specimen perpendicular to the loading axis: (a) Initial (b) $\epsilon = -0.5$ (c) $\epsilon = -1$.

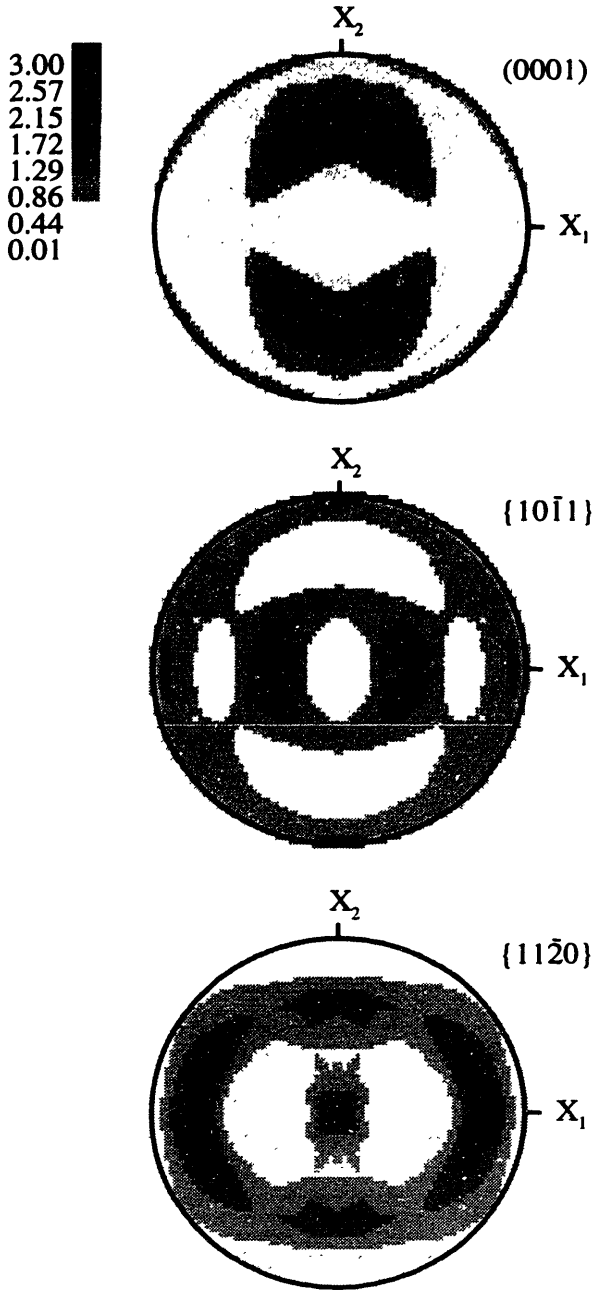

Figure 4-19: Experimentally measured crystallographic texture at $\epsilon = -1$ in CP-Titanium deformed in simple compression at 750°C.

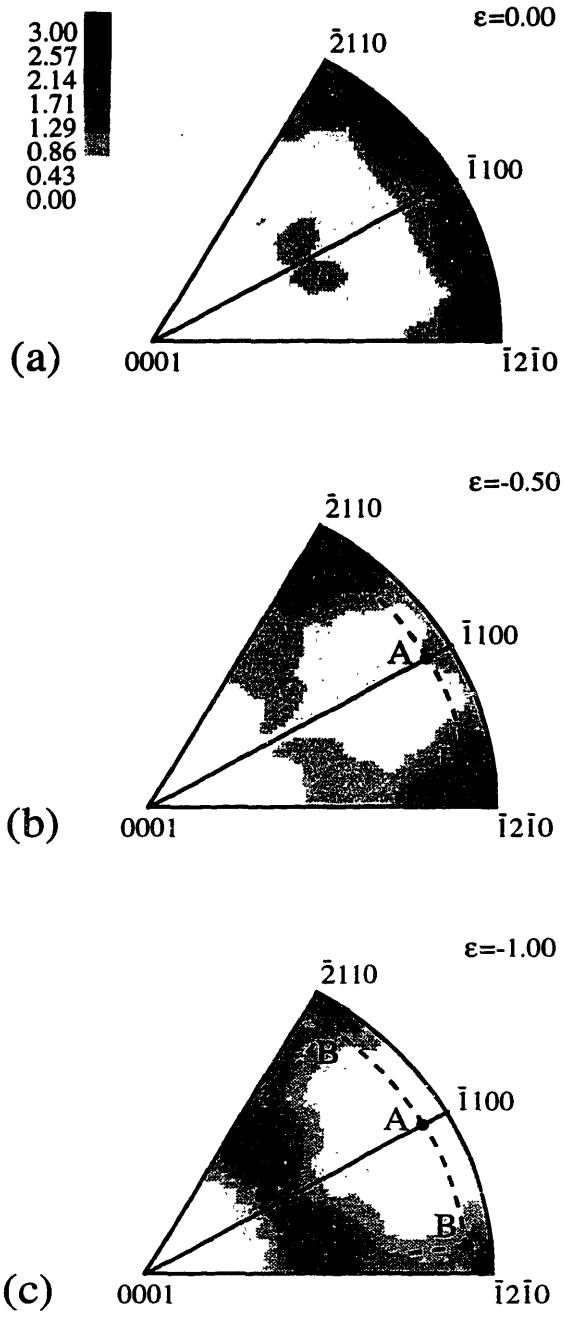

Figure 4-20: Inverse pole figure of the compression axis: (a) Initial (b) $\epsilon = -0.5$ (b) $\epsilon = -1$. The figures also show the lines of symmetry (bold lines) in the plot. The dashed lines (A-B-C) trace the evolution of the compression axis with strain.

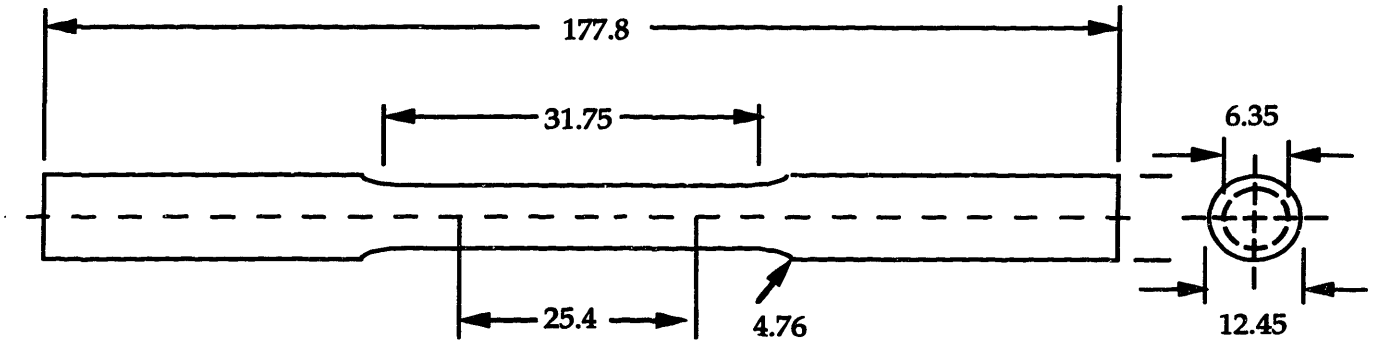

Figure 4-21: Geometry of tension specimens (All dimensions are in millimeters).

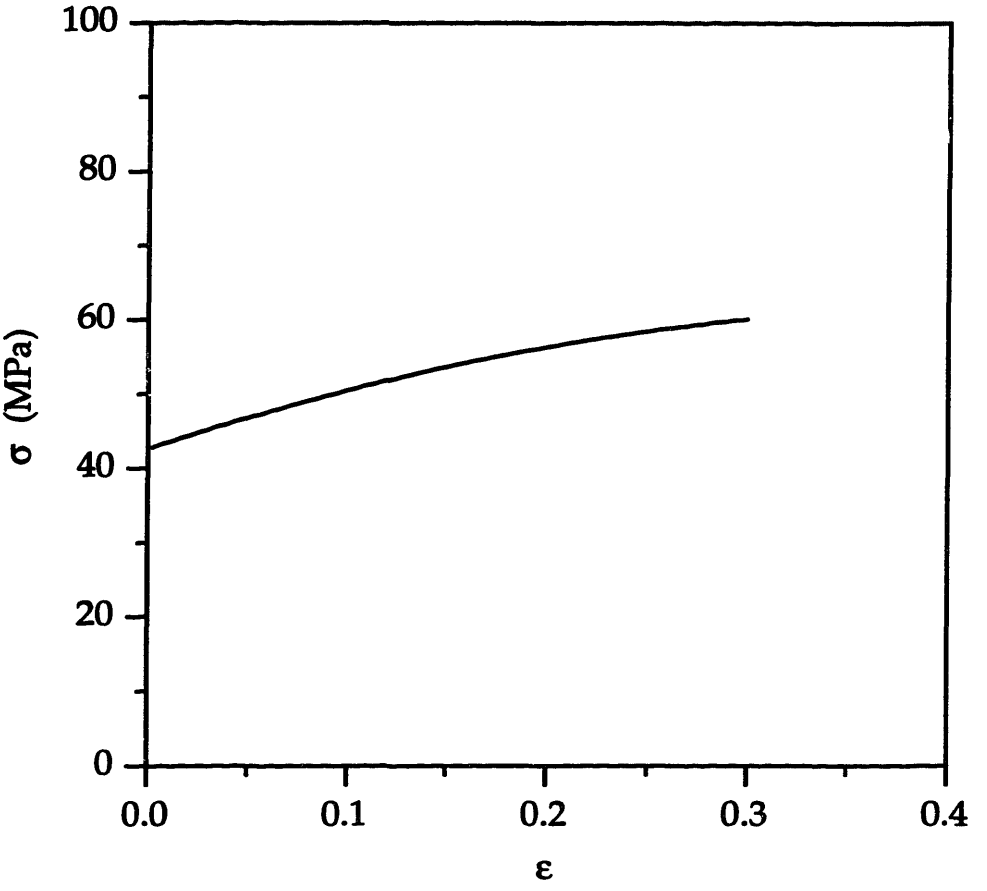

Figure 4-22: Experimentally measured stress-strain response during simple tension of CP-Titanium at 750°C.

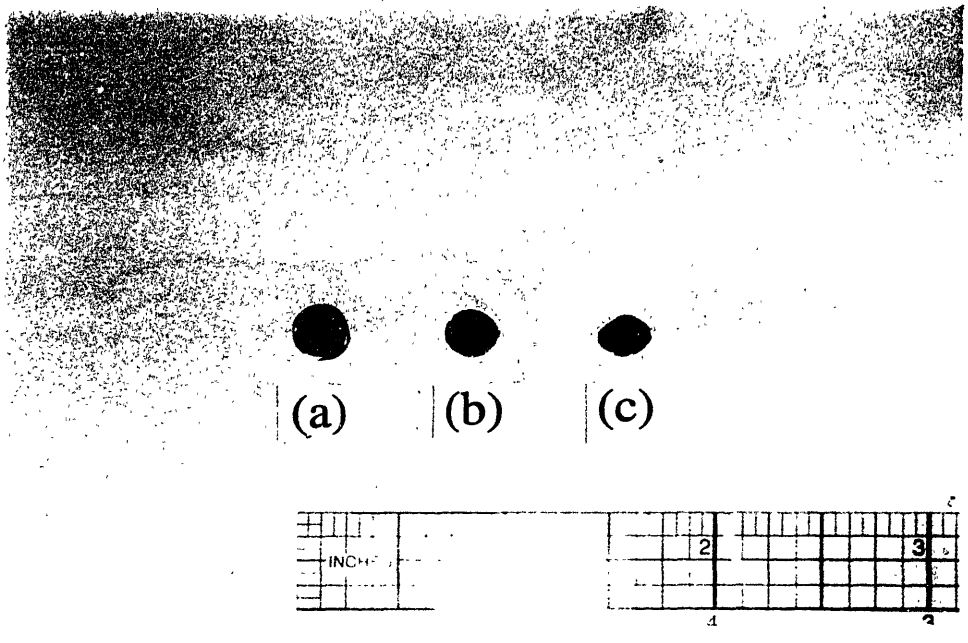

Figure 4-23: Photographs of the section of the tension specimen perpendicular to the tensile axis: (a) Initial (b) $\epsilon = 0.2$ (c) $\epsilon = 0.3$.

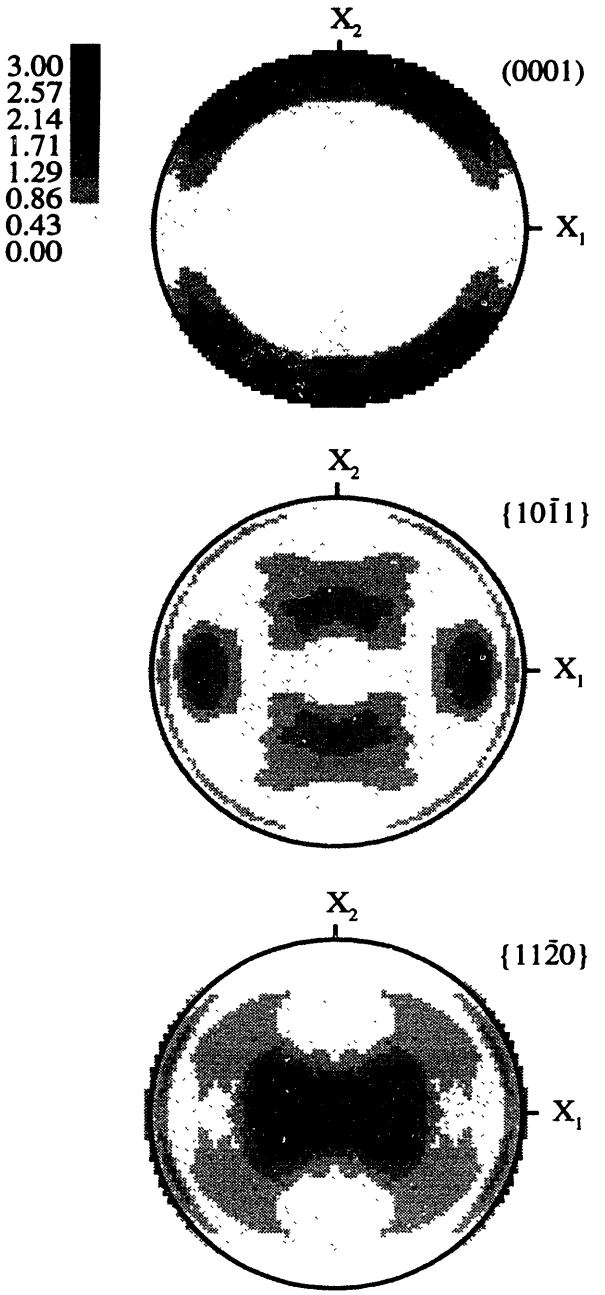

Figure 4-24: Experimentally measured crystallographic texture at $\epsilon = 0.3$ in CP-Titanium deformed in simple tension at 750°C.

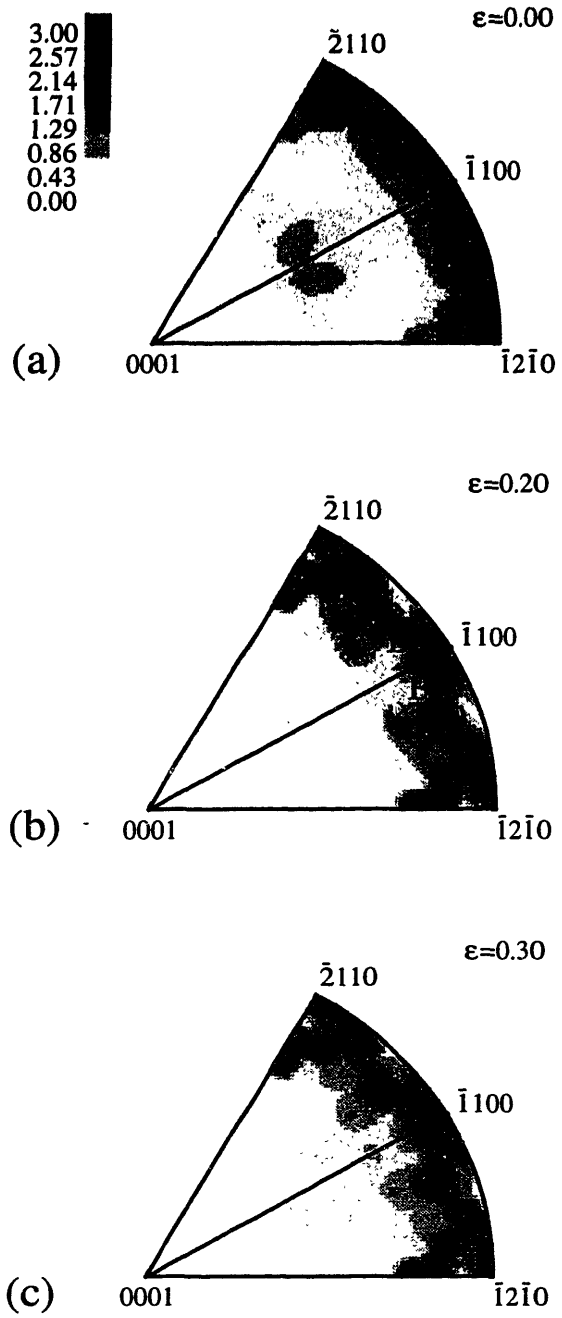

Figure 4-25: Inverse pole figure of the tension axis: (a) Initial (b) $\epsilon = 0.2$ (b) $\epsilon = 0.3$. The figures also show the lines of symmetry (bold lines) in the plot. The dashed lines (A-B) trace the evolution of the tension axis with strain.

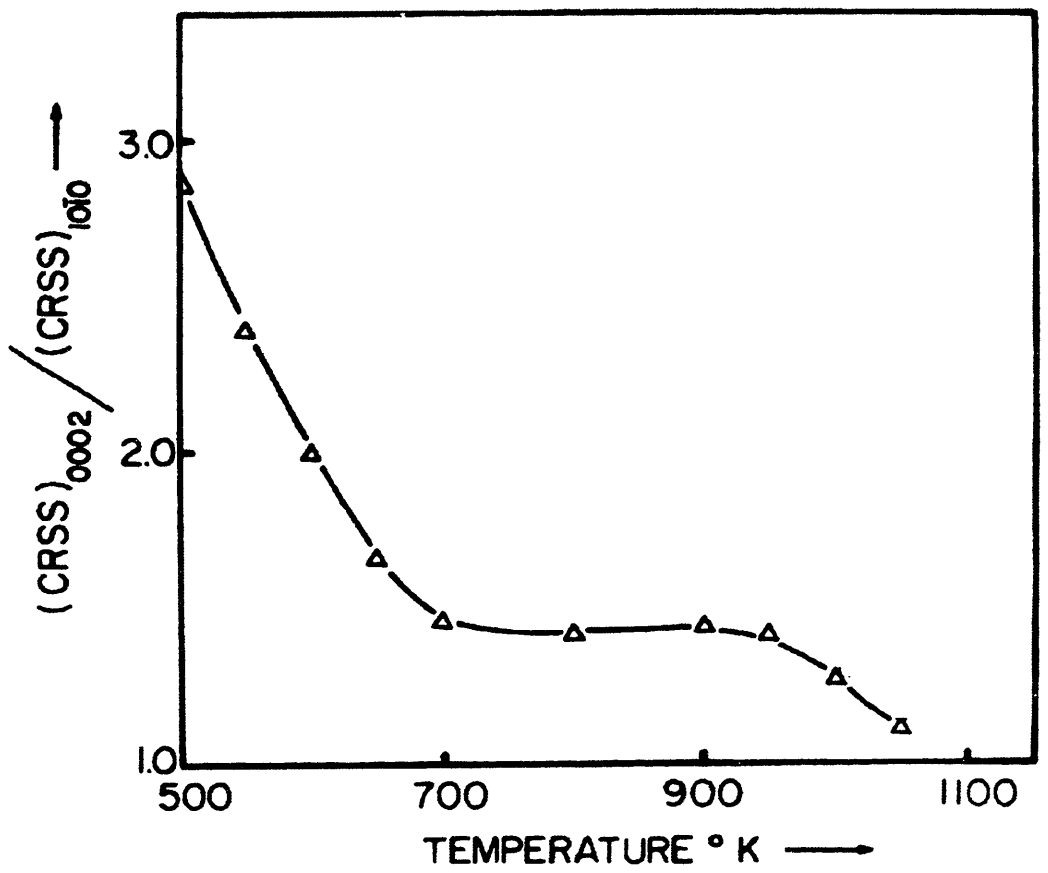

Figure 4-26: The ratio of the critical resolved shear stress for basal to that of prismatic slip in high-purity h.c.p. titanium (Akhtar [1975a])

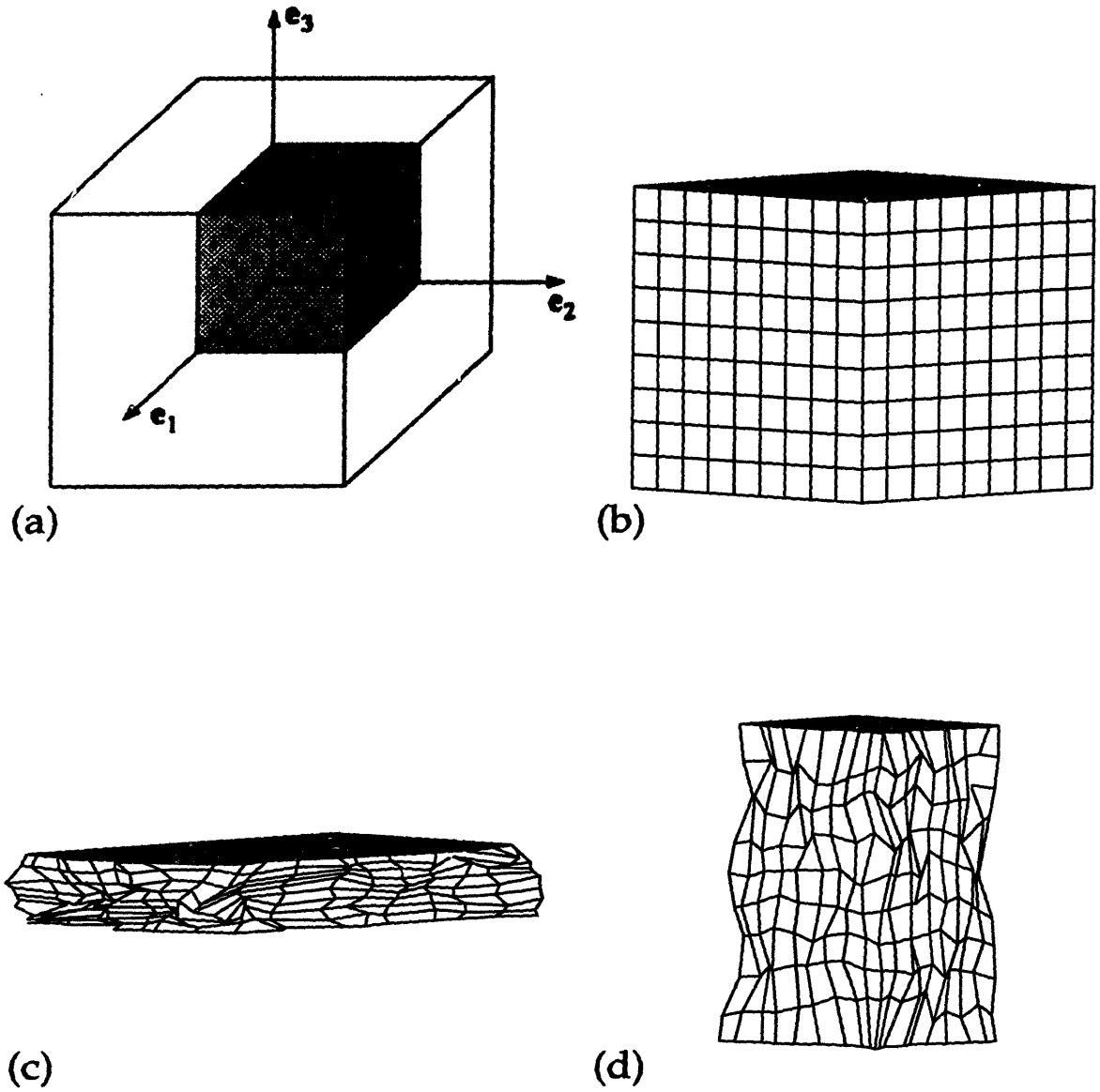

Figure 4-27: Initial and deformed finite element meshes in simple compression and tension simulations: (a) Octant of a cube (b) Initial finite element mesh (c) Deformed mesh at $\epsilon = -1$ in simple compression (d) Deformed mesh at $\epsilon = 0.4$ in simple tension.

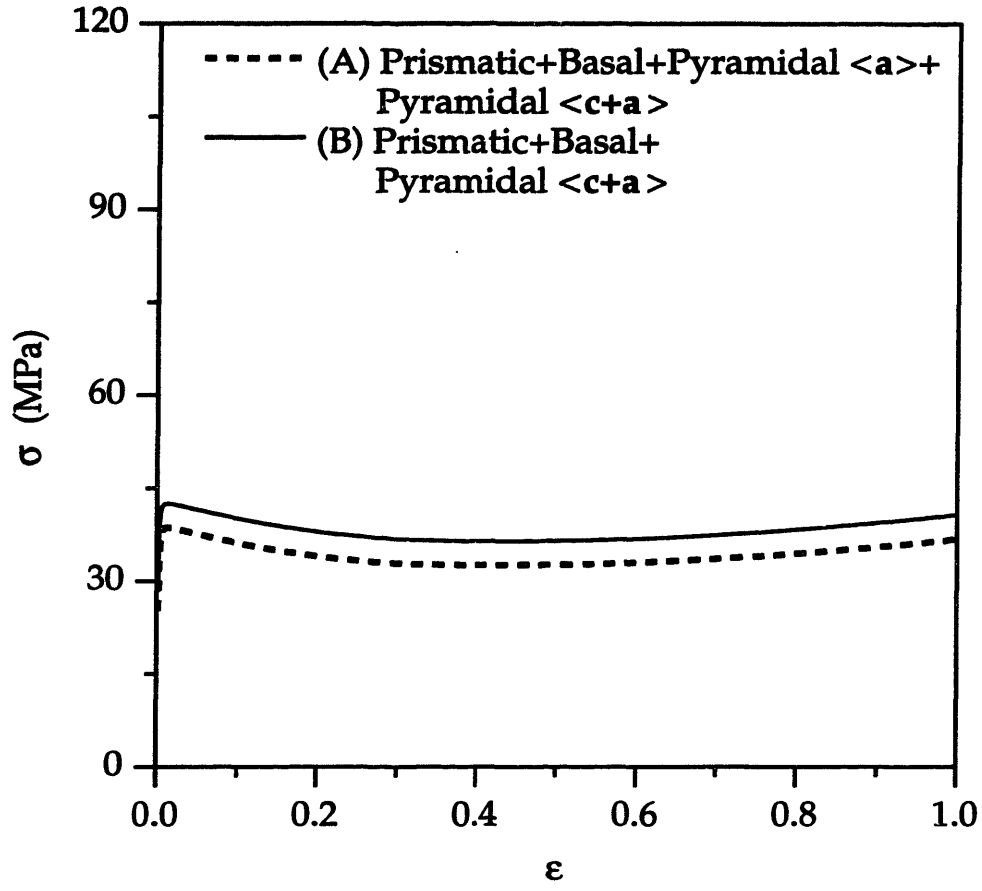

Figure 4-28: Stress-strain curves from simple compression simulation for the non-hardening case with two different assumptions for the slip systems.

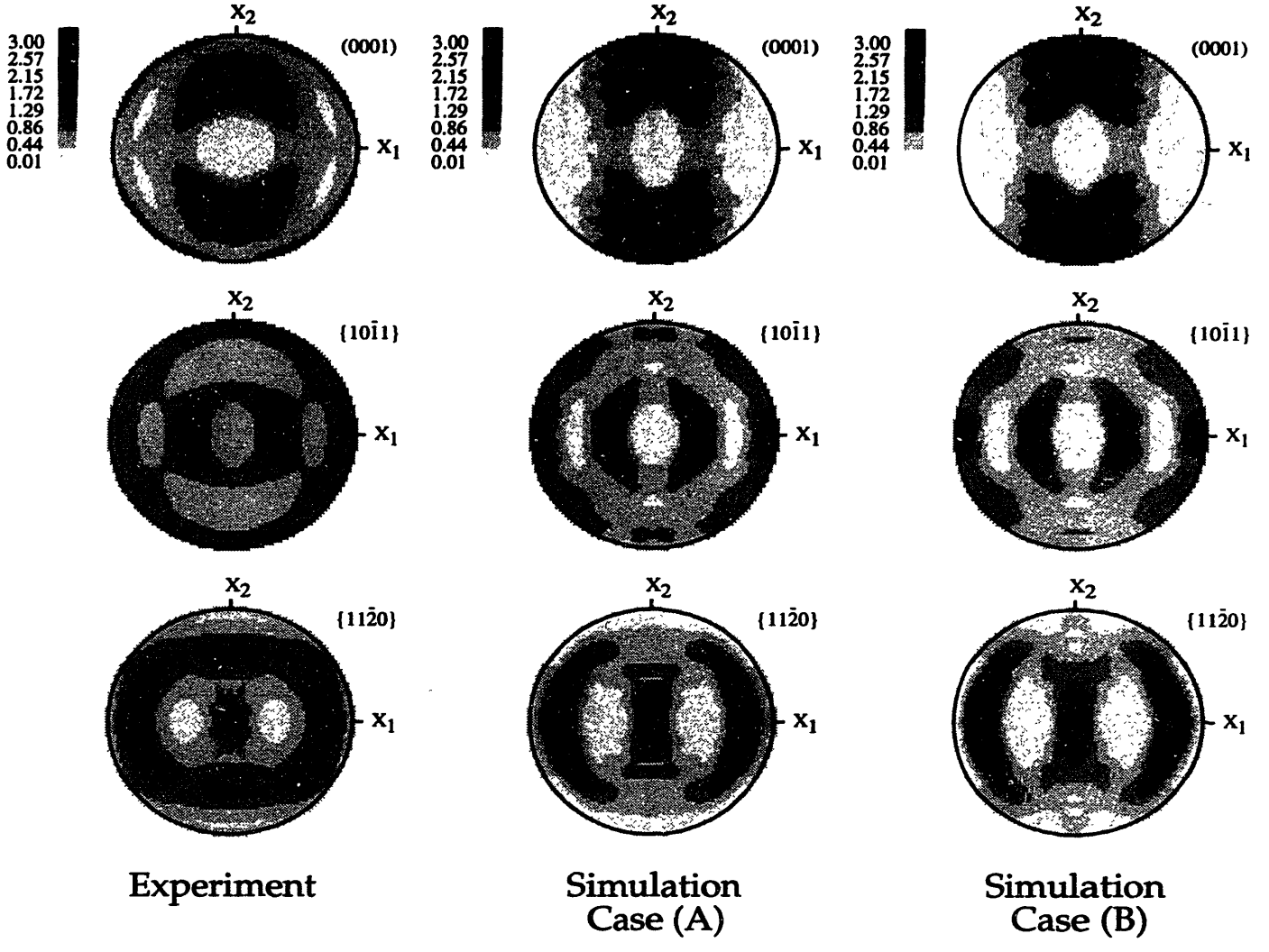

Figure 4-29: Experimentally measured texture after simple compression to $\epsilon = -1$ and calculated texture with two different assumpations for the slip systems.

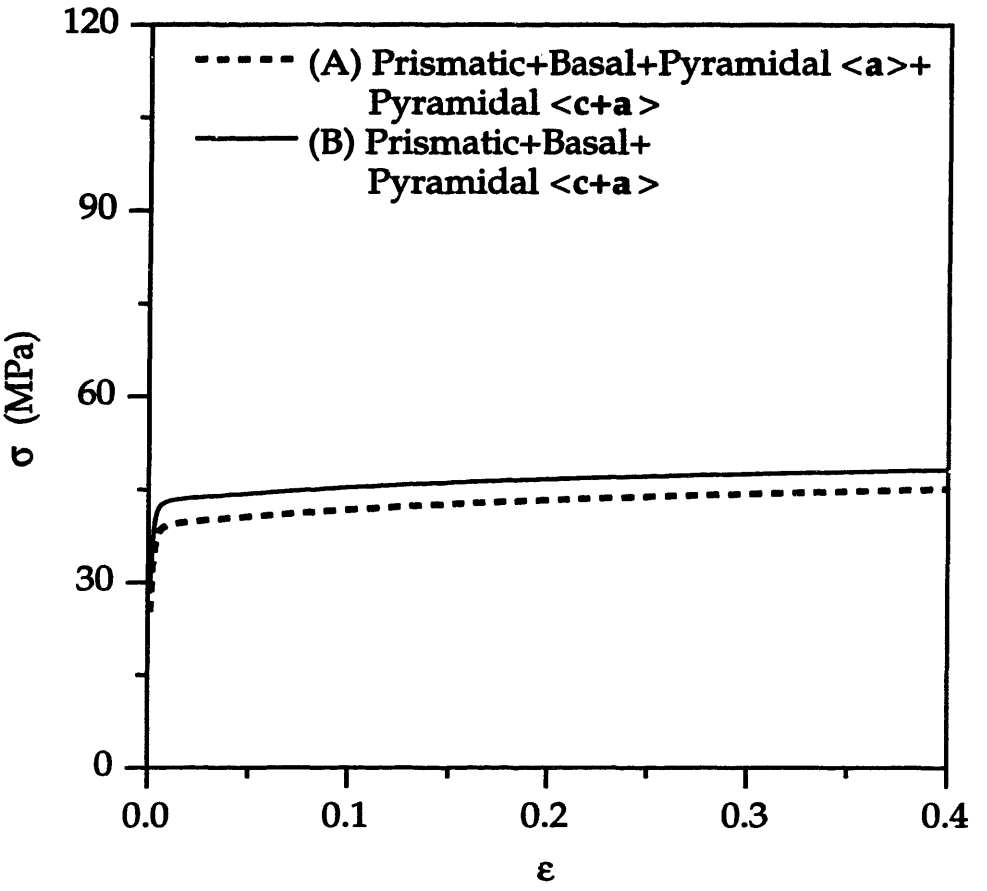

Figure 4-30: Stress-strain curves from simple tension simulation for the non-hardening case with two different assumptions for the slip systems.

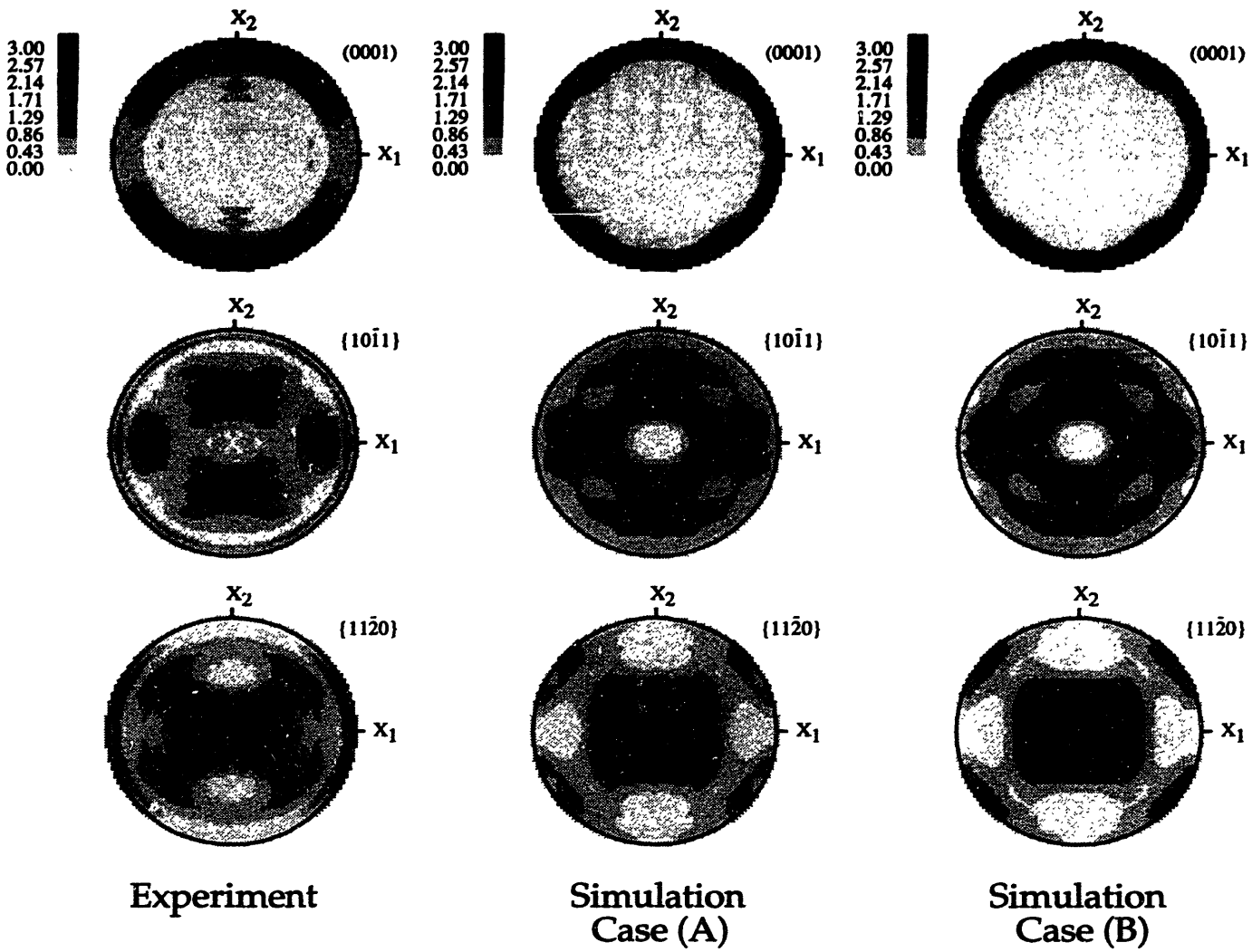

Figure 4-31: Experimentally measured texture after simple tension to $\epsilon = 0.3$ and calculated texture with two different assumpations for the slip systems.

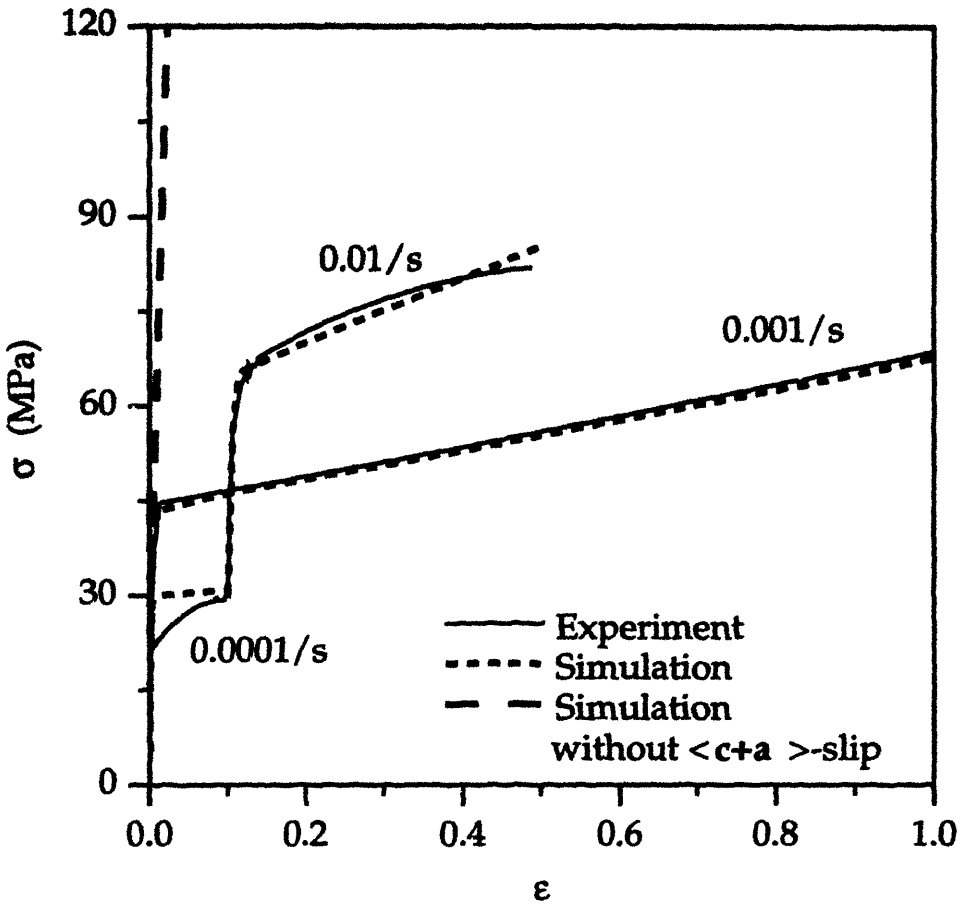

Figure 4-32: Experimentally measured stress-strain response in simple compression and strain-rate jump tests and the corresponding numerical fits from the simulation. The figure also shows the calculated stress-strain repsonse for simple compression in the absence of $< \mathbf{c}+\mathbf{a} >$ slip.

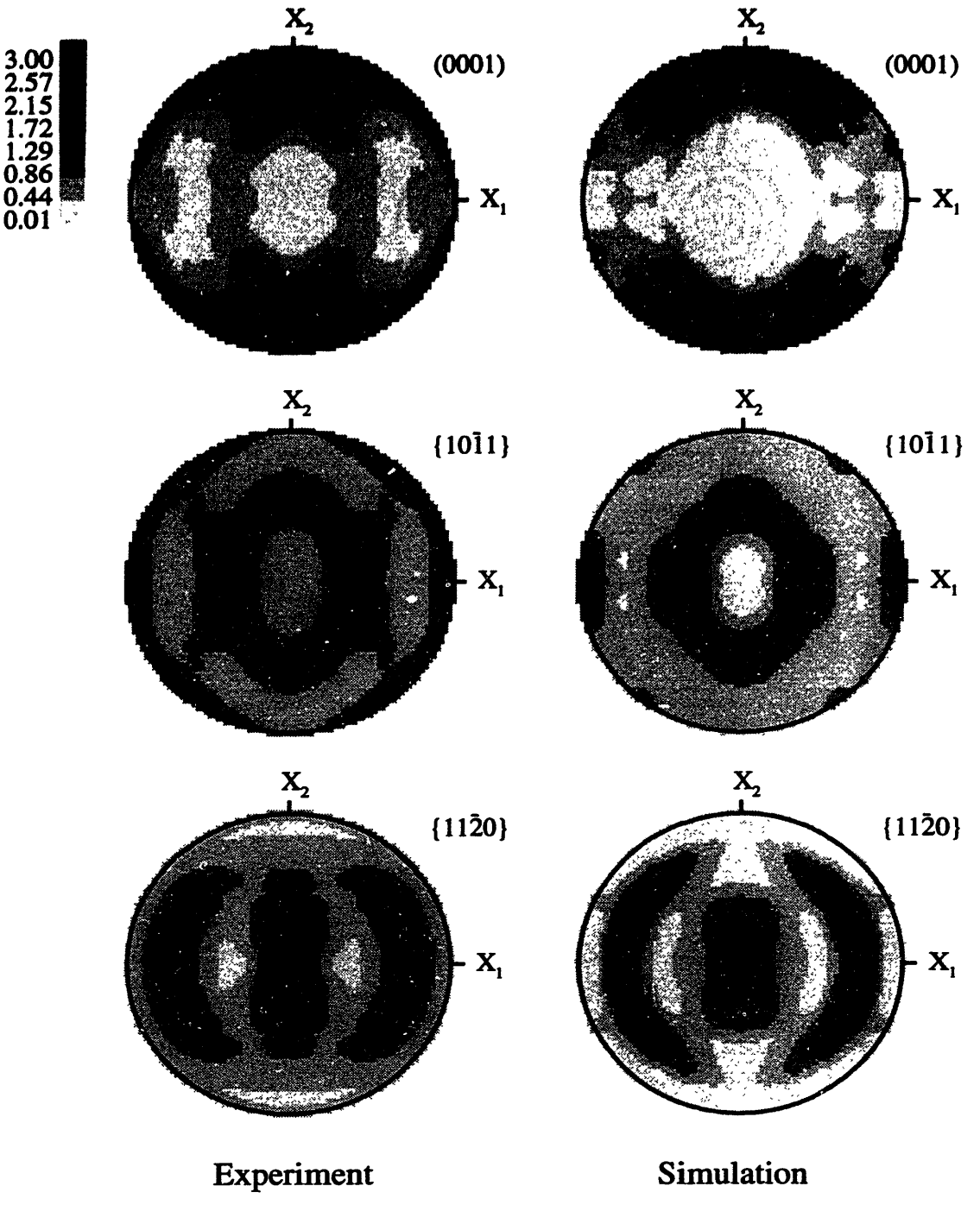

Figure 4-33: Comparison of the experimentally measured texture after simple compression to $\epsilon = -0.5$ with the texture predicted by the finite element model.

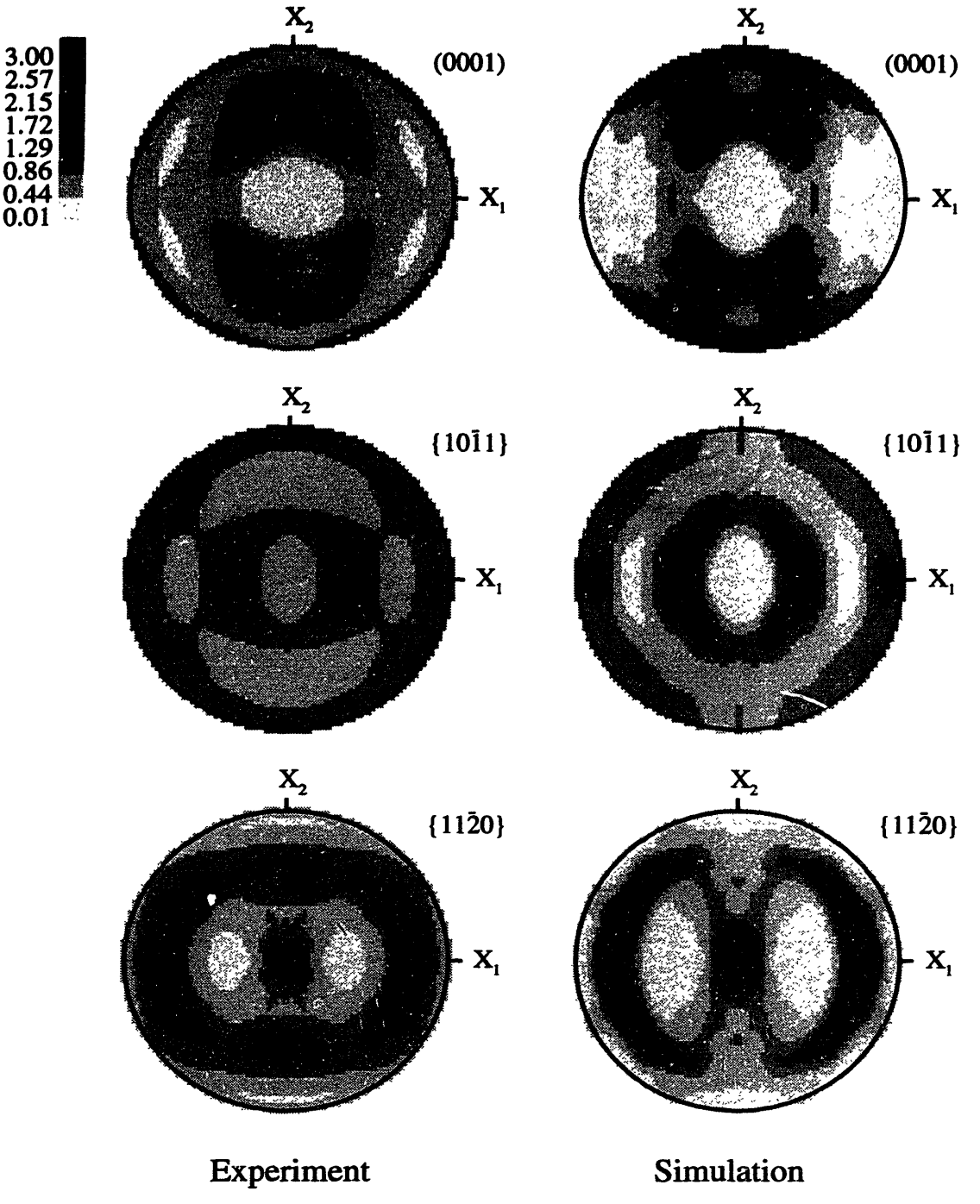

Figure 4-34: Comparison of the experimentally measured texture after simple compression to $\epsilon = -1.0$ with the texture predicted by the finite element model.

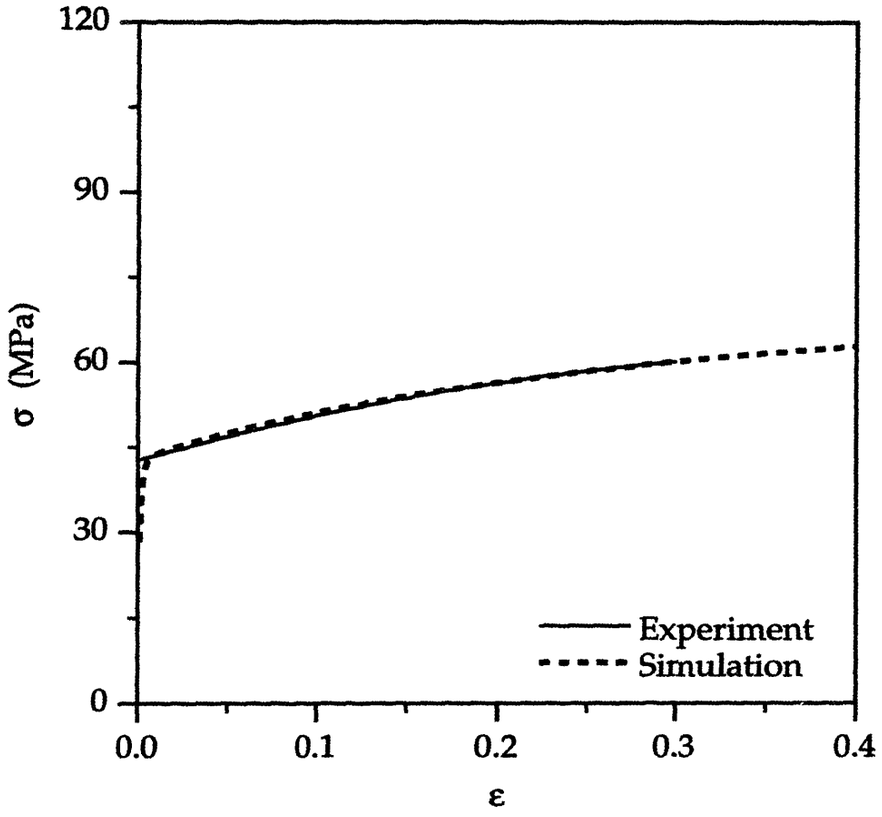

Figure 4-35: Comparison of the experimentally measured stress-strain response in simple tension with the numerical prediction.

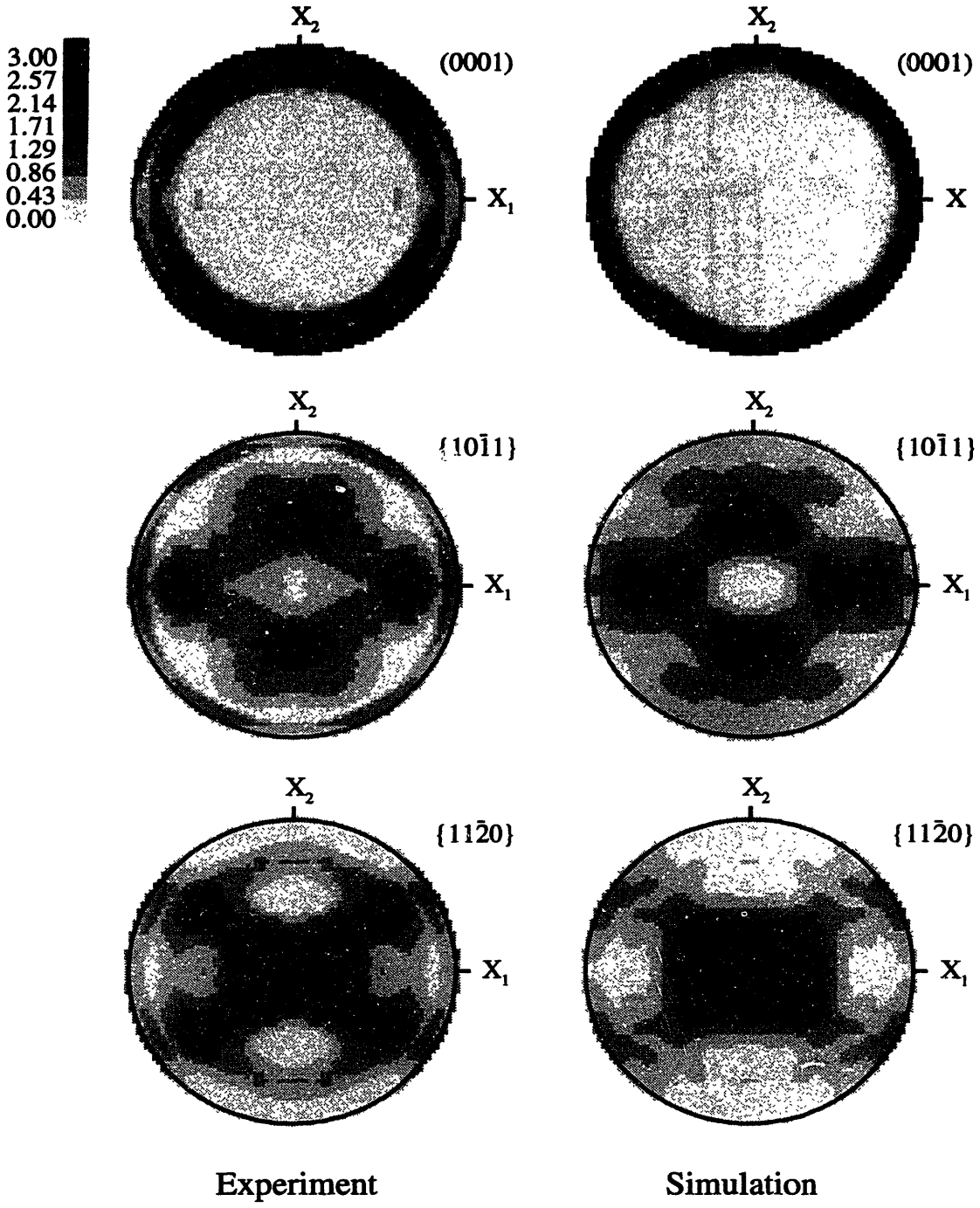

Figure 4-36: Comparison of the experimentally measured texture after simple tension to $\epsilon = 0.2$ with the texture predicted by the finite element model.

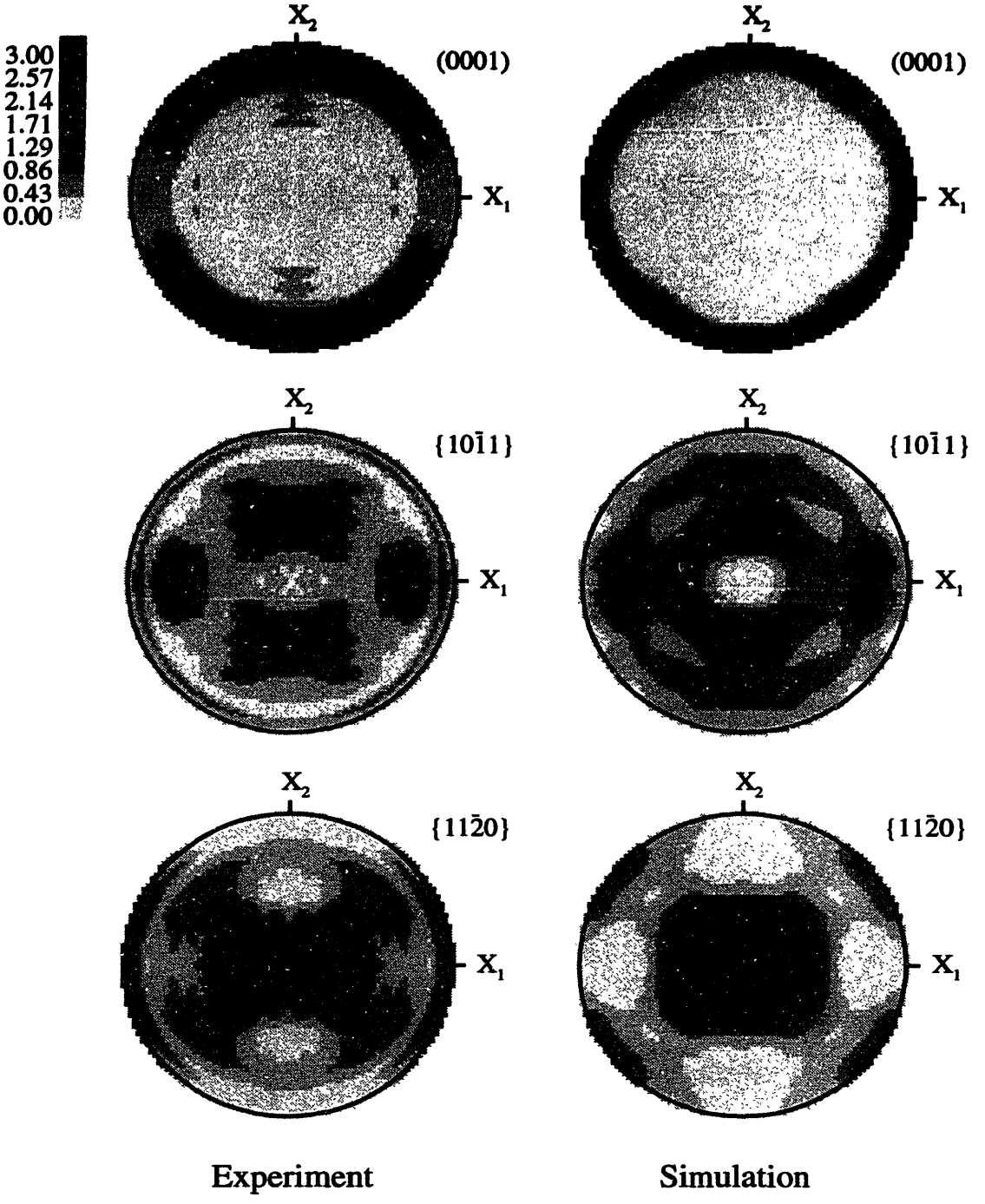

Figure 4-37: Comparison of the experimentally measured texture after simple tension to $\epsilon = 0.3$ with the texture predicted by the finite element model.

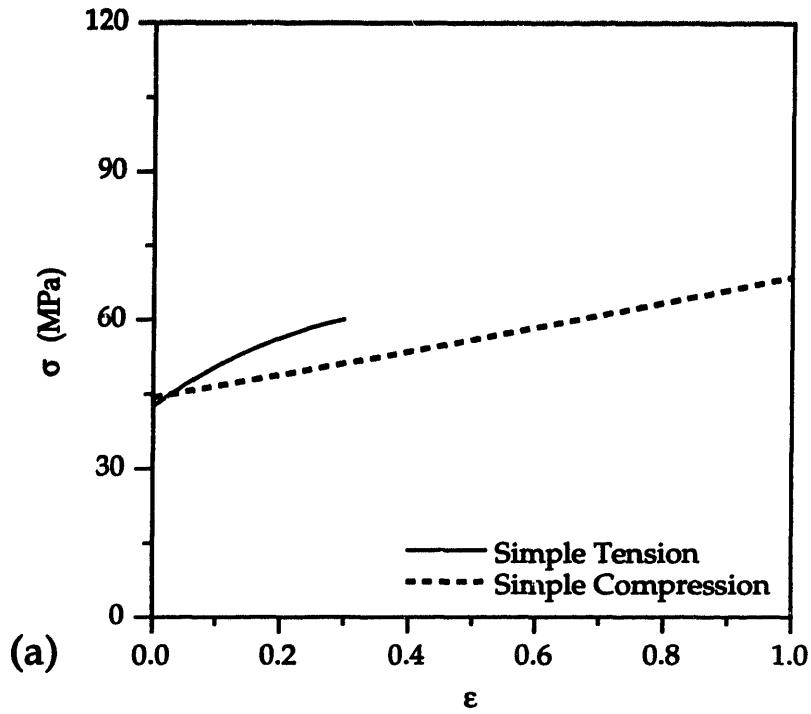

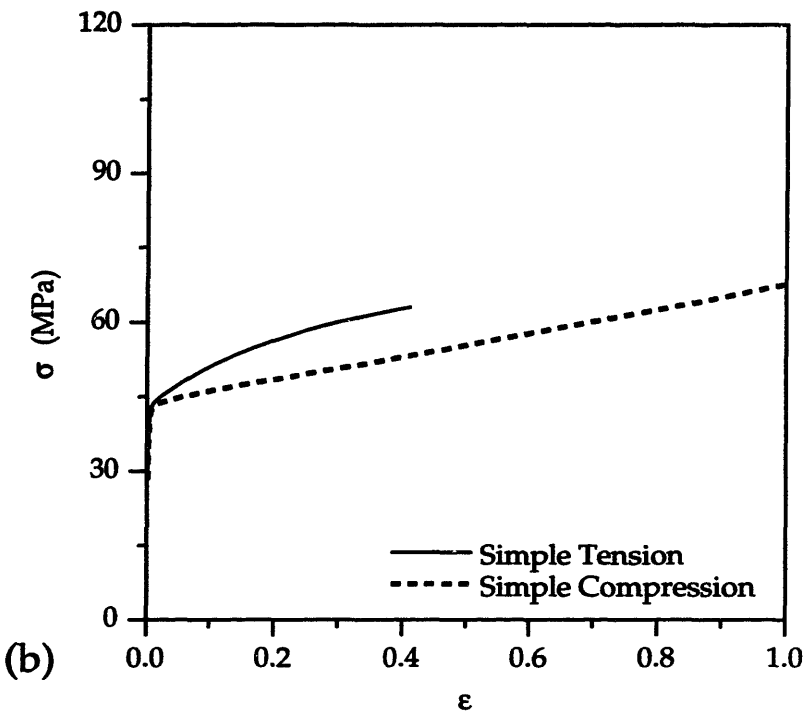

Figure 4-38: (a) Measured stress-strain response for simple compression and tension. (b) Simulation using the finite element model.

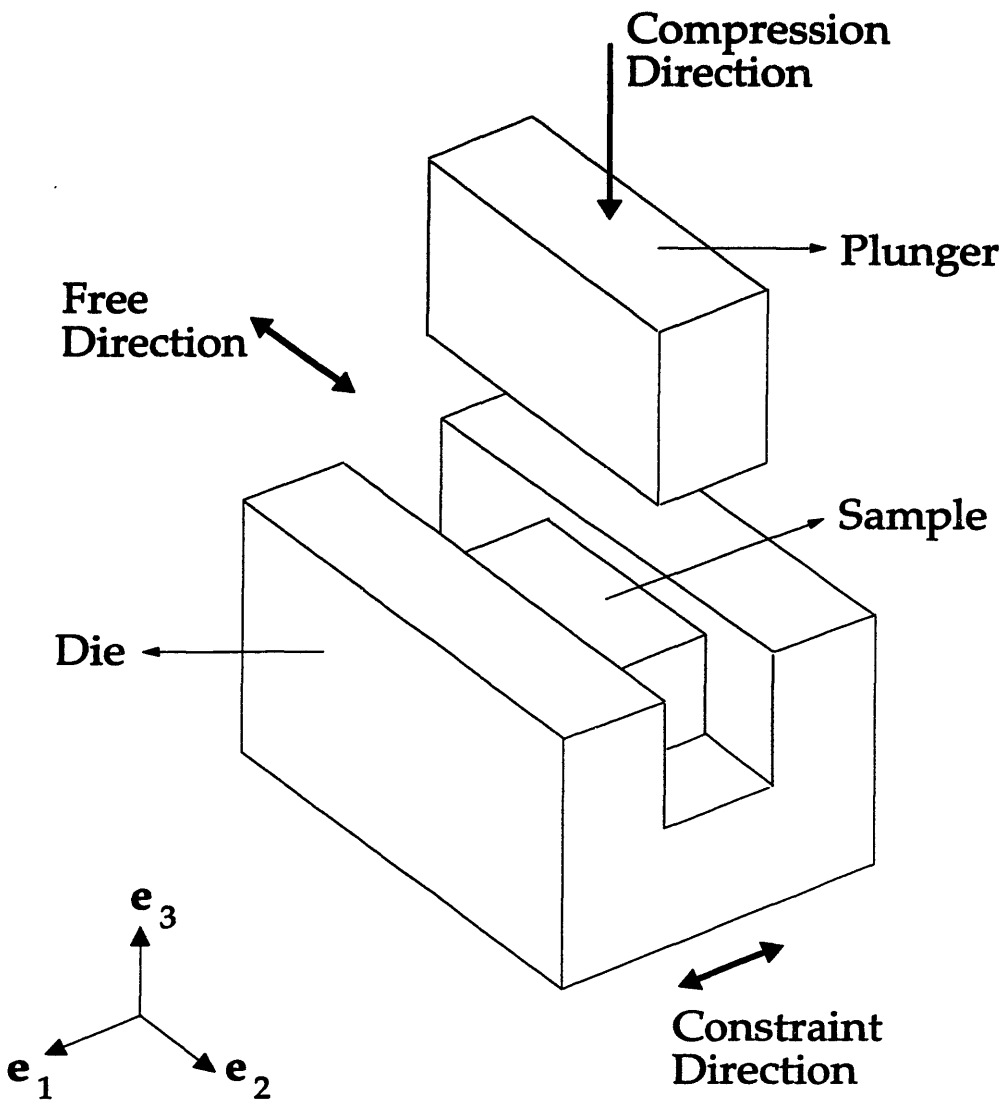

Figure 4-39: Schematic of the plane-strain compression apparatus.

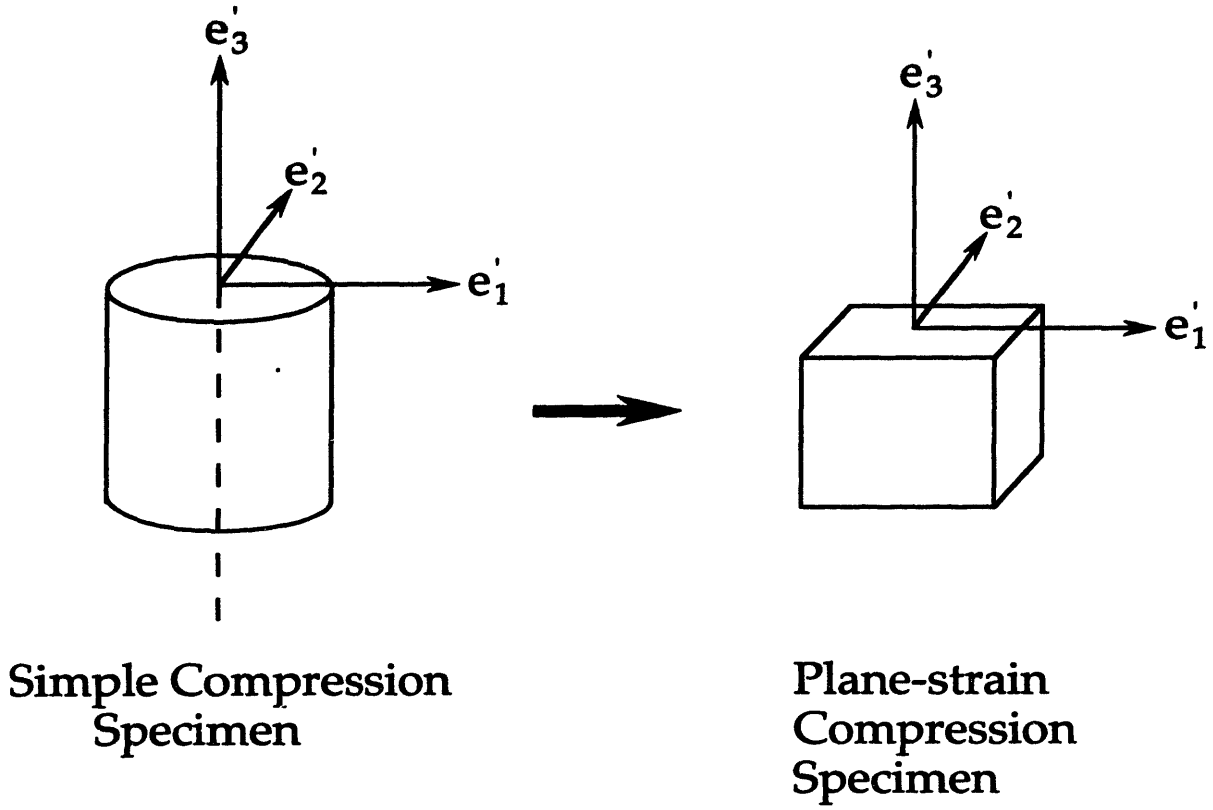

Figure 4-40: Schematic illustrating the orientation of the material axes in the plane-strain compression specimens and its relation to that in the simple compression specimen.

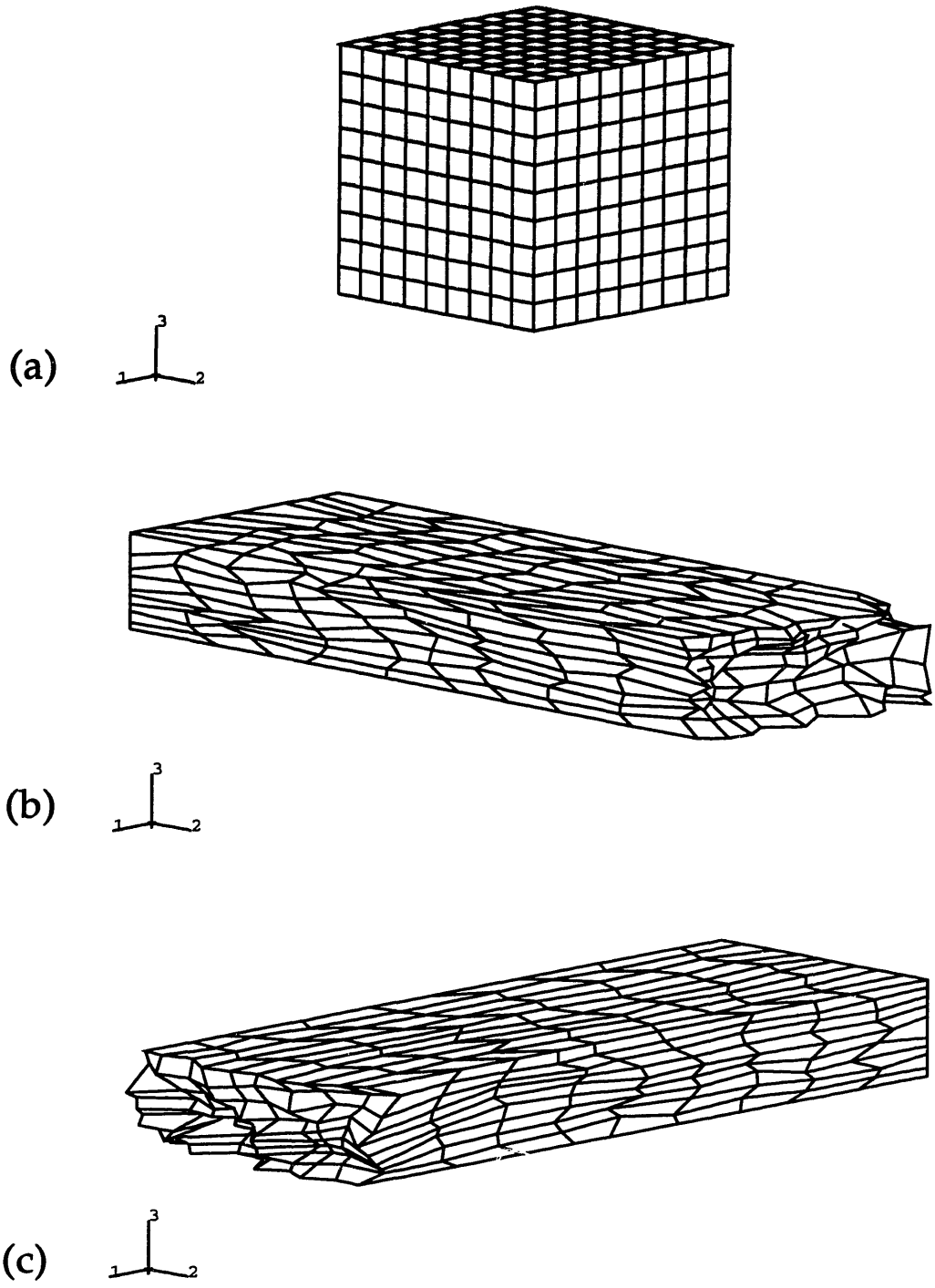

Figure 4-41: Initial and deformed finite element meshes in the plane-strain compression simulations : (a) Initial finite element mesh. (b) Deformed mesh at $\epsilon = -0.9$ for the case with $\mathbf{e}'_1$ as the constraint direction. (c) Deformed mesh at $\epsilon = -0.9$ for the case with $\mathbf{e}'_2$ as the constraint direction.

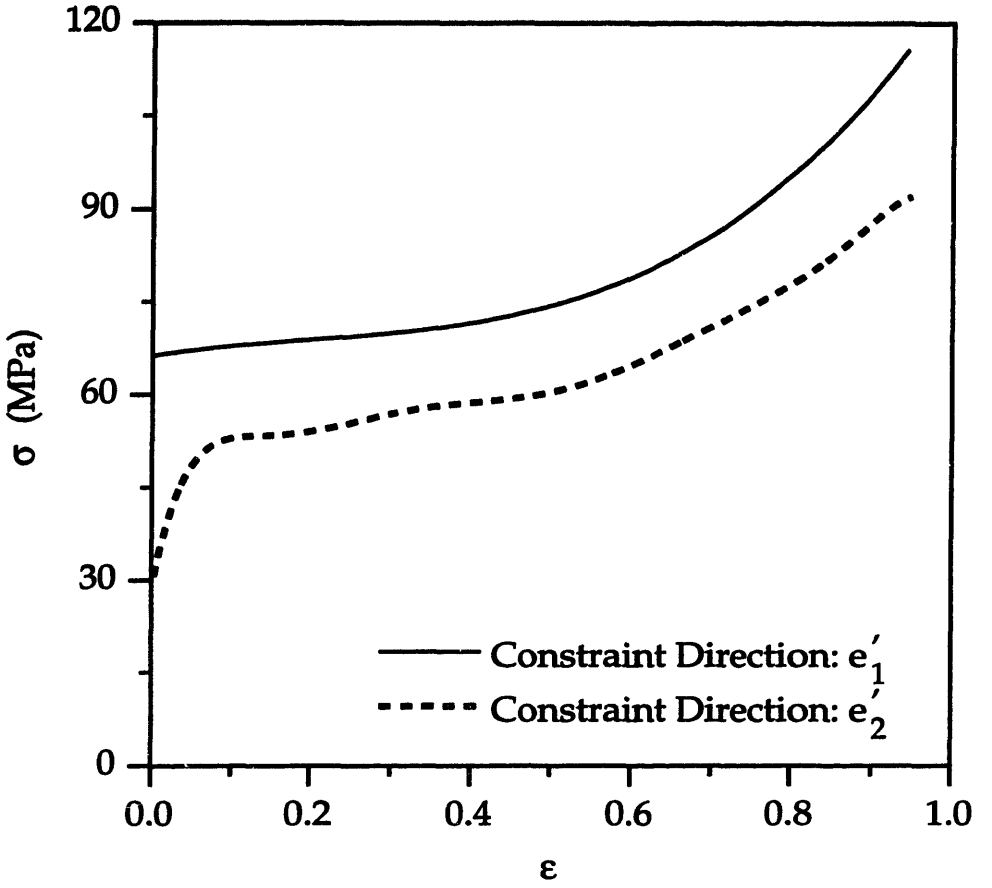

Figure 4-42: Experimentally measured stress-strain response during plane-strain compression of CP-Titanium at 750°C.

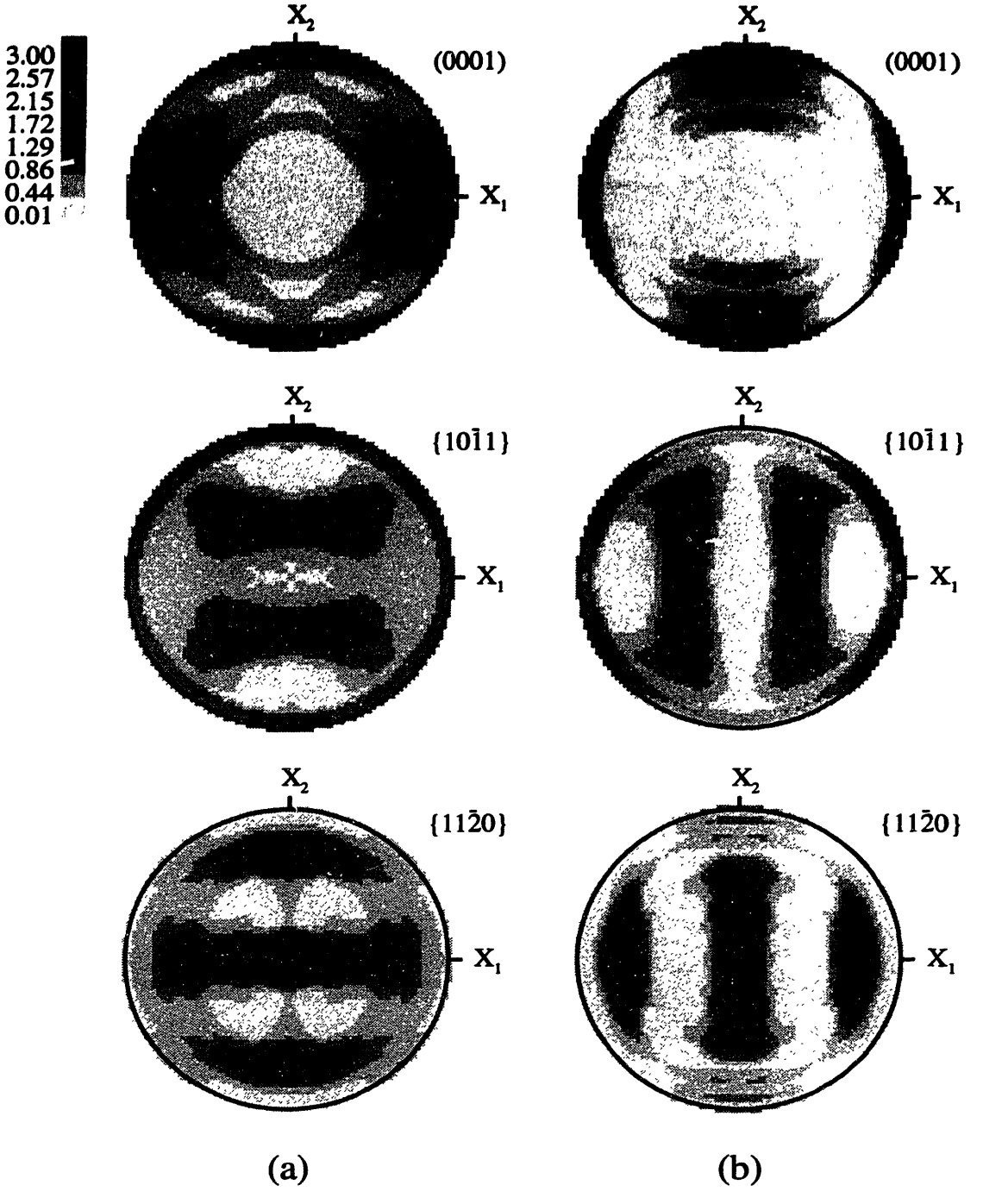

Figure 4-43: Experimentally measured crystallographic texture at $\epsilon = -0.9$ in CP-Titanium deformed in plane-strain compression at 750°C with: (a) $\mathbf{e}_1'$ as the constraint direction and (b) $\mathbf{e}_2'$ as the constraint direction.

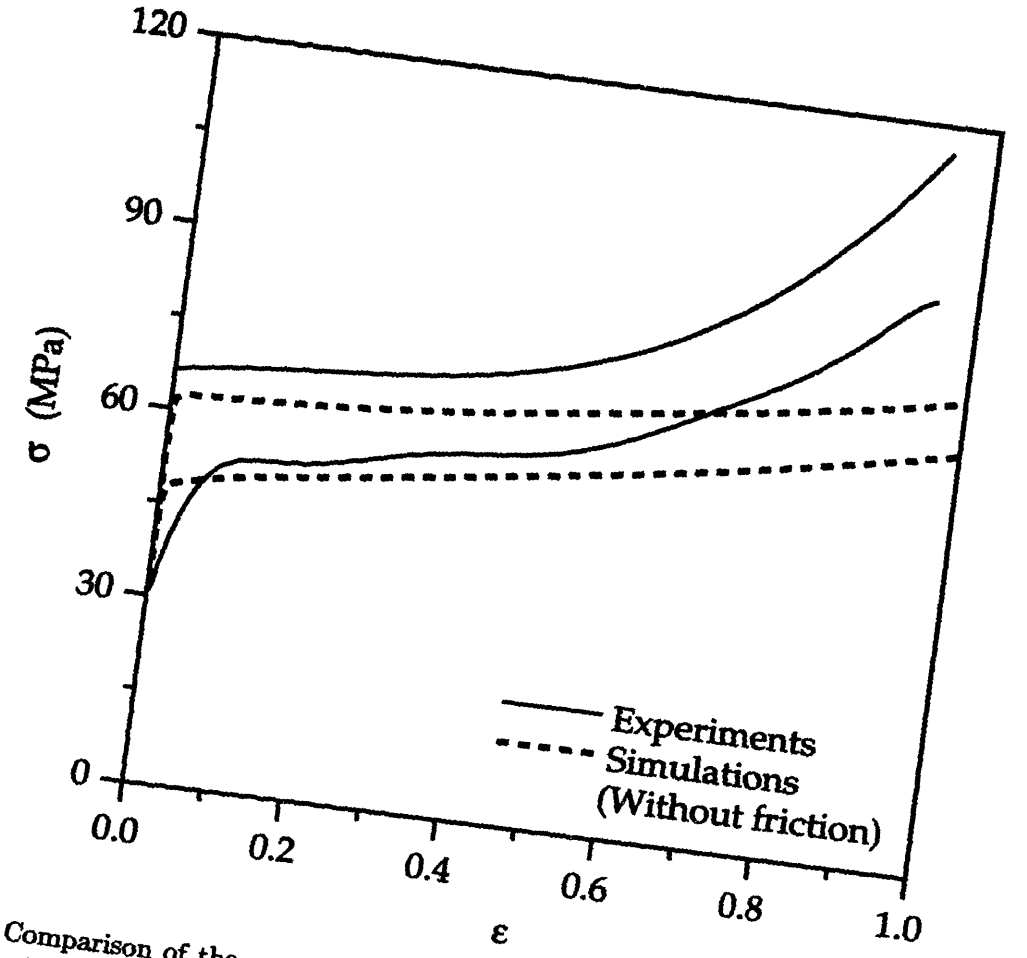

Figure 4-44: Comparison of the experimentally measured stress-strain response in plane-strain compression with the numerical predictions assuming no friction between contacting surfaces.

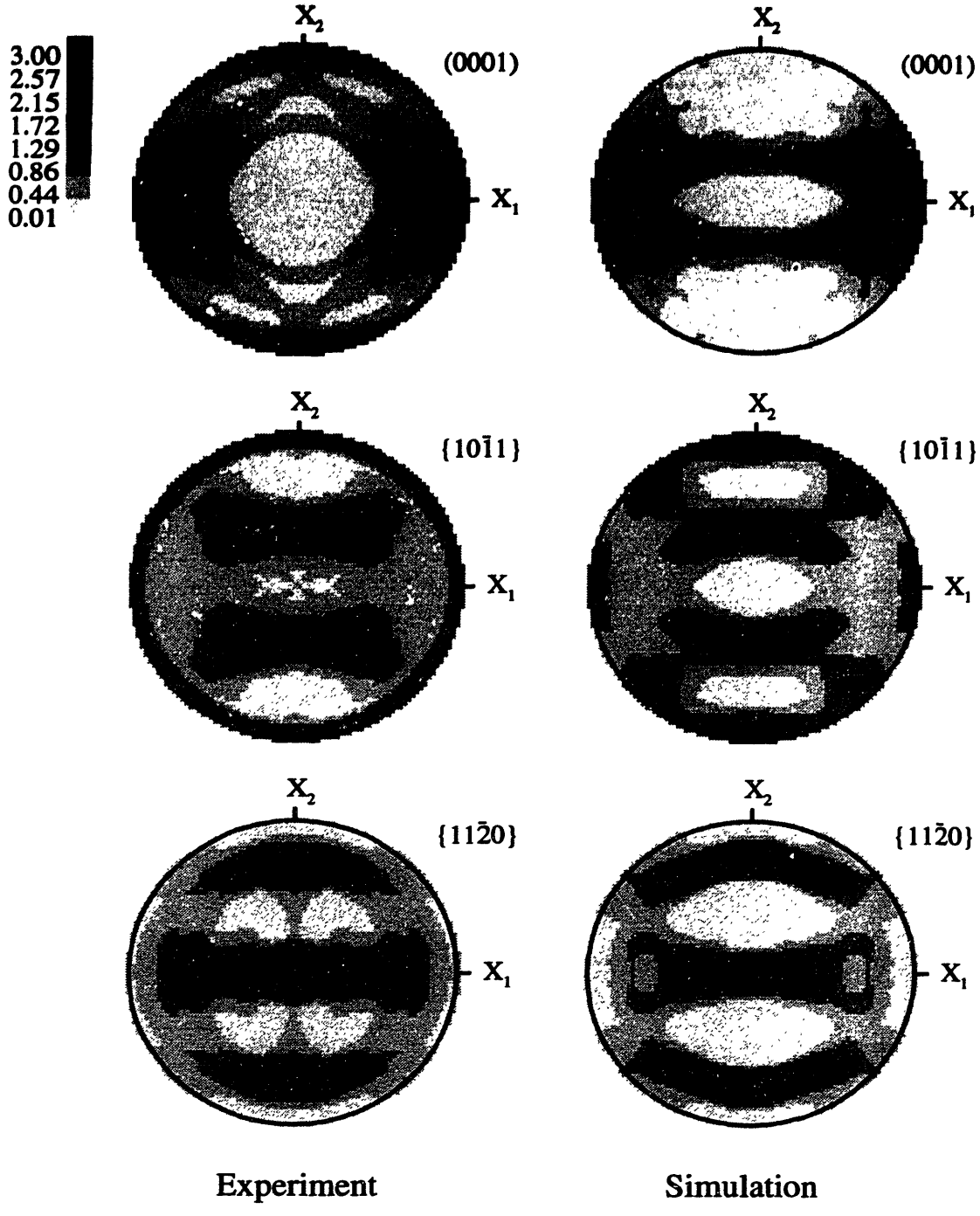

Figure 4-45: Experimentally measured texture after plane-strain compression to $\epsilon = -0.9$ with $\mathbf{e}'_1$ as the constraint direction and the corresponding texture predicted by the finite element model assuming no friction between contacting surfaces.

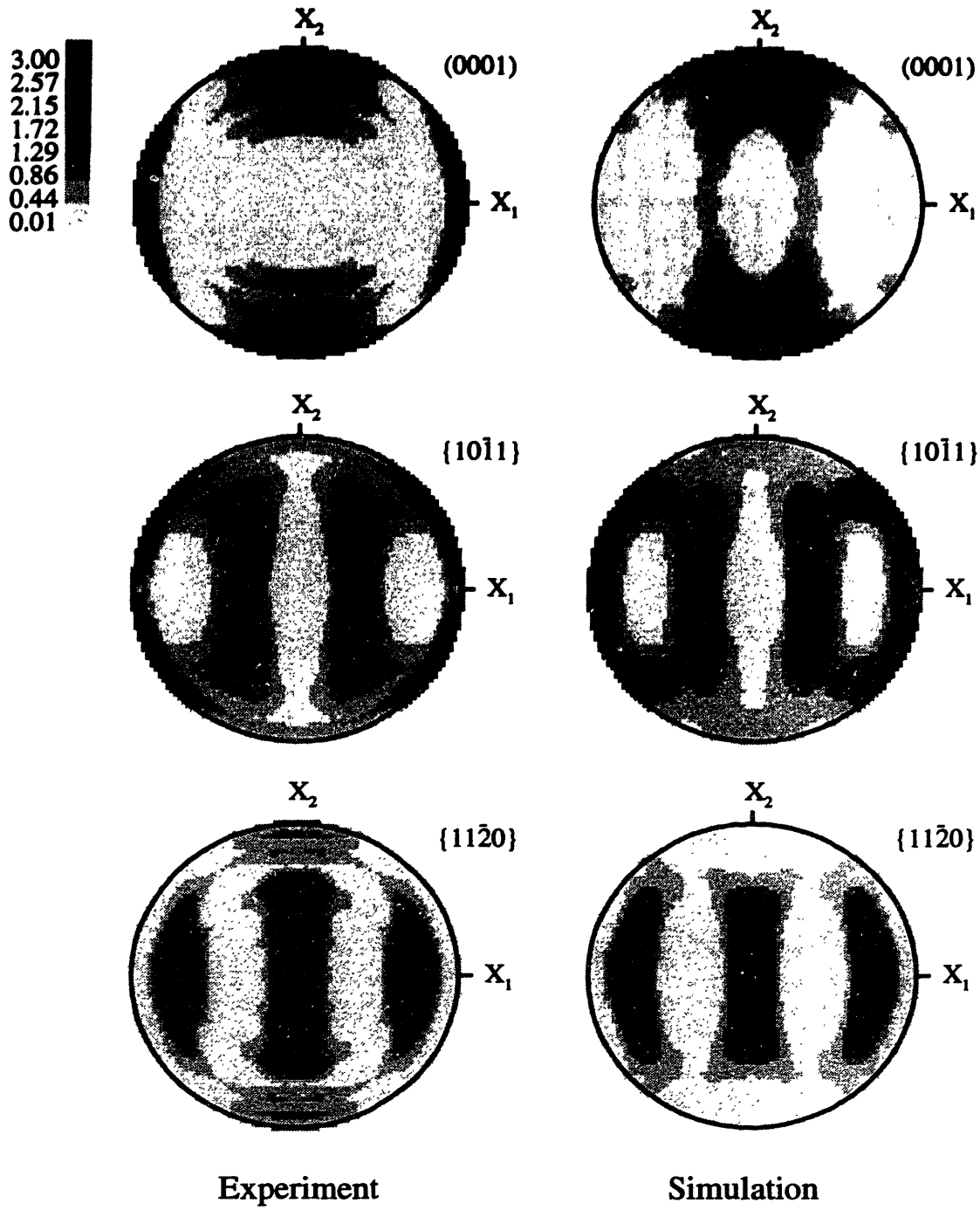

Figure 4-46: Experimentally measured texture after plane-strain compression to $\epsilon = -0.9$ with $\mathbf{e}_2'$ as the constraint direction and the corresponding texture predicted by the finite element model assuming no friction between contacting surfaces.

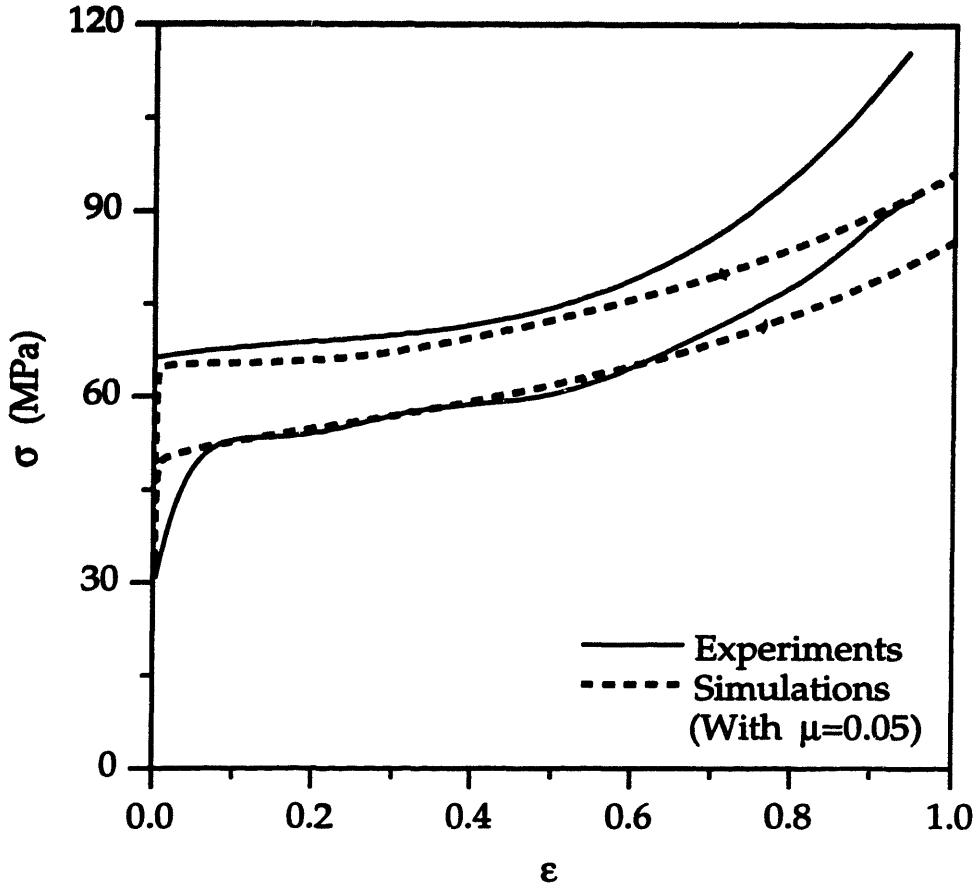

Figure 4-47: Comparison of the experimentally measured stress-strain response in plane-strain compression with the numerical predictions assuming a friction coefficient of $\mu = 0.05$ between contacting surfaces.

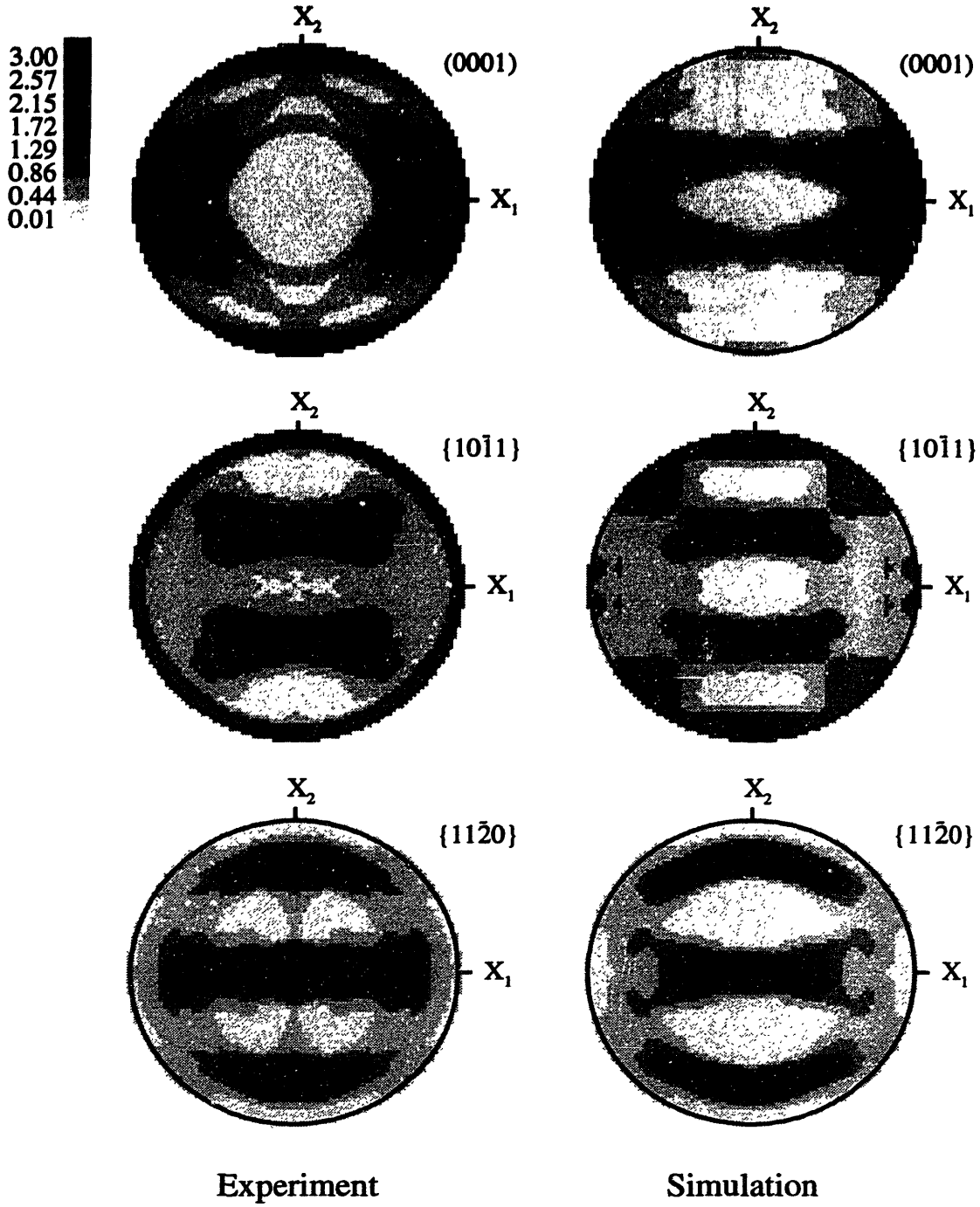

Figure 4-48: Experimentally measured texture after plane-strain compression to $\epsilon = -0.9$ with $\mathbf{e}_1'$ as the constraint direction and the corresponding texture predicted by the finite element model assuming a friction coefficient of $\mu = 0.05$ between contacting surfaces.

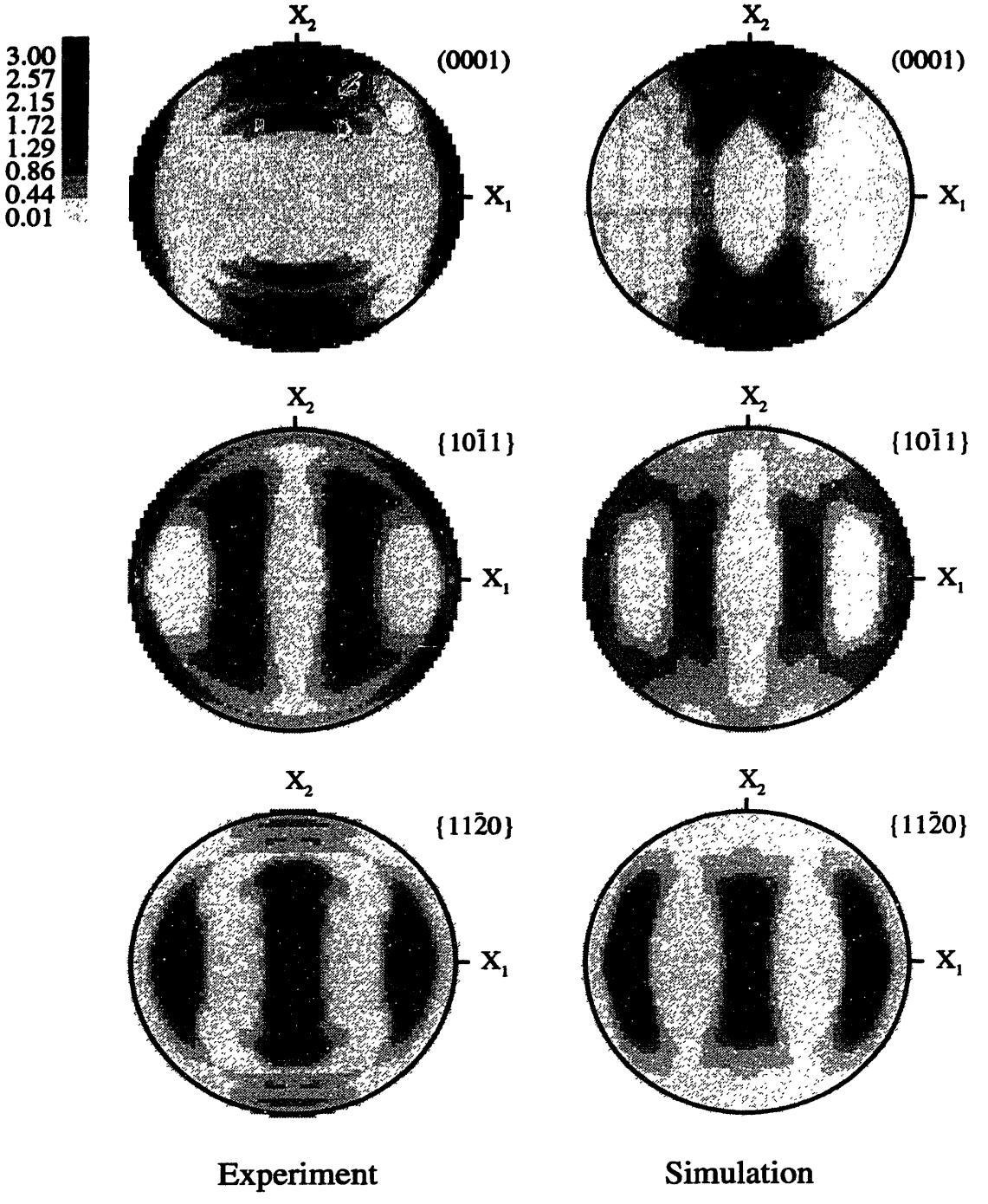

Figure 4-49: Experimentally measured texture after plane-strain compression to $\epsilon = -0.9$ with $\mathbf{e}_2'$ as the constraint direction and the corresponding texture predicted by the finite element model assuming a friction coefficient of $\mu = 0.05$ between contacting surfaces.

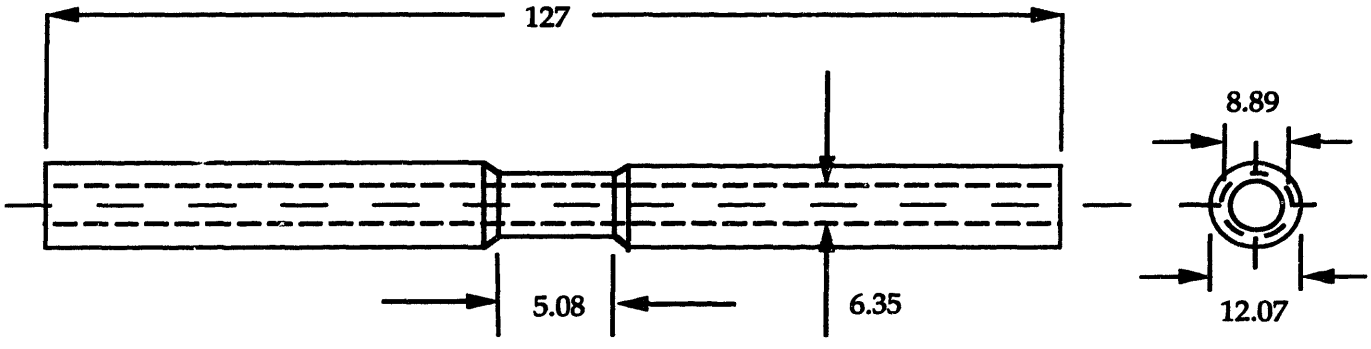

Figure 4-50: Geometry of tubular-torsion specimen (All dimensions are in millimeters).

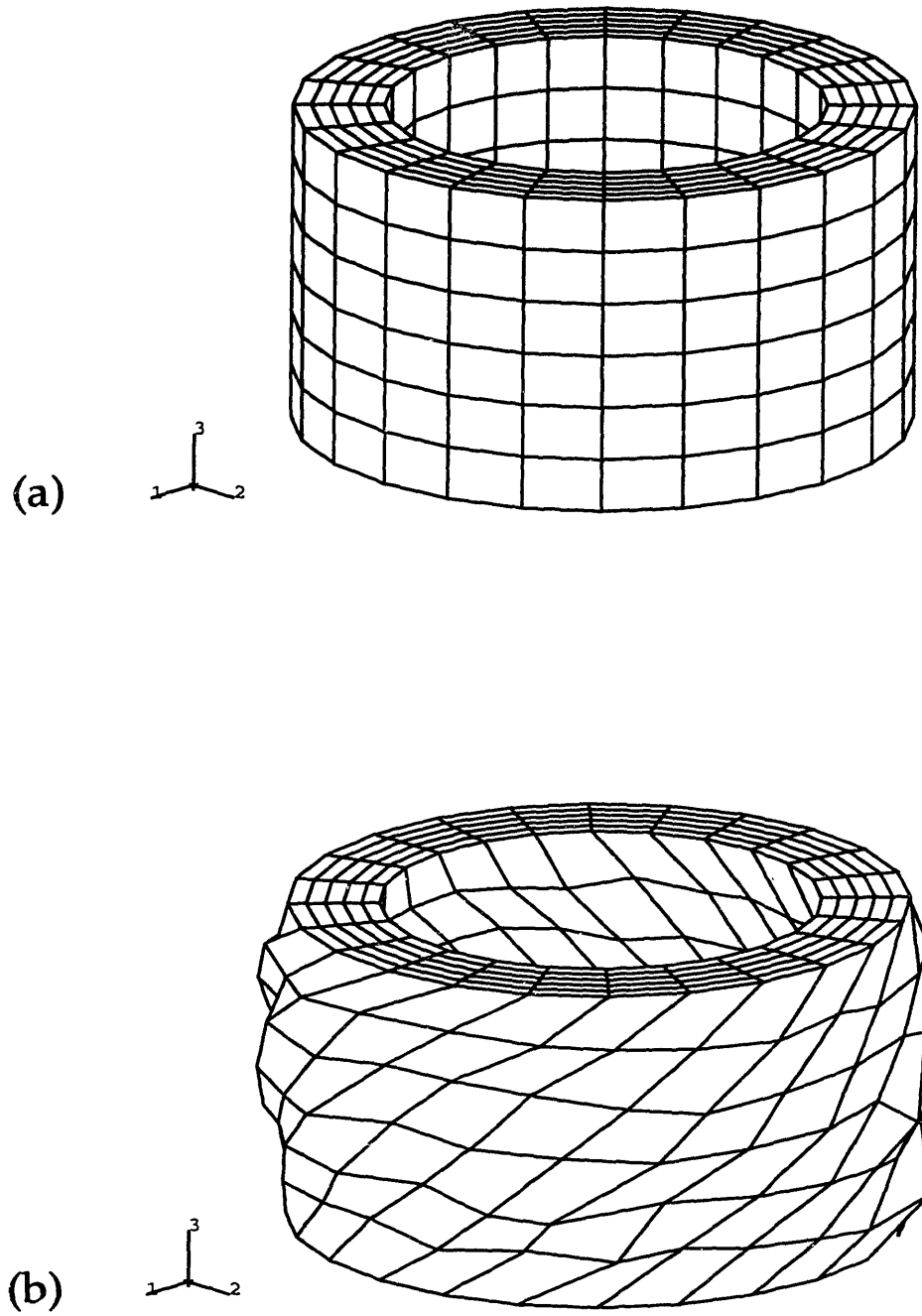

Figure 4-51: Initial and deformed finite element meshes in tubular torsion simulation: (a) Initial finite element mesh (b) Deformed mesh at $\gamma = 1$.

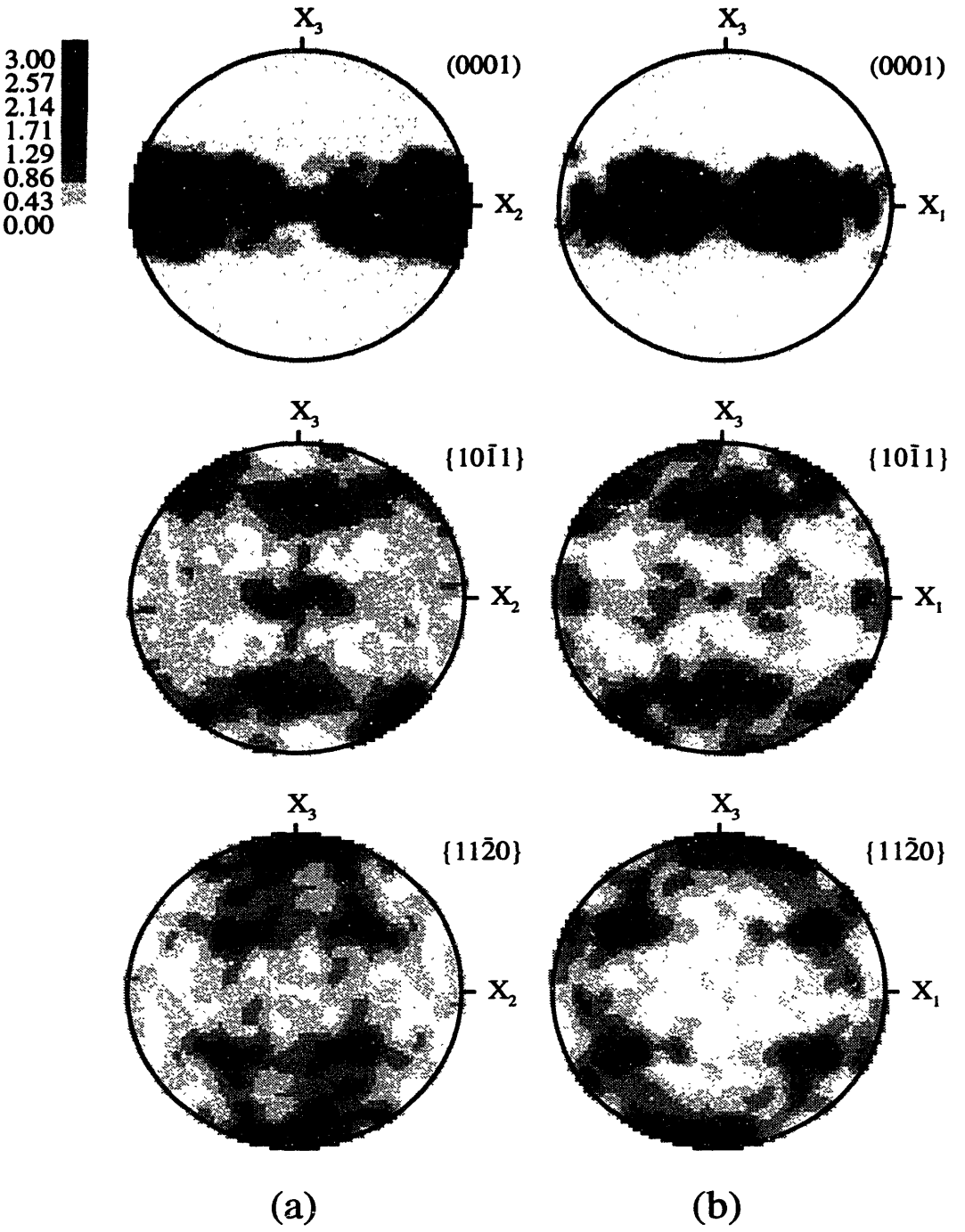

Figure 4-52: Initial pole-figures in the tubular torsion specimen measured perpendicular to: (a) 2-3 plane of the specimen (b) 1-3 plane of the specimen.

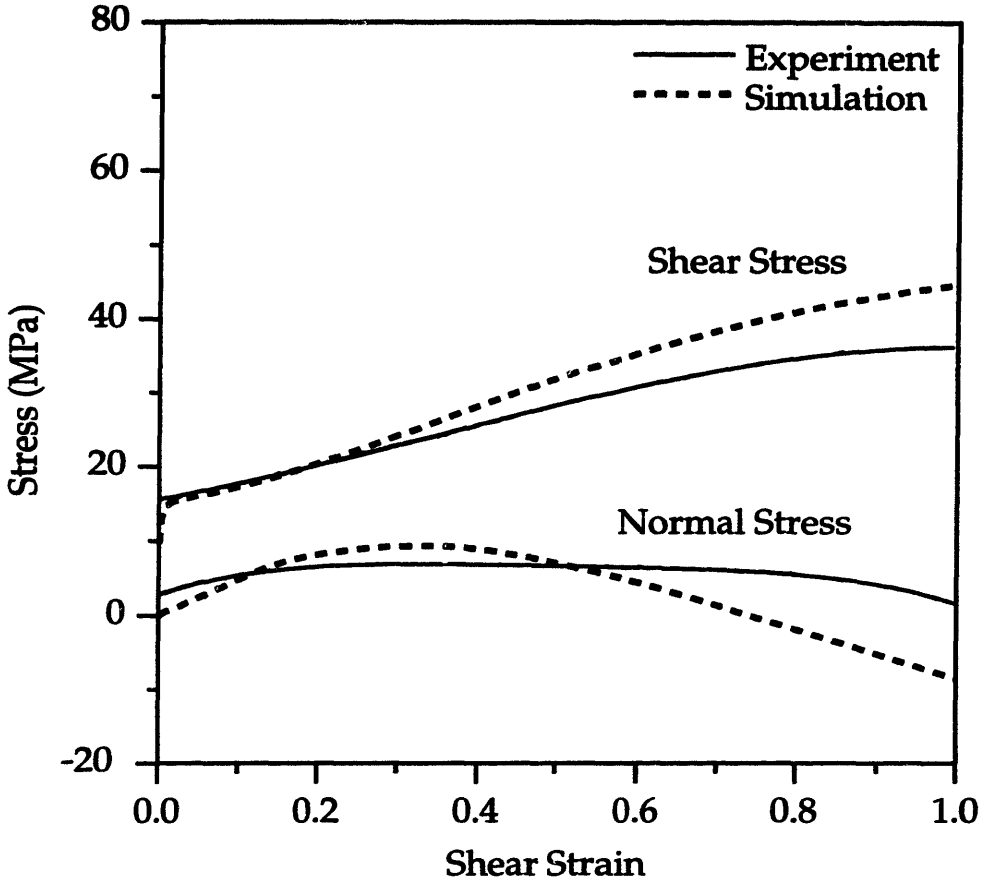

Figure 4-53: Comparison of the experimentally measured shear stress-shear strain res ponse and normal stress-shear strain response in tubular torsion with the predictions from the finite element model.

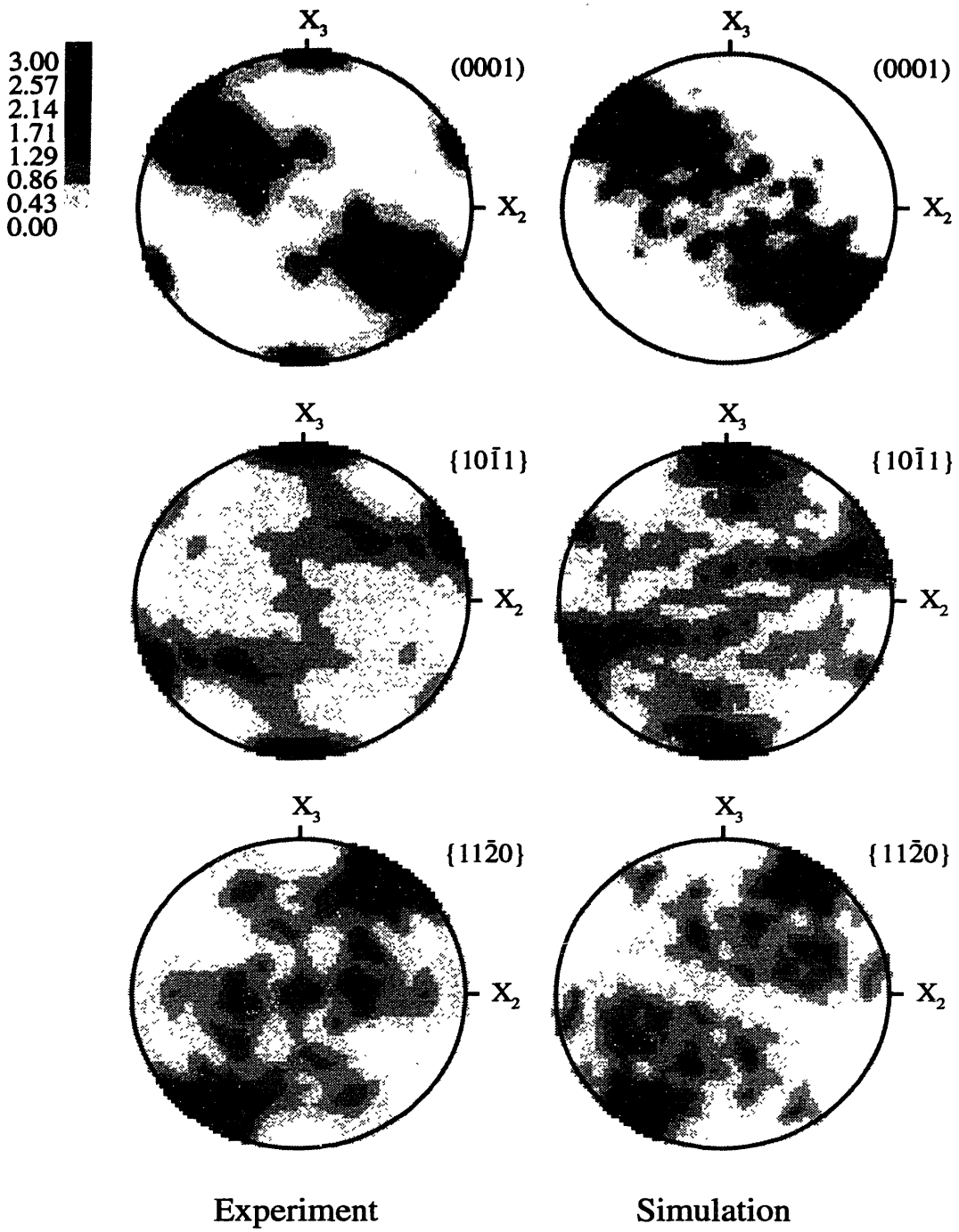

Figure 4-54: Experimentally measured texture after tubular torsion to $\gamma = 1$ and the corresponding texture predicted by the finite element model.

Chapter 5

Conclusions

A reasonably successful physically-based model for polycrystalline plasticity of face-centered-cubic materials has been developed. The model is essentially an extension of the previous work by Anand and co-workers (Kalidindi *et al.* [1992], Bronkhorst *et al.* [1992], Kalidindi *et al.* [1994]). The simple power-law relation for the plastic flow is replaced by a more physically-motivated constitutive function based on the thermally-activated theory of plastic flow (Kocks *et al.* [1976], Argon [1995]). The constitutive equations have been implemented in both "static,implicit" and "dynamic,explicit" finite element programs. The physical description for the plastic flow enables the the model to reproduce the macroscopic stress-strain response and the crystallographic texture evolution up to large strains ($\approx$ 100%) for a wide range of strain-rates (10^{-3} - 10^{2} sec^{-1}) and temperatures (77 - 298 K). The material parameters in the model have been determined by calibrating it against existing experimental data for aluminum (Duffy [1974], Senseny *et al.* [1978], and Carreker and Hibbard [1957]). The predictive capability of the model has been evaluated by comparing its predictions for the macroscopic stress-strain response and texture evolution in simple compression and plane-strain compression for two temperatures, 77K and 298K, with corresponding experimental results on Al1100-O. The predictions are in reasonable agreement with the experiments. The important differences in the behavior of f.c.c. and b.c.c. materials with regards to strain hardening and strain-rate and temperature history effects are also captured by the model. The predictions of the stress-strain repsonse compare well with existing experimental data on strain-rate and temperature jump tests (Dorn *et al.* [1949], Lopatin *et al.* [1992]).

In order to evaluate the applicability of the crystal plasticity model to actual deformation processing operations, the phenomenon of formation of earing defects in cup-drawing has been studied. Cup-drawing experiments were carried out on aluminum 2008-T4 sheets. The predictions of the model of the load-displacement response, the number of ears, their locations, and heights are in very good quantitative agreement with the experiments. This capability could serve as a design and analysis tool for cup-drawing and related sheet-metal forming applications.

A large deformation, crystal-plasticity based constitutive model for high-temperature deformation of titanium is presented. The constitutive model and the computational procedures have been implemented in a finite-element scheme. Quasi-static simple-compression, simple-tension and plane-strain compression experiments have been conducted on commercially-pure titanium at 750°C, and the resulting macroscopic stress-strain response and evolution in crystallographic texture have been measured. Full 3D finite element simulations of these deformation modes have been carried out and comparison of the predictions from the same against corresponding experiments shows the model to be reasonably accurate. To the best of our knowledge, this is the first-time a combined experimental and computational effort of this nature has been carried out to study the deformation of hexagonal materials.

5.1 Suggestions for Future Work

The following are some suggestions for future areas of research:

- Twinning is an important mode of plastic deformation in hexagonal materials at room temperature. The incorporation of twinning in a rate-dependent crystal plasticity model would facilitate the study of deformation processing of h.c.p. materials at room temperature. For a recent rate-independent crystal plasticity model for incorporating both crystallographic slip and twinning, see Staroselsky and Anand [1997]

- For polycrystalline materials of the low symmetry crystal structure, the Taylor-type averaging procedure does not work well. Other types of polycrystalline averaging schemes such as the self-consistent method (Hutchinson [1977]) and the constrained-hybrid method (Parks and Ahzi [1990]) have been developed for this situation.

There is a need to evaluate the applicability of these schemes to high-temperature deformation of h.c.p. titanium.

- Other details of microstructure such as porosity, localized shear bands, etc. and their evolution need to be incorporated in the constitutive model. Such details are necessary in order to predict failure during deformation processing.

Appendix A

Time Integration Procedures

The time-integration procedure for a Taylor-type polycrystal model[1] may be stated as follows. Let $\tau = t + \Delta t$. Then, given

(1) $\mathbf{F}(t)$, $\mathbf{F}(\tau)$, $\theta(t)$, $\theta(\tau)$

(2) $(\mathbf{m}_0^\alpha, \mathbf{n}_0^\alpha)$ — time independent quantities, for each grain,

(3) $\{\mathbf{F}^p(t),\ s^\alpha(t),\ \mathbf{T}(t)\}$ in each grain,

calculate

(a) $\{\mathbf{F}^p(\tau),\ s^\alpha(\tau),\ \mathbf{T}(\tau)\}$ for each grain,

(b) volume averaged macroscopic stress $\bar{\mathbf{T}}(\tau)$,

(c) texture $\left\{\mathbf{m}^\alpha(\tau)^{(k)}, \mathbf{n}^\alpha(\tau)^{(k)}\right\}$ at time τ. and march forward in time.

The computational procedures for items (a), (b) and (c) depend on the nature of the finite element procedure adopted. Fully-implicit Euler-backward schemes are employed for the "static,implicit" finite element procedure. For the "dynamic,explicit" finite element procedure, the computation of the time-integration steps are performed through a simple Euler-forward scheme. In the following, the computational methodology for each of these finite-element procedures is described.

A.1 Implicit Finite Element Procedure

For the computation of the list of variables in (a), the computing scheme of Kalidindi *et. al* [1992] is adopted:-

[1]The time-integration procedure for a single crystal model is obtained simply by setting the number of crystals in the Taylor-aggregate to be one.

(*i*) Compute

$$\mathbf{A} \equiv \mathbf{F}^{p^{-T}}(t)\,\mathbf{F}^{T}(\tau)\,\mathbf{F}(\tau)\,\mathbf{F}^{p^{-1}}(t), \tag{A.1}$$

$$\mathbf{T}^{*tr} \equiv \mathcal{C}\left[\frac{1}{2}\{\mathbf{A}-\mathbf{1}\}\right], \tag{A.2}$$

$$\mathbf{B}^{\alpha} \equiv \mathbf{A}\mathbf{S}_0^{\alpha} + \mathbf{S}_0^{\alpha^T}\mathbf{A}, \tag{A.3}$$

$$\mathbf{C}^{\alpha} \equiv \mathcal{C}\left[\frac{1}{2}\mathbf{B}^{\alpha}\right] \tag{A.4}$$

where $\mathbf{S}_0^{\alpha} = (\mathbf{m}_0^{\alpha} \otimes \mathbf{n}_0^{\alpha})$.

(*ii*) Solve

$$\mathbf{T}^{*}(\tau) \doteq \mathbf{T}^{*tr} - \sum_{\alpha} \Delta\gamma^{\alpha}\mathbf{C}^{\alpha}, \tag{A.5}$$

$$s^{\alpha}(\tau) = s^{\alpha}(t) + \sum_{\beta} h^{\alpha\beta}(\tau)\left|\Delta\gamma^{\beta}\right|, \tag{A.6}$$

with

$$\Delta\gamma^{\alpha} \equiv \dot{\gamma}^{\alpha}(\tau)\,\Delta t, \tag{A.7}$$

for $\mathbf{T}^{*}(\tau)$ and $s^{\alpha}(\tau)$ using the following two-level iterative procedure.

In the first level of iterations, solve (A.5) for $\mathbf{T}^{*}(\tau)$, keeping $s^{\alpha}(\tau)$ fixed at its best available estimate using a Newton-type iterative algorithm as follows:

$$\mathbf{T}^{*}_{n+1}(\tau) = \mathbf{T}^{*}_{n}(\tau) - \mathcal{J}_n^{-1}[\mathbf{G}_n], \tag{A.8}$$

where

$$\mathbf{G}_n \equiv \mathbf{T}^{*}_{n}(\tau) - \mathbf{T}^{*tr} + \sum_{\alpha} \Delta\gamma^{\alpha}\left(\mathbf{T}^{*}_{n}(\tau), s^{\alpha}_{k}(\tau)\right)\mathbf{C}^{\alpha}, \tag{A.9}$$

$$\mathcal{J}_n \equiv \mathcal{I} + \sum_{\alpha} \mathbf{C}^{\alpha} \otimes \frac{\partial}{\partial \mathbf{T}^{*}_{n}(\tau)}\,\Delta\gamma^{\alpha}\left(\mathbf{T}^{*}_{n}(\tau), s^{\alpha}_{k}(\tau)\right), \tag{A.10}$$

where the subscripts n and $n+1$ refer to estimates of $\mathbf{T}^{*}(\tau)$ at the end of n and $n+1$ iterations respectively, in the first level of the iterative scheme. The second level of the iterative procedure involves a simple update (without iterations) of $s^{\alpha}(\tau)$ using

$$s^{\alpha}_{k+1} = s^{\alpha}(t) + \sum_{\beta} h^{\alpha\beta}\left(s^{\beta}_{k}(\tau)\right)\left|\Delta\gamma^{\beta}\left(\mathbf{T}^{*}_{n+1}(\tau), s^{\beta}_{k}(\tau)\right)\right|, \tag{A.11}$$

where the subscript k refers to the value of $s^{\alpha}(\tau)$ at the end of the k^{th} update in the second level of the iterative scheme.

In the rate-independent limit of plastic flow, *i.e.*, for small values of $\frac{k_B\theta}{\Delta F^*}$, the set of equations (A.5) becomes very stiff and it becomes necessary to apply constraints to the Newton corrections (A.8) in the first level of the iterative procedure. In this work, the following constraint procedure has been adopted:

Let

$$|\Delta\gamma^{\alpha}|_{\max}(\tau) = \max_{\alpha}|\Delta\gamma^{\alpha}(\tau)| \tag{A.12}$$

If

$$|\Delta\gamma^{\alpha}|_{\max} < \Delta\gamma_{\text{tol}}, \tag{A.13}$$

then accept the Newton correction, else

$$(T^*_{ij})_{n+1}(\tau) = (T^*_{ij})_n(\tau) + \eta\ \Delta T^*_{ij}, \tag{A.14}$$

where η is a small factor. A value of η of 0.25 was found to give good results in the calculations in this study.

(*iii*) Compute

$$\mathbf{F}^p(\tau) \doteq \left\{1 + \sum_{\alpha} \Delta\gamma^{\alpha}\mathbf{S}^{\alpha}_o\right\}\mathbf{F}^p(t). \tag{A.15}$$

It was necessary to normalize $\mathbf{F}^p(\tau)$ by dividing the computed values of each of its components by the cube root of the computed determinant so as to ensure that the determinant of $\mathbf{F}^p(\tau)$ is unity.

(*iv*) Compute

$$\mathbf{T}(\tau) = \frac{1}{\det\mathbf{F}(\tau)}\mathbf{F}(\tau)\mathbf{F}^{p^{-1}}(\tau)\mathbf{T}^*(\tau)\mathbf{F}^{p^{-T}}(\tau)\mathbf{F}^T(\tau) \tag{A.16}$$

After calculating the Cauchy stress in each crystal $\mathbf{T}(\tau)$, the macroscopic stress in (b) is obtained by a simple volume-average,

$\bar{\mathbf{T}} = \sum_{k=1}^{N} v_k\ \mathbf{T}^{(k)}$,

The texture at time τ is evaluated as follows:

$$\mathbf{m}^{\alpha}(\tau)^{(k)} \;=\; \mathbf{F}^e(\tau)\mathbf{m}^{\alpha}_o = \mathbf{F}(\tau)\mathbf{F}^{p^{-1}}(\tau)\mathbf{m}^{\alpha}_o,$$

$$\mathbf{n}^{\alpha}(\tau)^{(k)} \;=\; \mathbf{F}^{e^{-T}}(\tau)\mathbf{n}_o^{\alpha} = \mathbf{F}^{-T}(\tau)\mathbf{F}^{p^{T}}(\tau)\mathbf{n}_o^{\alpha},$$

The time-stepping for the implicit finite element procedure is automatically controlled based on the maximum value of the slip increment. A parameter $R = \frac{\Delta\gamma^{\alpha}_{\max}}{\Delta\gamma_{\lim}}$ is used as a measure for controlling time-increments where $\Delta\gamma^{\alpha}_{\max}$ is the maximum value of $\Delta\gamma^{\alpha}$ over all the crystals and all the integration points in the finite element mesh and $\Delta\gamma_{\lim}$ is a prescribed value of slip increment based on the desired accuracy. A value of $\Delta\gamma_{\lim} = 0.02$ was found to give good results in this work. If the value of R is greater than 1 then the time-step is repeated with a time increment, $\Delta t_{\text{new}} = \frac{1}{2}\Delta t_{\text{old}}$. If $0.5 < R < 1$, the value of the time-increment is maintained and if $R < 0.5$, the time-increment is doubled *i.e.*, $\Delta t_{n+1} = 2\Delta t_n$. The efficiency and speed of the scheme depends on the rate- sensitivity of the material. The equations (A.5) become stiffer in the rate-independent limit requiring more iterations to solve for the stresses.

A.2 Explicit Finite Element Procedure

(*i*) Calculate

$$\mathbf{F}^{p^{-1}}(\tau) \doteq \mathbf{F}^{p^{-1}}(t)\{\mathbf{1} - \sum_{\alpha} \Delta\gamma^{\alpha}(t)\mathbf{S}_0^{\alpha}\} \tag{A.17}$$

$$\mathbf{F}^{e}(\tau) = \mathbf{F}(\tau)\mathbf{F}^{p^{-1}}(\tau) \tag{A.18}$$

$$\mathbf{E}^{e}(\tau) = \frac{1}{2}\{\mathbf{F}^{e}(\tau)^{T}\mathbf{F}^{e}(\tau) - \mathbf{1}\} \tag{A.19}$$

$$\mathbf{T}^{*}(\tau) = \mathcal{C}[\mathbf{E}^{e}(\tau)] \tag{A.20}$$

(*ii*) Compute the hardening modulii,

$$h^{\beta}(t) = h_0 \left|1 - \frac{s^{\beta}(t)}{s_s}\right|^{r} \operatorname{sign}\left\{1 - \frac{s^{\beta}(t)}{s_s}\right\} \tag{A.21}$$

$$h^{\alpha\beta}(t) = q^{\alpha\beta}h^{\beta}(t) \tag{A.22}$$

(*iii*) Calculate the slip system deformation resistances and the resolved shear stresses on each slip system at time τ

$$s^{\alpha}(\tau) = s^{\alpha}(t) + \sum_{\beta} h^{\alpha\beta}(\tau)\left|\Delta\gamma^{\beta}\right| \tag{A.23}$$

$$\tau^\alpha(\tau) = \mathbf{T}^*(\tau) \cdot \mathbf{S}_0^\alpha \tag{A.24}$$

(*iv*) Calculate the shear increments on the slip systems at time τ

$$\Delta\gamma^\alpha = \left\{ \begin{array}{ll} 0 & \text{if } \tau_*^\alpha \leq 0, \\ \dot{\gamma}_0^\alpha \Delta t \exp\left\{ -\frac{\Delta G_*^\alpha(\tau_*^\alpha, s_*^\alpha)}{k_B \theta} \right\} \operatorname{sign}(\tau^\alpha) & \text{if } 0 < \tau_*^\alpha < s_*^\alpha, \end{array} \right\} \tag{A.25}$$

A time-stepping scheme is not required for the explicit finite element procedure. The problem is solved with nearly equal increments in time subject only to slight variations due to changes in the stability limit arising from changes in the mesh geometry.

Appendix B

Analytical Jacobian for ABAQUS/Standard

An implicit finite element procedure employs a Newton-type iterative method for revising the estimates of the nodal displacements. This requires the evaluation of a Jacobian matrix that is consistent with the time-integration procedure used in the constitutive model. The fully implicit Euler-backward time integration scheme has been implemented in the finite element program ABAQUS/Standard [1996]. This program represents the symmetric Cauchy stress tensor $\mathbf{T}(\tau)$ and a symmetric relative strain tensor $\mathbf{E}_t(\tau)$[1] as vectors according to the following convention,

$$\mathbf{t} = \begin{bmatrix} T(\tau)_{11} \\ T(\tau)_{22} \\ T(\tau)_{33} \\ T(\tau)_{12} \\ T(\tau)_{13} \\ T(\tau)_{23} \end{bmatrix}, \mathbf{e} = \begin{bmatrix} E_t(\tau)_{11} \\ E_t(\tau)_{22} \\ E_t(\tau)_{33} \\ 2E_t(\tau)_{12} \\ 2E_t(\tau)_{13} \\ 2E_t(\tau)_{23} \end{bmatrix}, \tag{B.1}$$

[1]This relative strain increment is given as $\mathbf{E}_t(\tau) = \ln \mathbf{U}_t(\tau)$, where $\mathbf{U}_t(\tau)$ is the relative stretch obtained from the polar decomposition of the relative deformation gradient, $\mathbf{F}_t(\tau)$

where $T(\tau)_{ij}$ and $E_t(\tau)_{ij}$ are the components of the tensors $\mathbf{T}(\tau)$ and $\mathbf{E}_t(\tau)$, respectively. The Jacobian matrix required by ABAQUS is defined as,

$$\mathcal{W} = \frac{\partial \mathbf{t}}{\partial \mathbf{e}}. \tag{B.2}$$

The Cauchy stress tensor for the time $\tau = t + \Delta t$ is related to the second Piola-Kirchoff stress measure by,

$$\mathbf{T}(\tau) = \frac{1}{\det \mathbf{F}^e(\tau)} \left[\mathbf{F}^e(\tau) \mathbf{T}^*(\tau) \mathbf{F}^{e^T}(\tau) \right] \tag{B.3}$$

From (B.3) we obtain,

$$\mathrm{d}\mathbf{T} = \frac{1}{\det \mathbf{F}^e} \left[\mathrm{d}\mathbf{F}^e \mathbf{T}^* \mathbf{F}^{e^T} + \mathbf{F}^e \mathrm{d}\mathbf{T}^* \mathbf{F}^{e^T} + \mathbf{F}^e \mathbf{T}^* \mathrm{d}\mathbf{F}^{e^T} - (\mathbf{F}^e \mathbf{T}^* \mathbf{F}^{e^T}) \mathrm{tr}(\mathrm{d}\mathbf{F}^e \mathbf{F}^{e^{-1}}) \right] \tag{B.4}$$

In (B.4) all the variables are at time τ. In what follows, unless otherwise stated all variables are evaulated at time τ. Equation (B.2) can be rewritten in the indicial notation as follows,

$$\mathrm{d}T_{ij} = \mathcal{W}_{ijkl} \mathrm{d}E_{t,kl} \tag{B.5}$$

For convenience, let us define two fourth-rank tensors $\mathcal{S}$ and $\mathcal{Q}$ as,

$$\mathcal{S} = \frac{\partial \mathbf{F}^e}{\partial \mathbf{E}_t}; \; \mathcal{Q} = \frac{\partial \mathbf{T}^*}{\partial \mathbf{E}_t} \tag{B.6}$$

Rewriting (B.4) in the indicial notation and substituting (B.6) in this, we obtain the following expression for the Jacobian,

$$\mathcal{W}_{ijkl} = \frac{1}{\det \mathbf{F}^e} \left[\mathcal{S}_{imkl} T^*_{mn} F^{e^T}_{nj} + F^e_{im} \mathcal{Q}_{mnkl} F^{e^T}_{nj} + F^e_{im} T^*_{mn} \mathcal{S}_{jnkl} - F^e_{im} T^*_{mn} F^{e^T}_{nj} (\mathcal{S}_{pqkl} F^{e^{-1}}_{qp}) \right] \tag{B.7}$$

Note that $\mathcal{W}_{ijkl}$ in (B.7) can be reduced to the $\mathcal{W}_{IJ}$ form in (B.2) by the following

transformation,

$$\mathcal{W} = \begin{bmatrix} \mathcal{W}_{1111} & \mathcal{W}_{1122} & \mathcal{W}_{1133} & \frac{\mathcal{W}_{1112}+\mathcal{W}_{1121}}{2} & \frac{\mathcal{W}_{1113}+\mathcal{W}_{1131}}{2} & \frac{\mathcal{W}_{1123}+\mathcal{W}_{1132}}{2} \\ \mathcal{W}_{2211} & \mathcal{W}_{2222} & \mathcal{W}_{2233} & \frac{\mathcal{W}_{2212}+\mathcal{W}_{2221}}{2} & \frac{\mathcal{W}_{2213}+\mathcal{W}_{2231}}{2} & \frac{\mathcal{W}_{2223}+\mathcal{W}_{2232}}{2} \\ \mathcal{W}_{3311} & \mathcal{W}_{3322} & \mathcal{W}_{3333} & \frac{\mathcal{W}_{3312}+\mathcal{W}_{3321}}{2} & \frac{\mathcal{W}_{3313}+\mathcal{W}_{3331}}{2} & \frac{\mathcal{W}_{3323}+\mathcal{W}_{3332}}{2} \\ \mathcal{W}_{1211} & \mathcal{W}_{1222} & \mathcal{W}_{1233} & \frac{\mathcal{W}_{1212}+\mathcal{W}_{1221}}{2} & \frac{\mathcal{W}_{1213}+\mathcal{W}_{1231}}{2} & \frac{\mathcal{W}_{1223}+\mathcal{W}_{1232}}{2} \\ \mathcal{W}_{1311} & \mathcal{W}_{1322} & \mathcal{W}_{1333} & \frac{\mathcal{W}_{1312}+\mathcal{W}_{1321}}{2} & \frac{\mathcal{W}_{1313}+\mathcal{W}_{1331}}{2} & \frac{\mathcal{W}_{1323}+\mathcal{W}_{1332}}{2} \\ \mathcal{W}_{2311} & \mathcal{W}_{2322} & \mathcal{W}_{2333} & \frac{\mathcal{W}_{2312}+\mathcal{W}_{2321}}{2} & \frac{\mathcal{W}_{2313}+\mathcal{W}_{2331}}{2} & \frac{\mathcal{W}_{2323}+\mathcal{W}_{2332}}{2} \end{bmatrix} \tag{B.8}$$

For relatively small incremental stretch,

$$\mathbf{E}_t = \ln \mathbf{U}_t(\tau) \doteq \mathbf{U}_t(\tau) - \mathbf{1}, \mathbf{U}_t(\tau) \to \mathbf{1}.$$

So, $d\mathbf{E}_t \approx d\mathbf{U}_t$. With the aid of this approximation, we can modify $\mathcal{S}$ and $\mathcal{Q}$ as,

$$\mathcal{S} \approx \frac{\partial \mathbf{F}^e}{\partial \mathbf{U}_t}; \ \mathcal{Q} \approx \frac{\partial \mathbf{T}^*}{\partial \mathbf{U}_t} \tag{B.9}$$

In order to compute $\mathcal{W}_{ijkl}$ in (B.7), we need to calculate $\mathcal{S}$ and $\mathcal{Q}$. In what follows, we enumerate the steps for the same.

B.1 Calculation of Relevant Quantities

(i) Calculation of $\mathcal{S} = \frac{\partial \mathbf{F}^e}{\partial \mathbf{U}_t}$:

$$\mathbf{F}^e(\tau) = \mathbf{R}_t \mathbf{U}_t \mathbf{F}^e(t) \left\{ 1 - \sum_\alpha \Delta\gamma^\alpha \mathbf{S}_0^\alpha \right\} \tag{B.10}$$

where $\mathbf{R}_t$, $\mathbf{U}_t$ is obtained from the polar decomposition of the relative deformation gradient $\mathbf{F}_t$. Differentiating (B.10),

$$d\mathbf{F}^e = \mathbf{R}_t d\mathbf{U}_t \mathbf{F}^e(t) - \mathbf{R}_t d\mathbf{U}_t \mathbf{F}^e(t) \sum_\alpha \Delta\gamma^\alpha \mathbf{S}_0^\alpha - \mathbf{R}_t \mathbf{U}_t \mathbf{F}^e(t) \sum_\alpha d\Delta\gamma^\alpha \mathbf{S}_0^\alpha \tag{B.11}$$

With

$$\mathbf{R}^\alpha = \frac{\partial \Delta\gamma^\alpha}{\partial \mathbf{U}_t}, \tag{B.12}$$

we rewrite (B.11) in the indicial notation as follows,

$$\mathrm{d}F^e_{ij} = \left[R_{t,ik}F^e_{lj}(t) - R_{t,ik}F^e_{lp}(t)\sum_\alpha \Delta\gamma^\alpha \mathbf{S}^\alpha_{0,pj} - R_{t,im}U_{t,mn}F^e_{np}(t)\sum_\alpha R^\alpha_{kl}\mathbf{S}^\alpha_{0,pj}\right]\mathrm{d}U_{t,kl}. \tag{B.13}$$

Therefore,

$$\mathcal{S}_{ijkl} = R_{t,ik}F^e_{lj}(t) - R_{t,ik}F^e_{lp}(t)\sum_\alpha \Delta\gamma^\alpha \mathbf{S}^\alpha_{0,pj} - R_{t,im}U_{t,mn}F^e_{np}(t)\sum_\alpha R^\alpha_{kl}\mathbf{S}^\alpha_{0,pj}. \tag{B.14}$$

(*ii*) Calculation of $\mathcal{Q} = \frac{\partial \mathbf{T}^*}{\partial \mathbf{U}_t}$:

$$\mathbf{T}^*(\tau) = \mathbf{T}^{*^{tr}} - \sum_\alpha \Delta\gamma^\alpha \mathbf{C}^\alpha \tag{B.15}$$

Differentiating this expression,

$$\mathrm{d}\mathbf{T}^*(\tau) = \mathrm{d}\mathbf{T}^{*^{tr}} - \sum_\alpha \mathrm{d}\Delta\gamma^\alpha \mathbf{C}^\alpha - \sum_\alpha \Delta\gamma^\alpha \mathrm{d}\mathbf{C}^\alpha \tag{B.16}$$

Let

$$\frac{\partial \mathbf{T}^{*^{tr}}}{\partial \mathbf{U}_t} = \mathcal{D}. \tag{B.17}$$

$$\mathbf{T}^{*^{tr}} = \frac{1}{2}\mathcal{C}\left[\mathbf{A} - \mathbf{1}\right] \tag{B.18}$$

With

$$\frac{\partial \mathbf{A}}{\partial \mathbf{U}_t} = \mathcal{L}, \tag{B.19}$$

$$\mathrm{d}T^{*^{tr}}_{ij} = \frac{1}{2}\mathcal{C}_{ijmn}\mathcal{L}_{mnkl}\mathrm{d}U_{t,kl} \tag{B.20}$$

Therefore,

$$\mathcal{D}_{ijkl} = \frac{1}{2}\mathcal{C}_{ijmn}\mathcal{L}_{mnkl} \tag{B.21}$$

Next, let

$$\frac{\partial \mathbf{C}^\alpha}{\partial \mathbf{U}_t} = \mathcal{J}^\alpha \tag{B.22}$$

Since

$$\mathbf{C}^\alpha = \frac{1}{2}\mathcal{C}\left[\mathbf{A}\mathbf{S}^\alpha_0 + \mathbf{S}^{\alpha^T}_0\mathbf{A}\right],$$

$$\mathrm{d}\mathbf{C}^\alpha = \frac{1}{2}\mathcal{C}\left[\mathrm{d}\mathbf{A}\mathbf{S}^\alpha_0 + \mathbf{S}^{\alpha^T}_0\mathrm{d}\mathbf{A}\right],$$

Substituting for $\mathrm{d}\mathbf{A}$ from (B.19),

$$\mathrm{d}C^{\alpha}_{ij} = \frac{1}{2}\left\{\mathcal{C}_{ijmn}\mathcal{L}_{mpkl}S^{\alpha}_{0,pn} + \mathcal{C}_{ijmn}S^{\alpha^T}_{0,mp}\mathcal{L}_{pnkl}\right\}\mathrm{d}U_{t,kl} \tag{B.23}$$

Therefore,

$$\mathcal{J}^{\alpha}_{ijkl} = \frac{1}{2}\left\{\mathcal{C}_{ijmn}\mathcal{L}_{mpkl}S^{\alpha}_{0,pn} + \mathcal{C}_{ijmn}S^{\alpha^T}_{0,mp}\mathcal{L}_{pnkl}\right\} \tag{B.24}$$

The relation for $\mathrm{d}\mathbf{T}^*$, (B.16), can be rewritten in terms of $\mathcal{D}$, $\mathbf{R}^{\alpha}$ and $\mathcal{J}^{\alpha}$ as,

$$\mathrm{d}T^*_{ij} = \mathcal{D}_{ijkl}\mathrm{d}U_{t,kl} - \sum_{\alpha} R^{\alpha}_{kl}\mathrm{d}U_{t,kl}C^{\alpha}_{ij} - \sum_{\alpha}\Delta\gamma^{\alpha}\mathcal{J}^{\alpha}_{ijkl}\mathrm{d}U_{t,kl} \tag{B.25}$$

From (B.25), we obtain $\mathcal{Q}$ as

$$\mathcal{Q}_{ijkl} = \mathcal{D}_{ijkl} - \sum_{\alpha} C^{\alpha}_{ij}R^{\alpha}_{kl} - \sum_{\alpha}\Delta\gamma^{\alpha}\mathcal{J}^{\alpha}_{ijkl} \tag{B.26}$$

(*iii*) Calculation of $\mathcal{L} = \frac{\partial \mathbf{A}}{\partial \mathbf{U}_t}$:

$$\mathbf{A} = \mathbf{F}^{e^T}(t)\mathbf{U}_t(\tau)\mathbf{U}_t(\tau)\mathbf{F}^{e}(t) \tag{B.27}$$

On differentiation,

$$\mathrm{d}\mathbf{A} = \mathbf{F}^{e^T}(t)\mathrm{d}\mathbf{U}_t(\tau)\mathbf{U}_t(\tau)\mathbf{F}^{e}(t) + \mathbf{F}^{e^T}(t)\mathbf{U}_t(\tau)\mathrm{d}\mathbf{U}_t(\tau)\mathbf{F}^{e}(t) \tag{B.28}$$

In the indicial notation,

$$\mathrm{d}A_{ij} = F^{e^T}_{ik}(t)\mathrm{d}U_{t,kl}U_{t,lm}F^{e}_{mj}(t) + F^{e^T}_{im}(t)U_{t,mk}\mathrm{d}U_{t,kl}F^{e}_{lj}(t) \tag{B.29}$$

Therefore,

$$\mathcal{L}_{ijkl} = F^{e^T}_{ik}(t)U_{t,lm}F^{e}_{mj}(t) + F^{e^T}_{im}(t)U_{t,mk}F^{e}_{lj}(t) \tag{B.30}$$

(*iv*) Calculation of $\mathbf{R}^{\alpha} = \frac{\partial \Delta\gamma^{\alpha}}{\partial \mathbf{U}_t}$:

$$\Delta\gamma^{\alpha} = \Delta\gamma^{\alpha}(\mathbf{T}^*(\mathbf{U}_t)) \tag{B.31}$$

Here for the sake of simplicity, the change in the deformation resistances during increment Δt is neglected. Consequently, the plastic shear increment is dependent only on the resolved

shear stress. Equation (B.31) is differentiated using the chain rule as,

$$\Delta\gamma^{\alpha}\{\mathbf{U}_t + \alpha\mathbf{X}\} = \Delta\gamma^{\alpha}\{\mathbf{T}^*(\mathbf{U}_t) + \alpha\mathbf{X}\} \tag{B.32}$$

$$\frac{\mathrm{d}}{\mathrm{d}\alpha}\Delta\gamma^{\alpha}\{\mathbf{U}_t + \alpha\mathbf{X}\}|_{\alpha=0} = \frac{\partial\Delta\gamma^{\alpha}}{\partial\mathbf{U}_t}\cdot\mathbf{X} = \frac{\partial\Delta\gamma^{\alpha}}{\partial\mathbf{T}^*}\cdot\frac{\partial\Delta\mathbf{T}^*}{\partial\mathbf{U}_t}[\mathbf{X}] = \left[\frac{\partial\Delta\mathbf{T}^*}{\partial\mathbf{U}_t}\right]^T[\frac{\partial\Delta\gamma^{\alpha}}{\partial\mathbf{T}^*}]\cdot\mathbf{X} \tag{B.33}$$

Let

$$\mathbf{B}^{\alpha} = \frac{\partial\Delta\gamma^{\alpha}}{\partial\mathbf{T}^*} \tag{B.34}$$

Then,

$$R^{\alpha}_{ij} = B^{\alpha}_{kl}\mathcal{Q}_{klij} \tag{B.35}$$

We can now substitute the expression (B.35) in equation (B.26) to get the final expression for $\mathcal{Q}$ as follows,

$$\mathcal{Q} = \mathcal{D} - \sum_{\alpha}(\mathbf{C}^{\alpha}\otimes\mathbf{B}^{\alpha})\mathcal{Q} - \sum_{\alpha}\Delta\gamma^{\alpha}\mathcal{J} \tag{B.36}$$

Therefore,

$$\mathcal{Q} = \left\{\mathcal{I} + \sum_{\alpha}(\mathbf{C}^{\alpha}\otimes\mathbf{B}^{\alpha})\right\}^{-1}\left\{\mathcal{D} - \sum_{\alpha}\Delta\gamma^{\alpha}\mathcal{J}\right\} \tag{B.37}$$

where $\mathcal{I}$ is the fourth-rank identity tensor.

(v) Calculation of $\mathbf{B}^{\alpha} = \frac{\partial\Delta\gamma^{\alpha}}{\partial\mathbf{T}^*}$:

$$\mathbf{B}^{\alpha} = \frac{\partial\Delta\gamma^{\alpha}}{\partial\mathbf{T}^*} = \frac{\partial\Delta\gamma^{\alpha}}{\partial\tau^{\alpha}}\frac{\partial\tau^{\alpha}}{\partial\mathbf{T}^*} = \frac{\partial\Delta\gamma^{\alpha}}{\partial\tau^{\alpha}}\frac{1}{2}(\mathbf{S}_0^{\alpha} + \mathbf{S}_0^{\alpha^T}) \tag{B.38}$$

(vi) Calculation of $\mathcal{C}_{ijkl}$ in global co-ordinates:

Let $\mathcal{C}^c$ and $\mathcal{C}$ be the anisotropic elasticity tensor in the crystal and global basis respectively. Then, the stress-strain relation referred to the crystal basis is given by

$$\mathbf{T}^{*^c} = \mathcal{C}^c[\mathbf{E}^{e^c}]$$

If $\mathbf{Q}$ is the orthognal tensor that rotates the crystal basis to the global basis,

$$\mathbf{T}^* = \mathbf{Q}\mathbf{T}^{*^c}\mathbf{Q}^T;\ \mathbf{E}^{e^c} = \mathbf{Q}^T\mathbf{E}^e\mathbf{Q}.$$

$$\mathbf{T}^* = \mathbf{Q}\mathcal{C}^c[\mathbf{Q}^T\mathbf{E}^e\mathbf{Q}]\mathbf{Q}^T, \tag{B.39}$$

i.e.,

$$T^*_{ij} = Q_{im} C^c_{mnop} Q^T_{ok} Q_{lp} Q^T_{nj} E^e_{kl} \tag{B.40}$$

Therefore,

$$\mathcal{C}_{ijkl} = Q_{im} Q_{jn} Q_{ko} Q_{lp} C^c_{mnop} \tag{B.41}$$

B.2 Algorithm for computation of the Jacobian

1. Calculate

   $\mathcal{L}_{ijkl} = F^{e^T}_{ik}(t) U_{t,lm}(\tau) F^e_{mj}(t) + F^{e^T}_{im}(t) U_{t,mk}(\tau) F^e_{lj}(t)$

2. Calculate $\mathcal{C}_{ijkl}$ in global co-ordinates,

   $\mathcal{C}_{ijkl} = Q_{im} Q_{jn} Q_{ko} Q_{lp} \mathcal{C}^c_{mnop}$

3. Calculate

   $\mathcal{D}_{ijkl} = \frac{1}{2} \mathcal{C}_{ijmn} \mathcal{L}_{mnkl}$

4. Calculate

   (a) $\mathcal{G}^\alpha_{mnkl} = \mathcal{L}_{mpkl} S^\alpha_{0,pn} + S^{\alpha^T}_{0,mp} \mathcal{L}_{pnkl}$

   (b) $\mathcal{J}^\alpha_{ijkl} = \frac{1}{2} \mathcal{C}_{ijmn} \mathcal{G}^\alpha_{mnkl}$

5. Calculate

   $\mathbf{B}^\alpha = \frac{\partial \Delta\gamma^\alpha}{\partial \tau^\alpha} \frac{1}{2} (\mathbf{S}^\alpha_0 + \mathbf{S}^{\alpha^T}_0)$

6. Calculate

   (a) $\mathcal{K}_{ijkl} = \mathcal{I}_{ijkl} + \sum_\alpha (C^\alpha_{ij} B^\alpha_{kl})$

   (b) $\mathcal{Q}_{ijkl} = \mathcal{K}^{-1}_{ijmn} \mathcal{D}_{mnkl} - \sum_\alpha \Delta\gamma^\alpha \mathcal{J}^\alpha_{mnkl}$

7. Calculate

   (a) $R^\alpha_{ij} = B^\alpha_{kl} \mathcal{Q}_{klij}$

   (b) $\mathcal{S}_{ijkl} = R_{t,ik} F^e_{ij}(t) - R_{t,ik} F^e_{ip}(t) \sum_\alpha \Delta\gamma^\alpha \mathbf{S}^\alpha_{0,pj} - R_{t,im} U_{t,mn} F^e_{np}(t) \sum_\alpha R^\alpha_{kl} \mathbf{S}^\alpha_{0,pj}$

8. Calculate the Jacobian

$$\mathcal{W}_{ijkl} = \frac{1}{\det \mathbf{F}^e} \left[\mathcal{S}_{imkl} T^*_{mn} F^{e^T}_{nj} + F^e_{im} \mathcal{Q}_{mnkl} F^{e^T}_{nj} + F^e_{im} T^*_{mn} \mathcal{S}_{jnkl} - F^e_{im} T^*_{mn} F^{e^T}_{nj} (\mathcal{S}_{pqkl} F^{e^{-1}}_{qp}) \right]$$

9. Reduce the $\mathcal{W}_{ijkl}$ to the $\mathcal{W}_{IJ}$ form through equation (B.8). This Jacobian is for the constitutive response of a single crystal. Compute the Jacobian for the constitutive response of each of the crystals in the polcrystalline aggregate in a similar manner.

10. Calculate the overall Jacobian for the constitutive response at the integration point as a volume-average of the Jacobians associated with the constituent crystals, $\mathcal{W}_{IJ} = \sum_k v^{(k)} \mathcal{W}_{IJ}^{(k)}$

Appendix C

Procedures for Measuring Pole Figures

The crystallographic texture in the as-annealed and deformed specimens were obtained by x-ray[1] irradiation using a RIGAKU RU200 diffractometer equipped with a pole-figure goniometer. The specimens were all sectioned approximately at the mid-plane using a a diamond wheel mounted on a BUEHLER ISOMET low speed saw. This ensured that the cutting process did not alter the texture in the sample. The mounted samples were rough ground in an ABRAPOL automatic polisher to a 10 μm finish with the application of 150 N force. This was followed by fine-grinding for 10-15 minutes using a 5 μm SiC paper with the application of 100 N force. The specimens were then oxide-polished for 5-10 minutes to a mirror-finish ($\approx 0.05\mu m$) using colloidal-silica suspension with the application of 50 N force. The resulting surface was free of visible grinding marks.

For the measurement of the crystallographic texture, at first the 2θ positions for the specific crystallographic planes were located. For the 2θ scans, a 1° divergence slit, a 1° scatter slit and a 0.3 mm receiving slit were used. Partial pole figures were generated by using the Schultz reflection method on the {111}, {200} and {220} crystallographic planes in aluminum and (0002), $\{10\bar{1}1\}$ and $\{11\bar{2}0\}$ crystallographic planes in titanium. For the pole-figures, the slits used were a 1° divergence slit, a Schultz slit, a 6 mm receiving slit and a 7 mm scatter slit. The diffractometer used for the measurement of texture had a focussing circle 185 mm in radius. With this geometry for the focussing apparatus, the irradiated

[1]The x-rays were generated from a copper target serving as the rotating anode.

surface was approximately 5.2 mm × 1.2 mm in area. The average grain diameters for the aluminum and titanium specimens were 150 μm and 175 μm , respectively. Consequently, the irradiated surface samples about 280 grains in the aluminum specimens and 210 grains in the titanium specimens. The background radiation for each pole-figure was measured at approximately 2° from the corresponding 2θ peak. All the x-ray measurements were performed with a power level of 50 KV and 150 mA.

The experimental pole-figure data in its raw form is uncorrected and is in the form of discretized intensities as a function of the goiniometer position angles. The raw data was processed using the popLA software package (Kallend *et al.* [1994]). Each pole-figure was corrected for background and defocusing[2] In addition, spherical harmonics were used to extrapolate the outer 15° of each pole-figure which was not measured in the experiments. All the pole-figures presented in this study are *equal-area* projections of the specified crystallographic planes.

[2]The defocusing curve for the slit geometry used in the experiments was constructed theoretically using the methodology proposed by Tenckhoff [1970].

Appendix D

Single Crystal Studies on Titanium

In this chapter, the effect of different choices of slip systems on the stress-strain response, slip system activity, and the evolution of the crystal lattice orientation in simple tension and compression experiments on h.c.p. single crystals is anlayzed. This study is aimed at providing information regarding the operative slip systems in high-temperature deformation of h.c.p. titanium.

Fig. D-1(a) shows the inverse pole-figure of the rod axis for the annealed titanium rod. The rod axis is located predominantly in the neighborhood of the $[\bar{1}2\bar{1}0]$ direction. For the simulations, a single crystal orientation that is representative of this initial texture, Fig. D-1(b), is considered. Accordingly, the initial orientation of the single crystal is taken to be specified by the following three Euler angles (Kalidindi [1992]):

θ	ϕ	ω
85°	25°	0°

The simple tension and compression simulations are performed for each of the follcwing three different choices of slip systems:

(*i*) Basal-< **a** > slip systems only

(*ii*) Prismatic-< **a** > slip systems only

(*iii*) Pyramidal-< **a** > slip systems only.

The values of elastic parameters for single crystal h.c.p. titanium at 750°C are taken as

(Simmons and Wang [1971]):

$$C_{11} = 125.3\,\text{GPa},\ C_{12} = 99.4\,\text{GPa},\ C_{13} = 68.8\,\text{GPa},\ C_{33} = 154.5\,\text{GPa},\ C_{55} = 31.6\,\text{GPa}.$$

The slip systems are assumed to be non-hardening. Also, for all the simulations, the slip system deformation resistance is taken to be equal to $s_0 = 8$ MPa. For the slip system rate-sensitivity, the value measured from strain-rate jump tests on polycrystalline titanium at 750°C, $m = 0.16$, is used.

A single eight-noded brick ABAQUS C3D8 element is used to perform the finite element simulations in ABAQUS/Standard. The tension or compression direction is aligned with one of the element axes. The two loaded faces of the cube are constrained to remain parallel to each other and perpendicular to the tension or compression axis throughout the deformation. The simulations are carried out at a constant true axial strain rate of ± 0.001 s^{-1} to a final true strain of 0.25 in tension, and -0.25 in compression.

D.1 Simple Tension

Fig. D-2 shows the predictions of slip system activity, and evolution of the crystal orientation when only basal-< a > slip is allowed. Initially, the basal slip systems B1 and B2 are activated as shown in Fig. D-2(a). On straining, the tension axis rotates towards the $10\bar{1}0 - 11\bar{2}0$ boundary, Fig. D-2(b). On approaching the boundary at a macroscopic strain of $\epsilon \approx 0.05$, the Schmid factors on both the slip systems become very small resulting in an arrest in their activity.

Fig. D-3 shows the predictions of stress-strain curve, slip system activity, and evolution of the crystal orientation when only prismatic-< a > slip is allowed. Two prismatic slip systems, P1 and P2, are active, Fig. D-3(b). This results in the rotation of the tension axis towards the $0001 - 10\bar{1}0$ boundary as shown in Fig. D-3(c).

Fig. D-4 shows the predictions of stress-strain curve, slip system activity, and evolution of the crystal orientation when only pyramidal < a > slip is allowed. Two slip systems, R2 and R5, are active, Fig. D-4(b). The orientation of the the tension axis rotates towards the $(10\bar{1}0)$ pole, Fig. D-4(c).

D.2 Simple Compression

Fig. D-5 shows the predictions of stress-strain curve, slip system activity, and evolution of the crystal orientations for simple compression when only basal-< **a** > slip is allowed. Two slip systems, B1 and B2, are active, Fig. D-5(b). The compression axis rotates towards the (0001) pole along a great circle, Fig. D-5(c). The geometric softening in the stress-strain response, Fig. D-5(a) is due to the decrease in Schmid factor with strain.

Fig. D-6 shows the predictions of stress-strain curve, slip system activity, and evolution of the crystal orientations when only prismatic-< **a** > slip is allowed. Activity on slip systems P1 and P2 (see Fig. D-6(b)) causes the compression axis to rotate towards the $0001 - 11\bar{2}0$ boundary, Fig. D-6(c). Also, the compression axis has a slight tendency to rotate towards the $(11\bar{2}0)$ pole.

Fig. D-7 shows the predictions of stress-strain curve, slip system activity, and evolution of the crystal orientations when onlt pyramidal-< **a** > slip is allowed. Two slip systems, R2 and R5, are active, Fig. D-7(b). As in the case of prismatic slip, the compression axis rotates towards the $0001 - 11\bar{2}0$ boundary, Fig. D-7(c). But unlike the case of prismatic slip, the compression axis has a slight tendency to rotate away from the $(11\bar{2}0)$ pole.

D.3 Conclusions

The following conclusions can be made from the simple tension and compression simulations on the titanium single crystal:

1. In tension, basal-< **a** > slip rotates the tension axis towards the $10\bar{1}0 - 11\bar{2}0$ boundary. Prismatic-< **a** > slip rotates the tension axis towards the $0001 - 10\bar{1}0$ boundary while pyramidal-< **a** > slip rotates it towards the $(10\bar{1}0)$ pole.

2. In compression, basal-< **a** > slip rotates the compression axis towards the (0001) pole while prismatic-< **a** > slip or pyramidal-< **a** > slip rotates the compression axis towards the $0001 - 11\bar{2}0$ boundary.

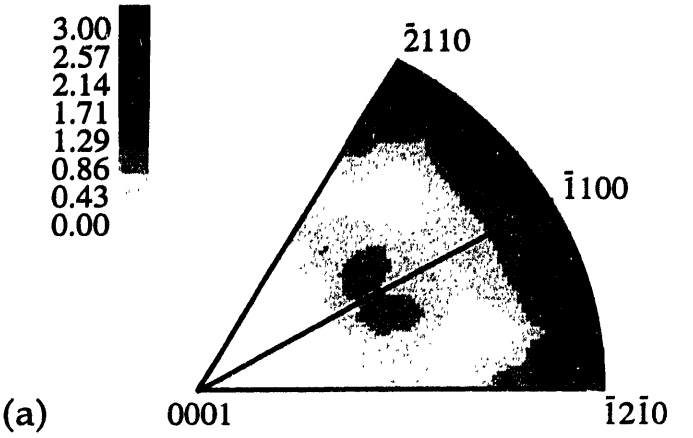

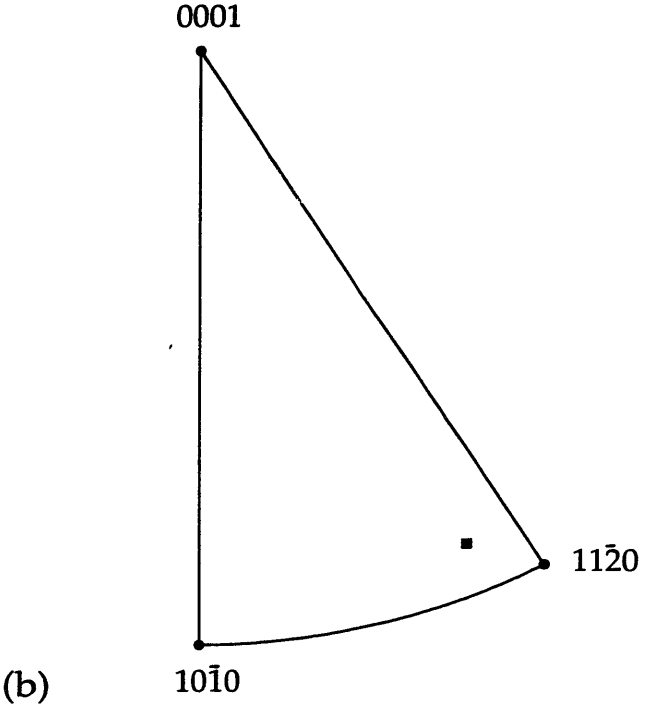

Figure D-1: (a) Inverse pole figure of the compression axis in the annealed titanium rod. The figure also shows the lines of symmetry (bold lines). (b) Primary orientation triangle showing the initial orientation of the single crystal considered in the simulation.

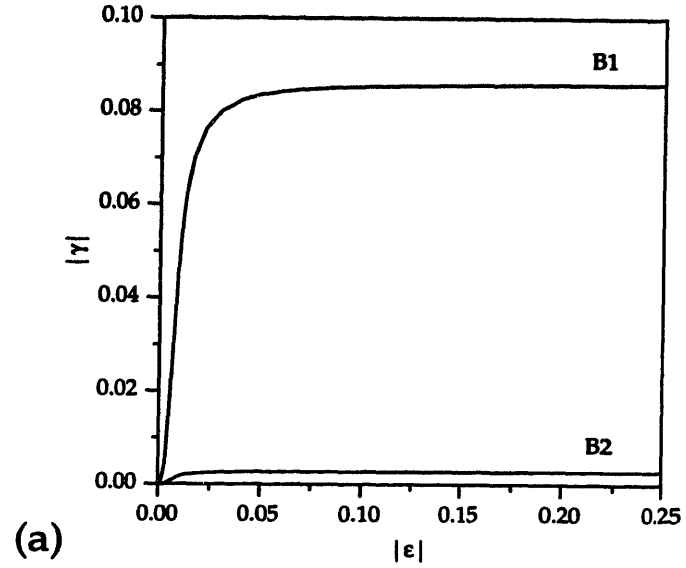

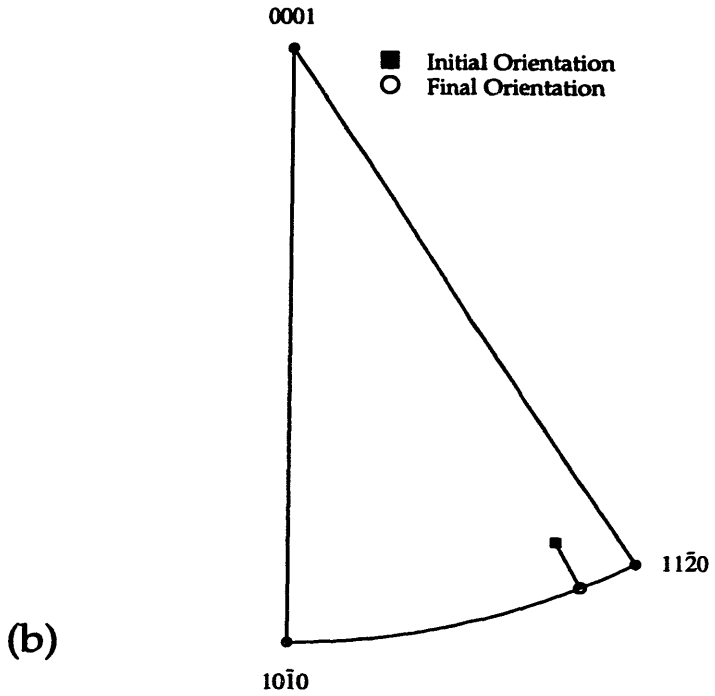

Figure D-2: Numerical simulation of simple tension of a titanium single crystal at 750°C when only basal-< a > slip is allowed: (a) The accumulated slip vs. macroscopic strain for active slip systems. (b) Inverse pole figure of the change in orientation of the tension axis.

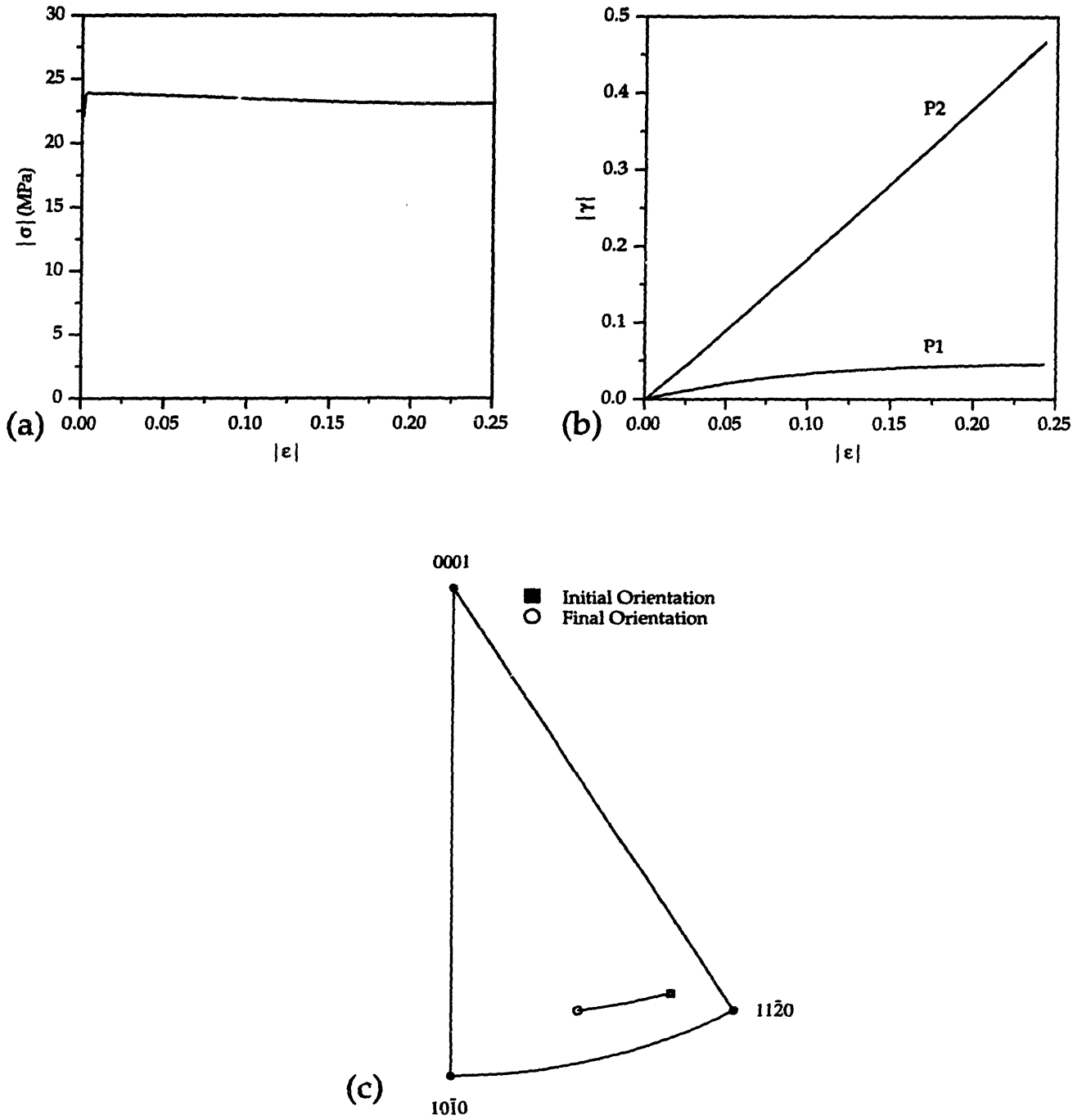

Figure D-3: Numerical simulation of simple tension of a titanium single crystal at 750°C when only prismatic-< a > slip is allowed: (a) The macroscopic stress-strain response (b) The accumulated slip vs. macroscopic strain for active slip systems. (c) Inverse pole figure of the change in orientation of the tension axis.

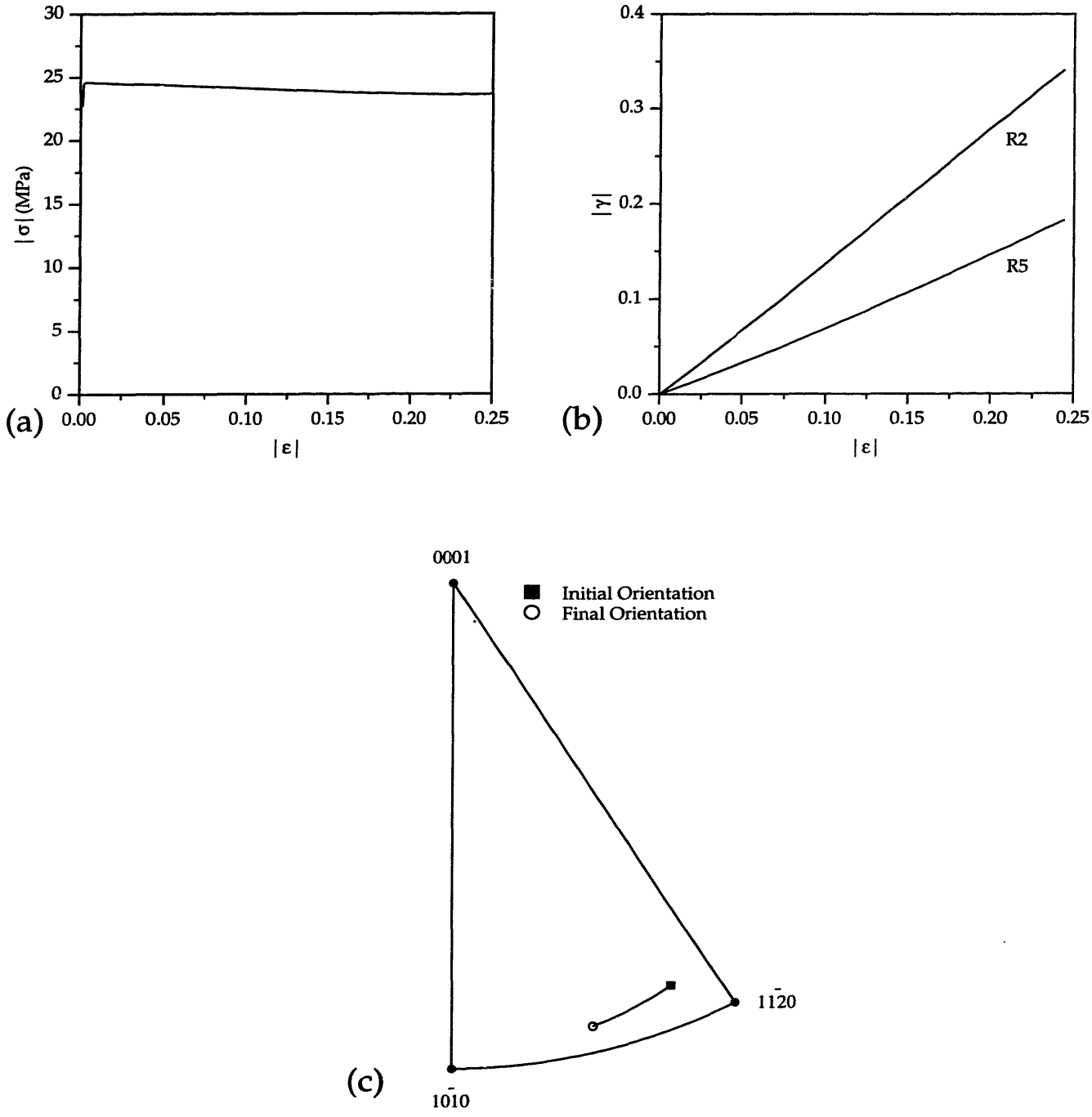

Figure D-4: Numerical simulation of simple tension of a titanium single crystal at 750°C when only pyramidal-< a > slip is allowed: (a) The macroscopic stress-strain response (b) The accumulated slip vs. macroscopic strain for active slip systems. (c) Inverse pole figure of the change in orientation of the tension axis.

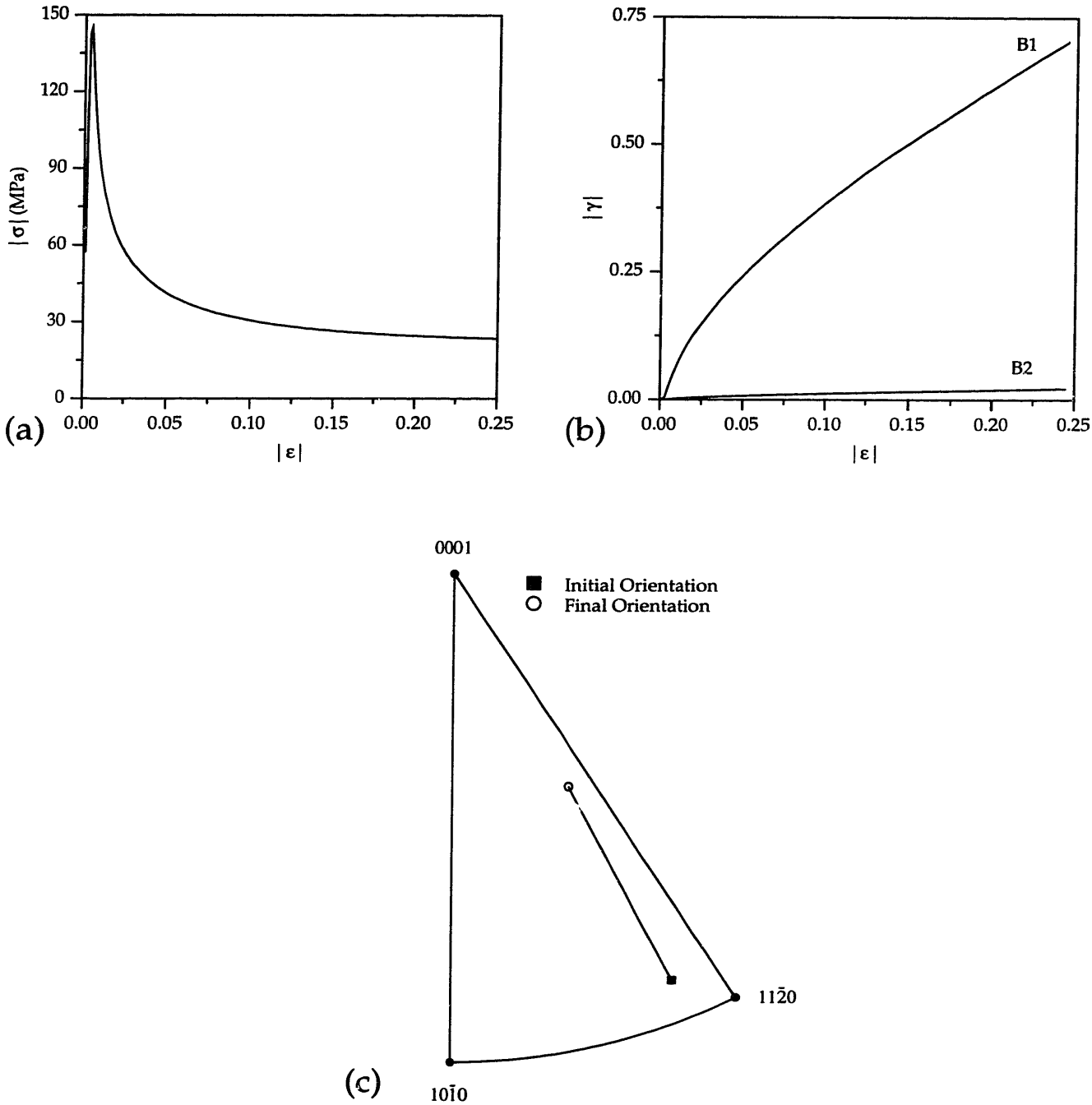

Figure D-5: Numerical simulation of simple compression of a titanium single crystal at 750°C when only basal-< **a** > slip is allowed: (a) The macroscopic stress-strain response (b) The accumulated slip vs. macroscopic strain for active slip systems. (c) Inverse pole figure of the change in orientation of the tension axis.

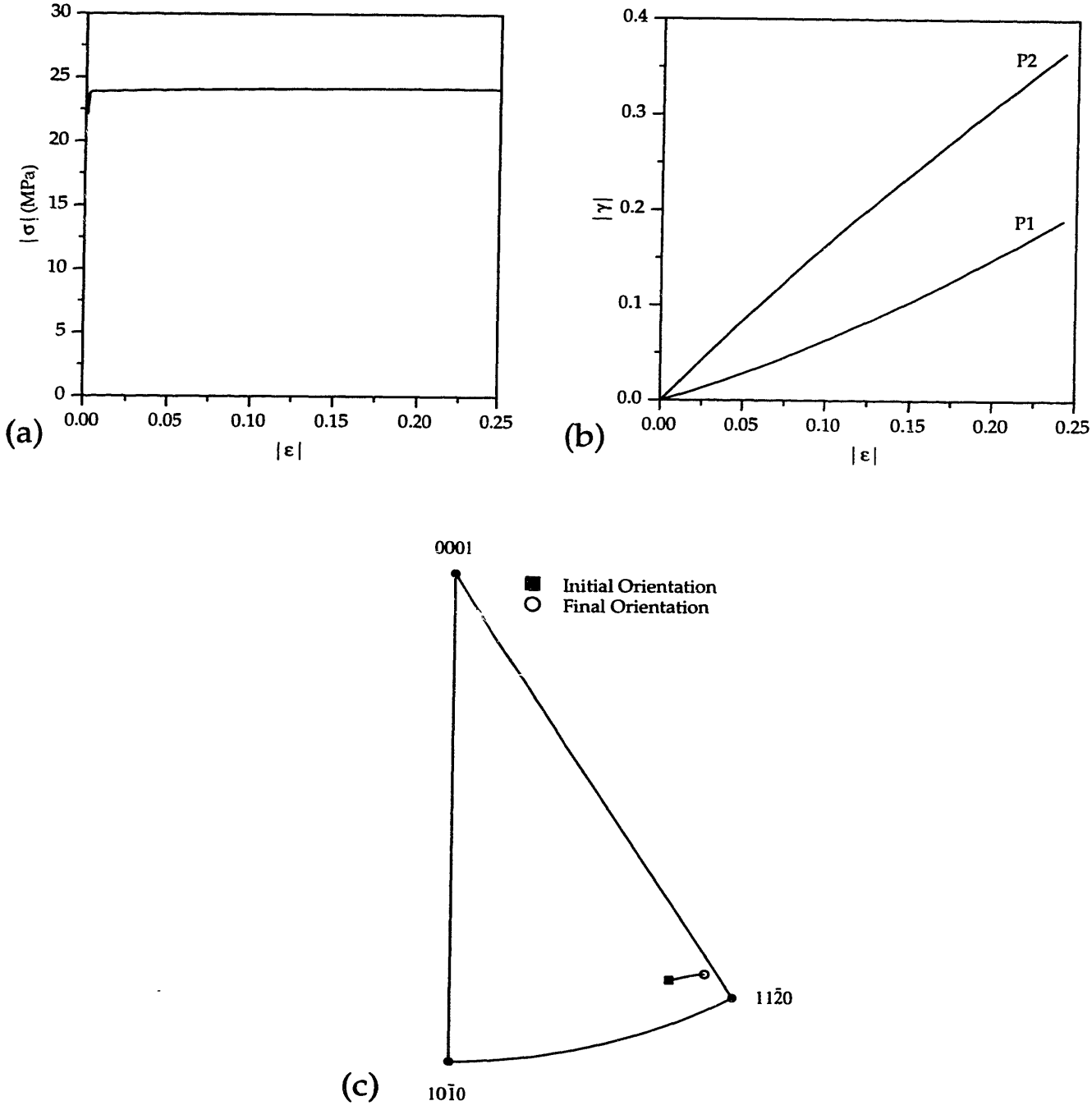

Figure D-6: Numerical simulation of simple compression of a titanium single crystal at 750°C when only prismatic-< **a** > slip is allowed: (a) The macroscopic stress-strain response (b) The accumulated slip vs. macroscopic strain for active slip systems. (c) Inverse pole figure of the change in orientation of the tension axis.

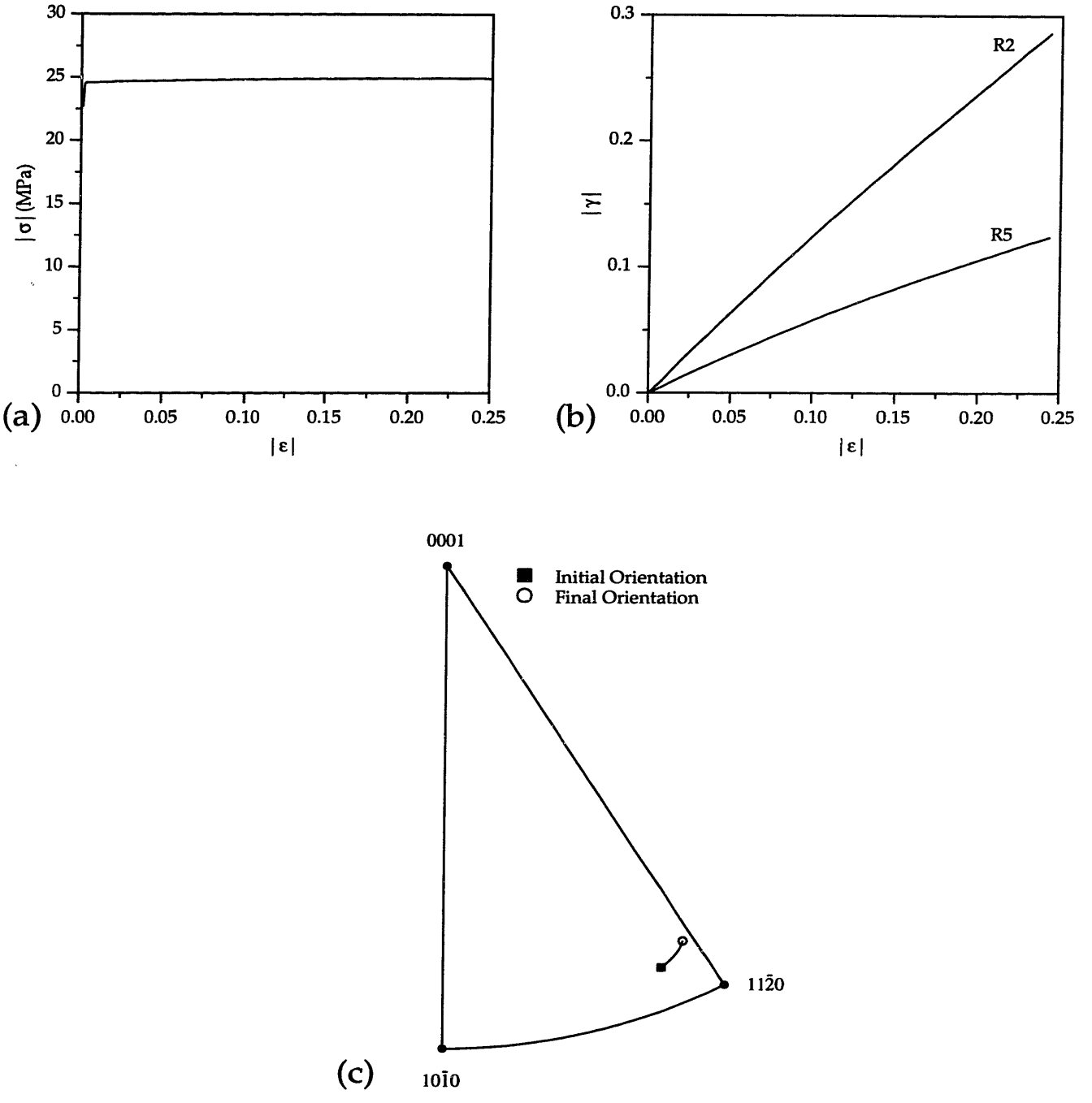

Figure D-7: Numerical simulation of simple compression of a titanium single crystal at 750°C when only pyramidal-< **a** > slip is allowed: (a) The macroscopic stress-strain response (b) The accumulated slip vs. macroscopic strain for active slip systems. (c) Inverse pole figure of the change in orientation of the tension axis.

Appendix E

Effect of Latent Hardening on the Polycrystalline Response of h.c.p. Titanium

In chapter 4, the following form for the slip system hardening was introduced:

$$\dot{s}^{\alpha} = \sum_{\beta} h^{\alpha\beta} \left|\dot{\gamma}^{\beta}\right|, \tag{E.1}$$

where $h^{\alpha\beta}$ describes the rate of strain hardening on slip system α due to shearing on the slip system β. For the slip system hardening matrix $h^{\alpha\beta}$, the following simple form was adopted:

$$h^{\alpha\beta} = q^{\alpha\beta}\, h_0^{\beta} \left|1 - \frac{s^{\beta}}{\tilde{s}(\frac{\dot{\gamma}^{\beta}}{\dot{\tilde{\gamma}}})^n}\right|^r \text{sign}\left(1 - \frac{s^{\beta}}{\tilde{s}(\frac{\dot{\gamma}^{\beta}}{\dot{\tilde{\gamma}}})^n}\right) \tag{E.2}$$

where $q^{\alpha\beta}$ is a matrix describing the latent hardening behavior of a titanium crystal, $\dot{\tilde{\gamma}}$ is a reference shearing rate and h_0, r, $\tilde{s}$ and n are slip system hardening parameters.

Also, the latent hardening matrix was taken to be decribed as:

$$q^{\alpha\beta} = \left\{ \begin{array}{ll} 1 & \text{if } \alpha \text{ and } \beta \text{ are coplanar slip systems,} \\ q_l & \text{otherwise.} \end{array} \right\} \tag{E.3}$$

Here, the parameter q_l is assumed to be a constant and the same for interaction between any two non-coplanar slip systems.

Since there is no experimental information available about the numerical value for q_l, in this chapter, numerical simulations of simple tension and compression are performed with three different choices of the latent hardening parameter q_l of 0, 1 and 1.5, respectively. The effect of the different choices of the latent hardening parameter on the evolution of texture and the stress-strain response in simple compression and tension of polycrystalline h.c.p. titanium is analyzed.

The simulations are carried out with the assumption of basal-$< \mathbf{a} >$, prismatic-$< \mathbf{a} >$ and pyramidal-$< \mathbf{c}+\mathbf{a} >$ slip systems. The initial texture is numerically represented by 729 unweighted grain orientations as shown in Fig. 4-14. The calculations are performed in ABAQUS/Standard with a finite element mesh comprising 729 C3D8 elements where each element represents a grain. The material parameters used for the calculations are estimated by fitting the predictions from the model for $q_l = 1$ with the measured stress-strain response for constant strain-rate and strain-rate jump compression tests, Fig. 4-32. The parameters estimated from this fit are:

Table E-1. Material Parameters for h.c.p. Titanium

s_0 $(0001) < 11\bar{2}0 >$	s_0 $\{10\bar{1}0\} < 11\bar{2}0 >$	s_0 $\{10\bar{1}1\} < 11\bar{2}3 > +$ $\{11\bar{2}2\} < 11\bar{2}3 >$	h_0	r	m	n
8.2 MPa	8.2 MPa	82 MPa	12 MPa	1	0.16	0.1

$\tilde{s}$ $(0001) < 11\bar{2}0 >$	$\tilde{s}$ $\{10\bar{1}0\} < 11\bar{2}0 >$	$\tilde{s}$ $\{10\bar{1}1\} < 11\bar{2}3 > +$ $\{11\bar{2}2\} < 11\bar{2}3 >$
18 MPa	18 MPa	180 MPa

Fig.E-1 shows the predicted stress-strain curves in simple compression for the three different values of q_l. The stress-strain responses for $q_l = 1$ and $q_l = 1.5$ are nearly the same but the stress-strain curve for $q_l = 0$ differs significantly from the other two. In order to capture the stress-strain response for values of the latent hardening parameter other than 1, there is a need to determine a "new" set of slip system hardening parameters for each

assumption for q_l. Such a task is not undertaken here. Fig. E-2 shows the predicted texture at $\epsilon = -1$ for the three different cases compared against the experimentally measured texture. We observe that the texture evolution is *quite insensitive to the changes in the latent hardening parameter*, q_l. The predictions of the stress-strain curves and the texture at $\epsilon = 0.3$ in simple tension for the three different assumptions for q_l are presented in Figs. E-3 and E-4, repsectively. Again, the stress-strain curves differ but the texture evolution for the three cases are nearly identical.

In conclusion, the study shows that the assumption for the latent hardening parameter q_l is not crucial for the calculation of texture evolution in polycrystalline h.c.p. titanium. For the simulations on polycrystalline h.c.p. titanium, the value of the latent hardening parameter is assumed to be $q_l = 1$. The effect of different values for q_l could be more significant in the deformation of single crystals. In this context, there is a need for careful experimental studies probing the latent hardening behavior of h.c.p. titanium and hexagonal materials in general.

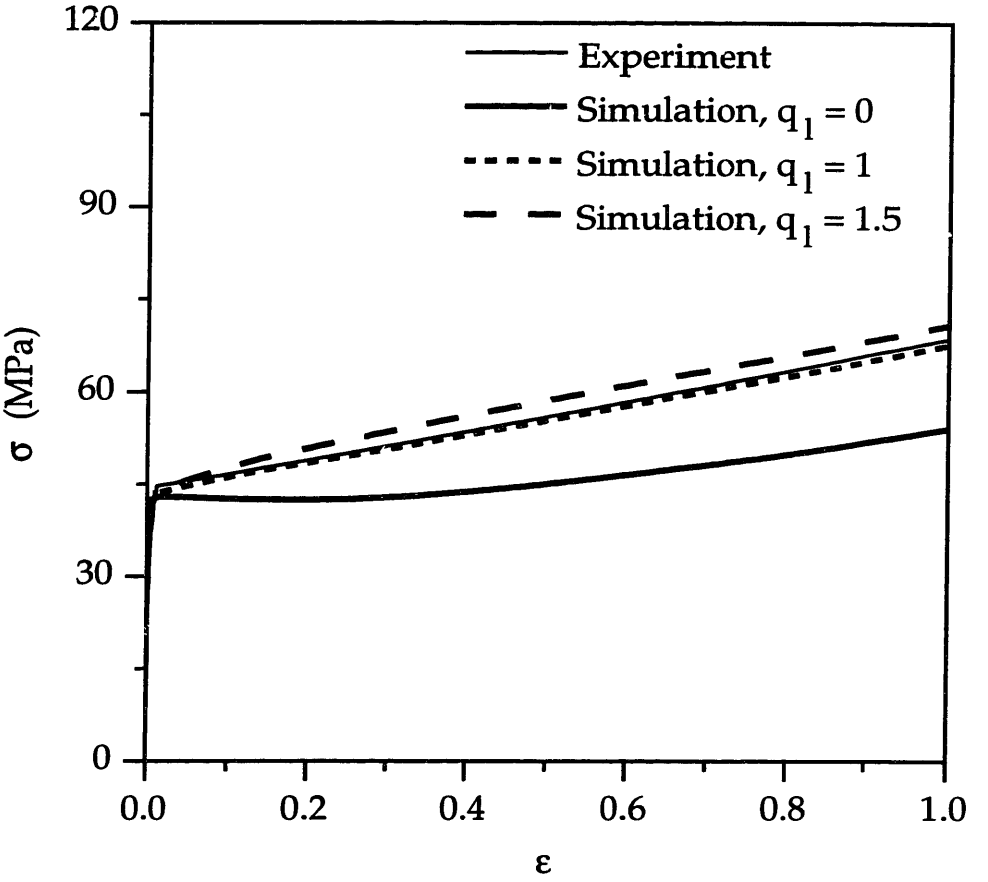

Figure E-1: Measured stress-strain response for simple compression and calculated stress-strain curves with three different assumptions for the latent hardening parameter q_l.

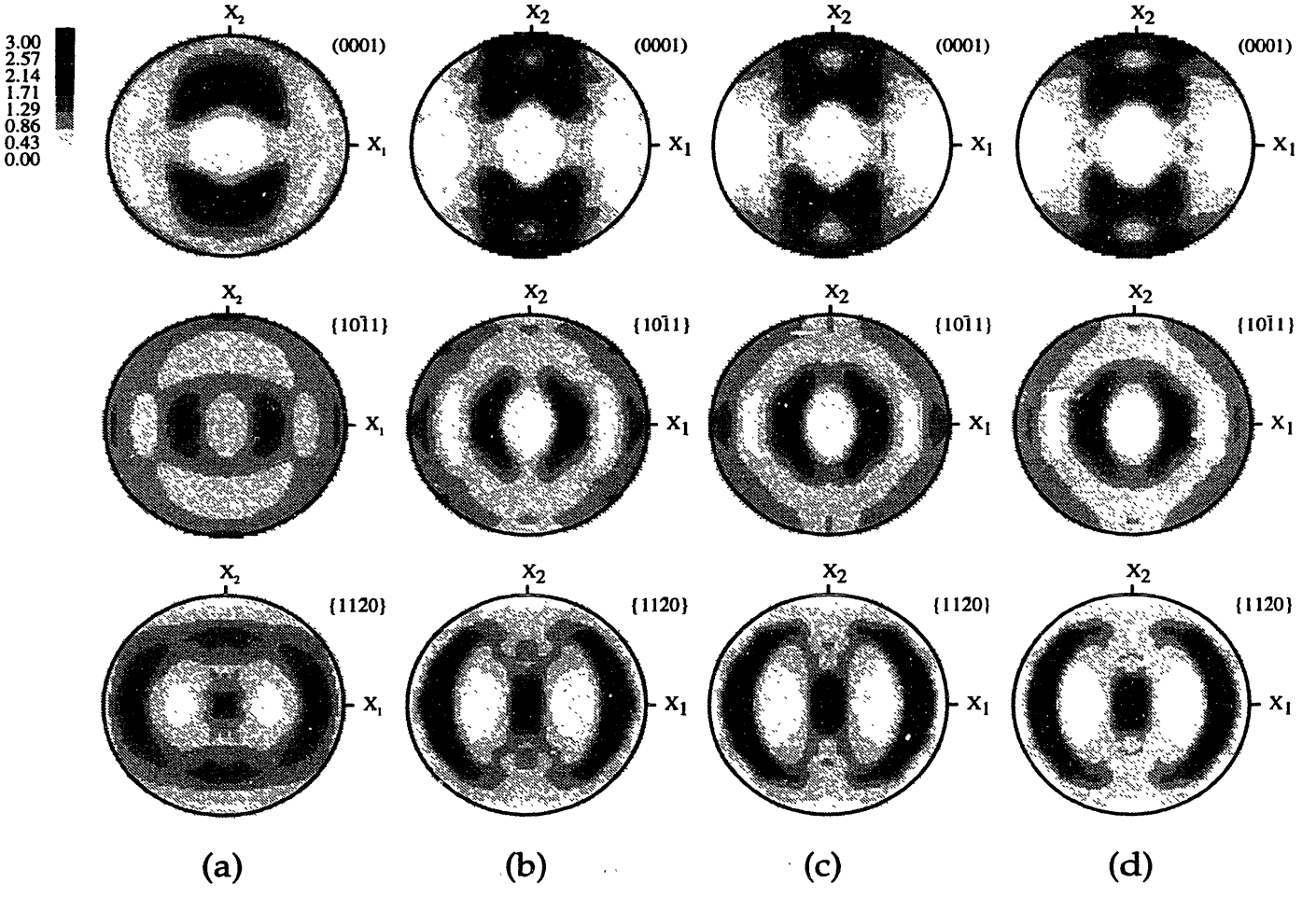

Figure E-2: (a) Experimentally measured texture after simple compression to $\epsilon = -1$; Numerically calculated texture with three different assumptions for the latent hardening parameter q_l: (b) $q_l = 0$ (c) $q_l = 1$ (d) $q_l = 1.5$

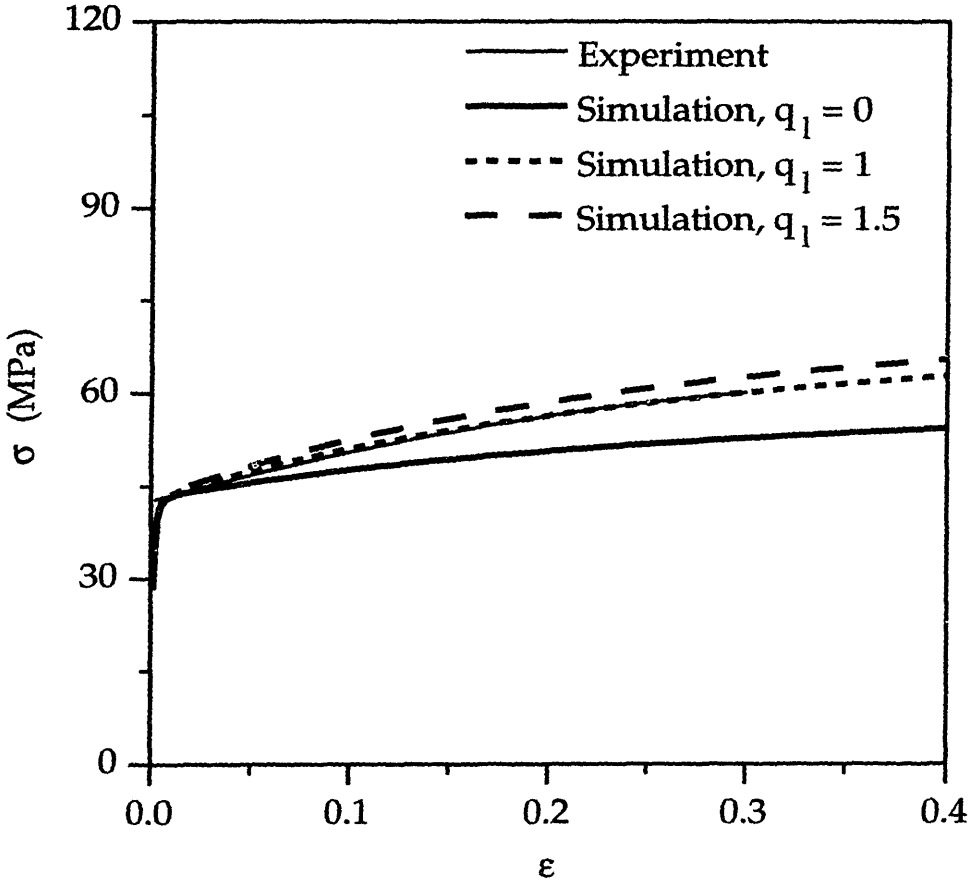

Figure E-3: Measured stress-strain response for simple tension and calculated stress-strain curves with three different assumptions for the latent hardening parameter q_l.

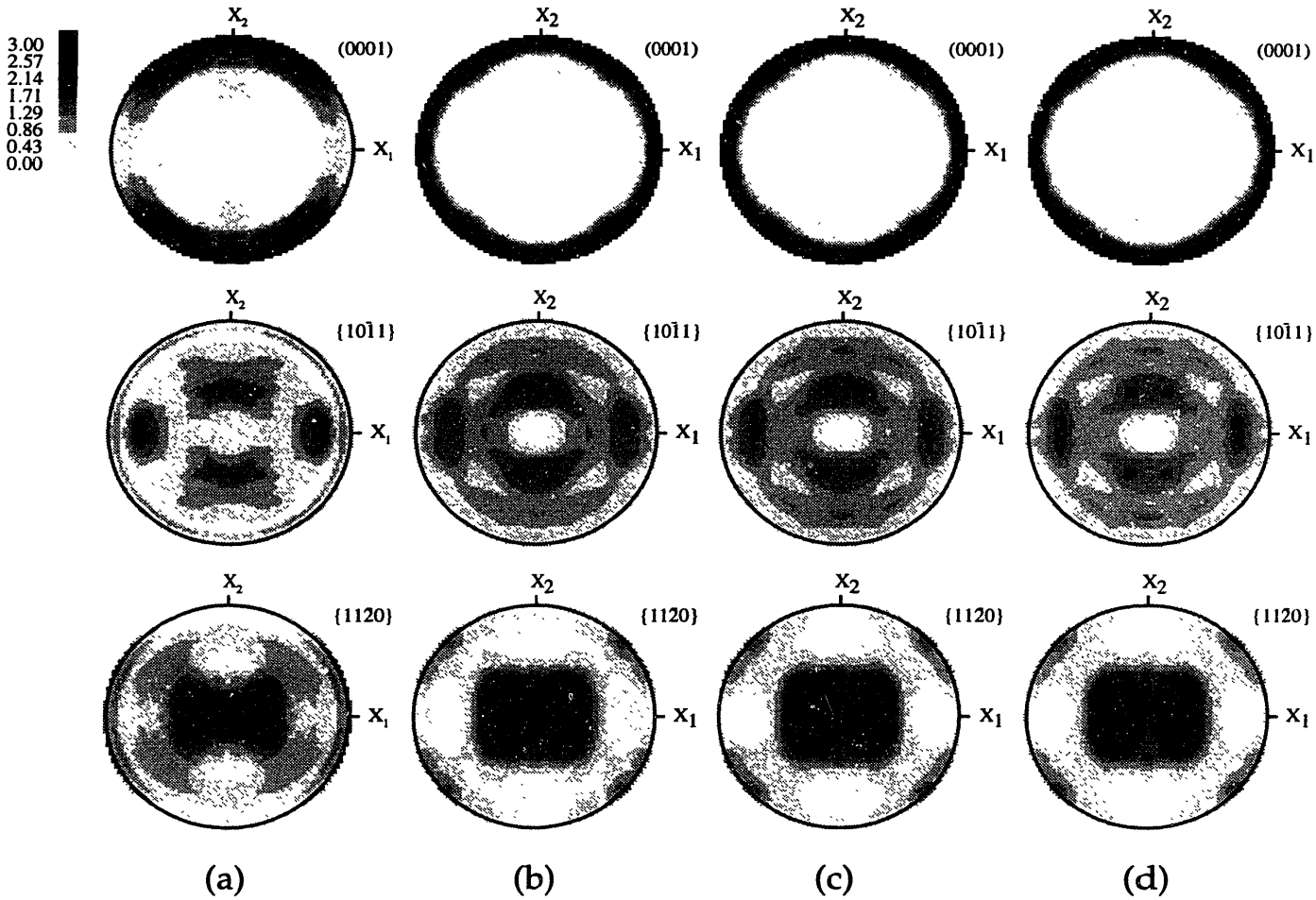

Figure E-4: (a) Experimentally measured texture after simple tension to $\epsilon = 0.3$; Numerically calculated texture with three different assumptions for the latent hardening parameter q_l: (b) $q_l = 0$ (c) $q_l = 1$ (d) $q_l = 1.5$

Bibliography

[abaqus, 1994] Hibbit , Karlsson & Sorenson, Inc., Providence, R.I. *ABAQUS Reference Manuals*, 1994.

[Akhtar and Teghtsoonian, 1975b] A. Akhtar and E. Teghtsoonian. Prismatic Slip in α-Titanium Single Crystals. *Metallurgical Transactions A*, 6A:2201–2208, 1975b.

[Akhtar, 1975a] A. Akhtar. Basal Slip and Twinning in α-Titanium Single Crystals. *Metallurgical Transactions A*, 6A:1105–1113, 1975a.

[Anand, 1982] L. Anand. Constitutive equations for rate-dependent deformation of metals at elevated temperatures. *ASME Journal of Engineering Materials and Technology*, 104:12–17, 1982.

[Argon and East, 1979] A.S. Argon and G.H. East. Forest Dislocation Intersections in Stage I Deformation of Copper Single Crystals. In P. Haasen, V. Gerold, and G. Kostorz, editors, *Proceedings of the 5th International Conference on the Strength of Metals and Alloys*, pages 9–16. Pergamon Press, Oxford, 1979.

[Argon, 1995] A.S. Argon. Mechanical Properties of Single Phase Crystalline Media: Deformation at Low Temperatures. In R.W. Cahn and P. Haasen, editors, *Physical Metallurgy*. Elsevier, Amsterdam, 1995.

[Asaro and Needleman, 1985] R.J. Asaro and A. Needleman. Texture development and strain hardening in rate dependent Polycrystals. *Acta Metallurgica*, 33:923–953, 1985.

[Asaro and Rice, 1977] R.J. Asaro and J.R. Rice. Strain localisation in ductile single crystals. *Journal of the Mechanics and Physics of Solids*, 25:309–338, 1977.

[Asaro, 1983a] R.J. Asaro. Micromechanics of Crystals and Polycrystals. *Advances in Applied Mechanics*, 23:1–115, 1983a.

[Asaro, 1983b] R.J. Asaro. Crystal plasticity. *ASME Journal of Applied Mechanics*, 50:921–934, 1983b.

[asm, 1990] *ASM Handbook: Heat Treating.* ASM International, The Materials Information Society, 1990.

[Bassani, 1993] J.L. Bassani. Plastic Flow of Crystals. *Advances in Applied Mechanics*, 30:191–258, 1993.

[Beaudoin *et al.*, 1994] A.J. Beaudoin, P.R. Dawson, K.K. Mathur, U.F. Kocks, and D.A. Korzekwa. Application of Polycrystalline Plasticity to Sheet Forming. *Computer Methods in Applied Mechanics and Engineering*, 117:49–70, 1994.

[Becker *et al.*, 1991] R. Becker, J.F. Butler, Jr., H. Hu, and L.A. Lalli. Analysis of an Aluminum Single Crystal with Unstable Initial Orientation (001)[110] in Channel Die Compression. *Metallurgical Transactions A*, 22A:45–58, 1991.

[Becker *et al.*, 1993] R. Becker, R.E. Smelser, and S. Panchanadeeswaran. Simulations of Earing in Aluminum Single Crystals and Polycrystals. *Modeling and Simulations in Materials Science and Engineering*, 1:203–224, 1993.

[Bronkhorst *et al.*, 1992] C.A. Bronkhorst, S.R. Kalidindi, and L. Anand. Polycrystalline plasticity and the evolution of crystallographic texture in FCC metals. *Philosophical transactions of the Royal Society of London A*, 341:443–477, 1992.

[Brown *et al.*, 1989] S. Brown, K. Kim, and L. Anand. An Internal Variable Constitutive Model for Hot Working of Metals. *International Journal of Plasticity*, 5:95–130, 1989.

[Campbell and Dowling, 1970] J.D. Campbell and A.R. Dowling. The Behavior of Materials Subjected to Dynamic Incremental Shear Loading. *Journal of the Mechanics and Physics of Solids*, 18:43–63, 1970.

[Carreker and Hibbard, 1957] R.P. Carreker and W.R. Hibbard. Tensile Deformation of Aluminum as a Function of Temperature, Strain Rate, and Grain Size. *Transactions of the AIME*, 209:1157–1163, 1957.

[Churchman, 1954] A.T. Churchman. The slip modes of titanium and the effect of purity on their occurence during tensile deformation of single crystals. *Proceedings of the Royal Society of London*, A 226:216–226, 1954.

[Conrad, 1964] H. Conrad. Thermally Activated Deformation of Metals. *Journal of Metals*, 16:582–588, 1964.

[Conrad, 1981] H. Conrad. Effect of Interstitial Solutes on the Strength and Ductility of Titanium. *Progess in Materials Science*, 26:123–403, 1981.

[Cottrell and Stokes, 1955] A.H. Cottrell and R.J. Stokes. Effects of temperature on the plastic properties of aluminium crystals. *Proceedings of the Royal Society of London*, A 233:17–34, 1955.

[Deve and Asaro, 1989] H.E. Deve and R.J. Asaro. The Development of Plastic Failure Modes in Crystalline Materials: Shear Bands in FCC Polycrystals. *Metallurgical Transactions*, 20A:579–593, 1989.

[Doner and Conrad, 1973] M. Doner and H. Conrad. Deformation Mechanisms in Commercial Ti-50A (0.5 at. pct. O_{eq}) at Intermediate and High Temperatures (0.3-0.6T_m). *Metallurgical Transactions A*, 4:2809–2817, 1973.

[Dorn *et al.*, 1949] J.E. Dorn, A. Goldberg, and T.E. Tietz. The Effect of Thermal-mechanical History on the Strain Hardening of Metals. *Transactions of the AIME*, 180:205–224, 1949.

[Duffy, 1974] J. Duffy. Some experimental results in dynamic plasticity. In *Mechanical Properties at High Rates of Strain*, pages 72–80. 1974.

[Duffy, 1982] J. Duffy. The Dynamic Plastic Deformation of Metals: A Review. *Materials Laboratory, Wright-Patterson Air Force Base, Ohio*, 1982.

[Eleiche, 1980] A-S. M. Eleiche. The Influence of Strain-Rate History and Temperature on the Shear of Commercially-Pure Titanium. *Titanium '80 Science and Technology: Proceedings of the Fourth International Conference on Titanium*, 2:831–840, 1980.

[Frost and Ashby, 1982] H.J. Frost and M.F. Ashby. *Deformation Mechanism Maps.* Pergamon Press, New York, 1982.

[Gil-Sevillano *et al.*, 1980] J. Gil-Sevillano, P. Van Houtte, and E. Aernoudt. Large Strain Work Hardening and Textures. *Progress in Materials Science*, 25:69–412, 1980.

[Groves and Kelly, 1963] G.W. Groves and A. Kelly. Independent Slip Systems in Crystals. *Philosophical Magazine*, 8:877–887, 1963.

[Harren *et al.*, 1988] S.V. Harren, H.E. Deve, and R.J. Asaro. Shear Band Formation in Plane Strain Compression. *Acta Metallurgica*, 36:2435–2480, 1988.

[Havner, 1992] K.S. Havner. *Finite Plastic Deformation of Crystalline Solids.* Cambridge University Press, 1st edition, 1992.

[Hill and Rice, 1972] R. Hill and J.R. Rice. Constitutive analysis of elastic-plastic crystals at arbitrary strain. *Journal of the Mechanics and Physics of Solids*, 20:401–413, 1972.

[Hill, 1965] R. Hill. Continuum Micro-Mechanics of Elastoplastic Polycrystals. *Journal of the Mechanics and Physics of Solids*, 13:89–101, 1965.

[Hirsch *et al.*, 1978] J. Hirsch, R. Musick, and K. Lucke. Comparison between earing, R-values and 3-dimensional Orientation Distribution Fuctions of rolled copper and brass sheets. *ICOTOM 5*, 2:437–446, 1978.

[Hoge and Mukherjee, 1977] K.G. Hoge and A.K. Mukherjee. The Temperature and Strain Rate Dependence of the Flow Stress of Tantalum. *Journal of Material Science*, 12:1666–1672, 1977.

[Hutchinson, 1977] J.W. Hutchinson. Creep and Plasticity of Hexagonal Polycrystals as Related to Single Crystal Slip. *Metallurgical Transactions A*, 8A:1465–1469, 1977.

[ICOTOM, 1991] ICOTOM. Proceedings of Ninth International Conference on Texture of Materials. *Textures and Microstructures*, 14-18:1–1251, 1991.

[Kalidindi and Anand, 1994] S.R. Kalidindi and L. Anand. Macroscopic Shape Change and Evolution of Crystallographic Texture in Pre-Textured FCC Metals. *Journal of the Mechanics and Physics of Solids*, 42:459–490, 1994.

[Kalidindi *et al.*, 1992] S.R. Kalidindi, C.A. Bronkhorst, and L. Anand. Crystallographic texture evolution in bulk deformation processing of FCC metals. *Journal of the Mechanics and Physics of Solids*, 40:536–569, 1992.

[Kallend *et al.*, 1994] J.S. Kallend, U.F. Kocks, A.D. Rollett, and J.R. Wenk. popLA: the Preferred Orientation Package from Los Alamos. 1994.

[Klepaczko, 1967] J. Klepaczko. Effects of Strain-Rate History on the Strain Rate Hardening Curve of Aluminum. *Arch. Mech. Stosowanej*, 19:211–229, 1967.

[Klepaczko, 1968] J. Klepaczko. Strain-Rate History Effects for Polycrystalline Aluminum and the Theory of Intersections. *Journal of the Mechanics and Physics of Solids*, 16:255–266, 1968.

[Klepaczko, 1975] J. Klepaczko. Thermally Activated Flow and Strain Rate History Effects for some Polycrystalline f.c.c. Metals. *Materials Science and Engineering*, 18:121–135, 1975.

[Kocks *et al.*, 1975] U.F. Kocks, A.S. Argon, and M.F. Ashby. Thermodynamics and Kinetics of Slip. In *Progress in Material Science*. Pergamon Press, London, 1975.

[Kocks *et al.*, 1991] U.F. Kocks, J.S. Kallend, and A.C. Biondo. Accurate Representation of General Textures by a Set of Weighted Grains. *Textures and Microstructures*, 14-18:199–204, 1991.

[Kocks, 1976] U.F. Kocks. Laws for Work-Hardening and Low-Temperature Creep. *Journal of Engineering Materials and Technology*, 98:76–85, 1976.

[Kothari and Anand, 1997] M. Kothari and L. Anand. Elasto-Viscoplastic Constitutive Equations For Polycrystalline Metals: Application to Tantalum. *Journal of the Mechanics and Physics of Solids*, 1997.

[Krausz and Eyring, 1975] A.S. Krausz and H.E. Eyring. *Deformation Kinetics*. Wiley, New York, 1975.

[Lee and Backofen, 1966] D. Lee and W.A. Backofen. An Experimental Determination of the Yield Locus for Titanium and Titanium-Alloy Sheet. *Transactions of TMS-AIME*, 236:1077–1084, 1966.

[Lii *et al.*, 1970] Y. Lii, V. Ramachandran, and R.E. Reed-Hill. Some Aspects of the Variation of the Strain Anisotropy in Titanium. *Metallurgical Transactions*, 1:447–453, 1970.

[Lindholm, 1964] U.S. Lindholm. Some Experiments with the Split Hopkinson Pressure Bar. *Journal of the Mechanics and Physics of Solids*, 12:317–335, 1964.

[Lopatin *et al.*, 1992] C.M. Lopatin, C.L. Wittman, J.P. Swensen, and P.F. Perron. Dependency of Strain Rate Path of Mechanical Properties of Tantalum in Compression. In R. Asfahani, E. Chen, and A. Crowson, editors, *High Strain Rate Behavior of Refractory Metals and Alloys*, pages 241–247. The Minerals, Metals and Materials Society, 1992.

[Lush, 1990] A. M. Lush. *Computational Procedures For Finite Element Analaysis of Hot-Working.* PhD thesis, Massachusetts Institute of Technology, June 1990.

[Mandel, 1974] J. Mandel. Thermodynamics and Plasticity. In D. Domingos, J.J. Nina, M. N.R, and J.H Whitlaw, editors, *Proceedings of the International Symposium on Foundations of Continuum Thermodynamics*, page 283. McMillan, London, 1974.

[Mathur and Dawson, 1989] K.K. Mathur and P.R. Dawson. On Modeling the Development of Crystallographic Texture in Bulk Forming Processes. *International Journal of Plasticity*, 5:67–94, 1989.

[Mathur and Dawson, 1990] K.K. Mathur and P.R. Dawson. Texture Development During Wire Drawing. *ASME Journal of Engineering Materials and Technology*, 112:292–297, 1990.

[McHargue and Hammond, 1953] C.J. McHargue and J.P. Hammond. Deformation Mechanisms in Titanium At Elevated Temperatures. *Acta Metallurgica*, 1:700–705, 1953.

[Nagtegaal and Taylor, 1968] J.C. Nagtegaal and L.M. Taylor. COMPARISON OF IMPLICIT AND EXPLICIT FINITE ELEMENT METHODS FOR ANALYSIS OF SHEET FORMING PROBLEMS. 242:1317–1326, 1968.

[Nemat-Nasser *et al.*, 1994] S. Nemat-Nasser, Y.F. Li, and J.B. Isaacs. Experimental/computational evaluation of flow stress at high strain rates with application to adiabatic shear banding. *Mechanics of Materials*, 17:111–134, 1994.

[Orowan, 1940] E. Orowan. Problems of plastic gliding. *Philosophical transactions of the Royal Society of London A*, 52:8–22, 1940.

[Parks and Ahzi, 1990] D.M. Parks and S. Ahzi. Polycrystalline Plastic Deformation and Texture Evolution for Crystals Lacking Five Independent Slip Systems. *Journal of the Mechanics and Physics of Solids*, 38:701–724, 1990.

[Paton and Backofen, 1970] N.E. Paton and W.A. Backofen. Plastic Deformation of Titanium at Elevated Temperatures. *Metallurgical Transactions A*, 1:2839–2847, 1970.

[Paton *et al.*, 1973] N.E. Paton, J.C. Williams, and G.P. Rauscher. The Deformation of α-phase Titanium. *Titanium Science and Technology*, 2:1049–1069, 1973.

[Peirce *et al.*, 1982] D. Peirce, R.J. Asaro, and A. Needleman. An analysis of nonuniform and localized deformation in ductile single crystals. *Acta Metallurgica*, 30:1087–1119, 1982.

[Prantil *et al.*, 1995] V.C. Prantil, J.T. Jenkins, and P.R. Dawson. Modeling Deformation Induced Textures in Titanium Using Analytical Solutions For Constrained Single Crystal response. *Journal of the Mechanics and Physics of Solids*, 43:1283–1302, 1995.

[Rice, 1971] J.R. Rice. Inelastic Constitutive Relations for Solids: An Internal Variable Theory and its Application to Metal Plasticity. *Journal of the Mechanics and Physics of Solids*, 19:433–455, 1971.

[Rollett *et al.*, 1987] A.D. Rollett, G.R. Canova, and U.F. Kocks. The Effect of the Cube Texture Component on the Earing Behavior of Rolled f.c.c. Metals. *Proceedings of the Conference on Formability and Metallurgical Structures, Orlando, FL*, pages 147–157, 1987.

[Rosi *et al.*, 1953] F.D. Rosi, C.A. Dube, and B.H. Alexander. Mechanisms of Plastic Flow in Titanium – Determination of slip and twinning elements. *Transactions of the AIME*, 197:257–265, 1953.

[Rosi *et al.*, 1956] F.D. Rosi, F.C. Perkins, and L.L. Seigle. Mechanisms of Plastic Flow in Titanium At Low and High Temperatures. *Transactions of the AIME*, 206:115–122, 1956.

[Schmid and Boas, 1935] E. Schmid and W. Boas. *Plasticity of Crystals.* Chapman and Hall, London, 1935.

[Schoenfeld *et al.*, 1995] S.E. Schoenfeld, S. Ahzi, and R.J. Asaro. Elastic-Plastic Crystal Mechanics for Low Symmetry Crystals. *Journal of the Mechanics and Physics of Solids*, 43:415–446, 1995.

[Senseny *et al.*, 1978] P.E. Senseny, J. Duffy, and R.H. Hawley. Experiments on Strain Rate History and Temperature Effects During the Plastic Deformation of Close-Packed Metals. *Journal of Applied Mechanics*, 45:60–66, 1978.

[Simmons and Wang, 1971] G. Simmons and H. Wang. *Single Crystal Elastic Constants and Calculated Aggregate Properties.* The M.I.T Press, Cambridge, 1971.

[Staroselsky and Anand, 1997] A. Staroselsky and L. Anand. Inelastic Deformation of F.C.C. Materials by Slip and Twinning. *Submitted to Journal of the Mechanics and Physics of Solids*, 1997.

[Taylor, 1938a] G.I. Taylor. Analysis Of Plastic Strain In A Cubic Crystal. In *Stephen Timoshenko 60th Anniversary Volume*, pages 218–224. McMillan, New York, 1938.

[Taylor, 1938b] G.I. Taylor. Plastic Strain in Metals. *Journal of the Institute of Metals*, 62:307–324, 1938.

[Tenckhoff, 1970] E. Tenckhoff. Defocusing for the Schulz Tecnhique of Determining Preferred Orientation. *Journal of Applied Physics*, 41:3944–3948, 1970.

[Teodosiu and Sidoroff, 1976] C. Teodosiu and F. Sidoroff. A theory of finite elastoviscoplasticity of single crystals. *International Journal of Engineering Science*, 14:165–176, 1976.

[Teodosiu, 1970] C. Teodosiu. A dynamic theory of dislocations and its applications to the theory of the elastic-plastic continuum. In R. Simmons J.A., de Wit and R. Bullough, editors, *Proceedings of the Conference on Fundamental Aspects of Dislocation Theory*, page 837. 1970.

[Tucker, 1961] G.E.G. Tucker. Texture and Earing in Deep Drawing of Aluminum. *Acta Metallurgica*, 9:275–286, 1961.

[Vecchio, 1994] K.S. Vecchio. High-Strain, High Strain-Rate Deformation of Tantalum and Tantalum-Tungsten Alloys. *Supplement J. de. Phsique III*, 4:301–306, 1994.

[Wenk, 1985] H.-R. Wenk. *Preferred Orientation in Deformed Metals and Rocks: An Introduction to Modern Texture Analysis.* Academic Press, Inc., 1985.

[Williams and Blackburn, 1968] J.C. Williams and M.J. Blackburn. The Identification of a Non-Basal Slip Vector in Titanium and Titanium-Aluminum Alloys. *Physica Status Solidi*, 25:K1–K3, 1968.

[Wilson and Butler, 1961] D.V. Wilson and R.D. Butler. The Role of Cup-Drawing Tests in Measuring Drawability. *Journal of the Institute of Metals*, 90:473–483, 1961.

THESIS PROCESSING SLIP

FIXED FIELD: ill. _____ name _____

index _____ biblio _____

▶ COPIES: (Archives) Aero Dewey (Eng) Hum

Lindgren Music Rotch Science

TITLE VARIES: ▶☐ _____

_____

_____

NAME VARIES: ▶☐ _____

_____

IMPRINT: (COPYRIGHT) _____

▶ COLLATION: 214 l

_____

▶ ADD. DEGREE: _____ ▶ DEPT.: _____

SUPERVISORS: _____

_____

NOTES:

cat'r: date:

page: F47

▶ DEPT: M.E.

▶ YEAR: 1998 ▶ DEGREE: Ph.D.

▶ NAME: BALASUBRAMANIAN, Srihari